University of Liverpool
Department of Chemistry
Surface Science Research Centre

Towards Formation of Graphene on Cu(110) Surface from Thermal Decomposition of Perylene

Thesis submitted in accordance with the requirements of the University of Liverpool for the degree of

Doctor of Philosophy in Chemistry

Dexter Tomas Rasonabe

October 2016

Abstract

This thesis spans three different topics of experiments based on measurements from low-energy electron diffraction (LEED), reflection-absorption infrared spectroscopy (RAIRS), and scanning tunneling microscopy (STM). The first topic is related to studies of the structure of perylene on the Cu(110) surface, in the interest of main applications in electronics and optoelectronics. The RAIRS measurements show chemisorption of perylene molecules in direct contact to the Cu(110) surface based on red-shift in the vibrational frequencies. The appearance of two sets of red shifts for the same set of vibrational modes supports the proposed model for the commensurate (5x5) superstructure from a past report. STM measurements of monolayer growth at room temperature, in conjunction with simple two-dimensional models, show co-existence of chiral commensurate superstructures, (5x5) superstructure, and (8x5) superstructures. The analysis suggests the most stable adsorption site for perylene on the Cu(110) surface is the atop site.

The second and main topic is related to studies of the structure of graphene formation on the Cu(110) surface at low and high growth temperatures, in the interest of fundamental studies of graphene-metal interfaces and to develop a simple synthetic method. The synthetic method is based on thermal decomposition of a hydrocarbon, but the process is unique from those in reports so far because the hydrocarbon used is the complex-molecule perylene, in contrast to a simple aliphatic hydrocarbon. The effectiveness of the conversion to graphene exceeds 50%. LEED measurements show increase in growth temperature develops the graphene formation from disordered epitaxial orientation towards the most stable epitaxial orientations at ±5° but cannot eliminate the partial disorder from less-stable epitaxial orientations around │±19°│ - │±30°│. Furthermore, direct visualization from STM measurements shows increase in growth temperature develops the graphene formation from percolated network of minute graphene domains and clusters into large domains in isolated islands. STM measurements also show the Moiré superstructures of graphene on the Cu(110) surface are chiral, a characteristic of importance to applications in enantioselective catalysis and

chiral resolution. Simple two-dimensional models are shown to be able to estimate the epitaxial orientation of graphene from the Moiré pattern. The statistical distribution of epitaxial orientation from the STM data shows another preference for some orientation somewhere between $|\pm 25°|$ and $|\pm 30°|$ exists, second to the most preferred orientations at ±5°.

The third topic is related to STM characterization of a Co-TPP overlayer on sub-monolayer graphene on the Cu(110) surface, in the interest of integration of graphene to organic materials and functionalization of graphene. The growth of the Co-TPP overlayer shows the adsorption on top of graphene is weaker than the adsorption on bare Cu(110) surface. Co-TPP forms self-assembled superstructures on top of graphene. The self-assembled Co-TPP superstructures demonstrate self-healing character.

Table of Contents

Acknowledgements

First and foremost I express deep appreciation to Professor Rasmita Raval for the chance to work on a postgraduate research, and for the valuable discussions. I thank Dr. Sam Haq for numerous contributions to the research and the thesis. I thank former fellow postgraduate research students Dr. Tommaso Sgrilli, Dr. Bareld Wit, and Dr. Takuma Omiya who shared knowledge and ideas on various topics and made massive deals of cooperation and support. Special thanks to Mr. Gary Ledger who sparked the idea of graphene formation from perylene and motivated me to pursue the experiments on Co-TPP. I thank the persons close to me, Alekzandra Nicole, Kate Destine, and Zinna Marie, for so much love, care, patience, motivation, and inspiration as I worked on the research and the thesis. I express innermost gratitude to our Creator for the mission.

Financial support came from the FP7 Marie Curie Actions of the European Commission under the Initial Training Network “Surface for Molecular Recognition at the Atomic Level (SMALL)“ (MCITN-238804).

Chapter 1
Introduction

1.1 The Research

Studies of surfaces deal with physical phenomena at the topmost few atomic or molecular layers of solid materials. The measurement techniques must be both sensitive and limited to the narrow extent of the surface in space. One specific approach utilizes model surfaces with well-defined structure and composition to ensure controlled reproducible outcome. The experiments can be performed under various conditions. Ultra-high vacuum (UHV) conditions maintain well-defined surfaces clean over the period of experiment.

Adsorption and self-assembled nanostructure formation of complex organic molecules offer an important means to introduce functionalities at surfaces[1]. Important applications include catalysis, sensors, electronics, and optoelectronics. However, there is a critical need for fundamental comprehension of molecule-surface interaction and intermolecular interaction. The ultimate target is the absolute control of molecular function and self-assembled formation to tailor the material properties for enhanced performance and novel functions. Well-defined metal surfaces offer model templates to control the experimentation of complex organic molecules at surfaces. One complex organic molecule is perylene. The interest in perylene can be traced to possible application as an organic semiconductor[2,3] in electronics[4,5] and optoelectronics[6]. Perylene on Cu(110) surface has been reported in a number of papers[7–12]. However, discrepancies in the conclusion on the multilayer structure of perylene on Cu (110) surface exist between two independent groups. The first research topic for the thesis studies perylene on Cu(110) surface and hopes to shed light on the discrepancies. The outcomes are presented in Chapter 3.

Graphene has become a material of tremendous interest when the report of first isolation came out in 2005[13]. The award of 2010 Nobel Prize in Physics to the pioneers of the experiments in graphene is a reflection of the tremendous

impact in various fields[14]. Examples of important commercial applications are electronics and optoelectronics[15]. There has been renewed interest in graphene on metal surfaces[16,17] and one of the important issues is to develop a method of synthesis[16,18]. The main objective of the thesis is to come up with an in-situ laboratory-scale method of preparation on the Cu(110) surface. The objective had been set at the time when not one report of graphene on Cu(110) surface had been found in the scientific literature. The next section introduces an overview of the common synthetic methods for producing graphene on metal surfaces. Attempts were made to prepare graphene on a Cu(110) surface from thermal decomposition of ethylene. Ethylene was leaked into the entire volume of a vacuum chamber to a pressure of 10^{-5} mbar, in contrast to the use of a nozzle for injection of ethylene over the surface of the Cu substrate as described in a past report[19]. Repeated quick ramps of the substrate from room temperature to 1250 K were made eight times under the ethylene pressure[19]. However the process did not lead to formation of graphene based on tests from LEED measurements, perhaps due to the volatile nature of ethylene on Cu surfaces.

There came the idea to use perylene – a complex aromatic hydrocarbon in contrast to simple aliphatic ethylene. Past reports show intact perylene molecules desorb from the multilayer but not from the monolayer at temperatures over 350 K [9,10] and the monolayer is stable up to 550 K until decomposition starts[10]. There are four possible criteria to utilize a particular hydrocarbon as a precursor to graphene in thermal decomposition on a metal surface. First the multilayer should be able to desorb in order to ensure the formation of graphene is held to no more than a monolayer i.e. there is no intention to prepare a complete monolayer of graphene for fundamental research purposes. Second the hydrocarbon should be able to hold onto the metal surface until thermal decomposition. Third the hydrocarbon should be able to deposit non-volatile carbon species on the metal surface upon thermal decomposition. Fourth the non-volatile carbon species should be able to diffuse on the metal surface and form graphene at temperatures below the melting point of the metal substrate. Perylene on Cu(110) surface satisfies the first and

second criteria based on the reports[9,10]. The unknown fact however remains whether the carbon entities deposited from the decomposition reaction are non-volatile and form a graphene overlayer. These issues are therefore there to be made clear from the outcome of attempts to prepare graphene on Cu(110) surface based on thermal decomposition of perylene on the surface. Indeed, the attempts found success hence the third and fourth criteria are satisfied. The second research topic for the thesis has turned out to be characterization of graphene formation on Cu(110) surface from thermal decomposition of perylene. The outcomes are presented in Chapter 4.

Commercial application of graphene has to address the issue of integration with other materials. Certain properties of the material need modification in order to become suitable for adaptation to the current modern technologies. One of the means to introduce functionalities into graphene is adsorption of complex organic molecules. On the other hand, graphene can be used as the well-defined surface to produce advances in studies of adsorption and superstructure formation of complex organic molecules to understand molecule-surface interaction and intermolecular interaction, for the same reason as absolute control of molecular function and self-assembled formation to tailor the material properties for enhanced performance and novel functions. The development of interest in adsorption of complex organic molecules on graphene is apparent in continued publication of reviews[16,20–25]. Porphyrins are part of the complex organic molecules of interest. The topic of porphyrins on surfaces has been reviewed in a recent publication[26]. One of the porphyrins is cobalt-tetraphenylporphyrin or Co-TPP, a molecule of scientific and technological interest as a catalyst in various reactions[27,28] and solar-energy conversion[29–31], as an active component in electrodes of fuel cells[32–34] and in sensors[35], as an oxide-induced switch[36] or a single-molecule diode[37] in molecular nano-devices. Moreover, the spin moment of the magnetic Co-atom at the core of the porphyrin molecule offers a prospect to store information as a bit of data for applications in molecular spintronics. Recent unpublished work based on X-ray magnetic circular dichroism (XMCD) experiments has shown well-ordered robust assemblies of single-molecule magnets on a non-magnetic

Cu(110) surface can allow spin moments to survive the adsorption process and retain intrinsic magnetisation, and therefore demonstrates the potential to fabricate a device and address individual adsorbed molecules as single discrete magnets for the next generation of ultra-dense data storage. However, Co-TPP on Cu(110) surface exhibits reduced magnetisation as the magnetic moment can be quenched due to interactions between the molecule and the surface. Perhaps a means to decouple the magnetic Co-atom from the Cu(110) surface and enhance the magnetic characteristics is to utilise graphene as a spacer at the interface between the molecule and the surface. Before further XMCD experiments determine whether graphene effects isolation of the magnetic Co-atom core from interactions with the Cu surface upon adsorption, there is first a need to define the Co-TPP overlayer on graphene. However, there exists no report on studies of Co-TPP adsorption on graphene so far.

Chapter 4 shows that Moiré superstructures of epitaxial graphene on Cu(110) surface are chiral. The word *chiral* describes an object whose mirror image is non-superimposable. Chiral surfaces and chiral functionalization of surfaces are important for applications in enantioselective catalysis and chiral resolution[38,39]. So far no report exists on molecular adsorption on a chiral Moiré superstructure of graphene on a metal surface. High-resolution STM measurements perform direct visualization of chiral formations at various length scales in real space upon molecular adsorption at well-defined surfaces[40]. The length scales[41] include the levels of chiral conformation of adsorbate and self-assembled chiral organization in extended periodic motif[42]. A report has been made on the chirogenesis of Co-TPP upon adsorption on Cu(110) surface at the levels of molecular conformation and supramolecular organization[43]. Reports made up to now are focused on chirogenesis of achiral molecules[43–47] and chiral expressions of intrinsic chiral molecules[47–54], both at achiral surfaces. The experimental work for Chapter 5 explores adsorption of Co-TPP molecules on top of graphene islands on the Cu(110) surface based on STM measurements to represent fundamental interest in the distinct combination of achiral molecule on chiral surface.

The thesis is an outcome of experiments on the surface of (110)-oriented single-crystal Cu substrates under UHV conditions. The specific measurement techniques were low-energy electron diffraction (LEED), reflection adsorption infrared spectroscopy (RAIRS), and scanning tunneling microscopy (STM).

1.2 Overview on Graphene and Synthesis on Metal Surfaces

The first observation of ‘graphene’ formation on metal surfaces can be traced back to the late 1960’s when carbon impurities segregated to the surface during preparation of single-crystal Pt substrates[55–58]. ‘Graphene’ on metal surfaces had become a topic of investigation in surface science from then on even before the first actual isolation of graphene but the terms used back then had been ‘monolayer graphite’, ‘graphitic carbon overlayer’, or ‘ultra-thin graphite film’[59]; the investigation of ‘graphene’ on metal surfaces in the past had been kept most of the time as a subject of studies within the mere interest of heterogeneous catalysis[60,61] and had been found to be a reason for deactivation of catalyst surfaces[62,63]. There had also been technological interest to understand the properties of ‘graphene’ interface with metals in intercalated graphite compounds for storage of energy and other applications[64]. ‘Graphene’ on metal surfaces in those times had been considered to possess similar properties to those of graphite[65–68]. However, in the 1990’s there has been renewed interest in the interfacial properties of ‘graphene’ on metal and metal-carbide surfaces from the perspective of fundamental studies on low-dimensional systems subsequent to observation of anomalous softening in the phonon dispersions[59].

Graphene has become a game-changer in the course of scientific and technological development for mankind upon the report of first isolation in 2005[13]. The isolation of graphene has led to discoveries of new-found phenomena, remarkable properties of the material[69–72], other two-dimensional materials[73], and promises of vast technological applications in various areas[15,74–77]. Graphene from then on has found distinction from graphite or just a mere monolayer of graphite, and has no longer been referred to in other terms but ‘graphene’. There has been renewed interest for graphene on metal surfaces[16,17]. The important issues for graphene on metal surfaces include the synthesis and mechanism of growth processes[16,18], the structure of graphene-metal interfaces[16,17], the interaction between graphene and various metal

surfaces[17], the extent to which the structure and interaction with the metal affects the properties of graphene[17] and performance of metal contacts in graphene-based devices[78].

There exist various methods to produce graphene on metal surfaces. Carbon atoms can be supplied from either the inside or the outside of the metal substrate. Formation of graphene from the former occurs in the spontaneous process of segregation of carbon atoms out from the bulk of certain substrate materials onto the surface at certain temperatures. Carbon atoms can exist in solid solution within most metals[79] and are present therein to some extent as impurities in common cases but can be made present also through intentional carbon-doping of pure metals. Graphene formation through segregation has been observed on transition-metal substrates of Co[80], Fe[81], Ni[82–84], Pd[80], Pt[55–58], and Ru[85–88]. However not all metals exhibit the phenomenon of carbon segregation. Data on the phase diagram for binary carbon-copper alloy shows C is neither soluble within Cu in the solid phase nor forms a carbide phase[89] so formation of graphene through carbon segregation can not be expected to occur on Cu substrates. Some metals are able to form a metal carbide phase[79] and exhibit precipitation of surface carbides at certain temperatures to preclude formation of graphene[90,91].

Formation of graphene from carbon atoms supplied outside of the metal substrate can be done through deposition of carbonaceous substances and subsequent reaction thereof. Various methods have been reported[18,92,93] and these methods include thermal decomposition of hydrocarbons[19,87,94–105], chemical vapour deposition[106,107], reduction of graphene oxide[108], heat/plasma-treatment of spin-coated polymer[109,110], molecular-beam epitaxy[111], laser ablation, and surface-assisted bottom-up fabrication from chemical reaction of molecular precursors[112–114]. The main motivation to the development of most of these processes has been to achieve industrial-scale production of graphene wafers with large domains for purposes of commercial applications. However synthesis of graphene on metal surfaces based on on-surface thermal decomposition of hydrocarbons has proved to be a simple laboratory-scale in-situ method for purposes of fundamental research under ultra-high vacuum

conditions. For the same reason, thermal decomposition of hydrocarbon is the method of choice for preparation of graphene on Cu(110) surface in the present investigation. Note, chemical vapour deposition in a mixture of methane and hydrogen is the industrial-scale method used in production of graphene on Cu substrates[106,115].

The process of graphene formation through thermal decomposition of hydrocarbons can be generalized into three main steps. The first step involves adsorption of hydrocarbon molecules on a metal surface. The second step involves a combination of break-down or dehydrogenation of the hydrocarbon molecules and bond formation between the hydrocarbon molecules on the metal surface at increased temperatures until some species of pure carbon deposit on the metal surface. The subsequent steps involve the epitaxial growth of graphene from these carbon species with sufficient temperature. Details of each phenomenon which occur within these steps in the actual formation of graphene for a particular combination of hydrocarbon and metal surface in a given set of growth parameters can be complicated and involve certain competition between kinetics and thermodynamics.

The technique to produce graphene on metal surfaces based on thermal decomposition of hydrocarbons can be performed in two variations. One variation is the pre-adsorption of hydrocarbon precursors on the metal surface at room temperature from exposure of the metal substrate under an environment of the hydrocarbon at certain pressures prior to elevation of substrate temperature under ultra-high vacuum conditions. The other variation is the exposure under an environment of the hydrocarbon at certain pressures whilst the metal substrate is elevated at certain temperatures. The methods utilized and reported so far for the preparation of graphene on metal surfaces based on thermal decomposition of hydrocarbons make use of just the simplest aromatic or the shortest-chain aliphatic hydrocarbon molecules as the precursor adsorbate. Used the most are ethylene (C_2H_4)[61,87,94,100,116] and propylene (C_3H_6)[96,99]. The other hydrocarbons are methane[117,118], acetylene[61,119,120], butene[65], cyclohexane[65,119,121], n-heptane[65,121], benzene[65,119,121,122], and toluene[65,121].

Metal surfaces are known to be reactive and act as catalysts of decomposition reactions for hydrocarbons. The multilayer of simple hydrocarbons on metal surfaces is expected to desorb due to the gaseous character of these compounds under vacuum. Simple hydrocarbons on top of graphene are expected to desorb at elevated temperatures due to the inert character of graphene. Therefore the decomposition reaction of simple hydrocarbons is limited to molecules in contact with the metal surface[62,63] and the formation of graphene on metal surfaces terminates upon monolayer saturation. The process however is assumed to occur under certain conditions when segregation of carbon atoms onto the surface out of the bulk of the substrate is suppressed or does not happen for the substrate metal.

The relative ease of graphene preparation on the surfaces of Fe[96], Ir[97,103], Ni[102,123], Pt[116,124], Rh[61,105], and Ru[87,95] metal substrates based on decomposition of short-chain hydrocarbon molecules is evident from the number of published reports and can be attributed to the catalytic nature of these metals. On the other hand, the preparation of graphene on Cu surfaces based on thermal decomposition of ethylene has been reported to require considerable ethylene pressure and repeated ramps of the substrate from ambient temperature to the growth temperature of graphene several times in order to form some graphene on the surface[19]. Compromise in level of vacuum in the preparation chamber intended for operation under UHV conditions could pose problems to the set-up and contamination to other experiments. Moreover, the melting point of Cu is close to the growth temperatures for graphene on Cu surfaces[19]. These issues could be the reason for the existence of a small number of reports on experiments for graphene on well-defined Cu surfaces[19,98].

References

1. Barlow, S. M. & Raval, R. Complex organic molecules at metal surfaces: bonding, organisation and chirality. *Surf. Sci. Rep.* **50,** 201–341 (2003).

2. Inokuchi, H., Kuroda, H. & Akamatu, H. On the electrical conductivity of the organic thin films: perylene, coronene and violanthrene. *Bull. Chem. Soc. Jpn.* **34,** 749–753 (1961).

3. Sano, M. & Akamatu, H. Semiconductivity and absorption spectrum of perylene single crystal. *Bull. Chem. Soc. Jpn.* **34,** 1569–1571 (1961).

4. Schön, J. H., Kloc, C. & Batlogg, B. Perylene: a promising organic field-effect transistor material. *Appl. Phys. Lett.* **77,** 3776 (2000).

5. Kim, S. H. *et al.* Organic field-effect transistors using perylene. *Opt. Mater. (Amst).* **21,** 439–443 (2003).

6. Toda, Y. & Yanagi, H. Electroluminescence of epitaxial perylene films. *Appl. Phys. Lett.* **69,** 2315 (1996).

7. Chen, Q., Rada, T., McDowall, A. & Richardson, N. V. Epitaxial growth of a crystalline organic semiconductor: perylene/Cu{110}. *Chem. Mater.* **14,** 743–749 (2002).

8. Chen, Q., McDowall, a. J. & Richardson, N. V. Growth and evolution of perylene thin films on Cu(110). *Chem. Mater.* **15,** 4113–4117 (2003).

9. Hänel, K. *et al.* Organic molecular-beam deposition of perylene on Cu(110): results from near-edge x-ray absorption spectroscopy, x-ray photoelectron spectroscopy, and atomic force microscopy. *J. Mater. Res.* **19,** 2049–2056 (2004).

10. Söhnchen, S., Hänel, K., Birkner, A., Witte, G. & Wöll, C. Molecular beam deposition of perylene on copper: formation of ordered phases. *Chem. Mater.* **17,** 5297–5304 (2005).

11. Witte, G., Hänel, K., Söhnchen, S. & Wöll, C. Growth and morphology of thin films of aromatic molecules on metals: the case of perylene. *Appl. Phys. A* **82,** 447–455 (2006).

12. Witte, G., Hänel, K., Busse, C., Birkner, A. & Wöll, C. Molecules coining patterns into a metal: the hard core of soft matter. *Chem. Mater.* **19,** 4228–4233 (2007).

13. Novoselov, K. S. *et al.* Electric field effect in atomically thin carbon films. *Science* **306,** 666–9 (2004).

14. Hancock, Y. The 2010 Nobel Prize in physics—ground-breaking experiments on graphene. *J. Phys. D. Appl. Phys.* **44,** 473001 (2011).

15. Wu, H.-Q., Linghu, C.-Y., Lu, H.-M. & Qian, H. Graphene applications in electronic and optoelectronic devices and circuits. *Chinese Phys. B* **22,** 098106 (2013).

16. Batzill, M. The surface science of graphene: Metal interfaces, CVD synthesis, nanoribbons, chemical modifications, and defects. *Surf. Sci. Rep.* **67,** 83–115 (2012).

17. Wintterlin, J. & Bocquet, M.-L. Graphene on metal surfaces. *Surf. Sci.* **603,** 1841–1852 (2009).

18. Whitener, K. E. & Sheehan, P. E. Graphene synthesis. *Diam. Relat. Mater.* **46,** 25–34 (2014).

19. Gao, L., Guest, J. R. & Guisinger, N. P. Epitaxial graphene on Cu(111). *Nano Lett.* **10,** 3512–6 (2010).

20. Wee, A. T. S. & Chen, W. Molecular interactions on epitaxial graphene. *Phys. Scr.* **T146,** 014007 (2012).

21. Hong, G. *et al.* Recent progress in organic molecule/graphene interfaces. *Nano Today* **8,** 388–402 (2013).

22. Huang, H. & Shen Wee, A. T. Adsorption on epitaxial graphene on SiC(0001). *J. Mater. Res.* **29,** 447–458 (2013).

23. Mao, H. Y. *et al.* Manipulating the electronic and chemical properties of graphene via molecular functionalization. *Prog. Surf. Sci.* **88,** 132–159 (2013).

24. Kong, L., Enders, A., Rahman, T. S. & Dowben, P. A. Molecular adsorption on graphene. *J. Phys. Condens. Matter* **26,** 443001 (2014).

25. MacLeod, J. M. & Rosei, F. Molecular self-assembly on graphene. *Small* **10,** 1038–49 (2014).

26. Auwärter, W., Écija, D., Klappenberger, F. & Barth, J. V. Porphyrins at interfaces. *Nat. Chem.* **7,** 105–20 (2015).

27. Zhang, F. *et al.* Cycloaddition reaction of propylene oxide and carbon dioxide over NaX zeolite supported metalloporphyrin catalysts. *Catal. Letters* **144,** 1894–1899 (2014).

28. Subbarayan, V., Jin, L.-M., Xin, C. & Zhang, X. P. Room temperature activation of aryloxysulfonyl azides by [Co(II)(TPP)] for selective radical

aziridination of alkenes via metalloradical catalysis. *Tetrahedron Lett.* **56,** 3431–3434 (2015).

29. Nishikubo, T., Hijikata, C. & Iizawa, T. Photochemical property of the polymer-bearing pendant norbornadiene moiety and storage stability of the resulting quadricyclane group in the polymer. *J. Polym. Sci. Part A Polym. Chem.* **29,** 671–676 (1991).

30. Iizawa, T., Hijikata, C. & Nishikubo, T. Synthesis and solar energy storage property of polymers containing norbornadiene moieties. *Macromolecules* **25,** 21–26 (1992).

31. Konigstein, C. Photoinduced hydrogen production from aqueous solution—frontiers and new trends. *Int. J. Hydrogen Energy* **22,** 471–474 (1997).

32. Zuo, G., Yuan, H., Yang, J., Zuo, R. & Lu, X. Study of orientation mode of cobalt-porphyrin on the surface of gold electrode by electrocatalytic dioxygen reduction. *J. Mol. Catal. A Chem.* **269,** 46–52 (2007).

33. Zhang, W., Chen, J., Wagner, P., Swiegers, G. F. & Wallace, G. G. Polypyrrole/Co-tetraphenylporphyrin modified carbon fibre paper as a fuel cell electrocatalyst of oxygen reduction. *Electrochem. commun.* **10,** 519–522 (2008).

34. Murayama, T., Tazawa, S., Takenaka, S. & Yamanaka, I. Catalytic neutral hydrogen peroxide synthesis from O_2 and H_2 by PEMFC fuel. *Catal. Today* **164,** 163–168 (2011).

35. D'Souza, F., Hsieh, Y., Wickman, H. & Kutner, W. β-cyclodextrin and carboxymethylated β-cyclodextrin polymer film modified electrodes, hosting cobalt porphyrins, as sensors for electrocatalytic determination of oxygen dissolved in solution. *Electroanalysis* **9,** 1093–1101 (1997).

36. Wäckerlin, C. *et al.* Controlling spins in adsorbed molecules by a chemical switch. *Nat. Commun.* **1,** 61 (2010).

37. Zoldan, V. C., Faccio, R. & Pasa, A. A. N and P type character of single molecule diodes. *Sci. Rep.* **5,** 8350 (2015).

38. Raval, R. in *Nanostructured Catal.* (Scott, S., Crudden, C. & Jones, C.) 179–193 (Kluwer Academic, 2003).

39. Forster, M. & Raval, R. in *Model Syst. Catal.* (Rioux, R.) 97–115 (Springer New York, 2010).

40. Mark, A. G., Forster, M. & Raval, R. Direct visualization of chirality in two dimensions. *Tetrahedron: Asymmetry* **21,** 1125–1134 (2010).

41. Raval, R. Nanoscale insights into the creation of chiral surfaces. *J. Mol. Catal. A Chem.* **305,** 112–116 (2009).

42. Raval, R. Chiral expression from molecular assemblies at metal surfaces: insights from surface science techniques. *Chem. Soc. Rev.* **38,** 707–21 (2009).

43. Donovan, P., Robin, A., Dyer, M. S., Persson, M. & Raval, R. Unexpected deformations induced by surface interaction and chiral self-assembly of Co(II)-tetraphenylporphyrin (Co-TPP) adsorbed on Cu(110): a combined STM and periodic DFT study. *Chemistry* **16,** 11641–52 (2010).

44. Liu, N., Darling, G. R. & Raval, R. Dynamic chiral flipping within strongly chemisorbed molecular monolayers at surfaces. *Chem. Commun.* **47,** 11324–6 (2011).

45. In't Veld, M., Iavicoli, P., Haq, S., Amabilino, D. B. & Raval, R. Unique intermolecular reaction of simple porphyrins at a metal surface gives covalent nanostructures. *Chem. Commun.* 1536–8 (2008).

46. Classen, T. *et al.* Hydrogen and coordination bonding supramolecular structures of trimesic acid on Cu(110). *J. Phys. Chem. A* **111,** 12589–603 (2007).

47. Humblot, V. & Raval, R. Chiral metal surfaces from the adsorption of chiral and achiral molecules. *Appl. Surf. Sci.* **241,** 150–156 (2005).

48. Forster, M., Dyer, M. S., Persson, M. & Raval, R. Assembly of chiral amino-acids at surfaces from a single molecule perspective: proline on Cu(110). *Top. Catal.* **54,** 13–19 (2011).

49. Forster, M., Dyer, M. S., Persson, M. & Raval, R. Tailoring homochirality at surfaces: going beyond molecular handedness. *J. Am. Chem. Soc.* **133,** 15992–6000 (2011).

50. Raval, R. Creating chiral architectures at metal surfaces. *J. Phys. Condens. Matter* **14,** 4119–4132 (2002).

51. Mark, A. G., Forster, M. & Raval, R. Recognition and ordering at surfaces: the importance of handedness and footedness. *Chemphyschem* **12,** 1474–80 (2011).

52. Barlow, S. & Raval, R. Nanoscale insights in the creation and transfer of chirality in amino acid monolayers at defined metal surfaces. *Curr. Opin. Colloid Interface Sci.* **13,** 65–73 (2008).

53. Raval, R. Chemistry: mirrors in flatland. *Nature* **425,** 463–4 (2003).

54. Lorenzo, M., Baddeley, C., Muryn, C. & Raval, R. Extended surface chirality from supramolecular assemblies of adsorbed chiral molecules. *Nature* **404,** 376–9 (2000).

55. Hagstrom, S., Lyon, H. & Somorjai, G. Surface structures on the clean platinum (100) surface. *Phys. Rev. Lett.* **15,** 491–493 (1965).

56. Lyon, H. B. Low-energy electron-diffraction study of the clean (100), (111), and (110) faces of platinum. *J. Chem. Phys.* **46,** 2539 (1967).

57. Morgan, A. E. & Somorjai, G. A. Low energy electron diffraction studies of gas adsorption on the platinum (100) single crystal surface. *Surf. Sci.* **12,** 405–425 (1968).

58. May, J. W. Platinum surface LEED rings. *Surf. Sci.* **17,** 267–270 (1969).

59. Oshima, C. & Nagashima, A. Ultra-thin epitaxial films of graphite and hexagonal boron nitride on solid surfaces. *J. Phys. Condens. Matter* **9,** 1–20 (1997).

60. McCarty, J. G. & Madix, R. J. The adsorption of CO, H_2, CO_2 and H_2O on carburized and graphitized Ni(110). *Surf. Sci.* **54,** 121–138 (1976).

61. Castner, D., Sexton, B. & Somorjai, G. LEED and thermal desorption studies of small molecules (H_2, O_2, CO, CO_2, NO, C_2H_4, C_2H_2 and C) chemisorbed on the rhodium (111) and (100) surfaces. *Surf. Sci.* **71,** 519–540 (1978).

62. Somorjai, G. A. Catalysis and surface science. *Surf. Sci.* **89,** 496–524 (1979).

63. Somorjai, G. A. Classification of catalytic reactions based on molecular surface science. *React. Kinet. Catal. Lett.* **35,** 37–87 (1987).

64. Dresselhaus, M. S. & Dresselhaus, G. Intercalation compounds of graphite. *Adv. Phys.* **30,** 139–326 (1981).

65. Zi-Pu, H., Ogletree, D. F., Van Hove, M. A. & Somorjai, G. A. LEED theory for incommensurate overlayers: application to graphite on Pt(111). *Surf. Sci.* **180,** 433–459 (1987).

66. Rosei, R. *et al.* Structure of graphitic carbon on Ni(111): A surface extended-energy-loss fine-structure study. *Phys. Rev. B* **28,** 1161–1164 (1983).

67. Rosei, R. *et al.* Electronic structure of carbidic and graphitic carbon on Ni(111). *Phys. Rev. B* **29,** 3416–3422 (1984).

68. Rosei, R. *et al.* Photoemission spectroscopy investigation of the electronic structure of carbidic and graphitic carbon on Ni (111). *Solid State Commun.* **46,** 871–874 (1983).

69. Novoselov, K. S. *et al.* Two-dimensional gas of massless Dirac fermions in graphene. *Nature* **438,** 197–200 (2005).

70. Geim, A. K. & Novoselov, K. S. The rise of graphene. *Nat. Mater.* **6,** 183–91 (2007).

71. Geim, A. K. & MacDonald, A. H. Graphene: exploring carbon flatland. *Phys. Today* **60,** 35–41 (2007).

72. Katsnelson, M. I. Graphene: carbon in two dimensions. *Mater. Today* **10,** 20–27 (2007).

73. Butler, S. Z. *et al.* Progress, challenges, and opportunities in two-dimensional materials beyond graphene. *ACS Nano* **7,** 2898–926 (2013).

74. Novoselov, K. S. *et al.* A roadmap for graphene. *Nature* **490,** 192–200 (2012).

75. Choi, W., Lahiri, I., Seelaboyina, R. & Kang, Y. S. Synthesis of graphene and its applications: a review. *Crit. Rev. Solid State Mater. Sci.* **35,** 52–71 (2010).

76. Sundramoorthy, A. K. & Gunasekaran, S. Applications of graphene in quality assurance and safety of food. *TrAC Trends Anal. Chem.* **60,** 36–53 (2014).

77. Brownson, D. A. C., Kampouris, D. K. & Banks, C. E. An overview of graphene in energy production and storage applications. *J. Power Sources* **196,** 4873–4885 (2011).

78. Xia, F., Perebeinos, V., Lin, Y., Wu, Y. & Avouris, P. The origins and limits of metal-graphene junction resistance. *Nat. Nanotechnol.* **6,** 179–84 (2011).

79. Predel, B. Phase equilibria, crystallographic and thermodynamic data of binary alloys · B-Ba – C-Zr. Landolt-Börnstein - Gr. IV *Phys. Chem. Numer. Data Funct. Relationships Sci. Technol.* **5b,** (Springer-Verlag, 1992).

80. Hamilton, J. C. & Blakely, J. M. Carbon segregation to single crystal surfaces of Pt, Pd and Co. *Surf. Sci.* **91,** 199–217 (1980).

81. Grabke, H. J., Paulitschke, W., Tauber, G. & Viefhaus, H. Equilibrium surface segregation of dissolved nonmetal atoms on iron(100) faces. *Surf. Sci.* **63,** 377–389 (1977).

82. Isett, L. C. & Blakely, J. M. Segregation isosteres for carbon at the (100) surface of nickel. *Surf. Sci.* **58,** 397–414 (1976).

83. Shelton, J. C., Patil, H. R. & Blakely, J. M. Equilibrium segregation of carbon to a nickel (111) surface: A surface phase transition. *Surf. Sci.* **43,** 493–520 (1974).

84. Eizenberg, M. & Blakely, J. M. Carbon monolayer phase condensation on Ni(111). *Surf. Sci.* **82,** 228–236 (1979).

85. Grant, J. T. & Haas, T. W. A study of Ru(0001) and Rh(111) surfaces using LEED and Auger electron spectroscopy. *Surf. Sci.* **21,** 76–85 (1970).

86. Marchini, S., Günther, S. & Wintterlin, J. Scanning tunneling microscopy of graphene on Ru(0001). *Phys. Rev. B* **76,** 075429 (2007).

87. Vázquez de Parga, A. *et al.* Periodically rippled graphene: growth and spatially resolved electronic structure. *Phys. Rev. Lett.* **100,** 056807 (2008).

88. Sutter, P. W., Flege, J.-I. & Sutter, E. A. Epitaxial graphene on ruthenium. *Nat. Mater.* **7,** 406–11 (2008).

89. Predel, B. Phase equilibria, crystallographic and thermodynamic data of binary alloys · B-Ba – C-Zr. Landolt-Börnstein - Gr. IV *Phys. Chem. Numer. Data Funct. Relationships Sci. Technol.* **5b,** (Springer-Verlag, 1992).

90. Gall', N. R., Rut'kov, E. V. & Tontegode, A. Y. Direct experimental study of the equilibrium diffusion of carbon atoms between the Mo(100) surface and the bulk. *J. Exp. Theor. Phys. Lett.* **73,** 671–673 (2001).

91. Gall', N. R., Rut'kov, E. V. & Tontegode, A. Y. Carbon diffusion between the volume and surface of (100) molybdenum. *Tech. Phys.* **47,** 484–490 (2002).

92. Bonaccorso, F. *et al.* Production and processing of graphene and 2d crystals. *Mater. Today* **15,** 564–589 (2012).

93. Liu, W.-W., Chai, S.-P., Mohamed, A. R. & Hashim, U. Synthesis and characterization of graphene and carbon nanotubes: A review on the past and recent developments. *J. Ind. Eng. Chem.* **20,** 1171–1185 (2014).

94. Que, Y. *et al.* Epitaxial growth of large-area bilayer graphene on Ru(0001). *Appl. Phys. Lett.* **104,** 093110 (2014).

95. Xu, W.-Y. *et al.* High quality sub-monolayer, monolayer, and bilayer graphene on Ru(0001). *Chinese Phys. B* **23,** 098101 (2014).

96. Vinogradov, N. A. *et al.* Formation and structure of graphene waves on Fe(110). *Phys. Rev. Lett.* **109,** 026101 (2012).

97. Meng, L. *et al.* Multi-oriented Moiré superstructures of graphene on Ir(111): experimental observations and theoretical models. *J. Phys. Condens. Matter* **24,** 314214 (2012).

98. Wilson, N. R. *et al.* Weak mismatch epitaxy and structural feedback in graphene growth on copper foil. *Nano Res.* **6,** 99–112 (2013).

99. Fedorov, A. V. *et al.* Structure of graphene on the Ni(110) surface. *Phys. Solid State* **53,** 1952–1956 (2011).

100. Günther, S. *et al.* Single terrace growth of graphene on a metal surface. *Nano Lett.* **11,** 1895–900 (2011).

101. Borca, B. *et al.* Electronic and geometric corrugation of periodically rippled, self-nanostructured graphene epitaxially grown on Ru(0001). *New J. Phys.* **12,** 093018 (2010).

102. Usachov, D. Y. *et al.* Graphene morphology on Ni single-crystal surfaces: experimental and theoretical investigation. *Bull. Russ. Acad. Sci. Phys.* **73,** 679–682 (2009).

103. N'Diaye, A. T., Coraux, J., Plasa, T. N., Busse, C. & Michely, T. Structure of epitaxial graphene on Ir(111). *New J. Phys.* **10,** 043033 (2008).

104. Usachov, D. *et al.* Experimental and theoretical study of the morphology of commensurate and incommensurate graphene layers on Ni single-crystal surfaces. *Phys. Rev. B* **78,** 085403 (2008).

105. Preobrajenski, A., Ng, M., Vinogradov, A. & Mårtensson, N. Controlling graphene corrugation on lattice-mismatched substrates. *Phys. Rev. B* **78,** 073401 (2008).

106. Antonova, I. V. Chemical vapor deposition growth of graphene on copper substrates: current trends. *Physics-Uspekhi* **56,** 1013–1020 (2013).

107. Grandthyll, S. *et al.* Epitaxial growth of graphene on transition metal surfaces: chemical vapor deposition versus liquid phase deposition. *J. Phys. Condens. Matter* **24,** 314204 (2012).

108. Obata, S., Tanaka, H. & Saiki, K. Reduction of a single layer graphene oxide film on Pt(111). *Appl. Phys. Express* **4,** 025102 (2011).

109. Yamada, T., Ishihara, M. & Hasegawa, M. Low temperature graphene synthesis from poly(methyl methacrylate) using microwave plasma treatment. *Appl. Phys. Express* **6,** 115102 (2013).

110. Sun, Z. *et al.* Growth of graphene from solid carbon sources. *Nature* **468,** 549–52 (2010).

111. Wofford, J. M. *et al.* Molecular beam epitaxy of graphene on ultra-smooth nickel: growth mode and substrate interactions. *New J. Phys.* **16,** 093055 (2014).

112. Treier, M. *et al.* Surface-assisted cyclodehydrogenation provides a synthetic route towards easily processable and chemically tailored nanographenes. *Nat. Chem.* **3,** 61–7 (2011).

113. Cai, J. *et al.* Atomically precise bottom-up fabrication of graphene nanoribbons. *Nature* **466,** 470–3 (2010).

114. Wang, H., Wang, X., Li, X. & Dai, H. Chemical self-assembly of graphene sheets. *Nano Res.* **2,** 336–342 (2009).

115. Li, X. *et al.* Large-area synthesis of high-quality and uniform graphene films on copper foils. *Science* **324,** 1312–4 (2009).

116. Lang, B. A LEED study of the deposition of carbon on platinum crystal surfaces. *Surf. Sci.* **53,** 317–329 (1975).

117. Ueta, H. *et al.* Highly oriented monolayer graphite formation on Pt(111) by a supersonic methane beam. *Surf. Sci.* **560,** 183–190 (2004).

118. Wu, M.-C., Xu, Q. & Goodman, D. W. Investigations of graphitic overlayers formed from methane decomposition on Ru(0001) and Ru(11-20) catalysts with scanning tunneling microscopy and high-resolution electron energy loss spectroscopy. *J. Phys. Chem.* **98,** 5104–5110 (1994).

119. Nieuwenhuys, B., Hagen, D., Rovida, G. & Somorjai, G. LEED, AES and thermal desorption studies of chemisorbed hydrogen and hydrocarbons (C_2H_2, C_2H_4, C_6H_6, C_6H_{12}) on the (111) and stepped [6(111) × (100)] iridium crystal surfaces; comparison with platinum. *Surf. Sci.* **59,** 155–176 (1976).

120. Himpsel, F. J., Christmann, K., Heimann, P., Eastman, D. E. & Feibelman, P. J. Adsorbate band dispersions for C on Ru(0001). *Surf. Sci.* **115,** L159–L164 (1982).

121. Baron, K., Blakely, D. W. & Somorjai, G. A. Low energy electron diffraction studies of the surface structures of adsorbed hydrocarbons (n-heptane, toluene, benzene, ethylene, and cyclohexane) on stepped (high miller index) platinum surfaces. *Surf. Sci.* **41,** 45–66 (1974).

122. Rut'kov, E. V. & Tontegode, A. Y. A study of the carbon adlayer on iridium. *Surf. Sci.* **161,** 373–389 (1985).

123. Gamo, Y., Nagashima, A., Wakabayashi, M., Terai, M. & Oshima, C. Atomic structure of monolayer graphite formed on Ni(111). *Surf. Sci.* **374,** 61–64 (1997).

124. Land, T. A., Michely, T., Behm, R. J., Hemminger, J. C. & Comsa, G. STM investigation of single layer graphite structures produced on Pt(111) by hydrocarbon decomposition. *Surf. Sci.* **264,** 261–270 (1992).

Chapter 2
Experiment

This chapter introduces a brief description of concepts and principles in the experiments in order to understand the approach of investigation, what sorts of information come from the measurements, and how the data are analyzed. The second section is a description of the experimental set-ups and the important components included. The rest of the sections relate how the experiments were made and how the data were handled.

2.1 Concepts and Principles

Ultra-High Vacuum (UHV)

UHV is the condition under pressures lower than about 10^{-9} mbar. The condition is integral to research in modern surface science as sample surfaces can remain clean on the atomic level for at least about an hour over the period of experiment. Cu(110) surface can remain clean under UHV conditions even for several hours. The residual gas environment in standard leak-free UHV chambers consists of a mixture of H_2, CO, CO_2, and just some H_2O. Moreover, diffusion of some CH_4 and other hydrocarbons from the vacuum pumps can contaminate the chamber, and some Ar can persist subsequent to use of argon-ion sputter source.

Organic Molecular Beam Deposition (OMBD)

OMBD is a method to prepare organic material on a substrate based on transmission of organic molecules onto the surface of the substrate upon evaporation or sublimation of a substance from a heated source under UHV condition. The most important aspects of OMBD are the fine control of deposition rate and the deposition to the purest level.

Two-Dimensional Lattices

The two-dimensional structure of a surface or an overlayer is formed when an atom or a set of atoms is attached to each point of a two-dimensional lattice in real space. The two-dimensional lattice is an infinite set of discrete points in space at position **r** and is defined in terms of fundamental translation vectors **a**, **b** as

$$\mathbf{r} = n\mathbf{a} + m\mathbf{b} \qquad \textbf{(2-1)}$$

where n and m are integers (0, ±1, ±2, …).

Each two-dimensional lattice in real space has an equivalent two-dimensional lattice in reciprocal space. The two-dimensional reciprocal lattice is an infinite set of points in reciprocal space at position **G** and is defined in terms of fundamental translation vectors **a***, **b*** as

$$\mathbf{G} = h\mathbf{a}^* + k\mathbf{b}^* \qquad \textbf{(2-2)}$$

where h and k are integers (0, ±1, ±2, …). The fundamental translation vectors **a***, **b*** in reciprocal space are related to the fundamental translation vectors **a**, **b** in real space as

$$\mathbf{a}^* = 2\pi \cdot \frac{\mathbf{b}\times\mathbf{n}}{|\mathbf{a}\times\mathbf{b}|} \quad , \quad \mathbf{b}^* = 2\pi \cdot \frac{\mathbf{n}\times\mathbf{a}}{|\mathbf{a}\times\mathbf{b}|} \qquad \textbf{(2-3)}$$

n is the unit vector normal to both **a** and **b**.

The notation (hk) specifies a particular set of planes normal to the plane of the two-dimensional lattice in real space; the numbers in the parenthesis are called Miller indices. A convenient feature in the use of Miller indices for specification of planes is the representation of symmetry. Equivalent sets of planes possess the same combination of indices in the absolute number. Braces $\{\}$ instead of round brackets $()$ are used when equivalent sets of planes need not be distinguished from one another. The vector to position **G** of coordinates (h,k) is perpendicular to (hk) planes. The magnitude of **G** is related to the distance d between (hk) planes as

$$G = \frac{2\pi}{d} \qquad \textbf{(2-4)}$$

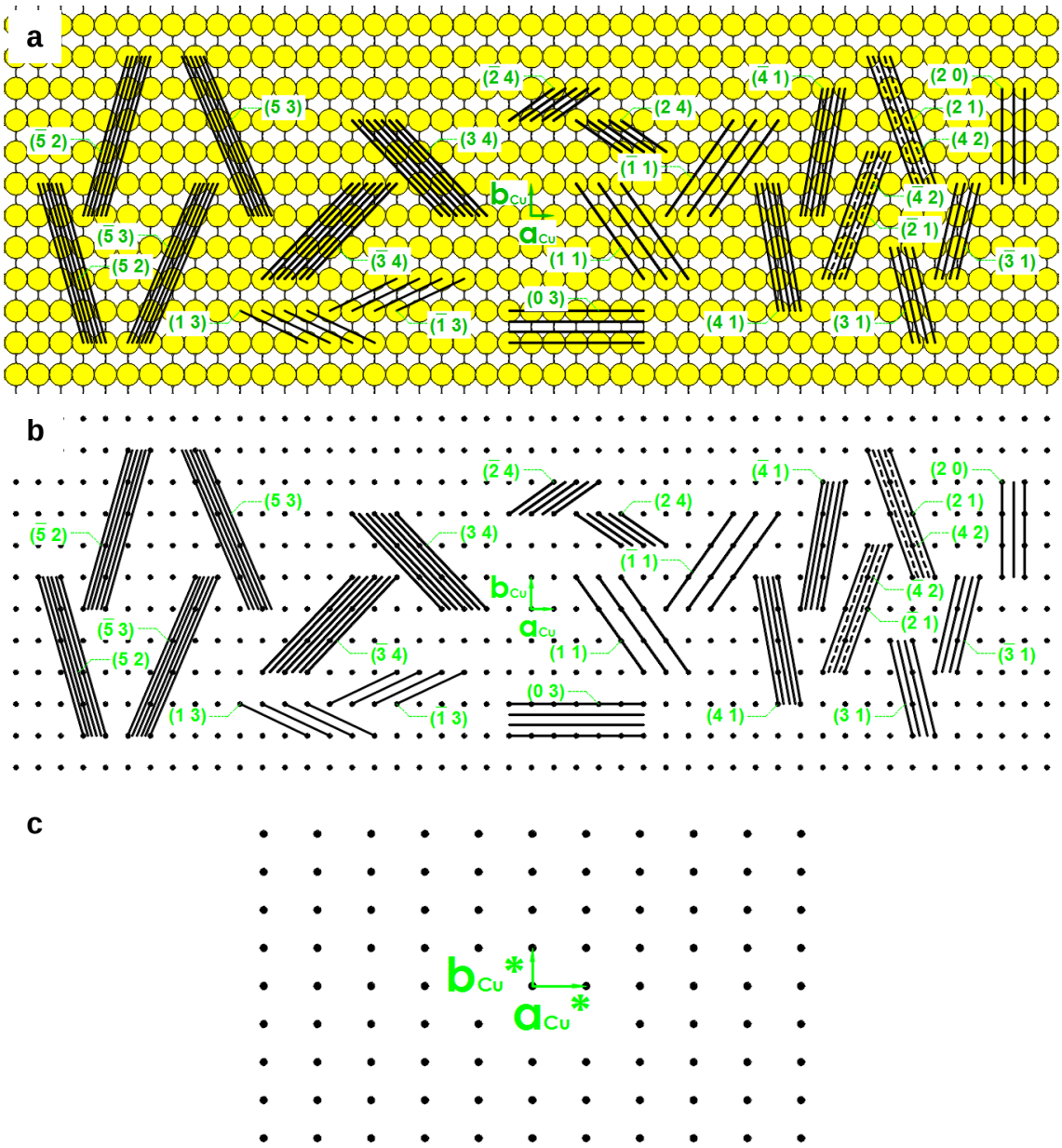

Figure 2-1. (a) Model for the structure of Cu(110) surface. (b) Model for the real-space lattice. (c) Model for the reciprocal lattice. Certain planes of interest and the fundamental translation vectors are superimposed.

Cu(110) Surface

The structure of Cu is face-centered cubic (FCC). The lattice constant is 3.61 Å. The (110)-oriented surface plane is cut across the diagonal lines on two opposite faces of the unit cell and is parallel to one of the axes of the unit cell. Figure 2-1a and Figure 2-1b show a model of Cu(110) surface and the two-

dimensional lattice. The fundamental translation vectors $\mathbf{a_{Cu}}$, $\mathbf{b_{Cu}}$ define the lattice and the unit cell of the surface structure. The magnitudes can be derived from the lattice constant of the FCC structure hence 2.55 Å for $\mathbf{a_{Cu}}$ and 3.61 Å for $\mathbf{b_{Cu}}$. The fundamental translation vectors $\mathbf{a_{Cu}^*}$, $\mathbf{b_{Cu}^*}$ in reciprocal space are derived from Equation (2-3) upon substitution of $\mathbf{a_{Cu}}$, $\mathbf{b_{Cu}}$; the magnitudes are 2.46 $Å^{-1}$ for $\mathbf{a_{Cu}^*}$ and 1.74 $Å^{-1}$ for $\mathbf{b_{Cu}^*}$ from

$$a_{Cu}{}^{*} = \frac{2\pi}{a_{Cu}} \quad , \quad b_{Cu}{}^{*} = \frac{2\pi}{b_{Cu}} \qquad \textbf{(2-5)}$$

Figure 2-1c shows a model of the reciprocal lattice. The symmetry properties stem from two-fold rotational axis and two mirror planes.

Certain sets of planes normal to the surface plane are shown in Figure 2-1 in the interest of analysis for the next chapter. A set of planes (hk) is identical to the set of planes $(\bar{h}\bar{k})$ based on inversion symmetry and is equivalent to the sets of planes $(\bar{h}k)$ and $(h\bar{k})$ based on mirror symmetry. The bar on top of a Miller index denotes an inversion.

Graphene

Graphene possesses a honeycomb structure – two carbon atoms in a network of sp^2 bonds are associated to each point of a two-dimensional hexagonal lattice. The fundamental translation vectors $\mathbf{a_{Gr}}$, $\mathbf{b_{Gr}}$ have a magnitude of 2.46 Å and the C–C bonds measure 1.42 Å[1,2]. Figure 2-2a and Figure 2-2b show a model of the carbon skeleton of graphene and the two-dimensional lattice; certain sets of planes are superimposed in the interest of analysis for the next chapter. The fundamental translation vectors $\mathbf{a_{Gr}^*}$, $\mathbf{b_{Gr}^*}$ in reciprocal space are derived from Equation (2-3); the magnitudes are equal at 2.94 $Å^{-1}$ from

$$a_{Cu}{}^{*} = \frac{4\pi}{\sqrt{3}\cdot a_{Cu}} = \frac{4\pi}{\sqrt{3}\cdot b_{Cu}} = b_{Cu}{}^{*} \qquad \textbf{(2-6)}$$

Figure 2-2c shows a model of the reciprocal lattice.

The symmetry properties come from a six-fold rotational axis and six mirror planes. A set of planes (hk) is identical to the set of planes $(\bar{h}\bar{k})$ based on inversion symmetry. However, proper account of symmetry for the

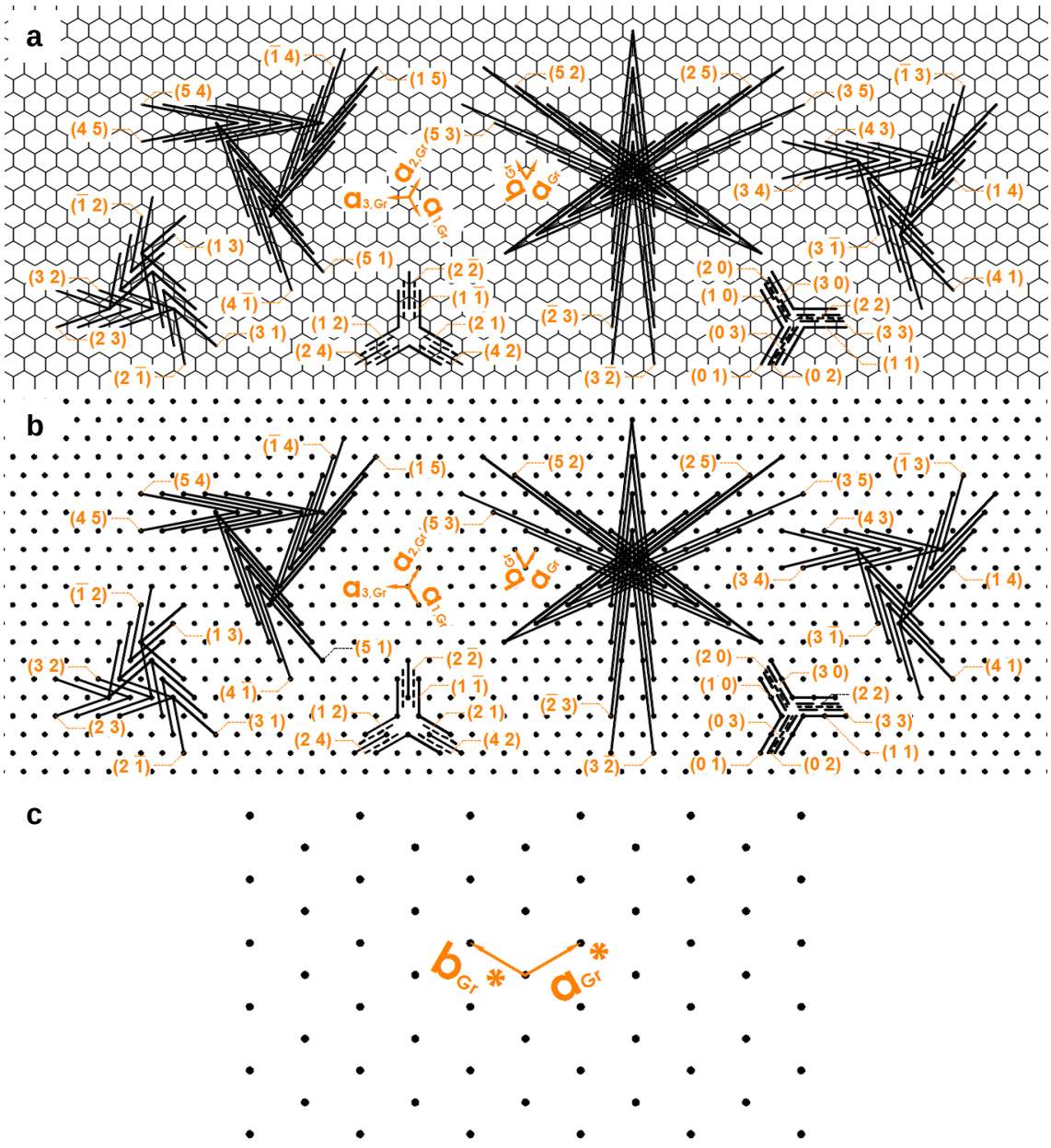

Figure 2-2. (a) Model for the carbon skeleton of graphene. (b) Model for the real-space lattice. (c) Model for the reciprocal lattice. Certain planes of interest, the fundamental translation vectors, and the three axes in Miller-Bravais scheme are superimposed.

hexagonal lattice requires specification of a set of planes in the Miller-Bravais notation to allow equivalent sets of planes to possess the same absolute-number combination of indices. The scheme uses a set of three indices hence the notation $(h'k'i')_{MB}$ and is based on a coordinate system from a set of three axes $\mathbf{a}_{1,Gr}$, $\mathbf{a}_{2,Gr}$, $\mathbf{a}_{3,Gr}$ at 120° to one another on the basal plane[3] as shown in Figure 2-2. The subscript MB is used here to make an explicit indication of the

use of Miller-Bravais notation to avoid confusion with the Miller notation. The formula of conversion for a set of planes from the Miller notation (hk) to the Miller-Bravais notation $(h'k'i')_{MB}$ can be derived as $(\bar{k}\ \ h\ -\bar{k}-h)_{MB}$ [3].

Reflection Absorption Infrared Spectroscopy (RAIRS)

RAIRS is a measurement technique to probe chemical bonds and vibrations in molecules adsorbed on metal surfaces based on absorption of infrared radiation. The simple harmonic oscillation approximates the energy levels E_ν of quantized vibrations of chemical bonds as

$$E_\nu = (\nu + \tfrac{1}{2})h\omega_0 \qquad \textbf{(2-7)}$$

where ν is the vibrational quantum number. The characteristic frequency ω_0 is

$$\omega_0 = \frac{1}{2\pi}\sqrt{\frac{k}{\mu}} \qquad \textbf{(2-8)}$$

where k is the force constant of the chemical bond and μ is the reduced mass of the component atoms[4]. The value of k depends on the vibrational potential and relates to the bond strength. RAIRS uses infrared radiation to excite fundamental transitions from $\nu = 0$ to $\nu = 1$. The surface of the metal acts as a mirror to reflect the infrared beam to a detector. The mode of measurement is illustrated in Figure 2-3. The reflection spectrum is measured for the clean surface $R_0(\bar{\upsilon})$ and the adsorbate-covered surface $R(\bar{\upsilon})$. The amount of absorbed radiation is characterized in terms of the reflectance

$$\mathrm{R} = \frac{R(\bar{\upsilon})}{R_0(\bar{\upsilon})} \qquad \textbf{(2-9)}$$

The vibrational transitions appear as bands in the reflectance spectrum and are expressed in terms of wavenumber $\bar{\upsilon}$ in the units of inverse centimeter (cm^{-1}). The $\bar{\upsilon}$ to the band is related to ω_0 as

$$\bar{\upsilon} = \frac{\omega_0}{c} \qquad \textbf{(2-10)}$$

where c is the speed of light. The basic vibrational motions are known as vibrational modes and are categorized as stretch, bend, and torsion. Combination bands can also be observed from simultaneous excitation of more than one vibrational mode. Vibrations of chemical bonds in adsorbed molecules

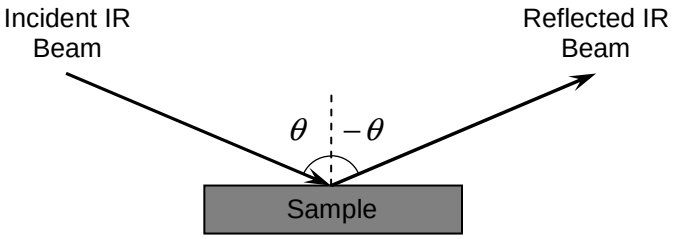

Figure 2-3. The mode of measurement in RAIRS. θ is made as close to 90° as possible at grazing incidence to maximize IR absorption.

are measured above the cut-off of substrate absorption at 500 – 1000 cm^{-1}. Hence, the vibrational frequencies of substrate-molecular adsorbate bonds are too low for RAIRS. The identification of bands can be made in comparison with the frequencies of known molecular species. Shifts in vibrational frequencies manifest subtle variations in chemical bonds as can be seen from Equation (2-8). The relative change in reflection is related to the concentration of adsorbates σ and the adsorbate polarizability $\alpha(\bar{\upsilon})$ as

$$\frac{\Delta R(\bar{\upsilon})}{R_0(\bar{\upsilon})} = \frac{R_0(\bar{\upsilon}) - R(\bar{\upsilon})}{R_0(\bar{\upsilon})} = \frac{8\pi^2 \bar{\upsilon}}{c} F(\varphi) \cdot \sigma \operatorname{Im} \alpha(\bar{\upsilon}) \qquad \textbf{(2-11)}$$

where φ is the angle of incidence and $F(\varphi)$ contains all the local field characteristics and the dielectric response of the system[5]. The amount of absorbed radiation cannot be expected to be proportional to the concentration when $\alpha(\bar{\upsilon})$ changes due to considerable lateral interactions between adsorbates[6].

The probability of a vibrational transition is proportional to the square of the transition dipole moment. The transition dipole moment is

$$M_{\nu\nu'} = \int_{-\infty}^{\infty} \psi(\nu) \cdot \mu \psi(\nu') d\tau \qquad \textbf{(2-12)}$$

where $\psi(\nu)$ is the initial state wavefunction, $\psi(\nu')$ is the final state wavefunction, and μ is the dipole moment of the molecule[6]. Dipole moments arise from electrical polarities of bonds. The integral must be non-zero in at least one of the components in x, y, or z direction for the vibrational transition to be possible. The symmetry properties of vibration based on the characters of the point group can be used to determine the IR-active vibrational modes and

depend on both the adsorbate and the adsorption site[7]. The strength of IR absorption depends both on the electric field vector of the incident radiation and the transition dipole moment[4]. The surface selection rule on metal surfaces only allows IR absorption for molecular vibrations whose dipole moments include a component in the surface normal[8]. The reason is the image-dipole effect in metal surfaces as a response of the valence electrons enhances both the electric field vector and the dipole moment perpendicular to the surface but cancels them both parallel to the surface. Adoption of the infrared beam at grazing incidence to the sample surface maximizes IR absorption.

Application of the surface selection rule to perylene on metal surfaces can be described using two extreme scenarios of adsorption – the molecular plane in the upright orientation perpendicular to the surface and in the flat-down orientation parallel to the surface. In the upright orientation in-plane bends and stretches produce dipole moments perpendicular to the surface whilst out of plane bends produce dipole moments parallel to the surface. The opposite is true for the flat-down orientation where out of plane vibrational motions produce dipole moments perpendicular to the surface whilst in-plane vibrational motions produce dipole moments parallel to the surface. The IR-active vibrational modes therefore come from in-plane vibrational motions for the upright orientation whereas out of plane vibrational motions for the flat-down orientation. The surface selection rule hence provides information on the orientation of perylene on metal surfaces.

Low-Energy Electron Diffraction (LEED)

LEED is a measurement technique for determination of the two-dimensional lattices of surface structures from the spatial distribution of the diffracted beams of low-energy incident electrons (20 – 1000 eV)[8,9]. The de Broglie wavelength λ of an electron is

$$\lambda = \frac{h}{\sqrt{2mE}} \qquad \textbf{(2-13)}$$

where E is the energy of the electron. The diffraction is the constructive interference of back-scattered electrons upon elastic collision of the low-energy incident electrons to the surface atoms. The low-energy electrons are almost

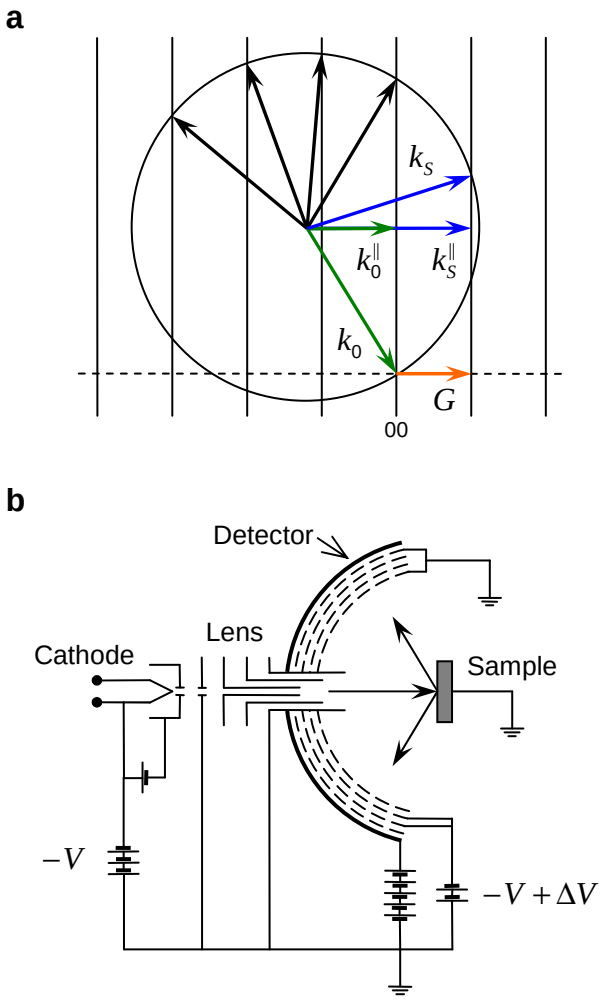

Figure 2-4. (a) The Ewald sphere construction for diffraction on two-dimensional periodic structures. The diffraction condition is satisfied when the electron wave vectors terminate at the intersection between the sphere and the reciprocal lattice rods. The component of a diffracted-electron wave vector parallel to the surface is illustrated for the scattered wave vector in blue colour to demonstrate how a scattered beam satisfies the condition for diffraction. (b) Schematic representation of LEED apparatus.

exclusive to information on surface structure for two reasons. First, the inelastic mean free path of low-energy electrons is 5 – 20 Å hence most elastic collisions occur in the few atomic layers of surfaces. Second, λ is of the order of or less than the lattice dimensions hence the premise for diffraction from surface atoms stands. The electron wave vector $\boldsymbol{k}$ describes the momentum of an electron beam and possesses a magnitude of

$$k = \frac{2\pi}{\lambda} \qquad \textbf{(2-14)}$$

The elastic collision of incident electrons to surface atoms satisfies the law of conservation of energy as

$$|\boldsymbol{k}_S| = |\boldsymbol{k}_0| \qquad \textbf{(2-15)}$$

where $\boldsymbol{k}_0$ is the incident-electron wave vector and $\boldsymbol{k}_S$ is the scattered-electron wave vector. The condition for diffraction on two-dimensional periodic structures can be expresses in terms of the law of conservation of momentum as

$$\boldsymbol{k}_S^{\parallel} - \boldsymbol{k}_0^{\parallel} = \boldsymbol{G} \qquad \textbf{(2-16)}$$

Here $\boldsymbol{k}_0^{\parallel}$ is the component of the incident-electron wave vector parallel to the surface, $\boldsymbol{k}_S^{\parallel}$ is the component of the diffracted-electron wave vector parallel to the surface, and $\boldsymbol{G}$ is the reciprocal lattice vector. Equation (2-16) shows the electrons exchange parallel momentum with the surface atoms in quantized units of the reciprocal lattice vector hence the diffracted beams occur at particular directions.

Figure 2-4a demonstrates diffraction on two-dimensional periodic structures in the Ewald sphere construction[9]. The electron wave vectors of the incident beams and the scattered beams possess equal magnitude in accordance with Equation (2-15) and are represented on the radius of the sphere. The reciprocal lattice points in a particular direction are represented as rods perpendicular to the surface. Equation (2-16) is satisfied when the electron wave vectors terminate at the intersection between the sphere and the reciprocal lattice rods. The projection of the points of intersection onto the surface plane reproduces the reciprocal lattice.

The standard apparatus for LEED allows direct visual inspection of the diffraction pattern and can be summarized from Figure 2-4b as follows. An electron gun generates a collimated monochromatic beam of low-energy electrons and consists of a cathode filament behind an electrostatic lens. The cathode is at a potential $-V$ to accelerate the emitted electrons to an energy of eV. The electron beam is made incident upon a sample. The back-scattered electrons from the sample move into a series of concentric grids before a hemispherical detector is reached. The last aperture of the lens, the sample, and the first grid nearest to the sample are connected to earth potential to ensure absence of electric field as the electrons move in space. The earth

potential to the sample avoids accumulation of electrostatic charge from the electron beam. The next two grids are held at a potential $-V+\Delta V$ to reject most of the electrons from inelastic scattering. The last grid is at earth potential to screen out high potential on the detector. The transmitted electrons past the last grid come from the diffracted beam and are reaccelerated to cause fluorescence in the detector. The diffraction spots on the detector are analogous to the points of intersection between the sphere and the reciprocal lattice rods in the Ewald sphere construction for diffraction from two-dimensional surface structures. In other words, the projection of the diffraction pattern from the detector onto the view plane in the view port of the apparatus reproduces the pattern of the reciprocal lattice. However, the sample must be located at the center of curvature of the detector and parallel to the view plane. The LEED pattern consists of discrete bright spots on a dark background. ΔV is adjusted to get the highest contrast.

Scanning Tunneling Microscopy (STM)

STM is a measurement technique to probe the topographic structure of a surface at atomic resolution based on the quantum-mechanical phenomenon of electron tunneling. Intimate treatment of the principles of STM requires extensive use of quantum mechanics. Here a brief description of the important ideas is in order. The instrument is illustrated in Figure 2-5a and consists of a sharp tip, a piezoelectric scanner, feedback electronics, and a computer. The sharp tip is made of a metal wire and prepared to atomic dimensions at the apex of the tip. The piezoelectric scanner moves the tip in x, y, z directions across an area of the sample surface. Piezoelectric ceramics are used in scanners as electromechanical transducers to convert electrical signals to high-precision motion upon expansion or contraction at a rate of about 1 Å per mV. The scanner is composed of three piezoelectric ceramics to allow independent motion in x, y, z directions.

The operation of STM can be summarized as follows. The sharp tip is approached within a few nanometers to the sample surface. The minute tip-sample gap allows some overlap of wavefunction between the closest tip atom

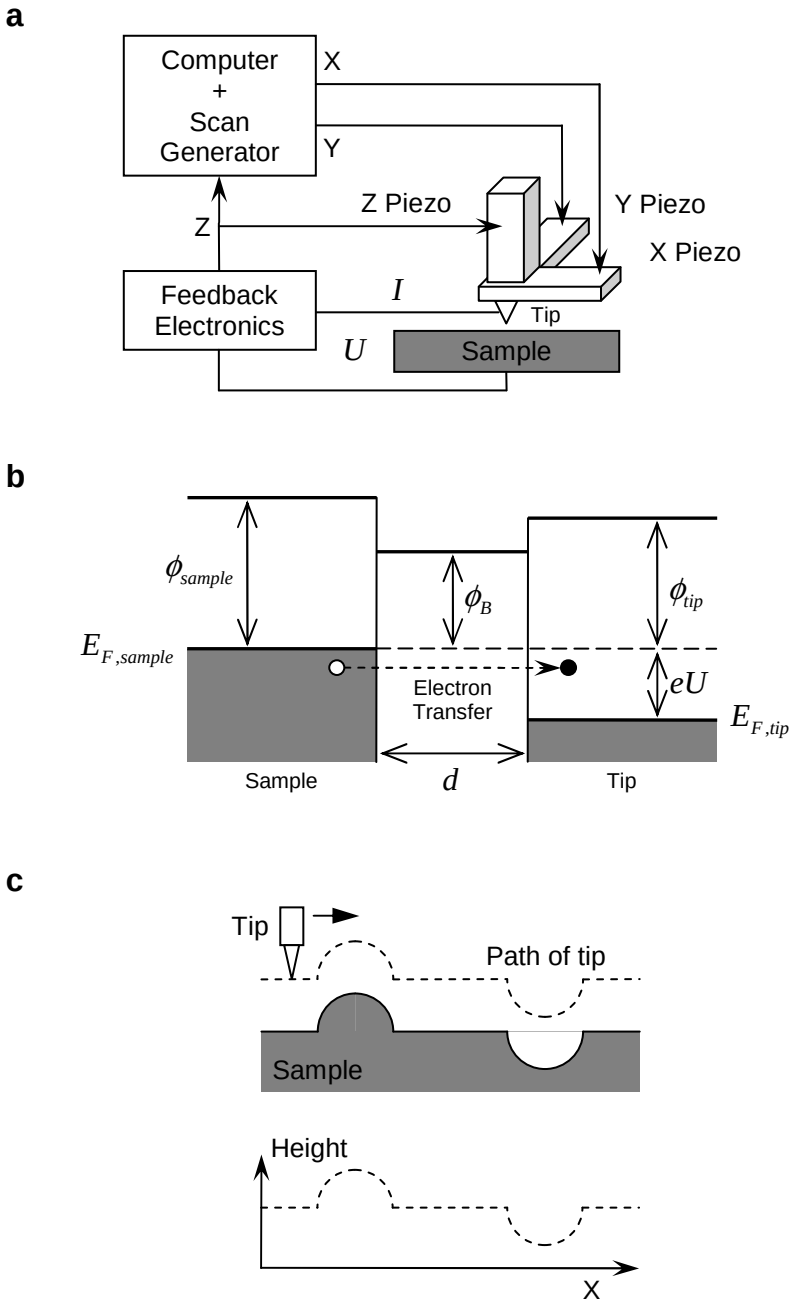

Figure 2-5. (a) Schematic illustration of STM instrument. (b) Energy level diagram of electron tunneling between tip and sample in STM. (c) Schematic illustration of STM measurement in constant current mode.

and the sample-surface atoms. The overlap of wavefunction leads to a finite probability the electrons tunnel in free space across the gap when a potential difference U is applied between the tip and the sample. Figure 2-5b illustrates an energy level diagram in the case of positive potential applied to the tip. The positive potential shifts the electronic energies on the tip to lower levels to offer

unoccupied electronic states. The electron transfer to the tip occurs despite the energy barrier ϕ_B of the tip-sample junction and is explained as the quantum-mechanical effect of the wave character of fundamental particles. In the case of negative potential biased to the tip, the electrons tunnel in the reverse direction. The amount of tunnel current I is a function of some parameters as

$$I \propto \frac{U \cdot D(U)}{d} \cdot \exp\left(-A\phi_B^{1/2} d\right) \qquad \textbf{(2-17)}$$

where d is the effective tunneling gap, $D(U)$ is the local density of electronic states (LDOS) near the Fermi level of the sample surface, and A is a constant[10]. The sample needs to be a conductor as the flow of electrons between the tip and the sample is measured. One mode of measurement is the constant-current mode as illustrated in Figure 2-5c. The variable parameters I and U are kept constant, x and y lateral positions are varied, and z vertical position is measured. In other words, the feedback electronics control the variation in z position of the tip at almost constant tip-sample gap whilst the piezoelectric scanner rasters the tip over the surface. Acoustic vibrations in the environment can affect the tip-sample gap and so must be isolated from the STM for stable operation. The computer acquires the data of the topographic features of the sample surface in terms of z as a function of x and y, and processes the data into a topographic image.

The STM is also sensitive to the LDOS in addition to the topographic position on the surface so features in STM images can be the outcome of one or both of these factors. The STM image corresponds to the topographic features of occupied electronic states when the tip bias potential is positive with respect to the sample whilst to those of unoccupied electronic states when the tip bias potential is negative. The exponential dependence of the tunnel current on the tip-sample gap determines the high vertical resolution of STM. The dimension of the tip at the apex determines the lateral resolution of STM.

2.2 Set-up and Equipment

Three separate set-ups were used for experiments. Names as Experiment Set-up No. 1, Experiment Set-up No. 2, and Experiment Set-up No. 3 are used here for ease of reference. The schematic representations are shown in Figure 2-6 – Figure 2-8 and are reproductions from the PhD thesis of Philip John Donovan where comprehensive description can be found[11]. Here just brief descriptions of the essence of the set-ups are made.

Each set-up consisted of a (110)-oriented single-crystal Cu substrate in a chamber for in-situ sample preparation. The equipment for sample preparation consisted of an evaporator, a sputter-ion gun, and a substrate heater. A set of manipulators, transfer rods, and wobble sticks connected to chamber and allowed adjustment in position and transfer of location for the sample.

The evaporator for OMBD was made from a glass tube with a 0.25 mm-diameter tantalum (Ta) wire wound about seven times in 1-mm pitch around the tube. The glass tube was about 1 mm in inside diameter, 10 – 15 mm in length, closed on one end but open on the other end. A substance in powder form was loaded into the evaporator from the open end of the glass tube until almost full. The Ta wire conducted heat to the substance in the tube as electrical power was supplied to the wire from constant-current source. The open end of the glass tube was directed to create a beam of molecules onto the surface of the Cu substrate from sublimation of a substance in the tube. The exact distribution of the beam intensities was unknown and there was no means to monitor the deposition rate. The beam was estimated to be cone in shape and Gaussian in profile at the cross section. The substrate was separated tens of centimetres from the evaporator so the beam was assumed uniform over the probed local area of the surface. A schematic representation of the entire evaporator unit for direct attachment to UHV chamber is shown in Figure 2-9.

Experiment Set-up No. 1 was attached to commercial RAIRS instrument for measurement of vibrational spectra and commercial LEED optics for measurement of diffraction pattern on a surface. The RAIRS instrument used a Fourier transform infrared (FT-IR) spectrometer under the trademark of Magna-IR 860 Spectrometer purchased from Nicolet Instruments Co. The IR

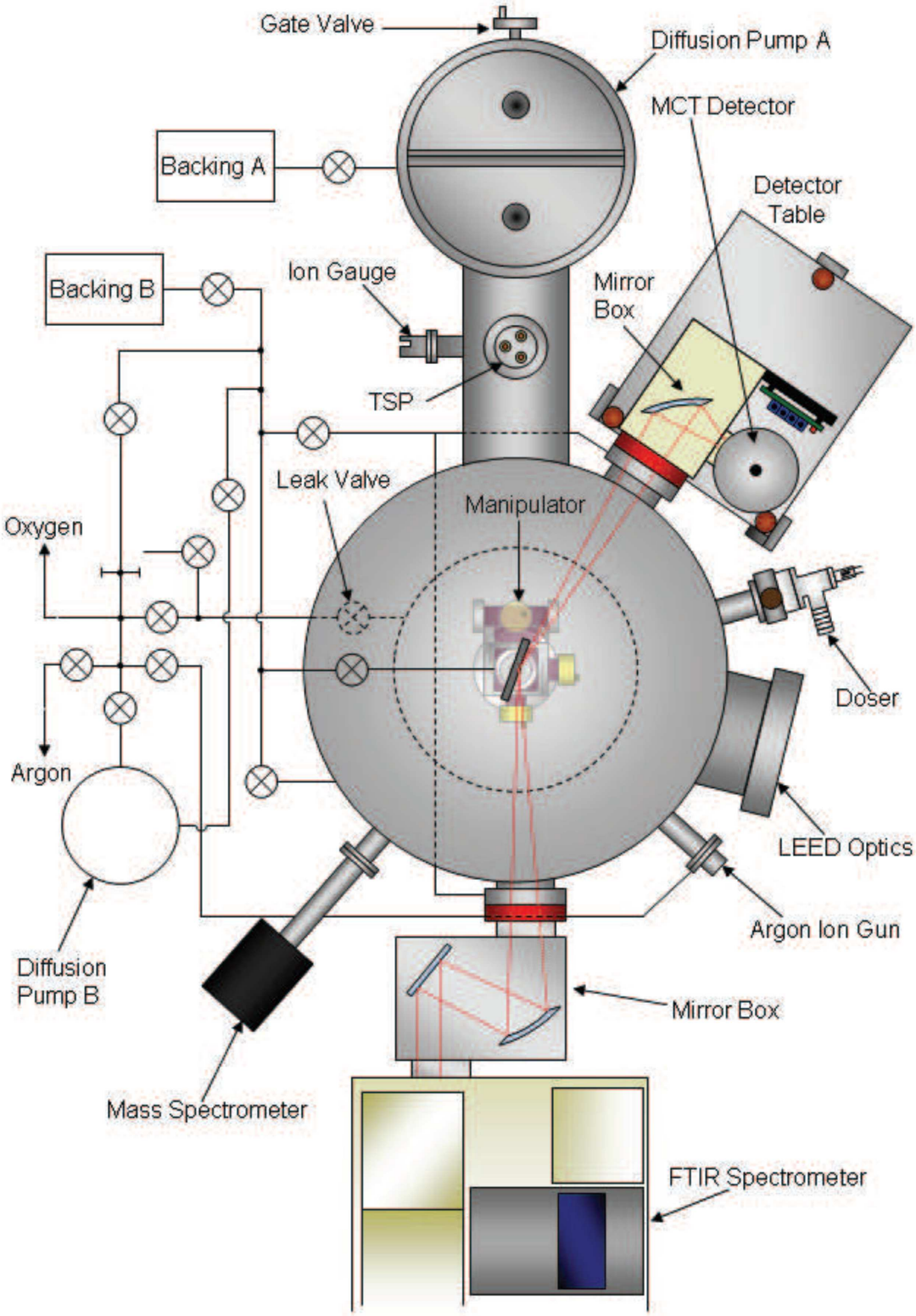

Figure 2-6. Schematic representation of Experiment Set-up No. 1 – a single UVH chamber for preparation and measurement is attached to LEED optics and FT-IR spectrometer. (Adapted from reference[11])

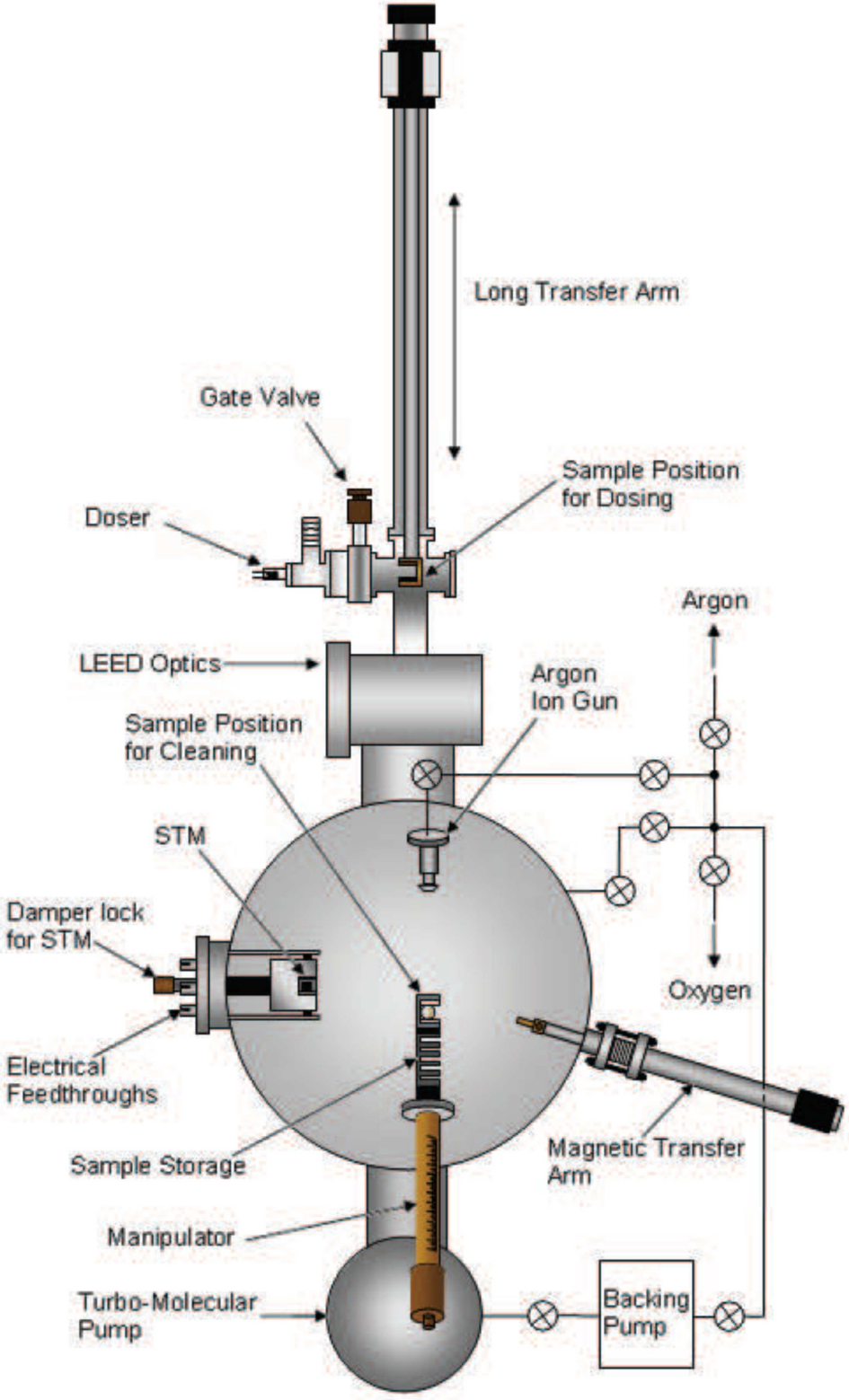

Figure 2-7. Schematic representation of Experiment Set-up No. 2 – a single UVH chamber for preparation and measurement is attached to STM instrument. (Adapted from reference[11])

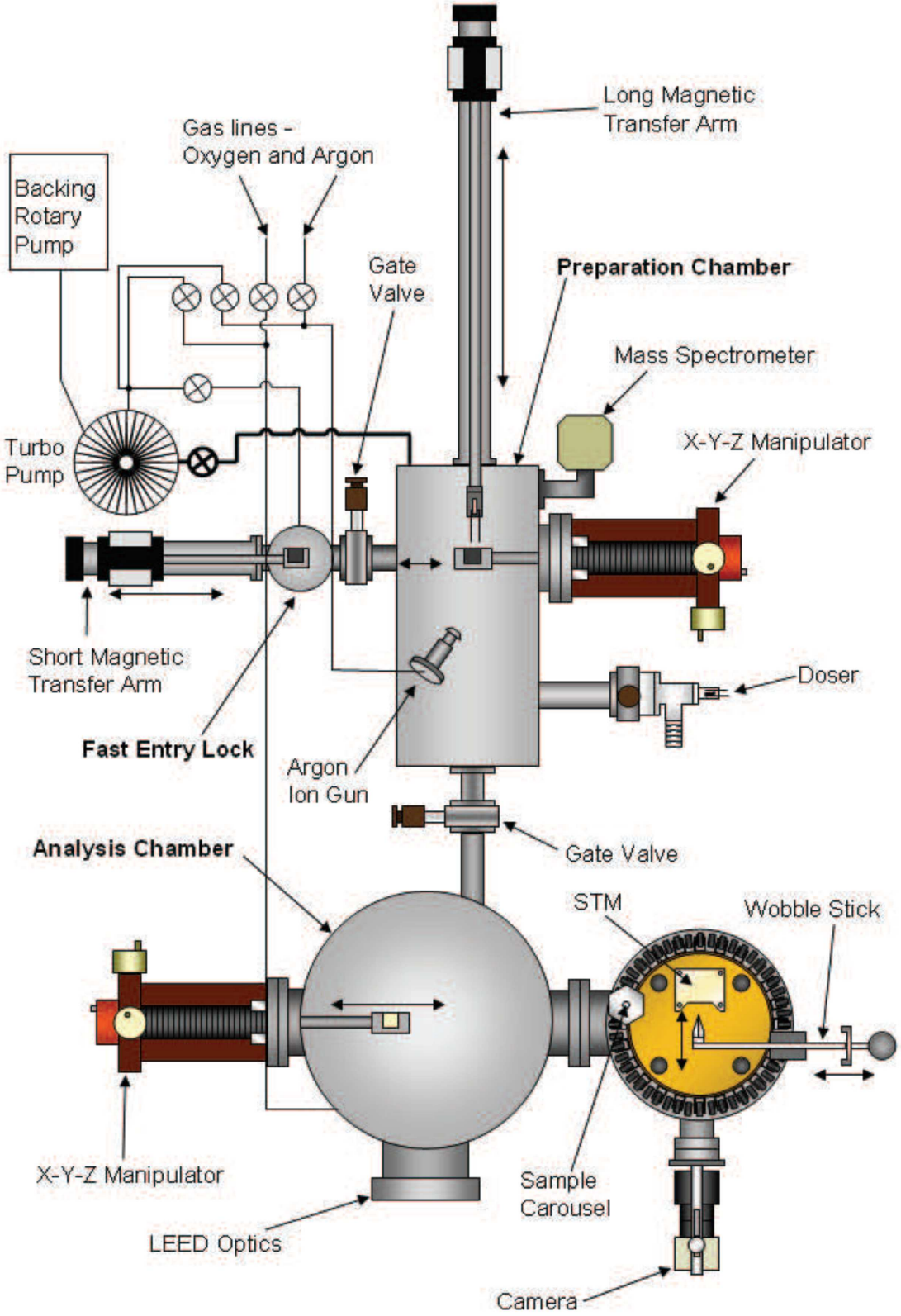

Figure 2-8. Schematic representation of Experiment Set-up No. 3 – one UVH chamber is used for preparation whilst another UHV chamber is used for measurement and attached to LEED optics and STM instrument. (Adapted from reference[11])

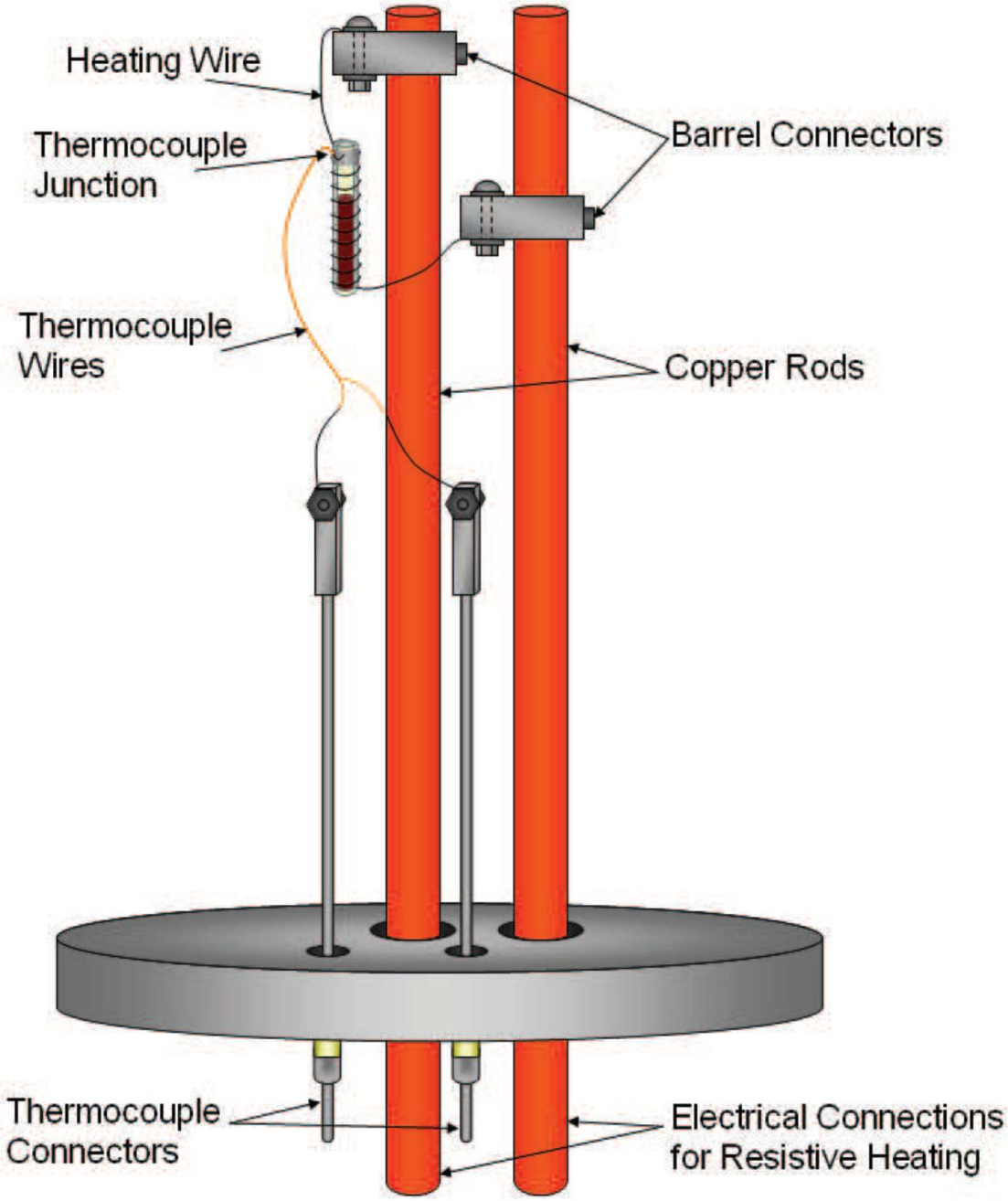

Figure 2-9. Schematic representation of entire evaporator unit for direct attachment to UHV chamber. (Adapted from reference[11])

source of the spectrometer limited measurement of a spectrum in wavenumbers to 650 cm^{-1} – 4000 cm^{-1}. Sample preparations and measurements were performed in one UHV chamber. Infrared radiation was transmitted into and out of the chamber through IR-transparent potassium bromide (KBr) windows. The detector was made of photoconductive mercury cadmium telluride (MCT) semiconductor. The path of the IR beam external to the UHV chamber was

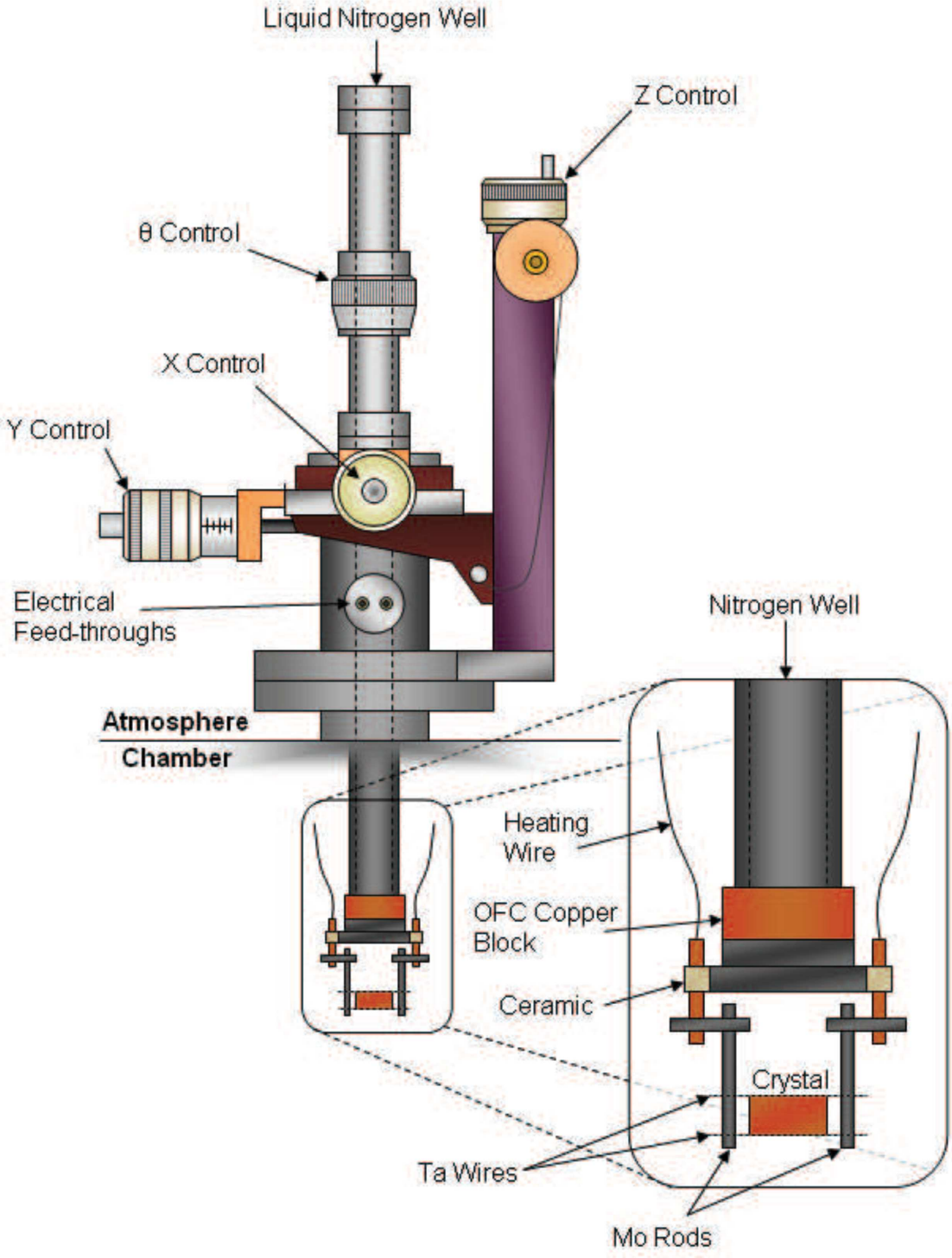

Figure 2-10. Schematic representation of Cu substrate fastened to Ta-heater wires on the arm of manipulator in Experiment Set-Up No. 1. (Adapted from reference[11])

purged with dry air to minimize interference from gas-phase absorption bands from atmospheric H_2O. The Cu substrate was fastened to the arm of a manipulator for translation and rotation – a schematic representation is shown in Figure 2-10. The pumping system consisted of a diffusion pump and a

mechanical rotary pump connected in series. The base pressure in the UHV chamber was in the scale of lower 10^{-9} – mid 10^{-10} mbar prior to commencement of each experiment. The substrate heater was tantalum (Ta) wires in direct contact to two parallel edges of the rectangular Cu substrate for conduction of heat as electrical power passed the resistive wires from constant-current source. The temperature of the substrate could be monitored from accurate measurement of a thermocouple sensor attached in direct contact to one edge of the substrate.

Experiment Set-up No. 2 was attached to commercial STM instrument purchased from SPECS Surface Nano Analysis GmbH. The STM tip was made of W wire and etched in aqueous NaOH electrochemical solution. The bias potential in STM measurements is applied to the sample from the tip. Sample preparations and STM measurements were performed in one UHV chamber. The Cu substrate was mounted on a sample plate for transfer from one location to another – a schematic representation is shown in Figure 2-11. The pumping system consisted of a turbo molecular pump and a mechanical rotary pump connected in series. The base pressure in the UHV chamber was around 10^{-10} mbar. The substrate heater was ceramic rods for heat radiation to the back side of the sample plate as electrical power passed resistive W wires in the ceramic rods from constant-current source. Absence of temperature probe in the set-up prohibited measurement of substrate temperature.

Experiment Set-up No. 3 was a commercial construction of Omicron NanoTechnology GmbH and had separate chambers for sample preparation and analysis. The chambers were connected to each other via a gate valve. The Cu substrate was mounted on a sample plate for transfer from one location to another in one chamber or from one chamber to the other. A transfer rod moved the sample between the chambers. The sample-preparation chamber had a base pressure of mid 10^{-9} – mid 10^{-10} mbar. LEED and STM measurements could be performed in the analysis chamber under an excellent base pressure of lower 10^{-10} – higher 10^{-11} mbar. The bias potential in STM measurements is applied to the tip whilst the sample is connected to earth. The pumping system consisted of an ion pump for the analysis chamber whereas a

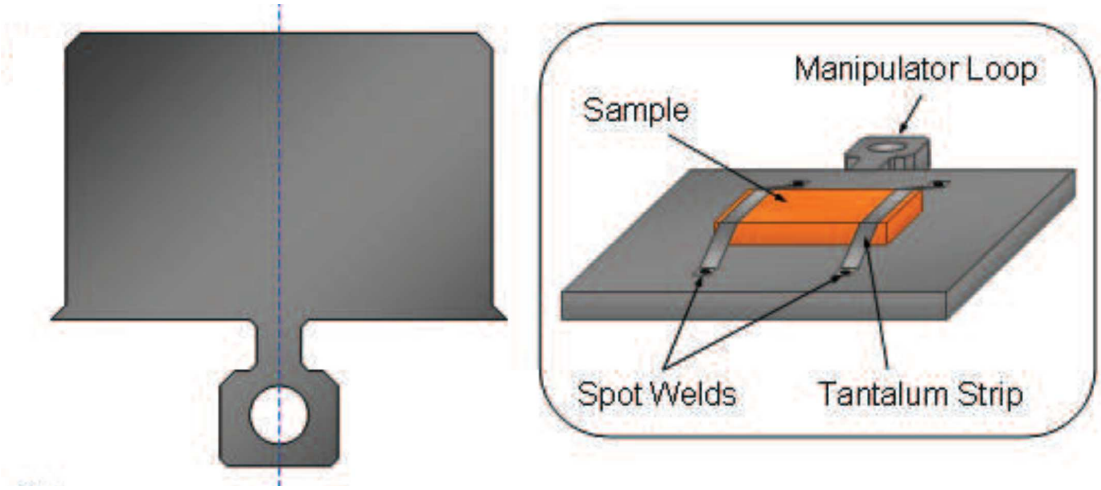

Figure 2-11. Schematic representation of sample plate for transfer of sample from one location to another and Cu substrate mounted on sample plate. (Adapted from reference[11])

turbo molecular pump and a mechanical rotary pump connected series for the sample-preparation chamber. The substrate heater was a cathode W filament under a variable electrostatic potential in a sample-plate platform for direct heat radiation and electron radiation to the back side of the sample plate – a schematic representation is shown in Figure 2-12. The electrical power to the cathode filament came from a constant-current source. Acceleration of electrons emitted from the cathode filament under an applied electric potential was needed to reach elevated temperatures. The electric potential from the cathode filament to the sample plate came from a constant-voltage source. In other words, the control parameters of the substrate heater were the amount of electrical current in the cathode filament and the applied electric potential difference for electron acceleration to the sample plate. The control parameters on the substrate heater depended much on the actual fabrication of the cathode filaments and the characteristics of the filament material over time apart from the intended temperature. A thermocouple sensor to monitor temperature was attached onto the sample-plate platform of the substrate heater in the proximity but not in direct contact to the sample plate. The consequent measurements possessed an enormous error from the actual temperature of the substrate. For example, the actual temperature of the Cu substrate could be estimated to be close to the melting point of 1360 K from the glowing-hot colour and brightness but the temperature measurement read 300 – 400 K lower. Nevertheless, the

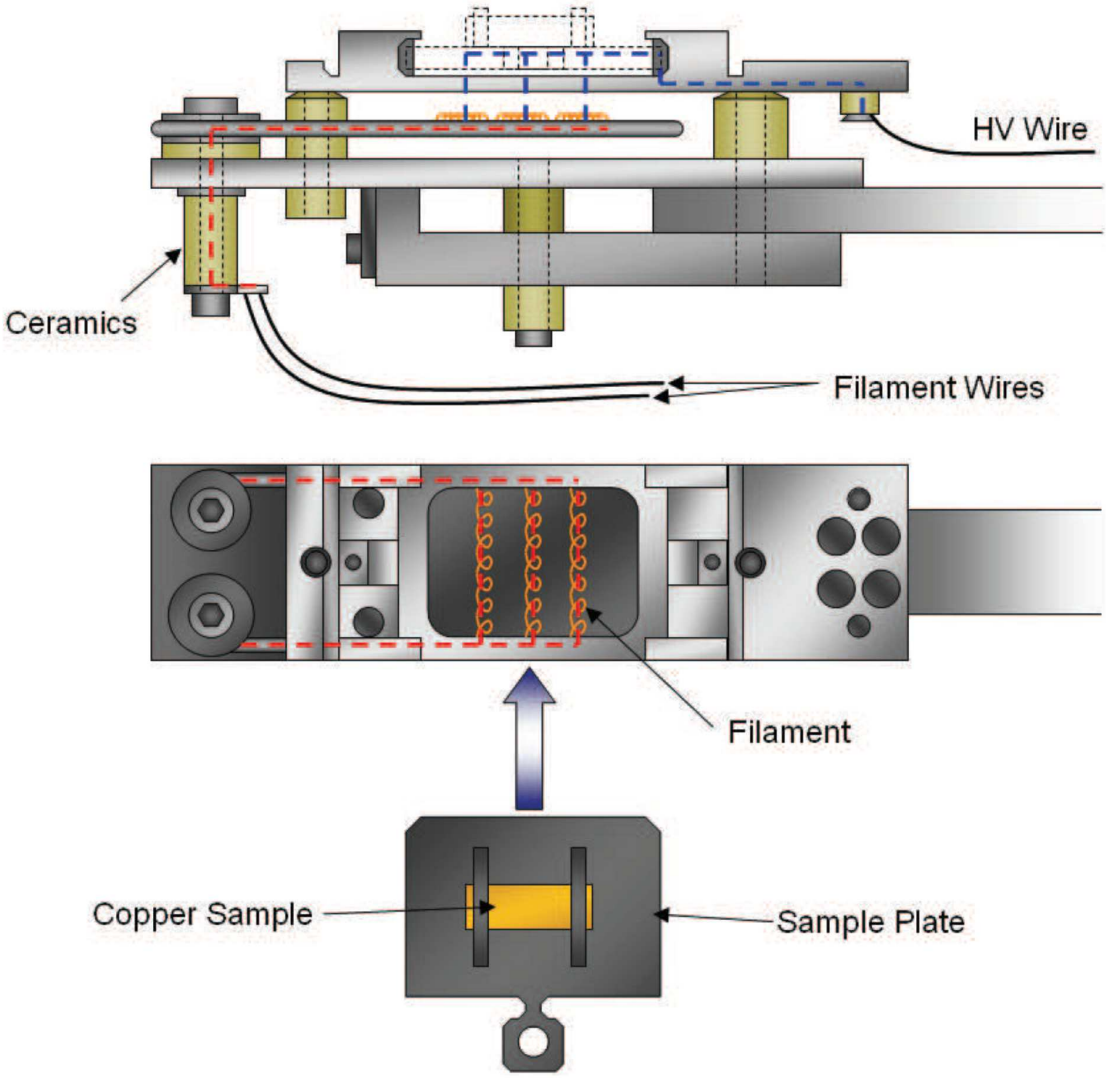

Figure 2-12. Schematic representation of substrate heater based on direct heat radiation and electron radiation from cathode W filaments under variable electrostatic potential to the back side of sample plate in Experiment Set-up No. 3. (Adapted from reference[11])

temperature measurements were used for reference to estimate substrate temperature.

Some issues about the substrate heater in Experiment Set-Up No. 3 posed slow pace for temperature ramps to high temperatures. First, adequate time had to be allowed for temperature measurements to respond at equilibrium. Temperature measurements were important to reduce the risk of melting the Cu substrate. Second, some contamination was released from the substrate heater upon approach to high temperatures. The deterioration of vacuum thereupon needed to be pumped out of the chamber for some period of time before the temperature ramp could be continued. Otherwise, electrical

breakdown of the medium around the substrate heater would happen and would lead to loss of the electric potential difference applied for electron acceleration to the sample plate.

2.3 Sample Preparation and Measurement

Pure Cu(110) Surface

Pure Cu(110) surfaces were prepared in situ on the polished side of the (110)-oriented single-crystal Cu substrates prior to experiments. Rounds of argon-ion (Ar^+) sputtering and anneal treatment were performed in succession. Each process lasted for a period of about half an hour in most cases. The Ar^+ beam was set to 500 – 1000 eV. The exact amount of Ar pressure in the chamber was adjusted to maximize the beam current to the Cu substrate. An Ar^+ beam current of 2.3 – 4.0 μA at 540 eV was usual to the Cu substrate under Ar pressure of lower 10^{-5} mbar in Experiment Set-up No. 1. An Ar^+ beam current of 1.0 – 4.0 μA at 500 – 1000 eV was usual to the sample plate in conjunction with the Cu substrate under Ar pressure of mid 10^{-6} – lower 10^{-5} mbar in Experiment Set-up No. 3. The anneal treatment of the substrate subsequent to each sputtering was set to temperatures 700 – 900 K; 775 K was usual in Experiment Set-up No. 1. The Cu(110) surface was considered pure, contamination-free, and well-defined when the characteristic rectangular LEED pattern appeared sharp on a dark background and/or when STM measurements demonstrated smooth flat terraces and rough step edges – the latter phenomenon has been attributed to unhindered diffusion of copper atoms at step edges[12].

An addition to the procedure for preparation of a pure Cu(110) surface when an overlayer of graphene had been formed on the substrate was adsorption of oxygen and subsequent quick anneal treatment to some temperature until the substrate became glowing-hot and bright but below the melting point. The process was meant to eliminate remnants of carbon contaminations as volatile oxides subsequent to repeated sputter cleaning and anneal treatment.

Molecules in Organic Molecular Beam Deposition

The present experiments made use of OMBD onto the surface of the Cu substrates. The molecules include perylene and Co-TPP. The evaporators were degassed in situ prior to use in sample preparations.

Perylene of ≥99% purity in golden-orange powder form was purchased from Sigma-Aldrich Co. The melting temperature of perylene is known to be about 551 K[13] and reports on OMBD of perylene mention sublimation temperatures of 370 – 470 K based on measurements from a thermocouple sensor. Deposition of perylene corresponded to a constant electrical current of 0.75 – 1.00 A in the Ta wires of the evaporator under UHV conditions. The specific amount of electrical current to the Ta wires of the evaporator depended on the actual fabrication of the evaporator, on the experiment set-up, and on the intended pace of the deposition. The test for the suitable electrical current to the evaporator in Experiment Set-Up No. 1 was made based on appearance of noticeable vibrational bands of perylene on the Cu(110) surface past some time period of deposition between increments in electrical current to the evaporator in real-time RAIRS measurements. An electrical current of 0.84 A to the evaporator for deposition of perylene was set appropriate for the time scale of RAIRS measurements in Experiment Set-Up No. 1. The deposition rate of perylene in Experiment Set-Up No. 2 was held fixed at an electrical current of 0.77 A in the evaporator as found suitable to allow measurements between intervals of deposition before monolayer saturation. The deposition rate of perylene as hydrocarbon precursors for synthesis of graphene on the Cu(110) surface in Experiment Set-Up No. 3 was held fixed at an electrical current of 1.00 A.

Co-TPP of ≥85% purity in dark-purple powder form was purchased from Sigma-Aldrich Co. The melting temperature of Co-TPP is known to be about 575 K from the specification sheet of the product. The deposition rate of Co-TPP in Experiment Set-Up No. 3 was held fixed at an electrical current of 1.25 A in the evaporator.

Experiment in Perylene on the Cu(110) Surface

The RAIR spectrum of the clean Cu(110) surface was taken as the reference prior to deposition of perylene to eliminate an influence from the properties of the instrument and the Cu(110) surface in Experiment Set-up No. 1. The sample measurements for perylene on the Cu(110) surface reported the properties of the perylene adsorbates. The RAIR spectra were reported in percentage reflectance so 100% reflectance corresponded to the spectrum for the clean Cu surface. Measurement of RAIR spectra was performed in real time with deposition of perylene on the Cu(110) surface. The temperature of the substrate was held at room temperature. Each measurement of the spectra in wavenumbers 650 cm^{-1} – 4000 cm^{-1} required a time period of not less than 15 minutes. The sets of real-time RAIRS measurements of perylene deposition at room temperature were performed for up to 300 minutes. The sample formed upon completion of each set of the real-time measurements was annealed at 450 K for an hour, and then cooled down back to room temperature before another RAIRS measurement.

STM measurements were performed in Experiment Set-Up No. 2 subsequent to each deposition in successive periods. The substrate was held at room temperature. The depositions were made in total for an extended period of time even past monolayer saturation. The end samples were annealed later on to certain temperatures up to around 500 K for certain periods and STM measurements were performed at room temperature.

Experiment in Graphene on the Cu(110) Surface: Synthesis Based on Thermal Decomposition of Perylene

The initial attempts to prepare graphene on Cu(110) surface based on thermal decomposition of perylene on the surface were performed in Experiment Set-up No. 1. The first step was to pre-adsorb perylene on the Cu(110) substrate held at room temperature. The deposition of perylene was performed until real-time measurement of RAIR spectra reached almost constant intensities for the IR bands from the multilayer as described in chapter 3. Flash anneal treatment was held at 1250 K for a few seconds. The ramp from room temperature to 1250 K took about a quarter of an hour. LEED measurement at room temperature was used to test for graphene formation. The outcome showed success as a hexagonal pattern was demonstrated.

The success of the attempt has led to an interest in further investigation with the use of STM for characterization of structure and growth formation. The subsequent experiments were performed in Experiment Set-up No. 3. Exact temperatures were not measured and controlled due to the absence of a temperature probe on the surface. Perylene was deposited on the Cu substrate held at room temperature for a period of about half an hour. Subsequent anneal treatment was made to a temperature of about 400 K but no more than about 450 K for a period of about half an hour to desorb the excess to monolayer saturation. The substrate heater was set to an electrical current of about 2.5 A in the cathode filament and the thermocouple on the sample-plate platform read about 400 K. The presence of a saturated perylene monolayer was confirmed based on observation of a commensurate (5x5) superstructure. Description of the superstructure is presented in chapter 3. The STM image in Figure 2-13 shows an example of a saturated perylene monolayer pre-adsorbed on the Cu substrate before anneal treatment to the growth temperatures of graphene. Formation of graphene was achieved upon anneal treatment to high temperatures until the Cu substrate appeared glowing-hot. The control parameters on the substrate heater were set to as high an electrical current as 6.0 A in the cathode filament and to as high an applied electric potential difference as 750 V for electron acceleration; the current of electron emission

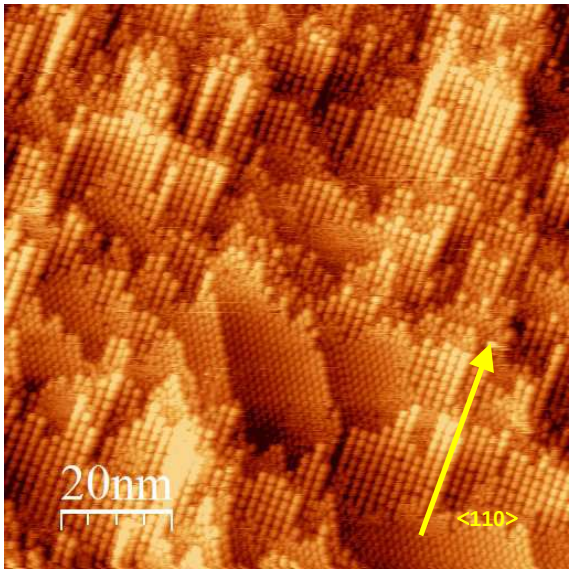

Figure 2-13. 1000 Å x 1000 Å STM topographic image of a pre-adsorbed saturated-monolayer perylene on a Cu(110) surface with an anneal treatment to some temperature less than 400 K for a period of half an hour. The image is not post-calibrated to correct dimensions. STM measurements were performed at U = -987 mV and I = 0.20 nA.

from the cathode filament to the sample plate went as high as 50 mA. The vacuum in the preparation chamber deteriorated as far as 10^{-7} mbar in the process. Experiences made from melting a Cu substrate and from the attempted experiments in Experiment Set-up No. 1, where exact temperatures could be measured, had revealed the color of the Cu substrate varies from faint orange at about 800 K to bright yellowish orange upon close approach to the melting temperature of about 1360 K. Temperature ramps from room temperature to high temperatures required up to an hour. Variation in the temperature ramps and in the growth temperatures was unavoidable for separate sample preparations due to issues about the substrate heater and the temperature measurements.

Experiment in Co-TPP on Sub-Monolayer Graphene on the Cu(110) Surface

Deposition of Co-TPP was made on a sample of graphene on the Cu(110) surface in Experiment Set-Up No. 3 as prepared in the other experiment. STM measurements were performed between intervals of deposition. The substrate was held at room temperature. The deposition was made in total for 30 minutes.

2.4 Data Process

RAIRS Measurement

The RAIR spectra for perylene molecules on the Cu(110) surface obtained straight from the FT-IR spectrometer contained non-linear distortion on the baselines. An example of these RAIR spectra is shown in Figure 2-14 from a total deposition period of 150 minutes. The baselines drifted into some wave-like distortions from one measurement to the other over the duration of the entire set of measurements for the entire period of deposition. The distortion can be attributed to subtle variations in instrument conditions over time, in particular the temperature and the position of the sample, and not on the variation of reflectance due to overlayer deposition as the distortion appeared even for a clean surface and varied between the sets of measurements for perylene on the Cu(110) surface. Nevertheless correction could be performed to compensate for the distortion and obtain a flat baseline at the level of 100% reflectance. The correction involved manual specification of the baseline on each spectrum, i.e. a line was drawn on the distorted baseline.

A common feature in each RAIR spectrum from the separate experiments is the dense appearance of an almost countless number of bands in 1350 – 2000 cm^{-1} and above 3500 cm^{-1} from an increase in concentration of atmospheric H_2O in the path of the IR beam. These bands were dominant in the spectra. The possible reason was increased local concentration of water vapour in the immediate environment of the spectrometer detector unit and condensation of moisture on the window of the detector device. At the time of the experiment, there was a problem of poor level of vacuum in the vacuum insulation jacket of the liquid nitrogen container to cool down the IR detector. The problem of poor vacuum in the detector unit was apparent from accumulation of ice on the external cover of the detector unit.

RAIRS is known to produce high-resolution spectra (cf. high-resolution electron-energy loss or HREEL* spectra for perylene[14,15]). However, a major

* High-resolution electron-energy loss spectroscopy (HREELS) is a vibrational spectroscopic technique based on inelastic scattering of electrons from surfaces but produces much lower spectral resolution than RAIRS.

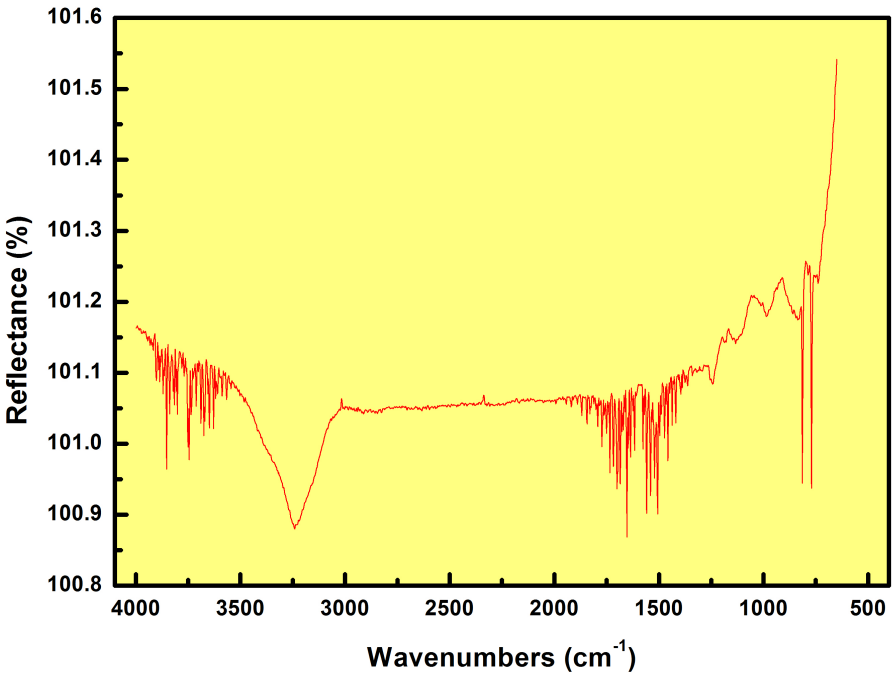

Figure 2-14. An example of a RAIR spectrum of perylene molecules on the Cu(110) surface obtained straight from the FT-IR spectrometer upon measurement after a total deposition period of 150 minutes.

drawback of RAIRS for molecules on surfaces can be the issue of weak IR bands. Perylene molecules at surfaces are expected to produce weak bands because aside from the sample concentrations are low, the chemical bonds in perylene are almost non-polar and the poly-aromatic molecular structure is almost rigid and almost flat. The worst-case scenario is when the bands are comparable to or even less than the distortion of the baseline and magnitude of variation in the amount of noise present; unfortunately however, the case is true in the present experiment and in particular for the samples up to the monolayer as can be expected from the low concentration of perylene and the weak dipole moments in perylene. Extreme care had to be taken with manual baseline correction to avoid unintentional elimination of actual vibrational bands. The magnitude of a band must be higher than the level of the baseline in a spectrum for the band to be considered. The existence of an actual band at a particular vibrational wavenumber in a RAIR spectrum can be assured from consistent appearance in separate experiments. Three separate sets of deposition on the

clean Cu(110) surface and real-time RAIRS measurements were performed. Each spectrum in the sets of measurements was examined for consistent and well-reproduced bands at particular frequencies. The existence of these bands was noted and particular distinction was made for them in the baseline correction process. Manual baseline correction was then performed for each spectrum.

Bands in 2000 – 3000 cm^{-1} and above 3500 cm^{-1} do not exist for perylene. Consistent bands for perylene were not observed in 3000 – 3500 cm^{-1} from the experiments. The bands from water do not set distinction from possible bands of perylene in 1350 – 2000 cm^{-1}. The analysis of RAIR spectra was therefore limited to 700 – 1350 cm^{-1}.

Post-Calibration of STM Measurement

Post-calibration is the application of correction factors to the dimension in X, Y, and Z axes of STM measurements. The correction factor for each axis is calculated from the ratio between the mean from a set of measurements of specific features on a post-calibration standard and the known dimension of the specific features in the same axis. The post-calibration standard was a set of atomic-resolution topographic STM measurements of the pure Cu(110) surface up to 200 Å x 200 Å for the STM measurements in Experiment Set-up No. 2 and of a well-ordered p(2x1) oxygen superstructure on the Cu(110) surface up to 400 Å x 400 Å for the STM measurements in Experiment Set-up No. 3. Figure 2-15 shows an example of the post-calibration standard for each of the experiment set-ups.

The post-calibration factors in the X and Y axes were calculated based on the ratio between the known dimensions and the STM measurements of the rectangular unit cells for the Cu(110) surface and for the p(2x1) oxygen superstructure. The unit cell of Cu(110) surface has known dimensions of 2.55 Å for $\mathbf{a_{Cu}}$ in the <110> direction on the substrate surface and 3.61 Å for $\mathbf{b_{Cu}}$ in the <001> direction on the substrate surface. STM measurements of the unit cell dimensions and orientations can come directly from profile scans on the topographic image or indirectly from the FFT spectra of the topographic image. However, the latter possesses added benefits for two reasons. One reason is the use of an entire image in the post-calibration standard instead of a limited number of selected locations. Another reason is the possible superposition of a number of individual FFT spectra into a single FFT spectrum. These reasons enable acquisition of better statistical averages for the measurements and of measurement precision. Figure 2-16 shows an example of superposition of a number of FFT spectra from a set of 200 Å x 200 Å STM measurements for the p(2x1) oxygen superstructure. The elliptical lines on the FFT spectra correspond to the 2D Gaussian surface fitted to each of the peaks from the periodic structure of p(2x1) oxygen. The dimensions of the unit cell are calculated as the reciprocal of the distance between the maxima of two peaks at inverse locations. The measurement precision comes from the widths of the 2D

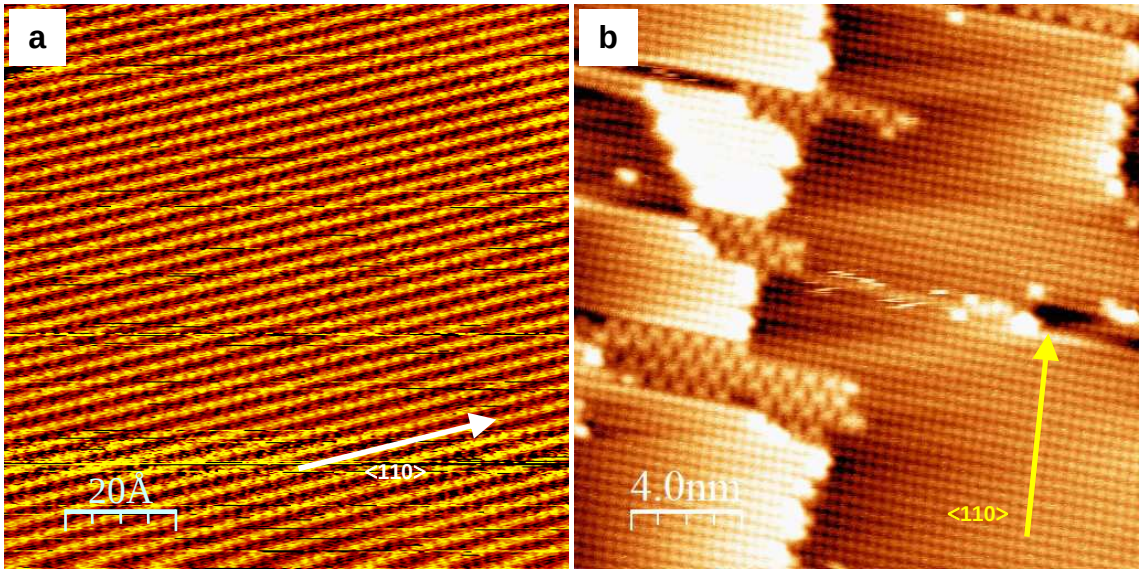

Figure 2-15. Examples of post-calibration standard of STM topographic measurement: (a) atomic-resolution 100 Å x 100 Å image of a Cu(110) surface at U = -508 mV and I = 0.19 nA; (b) atomic-resolution 200 Å x 200 Å image of a p(2x1) oxygen superstructure on a Cu(110) surface at U = +1000 mV and I = 0.40 nA.

Gaussian surfaces. The spread of the FFT peaks or in other words the variation of periodic distances could be due to some disorder in the superstructure and some drift of the piezoelectric scanner in the STM instrument. The same process is made for the FFT spectra of the post-calibration standard from the pure Cu(110) surface. The rest of the process towards the post-calibration factors is mere trigonometric calculations.

The post-calibration factors depend on the axis of scan, the scan size, and the scan direction. Figure 2-17 summarizes the post-calibration factor in X and Y axes as a function of scan size at 0°-scan direction for each of the experiment set-ups. The error bars come from the measurement precision. The calibration factor for Experiment Set-Up No. 2 approaches 1.00 in X axis as the scan size increases and is about constant around 1.25 in Y axis. The calibration factors for scans over 200 Å in Experiment Set-Up No. 2 can be estimated around 1.00 in X axis and 1.25 in Y axis. Indeed, post-calibration factors for 500 Å x 500 Å STM measurements in Experiment Set-up No. 2 were derived from comparison of same features of perylene on the Cu(110) surface between a 500 Å x 500 Å STM measurement and a post-calibrated 200 Å x 200 Å STM measurement on same location; the factors were found 1.05 in X axis and 1.27 in Y axis. The relative error remains almost the same at 2.1% in X axis and

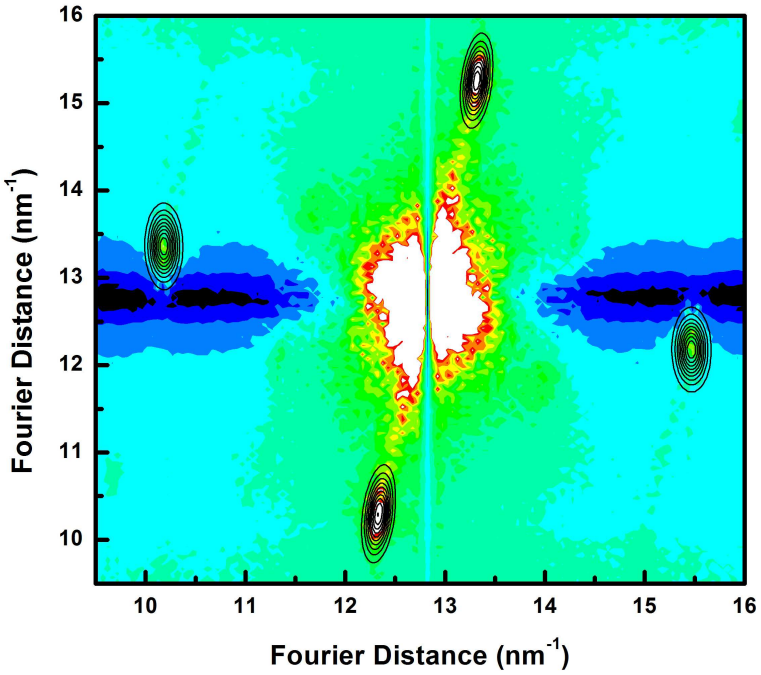

Figure 2-16. A superposition of a number of FFT spectra from a set of 200 Å x 200 Å STM measurements for the p(2x1)-oxygen post-calibration standard.

decreases to 4.3% in Y axis as the scan size increases. On the other hand, the calibration factor for Experiment Set-Up No. 3 is about constant close to 0.98 in X axis and approaches 1.10 in Y axis as the scan size increases. The relative error varies in X axis and decreases in Y axis as the scan size increases. Calibration factors for scans over 400 Å in Experiment Set-Up No. 3 can be estimated as 0.98 in X axis and 1.10 in Y axis from extrapolation of the plot; the relative error can be estimated as 10% for both axes.

Software for Data Analysis

Analyses of STM measurements made use of the software STM Image Analysis version 2.1 for the data from Experiment Set-up No. 2 and the software WSxM version 5.0 for the data from Experiment Set-up No. 3[16]. 2D models were created in AutoCAD 2015. Graphs and the 2D Gaussian surface for the FFT peaks were made in the software OriginPro 9. Some spreadsheet calculations were made in Microsoft Excel.

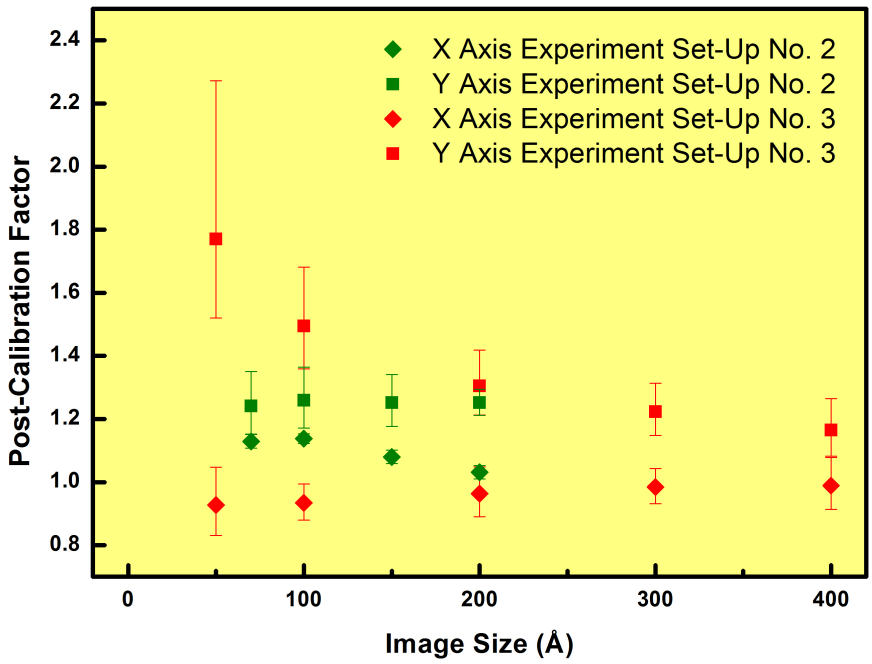

Figure 2-17. Dependence of post-calibration factor in the X and Y axes to scan size at 0°-scan direction for Experiment Set-Up No. 2 based on a pure Cu(110) surface and for Experiment Set-Up No. 3 based on a p(2x1) oxygen superstructure on a Cu(110) Surface.

References

1. Chung, D. D. L. Review graphite. *J. Mater. Sci.* **37,** 1475–1489 (2002).

2. Trucano, P. & Chen, R. Structure of graphite by neutron diffraction. *Nature* **258,** 136–137 (1975).

3. Frank, F. C. On Miller–Bravais indices and four-dimensional vectors. *Acta Crystallogr.* **18,** 862–866 (1965).

4. Kolasinski, K. W. *Surface Science*. (John Wiley & Sons, Ltd, 2012).

5. Chabal, Y. J. Surface infrared spectroscopy. *Surf. Sci. Rep.* **8,** 211–357 (1988).

6. Hayden, B. E. *Vibrational Spectroscopy of Molecules on Surfaces*. 267–344 (Springer US, 1987).

7. Richardson, N. V. & Sheppard, N. *Vibrational Spectroscopy of Molecules on Surfaces*. 1–48 (Springer US, 1987).

8. Attard, G. & Barnes, C. *Surfaces*. (Oxford University Press, 1998).

9. Oura, K., Katayama, M., Zotov, A. V., Lifshits, V. G. & Saranin, A. A. *Surf. Sci. An Introd.* 47–75 (Springer Berlin Heidelberg, 2003).

10. Oura, K., Katayama, M., Zotov, A. V., Lifshits, V. G. & Saranin, A. A. *Surf. Sci. An Introd.* 145–169 (Springer Berlin Heidelberg, 2003).

11. Donovan, P. J. PhD Thesis on Adsorption and Self-assembly of Cobalt(II)-Tetraphenylporphyrin on Cu(110) at the University of Liverpool. (2010).

12. Nita, F. & Pimpinelli, A. When smoothening makes it rough: unhindered step-edge diffusion and the meandering instability on metal surfaces. *Phys. Rev. Lett.* **95,** 106104 (2005).

13. Oja, V. & Suuberg, E. M. Vapor pressures and enthalpies of sublimation of polycyclic aromatic hydrocarbons and their derivatives. *J. Chem. Eng. Data* **43,** 486–492 (1998).

14. Chen, Q., Rada, T., McDowall, A. & Richardson, N. V. Epitaxial growth of a crystalline organic semiconductor: perylene/Cu{110}. *Chem. Mater.* **14,** 743–749 (2002).

15. Unwin, P. J. & Jones, T. S. Vibrational properties of ordered perylene thin films on GaAs(100) and InAs(111)A. *Surf. Sci.* **532-535,** 1011–1016 (2003).

16. Horcas, I. *et al.* WSXM: a software for scanning probe microscopy and a tool for nanotechnology. *Rev. Sci. Instrum.* **78,** 013705 (2007).

Chapter 3
Perylene on Cu(110) Surface

The chapter introduces facts about the chemical structure, the molecular structure, and the crystal structure of perylene. The second section reviews growth, structure, and interaction of perylene on various kinds of substrates in order to understand the behaviour of perylene on surfaces on the whole. One part of the review is devoted to perylene on Cu(110) surface. The subsequent sections present the outcomes of the present studies of perylene on Cu(110) surface based on RAIRS and STM measurements. The present studies of perylene on Cu (110) surface are preludes to the experimental work on the synthesis of graphene on Cu(110) surface in the next chapter, but hopes to add some data to resolve the discrepancies between independent groups in the conclusions on the multilayer structure of perylene.

3.1 Related Facts about Perylene

Perylene is $C_{20}H_{12}$ aromatic hydrocarbon and can be viewed as two naphthalene molecules connected in centrosymmetry. The chemical structure is shown in Figure 3-1a. The directions are indicated for the long molecular axis **L** and the short molecular axis **M**. The carbon-carbon bonds at the connection between the naphthalene parts are called peri-bonds[1]. The effect of resonance at the naphthalene parts is evident in calculations[1–9] and measurements of the interatomic carbon-carbon distances[1,10–13]. The mean carbon-carbon distance at the naphthalene parts measures about no more than 1.41 Å[1,10–13]. On the other hand, the peri-bonds appear in formal structure representation as sp^2 - sp^2 single bonds, and is almost devoid of aromatic conjugation at the center of the carbon skeleton so the aromatic character of the molecule is much localized in each of the naphthalene parts[14]. There had been discrepancies on the measurement for peri-bonds[1,10–13], but the bond distance has become established at 1.473 Å later on[12], whilst for comparison the pure sp^2 - sp^2 single bond is 1.534 Å[15]. The distance for the peri-bonds correlates to π-bond order of

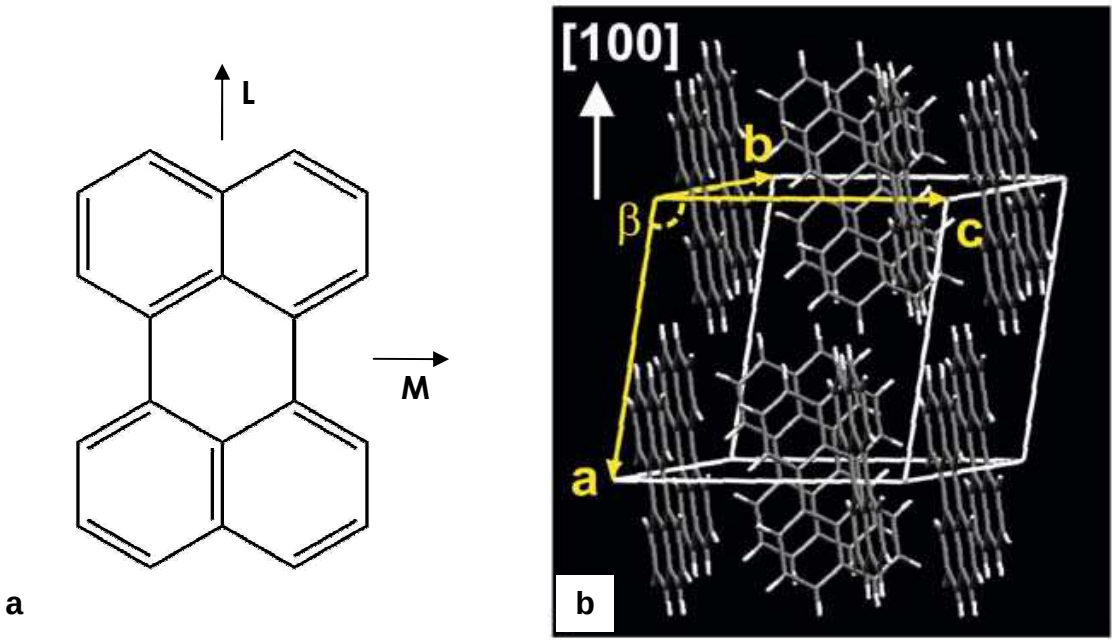

Figure 3-1. (a) Chemical structure of perylene; the directions are indicated for the long molecular axis L and the short molecular axis M. (b) The solid-state structure of the α – polymorph of perylene (adapted from reference[50]).

0.21[15] hence some delocalization of electrons between the naphthalene parts. Calculations do show there exists partial π-bond character in the peri-bonds[1–9].

So far none of the calculations can provide complete explanation of the measured distances for the bonds in perylene[1–9]. There are speculations that intramolecular steric repulsions between the hydrogen atoms in ortho-positions to the peri-bonds exist[1,4,6,9–11,13,16–18], and cause deformation of the molecular structure and deviation from a planar conformation[4,6,9,10,13,18]. One important deformation could be the stretch of the peri-bonds[1,4,6,9–11,13,16–18]. The peri-bonds impart some flexible character to the almost-rigid carbon skeleton of perylene[19–21]. Indeed, the naphthalene parts of perylene can twist in opposite directions at the peri-bonds about the long molecular axis[9,17,18]. The molecular conformation of perylene exists as an equilibrium between twisted and planar[18].

Perylene in solid state exists in two forms – the α-polymorph[1,13] and the β-polymorph[22]. The most stable form is the α-polymorph[22]; the crystal structure is shown in Figure 3-1b. The α-perylene consists of four molecules in the unit cell of a monoclinic lattice[1,13] and the lattice parameters measure a = 11.27 Å, b = 10.82 Å, c = 10.26 Å, β = 100.55° [1]. The four perylene molecules in the unit cell group in dimers where the molecular planes face each other in staggered

positions at a perpendicular distance of 3.46 Å[1,13]. The molecules are somehow bent from a planar conformation into a bow shape about the **L** axis[1]. The bond lengths and bond angles at symmetrical positions in the chemical structure of perylene are not equal but show deviations from one another[1]. The plane on the b-c axes otherwise known as the (001)-oriented plane exhibits as the preference of texture on the surface of α-perylene[23]. The nearest approach between perylene molecules occurs in the plane. The molecules stand almost upright, the long molecular axis at 85° from the plane[24], and the dimers pack at the level of the plane in a herringbone structure. The overlap and extension of π-orbitals in the (001)-oriented plane excites interest in optimization of α-perylene as an organic semiconductor for applications in electronics and optoelectronics[25].

3.2 A Review of Perylene on Surfaces

The section reviews reports on growth, structure, and interaction of perylene on surfaces at room temperature under UHV conditions unless the conditions are specified otherwise. The surfaces are metals, inert insulators, and inorganic semiconductors.

On Metal Surfaces up to Monolayer Saturation

The consensus from the reports of perylene on metal surface at sub-monolayer coverage is that it exhibits mobile behaviour. The intermolecular van der Waals interaction and the variation in molecule-substrate interaction with adsorption sites must be too weak to suppress molecular diffusion and to impose stable molecular formation. Induced dipole interaction in hydrocarbons is one of the weakest forms of van der Waals interaction. Most of the STM investigations on metal surfaces at sub-monolayer coverage have reported no images of perylene unless performed at low temperatures[26–32] whilst others have observed some mobile or unstable structures of aggregated molecules but have been unable to demonstrate resolution of individual molecules[33–35].

Perylene molecules in direct contact with the metal surface adsorb in a flat-down orientation[26–30,32,36–41] so here the description of superstructures is made on such context unless stated otherwise. The reason for the flat-down adsorption is the favourable overlap between the π-orbital states of the molecule and the valence band states of the surface[29,36–38,42]. Electron transfer between these states is possible for some metal surfaces based on the lowered binding energies of molecular orbital states in UPS spectra and the dipole excitation of specific vibrational modes in HREEL spectra[27,29,36,37,42]. Indeed, reduction of the work function has been reported[29,36,37,42]. The adsorption energies of an isolated perylene molecule on metal surfaces can be a few hundred meV's as on Ag surface up to tens of eV's as on Ru surface[26,30,36,38,39,43]. Rotation of molecular orientation and variation of adsorption site can change these adsorption energies up to few hundred meV's on Ag surfaces and up to ten eV's on Ru surface[26,30,36,38,39,43]. The molecule-substrate interaction on Ag surface is weak due to mismatch in energy levels

between the π-orbital states of the molecule and the valence d-band states of the surface[39]; indeed, the partial charge density of perylene on the surface remains almost unchanged from the partial charge density of free perylene molecule[39]. Intermolecular interaction between two perylene molecules in the flat-down adsorption on metal surface can provide additional stabilization up to 40 meV[43].

Perylene is selective to particular adsorption sites on metal surfaces as the molecule tends to maximize the overlap between the π-orbital states of the molecule and the valence band states of the surface. The description of preference to a particular adsorption site is made in terms of the location of the center of the molecule on the surface. In fact one report has proposed the non-aromatic nucleus at the center of the molecule forms chemical bond to metal surfaces and the finite size of such non-aromatic nucleus could be another reason perylene is able to select specific adsorption sites[27].

Uniform coverage of a perylene monolayer on metal surface proceeds before formation of multilayer[26–30,32–34,38–40,43]. The subsequent review of perylene superstructures on metal surfaces below focuses on coverages close to or at monolayer saturation. Superstructures in solutions are included as occasional agreement with those under UHV conditions is observed[44]. The superstructures on metal surfaces depend on substrate temperature[26,28,29,33,37–39,43] but the relation to deposition rate remains to be confirmed. The superstructure on (110)-oriented surface can be chiral due to the two-fold symmetry of the surface when the two unit cell vectors are not in the direction of the high-symmetry axes of the surface. The chiral superstructures exist in pairs and are related to each other as mirror images due to reflection across mirror planes on the high-symmetry axes of the surface.

The growth on Ru(0001) has been studied using LEED[32,36], STM[32], and UPS[36]. The saturated monolayer can form p(4x4) superstructure[36], or a coexistence between (12x12) superstructure phase and disordered phase of random-distributed molecules[32]. DFT calculations show the most favourable orientation when the long molecular axis is parallel to the close-packed <1000> directions[36] – in agreement with STM measurements[32]. The molecular

orientation leads to the highest symmetry when the center of the molecule is located at the atop site or the bridge site[36]. Decomposition of the monolayer occurs above 475 K and leads to some residual hydrocarbon[36].

The growth on Ag(110) has been studied using LEED[26,33,37,38], STM[26,38,39,43], and UPS[37]. The growth process shows evolution in structure as deposition approaches monolayer saturation[26,33,37,38]; the structure starts from a disordered but homogeneous distribution of the molecules and proceeds towards various ordered superstructures in a number of transformations[26,33,37,38]. The saturated monolayer can form incommensurate[33], or commensurate[26,37–39,43] superstructures under various growth temperatures. Except for the c(6x2) superstructure[37], the superstructures are chiral. For some superstructures, the long molecular axis is parallel to the close-packed <110> directions[26,39]; DFT calculations show the molecular orientation corresponds to the most stable adsorptions[26,39,43]. However, there are discrepancies in the reported adsorption energies and the location of the most stable adsorption site; in two reports the hollow site is the most stable at 311 meV in one[26] and 530 meV in the other[39], but in another report the short-bridge is the most stable at 554 meV[43]. The reason for these discrepancies is not clear but differences can be seen from the details of the calculations such as the simulation software, the approximation for the exchange correlation, and the description for the ion-electron interaction. For the other superstructures where the molecules form as dimers, trimers, and close-packed ‘monomers’ in molecular rows in the <111> directions, the long molecular axis is rotated 50° from the close-packed <110> directions[38,43]; DFT calculations for the molecular orientation show stable adsorption at 302 meV when the center of the molecule is located at the short-bridge site[38]. Inclusion of intermolecular interaction into the calculations shows the adsorption for the close-packed ‘monomers’ becomes more stable at 327 meV [43]; the molecules in the dimers and the trimers keep the adsorption at the short-bridge site, but the adsorption energies decrease to 273 meV and 264 meV as the molecules compress into the dimer and the trimer due to increase in both intermolecular repulsion and molecule-substrate separation[43]. Decomposition of the monolayer occurs above 410 K [37].

The growth on Ag(111) has been studied using HREELS[27], LEED[27,45], NEXAFS[45], and STM[27] . The growth process evolves in a similar manner to the observation on Ag(110) surface[27]. The saturated monolayer forms the molecules in an incommensurate hexagonal lattice but possesses no order in molecular orientation[27]. However, STM has been reported to be unable to obtain measurements for the monolayer[27]. The flat-down orientation of molecules on the surface has been found to be meta-stable as the molecules reposition towards an upright orientation at increased temperatures[27,45] – which is not unexpected as solid-state perylene forms the stable α-polymorph when the molecule-substrate interaction is weak, and the texture of α-perylene on surfaces prefers the (001)-oriented plane where the molecules stand almost upright[46]. Desorption of the monolayer occurs from 480 K[27].

The growth on (1x2)-reconstructed Au(110) has been studied using LEED[33,34], STM[33,34], and XPS[33]. Molecular chains form in the <110> direction with structural transitions into more compact inter-chain separations of four, three, and two units of the interatomic distance a in the <001> direction on the surface as deposition approaches monolayer saturation[33,34]. The free surface of Au(110) is known to form favourable 1 x *N* reconstructions[47]. The structural transitions are presumed to be a consequence of perylene-induced reconstruction of the Au(110) surface into (1x4), (1x3), and (1x2)[34]. The 4a-spaced and the 3a-spaced molecular chains possess no 2D order and the molecules tend to remain mobile prior saturation[33,34]. Weak intermolecular and molecule-substrate interaction is consistent with XPS measurements[33]. The saturated monolayer forms a commensurate (7.5x2) superstructure in anti-phase domains[33,34]. The unit cell consists of two molecules tilted towards the surface normal at non-equivalent positions[33,34].

The growth on Au(111) has been studied using LEED[28,33], STM[28,29,40], UPS[29,42], and XPS[29]. The growth process evolves in a similar manner to the observation on Ag surfaces[28,33]. The saturated monolayer forms a commensurate (4x4) superstructure[28,29,33]. The long molecular axis is parallel to the <112> direction[28,29]. DFT calculations for the molecular orientation show the location of stable adsorption can be the fcc site or the bridge site as the

difference in adsorption energies is just 3 meV[28]. Electrochemical STM measurements also show formation of a (4x4) superstructure in 0.1 M $HClO_4$ solution, despite additional factors such as the role of the electrolyte solution and the charged interface[40]. The saturated monolayer can also form other superstructures under certain growth conditions.

The adsorption on Cu(111) in 0.1 M $HClO_4$ solution has been studied *in situ* using electrochemical STM[41]. The saturated monolayer forms four-fold commensurate molecular chains in the close-packed <110> directions and the long molecular axis is parallel to the chain direction[41]. The distance between the molecular chains is twice the distance between the surface lattice points in the <112> direction perpendicular to the chains.

The growth on Cu(100) has been studied using LEED[31], STM[30], and XPS[31]. The saturated monolayer forms c(8x4)[30,31] and c(8x6)[30] superstructures. Each of the superstructures contains two molecules in the unit cell and appears in two symmetry-equivalent domains due to the four-fold symmetry of the surface[30]. The long molecular axis is parallel to the close-packed <110> directions for both superstructures[30]. This molecular orientation matches the four-fold symmetry of the surface. DFT calculations show the most stable adsorption corresponds to this molecular orientation and the center of the molecule located at the atop site, and the molecular plane exhibits a minor bend[30]. The adsorption leads to the four aromatic nuclei of the molecule located almost at the bridge site[30]. The c(8x4) superstructure is stable up to 500 K[31].

On Metal Surfaces at Multilayer Coverage

There are three principal modes of overlayer growth on surfaces. The Frank-van der Merwe mode forms a complete layer before the next layer starts. The Vollmer-Weber mode nucleates and grows three-dimensional islands. The Stranski-Krastanov mode nucleates and grows 3D islands after formation of a complete two-dimensional layer.

The growth on Au(111) and Ag(111) surfaces occurs in the Stranski-Krastanov mode[27,29,48–51]. Regions of the monolayer remain exposed at multilayer coverage[27,28,33]. The structure of the 3D islands on the Au(111) surface tends towards a (001)-oriented α-perylene crystal[28,48,49]. Based on STM measurements, the growth immediately after monolayer saturation of the (4x4) superstructure on the Au(111) surface forms 2D islands where the molecules are tilted from the surface with an apparent height of 4 – 5 Å and form dimers in an oblique structure[28]. In other words, the flat-down structure in the monolayer does not transfer to the multilayer. Most reports explain the growth behaviour of perylene multilayer on these surfaces as the effect of dominance of the intermolecular interaction in an α-perylene crystal over the molecule-substrate interaction upon saturation of the monolayer, whilst at the same time the texture of α-perylene on the surface has preference for the (001)-oriented plane[28,33,48,49]. Indeed a decrease in molecule-substrate interaction can account for the reduction of growth rate upon monolayer saturation[28,33].

Desorption of the multilayer starts at 400 K on Ru(0001) surface[36] and below 410 K on Ag(110) surface[37].

On Cu(110) Surface

The growth on Cu(110) is reviewed here as a separate section in the interest of the studies in the present chapter. There exists two sets of reports on the growth of perylene on Cu(110) surface. One is from the research group of N.V. Richardson and co-workers who supported an exceptional case of epitaxial growth for the multilayer with molecules in a flat-down orientation[52]. The other is from the research group of C. Wöll and co-workers who made an independent investigation but then came to a different conclusion on the growth of the multilayer[53] – consistent with the growth of perylene on other metal surfaces in the multilayer[27–29,33,48–51]. Hereafter 'NR group' for the former and 'CW group' for the latter are used as abbreviations.

The phase diagram in Figure 3-2 shows a map of the coverage and temperature dependence to summarize the approximate location of the preparation conditions for the reported structures of perylene on the Cu(110) surface. Note the diagram does not have to represent thermodynamic phases as kinetics could be an influence on the formation of the structures. The temperature for the structures on the diagram relates to the substrate temperature in the process of deposition or to the anneal temperature subsequent to deposition at lower temperature. The absence of boundaries for each structure means the structures can coexist and the exact limits of existence are unknown.

NR group included measurements from LEED[35,52], HREELS[52], and STM[35,52]. The saturated monolayer forms a c(8x4) superstructure[35]. The size of the unit cell can accommodate two molecules in a flat-down orientation and a possible disorder in the molecular orientation about the surface[35]. DFT calculations of intermolecular interaction for the most favourable orientation between two adjacent flat-down perylene molecules in the c(8x4) superstructure show weak attraction with an interaction energy of 8 meV when the long molecular axes are in the <001> direction[35]; indeed, some disorder in molecular orientation can be expected as the intermolecular interaction for the molecular orientation is just about 1 meV more stable than those for other possible combinations of molecular orientation[35]. The c(8x4) superstructure transforms at

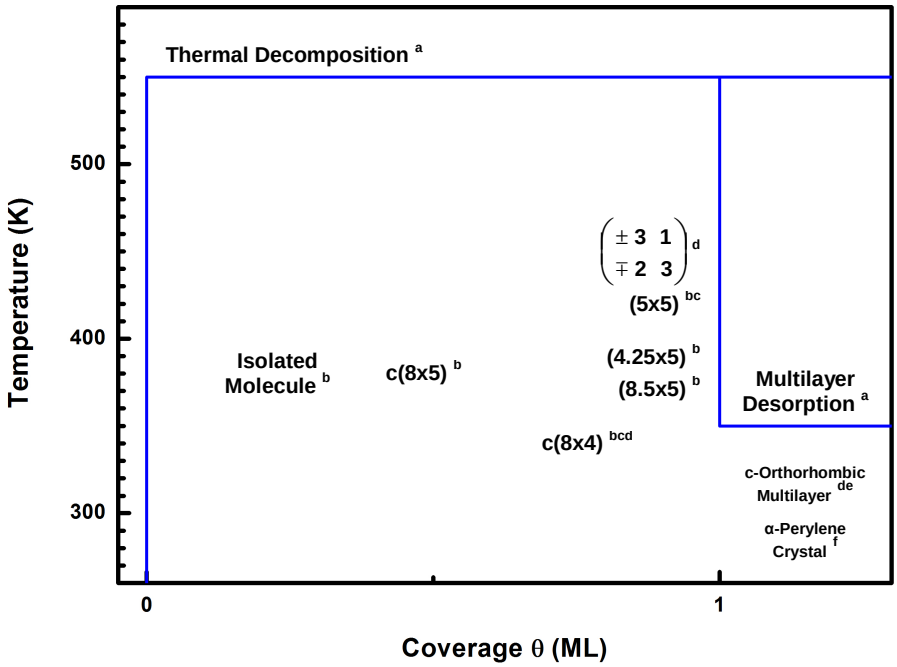

[a] Based on temperature-dependent TDS, XPS, and HAS measurements in CW group[31,54].
[b] Based on HAS measurements at 110 K in CW group[31].
[c] Based on STM measurements at 110 K and room temperature in CW group[31,55].
[d] Based on LEED and STM measurements at room temperature in NR group[35,52].
[e] Flat-down molecules based on HREELS measurements at room temperature in NR group[52]. However, CW group has questioned the conclusion from NR group[31,54] – formation of the structure as a multilayer in the layer-growth mode.
[f] (001)-textured formation in the island-growth mode based on XPS, NEXAFS, AFM, SEM, and polarization microscopy measurements in CW group[50,54].

Figure 3-2. Map of the preparation conditions for particular structures of perylene on Cu(110) surface in terms of coverage-temperature diagram. A unit of monolayer coverage corresponds to monolayer saturation.

450 K into a commensurate chiral superstructure of close-packed molecules in a rectangular unit cell[35]. The size of the unit cell can accommodate just one molecule in a flat-down orientation[35]. The nature of the superstructure imposes restrictions on the orientation of the long molecular axis to the high-symmetry axes of the surface[35]. Molecular chains form in the <110> direction at the edges of terraces[35]. The appearance of the molecular chains has been interpreted as a demonstration of initial growth of an ordered multilayer over the surface of the monolayer superstructures[35]. The extent of the molecular-chain formation is limited in the environment of the chiral superstructure[35]. On the other hand,

further exposure of the c(8x4) superstructure increases the extent of the molecular-chain formation[35].

Formation of multilayers has been assumed after deposition for a certain period of time[52]. Most of the molecules adopt a flat-down orientation[52]. The surface of the overlayer can be described in a rectangular unit cell whose vectors are 8-fold commensurate in the <110> direction but incommensurate in the <001> direction[52]. The visible features are well-ordered close-packed molecular chains of flat-down molecules in the <110> direction[52]. The orientations of the long molecular axes alternate between the <110> and <001> directions in each molecular chain[52]. Adjacent terraces on the overlayer are separated across step edges with a height of 1.7 Å[52]. The relative position of molecular chains between adjacent terraces across step edges registers in-phase in the <001> direction but out of phase in the <110> direction[52]. Based on these features, a novel ABAB-stacked epitaxial formation of a centered orthorhombic perylene crystal has been proposed with six flat-down perylene molecules in one unit cell of dimensions 20.7 Å x 19.3 Å x 3.4 Å [52]. Hole defects appear as deep as 3 nm – equivalent to about 18 monolayers[52]. The surface of the overlayer shows extreme flatness so a Frank-van der Merwe growth mode has been proposed. The 8-fold commensurate period in the <110> direction is a feature common to both the c(8x4) superstructure in the saturated monolayer and the centered orthorhombic structure in the epitaxial multilayer[35]. The epitaxial multilayer has therefore been assumed to form on top of the c(8x4) superstructure[35].

The stability of perylene on Cu(110) surface has been followed based on temperature-dependent HREELS measurements[52]. The multilayer is stable up to 465 K, and then desorbs up to 540 K [52]. The monolayer is stable up to 600 K, then desorbs at higher temperatures, but upright molecules remain, perhaps those molecules adsorbed at surface defects[52].

CW group included measurements from NEXAFS[54] ,TDS[31,54], XPS[31,50,54], HAS[31], LEED[31], STM[31,55], AFM[50,54], OPM[50] and SEM[50]. The outcome of the investigation into the stability of perylene on Cu(110) surface in CW group disagrees with that of the NR group[31,52,54]. Desorption of the

multilayer occurs with zero-order kinetics from about 350 K and peaks at about 380 K with an activation energy of 1.26 eV[31,54]. The saturated monolayer remains stable up to 550 K without desorption of intact perylene molecules before decomposition at higher temperatures[31,54]. The thermal characteristics manifest the difference in strength between the molecule-substrate interaction in the monolayer and the intermolecular interaction in the multilayer[54,55].

The formation of well-ordered superstructures is dependent on coverage and temperature[31]. The measurements of the superstructures were based on He diffraction for accurate determination and the experiments were performed at a substrate temperature of 380 K to limit the formation to no more than monolayer saturation and to exclude formation of multilayers[31]. The formation starts from a dilute phase of isolated molecules[31]. Further exposure forms a c(8x5) superstructure in coexistence with the dilute phase of isolated molecules before a c(8x4) superstructure appears[31]. Monolayer saturation forms a (4.25x5) superstructure and some minor coexistence of an (8.5x5) superstructure[31]. The unit cell of the (4.25x5) superstructure consists of two molecules. Some molecular chains exist and extend from step edges onto the surface terraces in addition to close-packed superstructures[55]. Transformation of the saturated monolayer into a (5x5) superstructure occurs after some time period of anneal treatment at elevated temperatures up to 450 K with some coexistence of c(8x4) and other superstructures[31,55]. Perylene molecules in the saturated monolayer are intact and possess a flat-down orientation[31,54,55].

STM measurements show the saturated monolayer of the (5x5) superstructure consists of molecular chains in the <110> direction with the long molecular axes in the same direction, and includes adsorbate-induced reconstruction of the Cu(110) surface underneath the saturated monolayer into a periodic modulation of upper and lower terraces across monatomic Cu steps[31,55]. He-diffraction measurements for the superstructure corroborate an increase in the number of Cu-surface steps of 1.3 Å in height[31]. For comparison, the effective thickness of perylene on the Cu(110) surface is 2.1 Å based on He-diffraction measurements for the c(8x5) superstructure[31]. Each of the terraces on the surface reconstruction consists of three close-packed rows of

Cu atoms and accommodates one molecular chain[55]. The (5x5) superstructure contains some amount of local disorder from minute shifts of position in the direction of the molecular chains between molecules across upper and lower terraces[55]. The distribution of shifts is related to the atomic corrugation on the close-packed atomic rows of the Cu surface[55]. The (5x5) superstructure has been noted to possess some resemblance in two-dimensional features to the centered orthorhombic epitaxial structure in the report from NR group[31,52,55].

The close-packed nature of the (4.25x5) superstructure prohibits molecular orientation in the <110> direction and assembles the molecules into a herringbone formation[31,55]. The (5x5) superstructure is less dense-packed[31,55] but reverts to the (4.25x5) superstructure upon subsequent exposure to perylene deposition at 380 K[31]. The transformation into the (5x5) superstructure has been considered to give an enhancement of molecule-substrate interaction from re-orientation of the molecular orientation to the <110> direction whilst at the same time the molecules are still close-packed[55]. The creation of steps in the surface reconstruction has been estimated to need about 0.1 eV per adsorbed perylene molecule[55]. Adsorption of a perylene molecule on the centre of three close-packed atomic rows of the Cu surface with the long molecular axis in the <110> direction has been expected to be favourable because of match in dimension and symmetry between perylene and the Cu(110) surface[55]. The same adsorption configuration has been assumed in c(8x5) and c(8x4) superstructures[31].

STM measurements show the surface reconstruction evolves into even more complex periodic patterns of narrow terraces in staircases when the anneal treatment of the saturated monolayer is made over extended periods of time[55]. The surface modulation underneath the monolayer exhibits increase in amplitude and period as the transformation proceeds further from the (5x5) superstructure to a (5x10) superstructure and then towards formation of (551)-oriented facets[55].

Growth of the multilayer has been investigated[50,54]. In contrast to the flat-down molecular orientation and Frank-van der Merwe growth mode for the multilayer in the report from NR group, the long molecular axis repositions

towards almost upright orientation as the multilayer coverage increases[54] and 3D islands form in the Stranski-Krastanov growth mode[50]. The multilayer formation is homogeneous at lower temperatures but transforms into islands at room temperature[50]. Minimization of surface tension from an increase of volume to surface ratio has been considered to drive the morphological transformation[50]. The islands form smooth terraces[50]. The height of step edges between smooth terraces measures 1.0 nm, in close agreement with the separation between molecules in an almost upright orientation from adjacent (001)-planes in the α-perylene crystal[54]. Growth in the lateral direction is anisotropic as seen from the rectangular shape of the islands[50]. The shape has been considered reasonable for the herringbone structure of α-perylene crystals in two dimensions[50]. The islands past the coalescence stage of growth become conical-shaped due to the presence of screw dislocation[50]. Perylene is polycrystalline as a film on Cu(110) surface[50].

On Inert Surfaces

This section is included in the review as growth on inert surfaces resembles the growth of 3D islands in the Stranski-Krastanov mode on metal surfaces. Inert surfaces possess weak interaction with perylene at the interface[56,57]. Most of the experiments have been focused on Al_2O_3[49,56,58], SiO_2[46,51,59], and SiO_X[59] surfaces. The molecule-substrate interaction is weaker than intermolecular interactions[46,49]. As a consequence, perylene favours an almost upright orientation on these surfaces to form islands of (001)-oriented α-perylene[46,49,56,58]. The dependence of nucleation and growth on deposition parameters exists in accordance with the concepts of the atomistic theory of nucleation and growth – high growth temperatures[46,56,59], low deposition rates[46,58,59], and decreased molecule-substrate interactions[59,60] lead to low density of islands, large island size, and high crystal quality. Nucleation of 3D islands occurs at accessible conditions over a large window whilst nucleation of 2D islands occurs at low substrate temperatures and high deposition rates[46,56]. TiO_2(110) possesses the distinction from the other inert surfaces as growth proceeds in the Stranski-Krastanov mode – the monolayer consists of

molecules in a flat-down orientation but shows no superstructure order[57]. Perylene desorbs from Al_2O_3 substrate under vacuum even at room temperature[56]; complete desorption has been found at 550 K[56].

Comparison Between Growths on Au(111) and Inert Surfaces

The growth of 3D islands on inert 1-octadecanethiol SAM-modified Au(111)[48], glass[51], and Al_2O_3 surfaces[49] has been studied in conjunction with growth on Au(111) surface for comparison. Better texture towards (001)-oriented α-perylene islands characterizes the growth on SAM[48] and Al_2O_3 surfaces[49], consistent with the flat-top facets of islands[48]. The extent of texture can be explained as an effect of difference in molecule-substrate interaction[48]. The molecule-substrate interaction on inert Al_2O_3 and SAM-coated Au surfaces imposes no constraint to molecular orientation but allows the almost-upright orientation from the start of nucleation. On the other hand, the molecule-substrate interaction on Au(111) surface causes transition in molecular orientation from flat-down to almost upright.

The island density increases with deposition time both on SAM-modified Au(111) and glass surfaces until the islands start to connect together, in contrast to almost-constant island density on a Au(111) surface at the same deposition rate[48,51]. Higher island density and smaller island size exists on SAM-modified Au(111) surface[48]. The change in local structure with time is less rapid on glass – a behaviour consistent with a uniform size distribution of small islands on glass in contrast to an uneven size distribution of large islands on Au surface[51]. Growth in the lateral direction is isotropic on glass surfaces whilst anisotropic on Au surfaces[49,51]. This evidence points to less rapid diffusion on SAM and glass surfaces than on the complete layer of flat-down perylene molecules on a Au(111) surface.

On Inorganic Semiconductor Surfaces

Growth of perylene on GaAs(100) and InAs(111) surfaces shows differences in vibrational features between the monolayer and the multilayer but the vibrational features become consistent with those of the organic crystal in the multilayer[61]. The molecular orientation moves from flat-down towards upright subsequent monolayer saturation but remains almost flat-down[61]. The multilayer has weakened molecule-substrate interaction but has increased crystalline order[61]. The pattern in the surface plane for the multilayer adopts a (3x3)R±45° square structure on GaAs(100) and a rectangular structure with two molecules in the unit cell on the InAs(111)[61]. Rapid desorption of the multilayer on GaAs(100) surfaces occurs above 400 K but the monolayer remains stable up to 620 K whilst desorption of multilayers on InAs(111) occurs at room temperature[61].

Growth on Si(100) surfaces forms 3D islands in accordance with the concepts of the atomistic theory of nucleation and growth[62]. However, the distinction between pure-island growth mode or Stranski-Krastanov mode has not been found[62]. The molecular orientation tends to incline towards the surface for the monolayer but moves towards an upright position for the multilayer[62]. On the other hand, the molecular orientation on Si(111) for both cases of monolayer and multilayer has been found to be flat-down[62,63] despite weak substrate-molecule interaction[62]. The multilayer structure with flat-down molecular orientation has been considered an isolated case of exceptional formation in view of the herringbone arrangement in the crystal structures known so far for perylene[62]. Desorption of the multilayer occurs before decomposition above 600 K and residual carbon remains present even at 1220 K[62].

3.3 RAIRS Characterization of Perylene on the Cu(110) Surface

Identification of IR Bands

Measurements of RAIR spectra were performed in real time with deposition of perylene on a Cu(110) surface at room temperature. Figure 3-3 shows a series of baseline-corrected RAIR spectra from measurements at regular time intervals within a deposition period of 150 minutes. The spectra are shown in red-coloured lines with the order of succession in time from top to bottom. The spectra are off-set from one another at regular separation in the vertical axis of the plot for ease of comparison. Consistent RAIR bands are noted and the wavenumber position is shown as a label next to the band. In the initial period of adsorption, RAIR bands are observed at 740 cm^{-1}, 785 cm^{-1}, 1240 cm^{-1}, and 1325 cm^{-1}. However, the RAIR band at 1325 cm^{-1} attenuates as RAIR bands at 770 cm^{-1} and 813 cm^{-1} develop.

Table 4-1 summarizes a comparison with the IR-active vibrational modes for perylene in past reports from experiments[61,64–67] and theoretical calculations[11,68,69]. Assignment of the RAIR bands in the present measurements can be made on the basis of direct comparison with those in Table 4-1. The RAIR band at 770 cm^{-1} corresponds to the vibrational mode with B_{3u} symmetry due to an out-of-plane bend of the twenty-four C–C bonds[69]. The RAIR band at 813 cm^{-1} corresponds to the vibrational mode with B_{3u} symmetry due to an out-of-plane bend of the twelve C–H bonds[69]. The rest of the RAIR bands however cannot find direct assignment to the reported vibrational modes of perylene[69].

The metal-surface selection rule inherent in RAIRS for flat-down adsorption of planar molecules limits the IR spectrum to out-of-plane vibrational modes. Moreover, substrate-molecule interaction can cause a red-shift in vibrational frequencies[70]. Perylene molecules on Cu(110) and other metal surfaces are known to possess flat-down orientations up to complete saturation of the first monolayer before growth of the multilayer. The flat-down adsorption of perylene on metals is known to be favourable for formation of chemical bonds from overlap between the π-orbital states of the molecule and the valence band

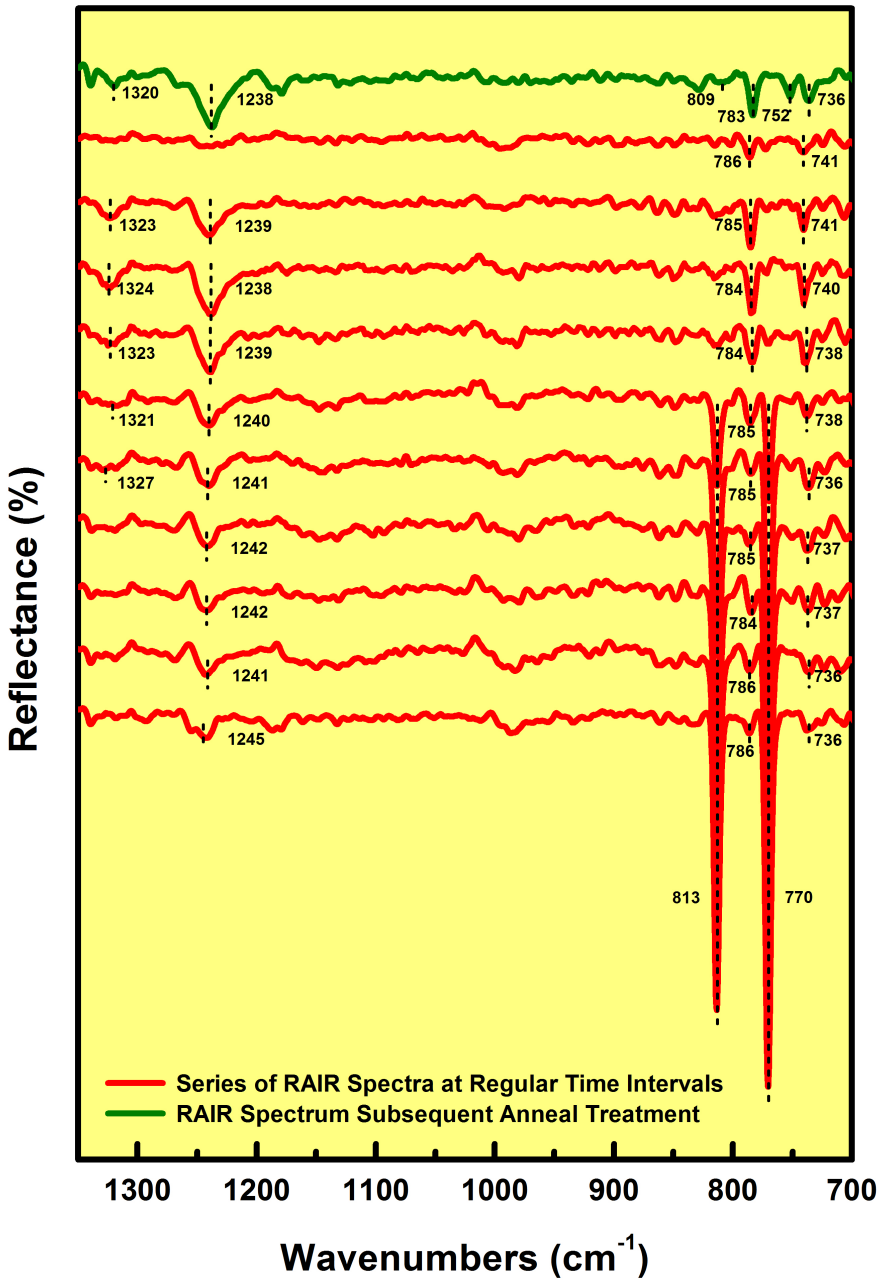

Figure 3-3. RAIRS measurements for perylene on a Cu(110) surface. The spectra in red-coloured lines are real-time measurements at regular time intervals during deposition and are presented from top to bottom in the order of succession with time. The spectrum in green-coloured line is measurement subsequent to anneal treatment at 450 K after the real-time measurements.

states of the metal surface[29,36–38,42], with possible electron transfer from the valence d-band of the surface to the π-orbital of perylene[27,29,36,37,42]. The RAIR bands at 740 cm^{-1}, 785 cm^{-1}, 1240 cm^{-1}, and 1325 cm^{-1} must come from red-

shifted out-of-plane vibrational modes. The report for perylene on GaAs(100) surface has demonstrated red shifts of 15 – 25 cm^{-1} in vibrational frequencies[61]. Possible reasons for the red-shift in vibrational frequencies of molecules in direct contact with the Cu surface due to molecule-substrate interaction include distortion from the planar structure of the perylene molecule and weakened C–C and C–H bonds. On the other hand, the direct correspondence of the RAIR bands at 770 cm^{-1} and 813 cm^{-1} in the present measurements with the reported vibrational modes of perylene shows evidence of interaction limited to Van der Waals. The sudden appearance of these RAIR bands at some point in time of deposition is consistent with suppression of substrate-molecule interaction in the multilayer upon saturation of the monolayer. In other words, the RAIR bands at 770 cm^{-1} and 813 cm^{-1} characterizes growth of the multilayer whilst the RAIR bands at 740 cm^{-1}, 785 cm^{-1}, 1240 cm^{-1}, and 1325 cm^{-1} characterizes growth up to saturation of the first monolayer. The data in Table 4-1 from past reports show most of the IR-active vibrational modes come from in-plane vibrations. In contrast, not even one of the prominent in-plane IR-active vibrational modes is present in the RAIR spectra of the multilayer. The absence of in-plane vibrational modes suggests molecules in the multilayer possess an orientation parallel to the surface plane in accordance with the surface selection rule. Minor contributions of in-plane vibrational modes to the IR bands at 770 cm^{-1} and 813 cm^{-1} can then be ruled out.

The past reports show the vibrational modes at 770 cm^{-1} and 813 cm^{-1} manifest as the prominent IR bands of perylene[69]. Then these vibrational modes can be expected to appear as RAIR bands up to complete saturation of the first monolayer, but can be shifted to different frequencies as the molecules in direct contact with the Cu surface can be under the influence of molecule-substrate interaction. The RAIR bands at 770 cm^{-1} and 813 cm^{-1} of the multilayer are positioned 43 cm^{-1} apart from each other. For comparison, the RAIR bands at 740 cm^{-1} and 785 cm^{-1} of the molecules in direct contact with the Cu surface are positioned 45 cm^{-1} apart from each other. The differences in position of the RAIR bands are almost the same to suggest the former set and the latter set of RAIR bands are the counterparts of each other and come from the same set of

vibrational modes. In other words, the RAIR band at 740 cm^{-1} is shifted 30 cm^{-1} from 770 cm^{-1} due to molecule-substrate interaction of the molecules in direct contact with the Cu surface. Likewise, the RAIR band at 785 cm^{-1} is shifted 28 cm^{-1} from 813 cm^{-1}. The amounts of red shift in vibrational frequencies are almost the same for the two vibrational modes. The persistence of the RAIR bands at 740 cm^{-1} and 785 cm^{-1} even in the later period of deposition suggests the molecules in direct contact with the Cu surface remain in flat-down orientation in the presence of the multilayer or areas of the saturated monolayer remain exposed.

The RAIR bands at 1240 cm^{-1} and 1325 cm^{-1} cannot be identified with IR-active and even with IR-inactive vibrational modes, as there exists no out-of-plane vibration of frequencies higher than 1000 cm^{-1} in perylene[69]. Dimer modes in α-perylene[67] can be ruled out as the molecules prefer maximum contact with the Cu surface in a flat-down orientation. The surface phonons for Cu(110) surface[71] occur below 200 cm^{-1} so the frequencies of the bands could be too high to be combination bands due to simultaneous excitation of vibrational modes of perylene and phonons of the Cu surface[61]. The most probable explanation for the RAIR bands therefore is combinations of vibrational modes[64,67]. The unknown amount of red shift complicates straight-forward identification of the components of the combinations. The strengths of the RAIR bands indicate one of the components is the vibrational mode at 740 cm^{-1} or 785 cm^{-1}. Various combinations have been examined and the combinations can be

$$1240\ cm^{-1} = 740\ cm^{-1} + 500\ cm^{-1}$$

$$1325\ cm^{-1} = 740\ cm^{-1} + 585\ cm^{-1}$$

The vibrational mode at 500 cm^{-1} could be shifted 30 cm^{-1} from the IR-inactive vibrational mode at 530 cm^{-1}, which comes from an out-of-plane bend of C–C bonds with A_u symmetry[69]. The vibrational mode at 585 cm^{-1} could be shifted 40 cm^{-1} from the IR-inactive vibrational mode at 625 cm^{-1}, which come from an out-of-plane bend of C–C bonds with B_{2g} symmetry[11,64]. There exists no report of the present combinations. However, the combination bands in the past reports for perylene[64,67] can be described as combinations between IR-active out-of-

plane modes of B_{3u} symmetry and IR-inactive out-of-plane modes of A_u or B_{2g} symmetry[11,68,69]. The proposed combination bands are tentative and need to be confirmed from RAIRS measurements of deuterated perylene.

Table 3-1. Vibrational frequencies in the IR spectra for perylene on the Cu(110) surface from the present measurements in comparison with experimental data and theoretical calculations from past reports.

Symmetry[a,h]	Mode[b,h]	Reported Experimental IR Frequencies (cm^{-1})					Perylene on the Cu(110) Surface IR Frequencies (cm^{-1})		
		Crystal[c]	Film[d]	KBr[e]	Ar[f]	CS_2[g]	Multilayer	Sub-monolayer	Annealed
A_u[11] --	OP Vibration[11] Dimer[67]	752	751	752	--	--	--	--	--
B_{3u}	OP CCC Bend	768	762	768	772	770	770	740	736 752
B_{2u}[68,69]	IP CCC Bend[69]	--	--	--	--	--	--	--	--
B_{1u}[68,69]	IP CCC Bend[69]	790	791	791	791	793	--	--	--
B_{1u}[68,69]	IP CCC Bend[69]	--	--	--	811	--	--	--	--
B_{3u}	OP CCH Bend	813	810	812	815	812	813	785	783 809
B_{1u}[11]	IP Vibration[11]	--	--	850	--	--	--	--	--
B_{3u}[69]	OP CCH Bend[69]	889	889	889	--	--	--	--	--
A_u[11] --	OP Vibration[11] Dimer[67]	900	898	900	--	--	--	--	--
--	--	910	--	910	--	--	--	--	--
A_u[11] --	OP Vibration[11] Dimer[67]	960	958	959	--	--	--	--	--
B_{1u}[11]	IP Vibration[11]	--	--	963	--	--	--	--	--
B_{3u}	OP CCH Bend	967	966	968	970	967	--	--	--
B_{1u}[11]	IP Vibration[11]	--	--	980	--	--	--	--	--
B_{2u}	IP CC Stretch	1042	1043	1042	1047	1043	--	--	--
B_{1u}[68,69] B_{2u}[11]	IP CC Stretch[69] IP Vibration[11]	1085	1086	1085	1088	1085	--	--	--
B_{2u}	IP CCH Bend	1127	1126	1127	1131	1128	--	--	--
--	Dimer[67]	1137	1137	1137	--	--	--	--	--
B_{1u}	IP CCH Bend	1150	1150	1151	1150	1157	--	--	--
B_{2u}[68,69]	IP CCH Bend[69]	1187	1187	1187	1186	1183	--	--	--
B_{2u}[11,69] --	IP CCH Bend[11,69] Dimer[67]	1211	1210	1211	--	1214	--	--	--
B_{1u}	IP CCH Bend	1217	1216	1217	1216	--	--	--	--
--	--	--	--	--	--	--	--	1240	1238
B_{2u}	IP CC Stretch	1281	1281	1281	1279	1280	--	--	--
B_{1u}[11]	IP Vibration[11]	1288	1287	1288	1288	1288	--	--	--
--	--	--	--	--	1295	--	--	--	--

--	Dimer[67]	1325	1325	1325	--	1325	--	--	--
--	--	--	--	--	--	--	--	1325	1320
B_{2u}	IP CC Stretch	1333	1332	1333	1335	1333	--	--	--
B_{1u}	IP CC Stretch	--	1367	1367	--	1367	--	--	--
--	--	1375	1373	1378	1374	1372	--	--	--
B_{1u}	IP CC Stretch	--	1382	1382	1385	1383	--	--	--
B_{1u}[69]	IP CCH Bend[69]	--	1392	1392	1396	1395	--	--	--

[a] Symmetry of the IR-active fundamental modes of vibration for perylene in the planar conformation[11,68,69]. Reference is not specified in cases when the reports are in agreement to one another.
[b] Interpretation as dimer mode in the report of Ding *et al.*[67]; refers to the distinct vibrations of perylene dimer in the α-phase crystal. Vibrational motion is specified for each of the IR-active fundamental modes[11,69]; IP: in-plane, OP: out-of-plane. Reference is not specified in cases when the reports are in agreement to one another.
[c] Single-crystal α-perylene[64].
[d] 1000-nm perylene film on Au(111) surface[67].
[e] Perylene in KBr pellets[64].
[f] Perylene molecules in argon matrix[65,66].
[g] Perylene in CS_2 solution[64].
[h] Assignment of symmetry and vibrational motion to experimental IR data based on comparison with theoretical calculations[11,68,69].

Variation in IR Absorption Intensities with Coverage

The plot in Figure 3-4 shows the variation in RAIR absorption intensities for the vibrational modes with time period of deposition hence coverage. The vibrational modes at 740 cm^{-1}, 785 cm^{-1}, 1240 cm^{-1}, and 1325 cm^{-1} of perylene molecules with immediate metal contact increase the RAIR absorption intensities over time in the initial period of deposition as molecules accumulate on the surface. The maxima of RAIR absorption intensities for these modes coincide with one another at a deposition time of about half an hour and should correspond to monolayer saturation. Further deposition upon monolayer saturation produces a slight drop in RAIR absorption intensities of these modes whilst at the same time the IR absorption intensities at 770 cm^{-1} and 813 cm^{-1} in the multilayer start to increase. The drop in RAIR absorption intensities in the first monolayer could be due to intermolecular interactions between the first and the second monolayer.

The RAIR absorption at 740 cm^{-1} seems weaker than the absorption at 785 cm^{-1} in the sub-monolayer regime whilst these RAIR absorptions seem to become almost equal just prior to multilayer formation. The RAIR absorptions for these bands relative to each other in the sub-monolayer regime are somewhat consistent with those reported for the same vibrational modes in isolated perylene molecules[52,69]. In contrast, the same vibrational modes but in the multilayer at 770 cm^{-1} and 813 cm^{-1} come with opposite relations in terms of IR absorption. The same trend has been reported for perylene on GaAs surface in the sub-monolayer and the multilayer[61]. These observations suggest the effect of intermolecular interaction manifests as a variation in absorption of RAIR bands relative to one another[67].

The RAIR absorption intensities at 770 cm^{-1} and 813 cm^{-1} in the multilayer are almost constant after a deposition period of about two hours and consistent in separate experiments. The explanation of the constant RAIR absorption intensities can be constant coverage of the multilayer, which can be traced to the condition of deposition as described below. The condition of deposition can be determined from calculation of the pressure of the perylene molecular beam over the surface based on the kinetic theory of gases. The first

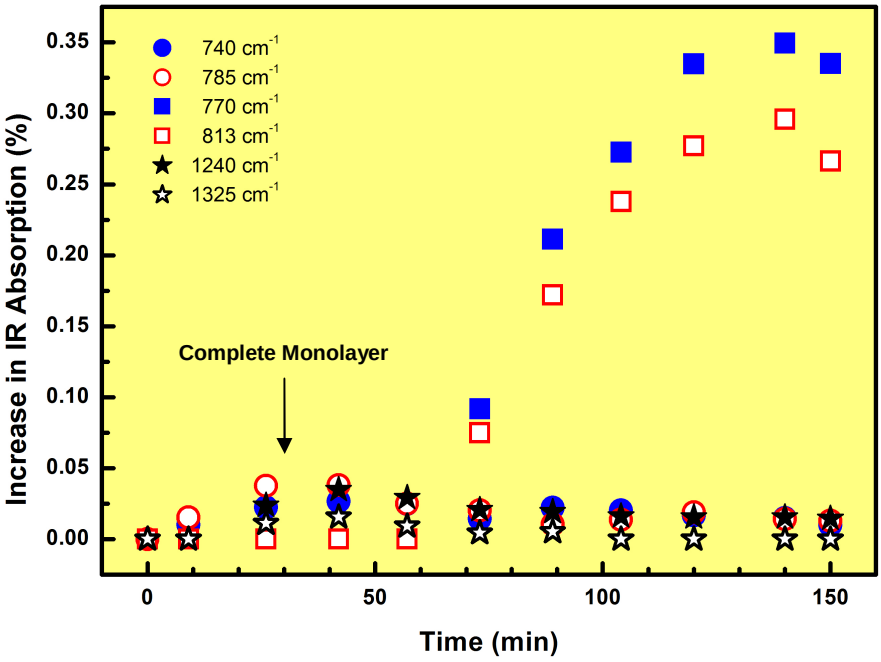

Figure 3-4. Amount of decrease in reflectance with deposition time for the IR bands from the real-time measurements in Figure 3-3.

approximation treats the molecular beam as an ideal gas; the molecular flux I on the surface from the environment is expressed as[72]

$$I = \frac{p}{\sqrt{2\pi\, m k_B T}} \qquad \textbf{(3-1)}$$

Here p is the pressure, m is the mass of the molecule, k_B is the Boltzmann's constant, and T is the temperature. m can be calculated from Avogadro's number and the molecular weight of perylene – which is 252.31 g mol^{-1} – and has a value of 4.1898 x 10^{-25} kg. Perylene is emitted from an evaporator source in common OMBD experiments at temperatures near or above 400 K [27,30,32,34–39,50,54,57,61] (cf. melting temperature of perylene at 551 K [73]). The value of I under a sticking coefficient close to one for metal surfaces can be obtained from the relation

$$n_0 = I\tau \qquad \textbf{(3-2)}$$

where n_0 is the molecular density on the surface at monolayer saturation and τ is the time period needed for monolayer saturation. Close-packed perylene molecules on a Cu(110) surface[35] consist of one molecule in an area of 101.4

$Å^2$ so n_0 has a value of 9.864 x 10^{17} m^{-2}. The value of τ is estimated as 30 minutes (1800 s) based on the time period to reach the maxima of RAIR absorption intensities for the vibrational modes of perylene molecules in direct contact with the Cu surface. The calculated value for the pressure is therefore 7 x 10^{-8} Pa (7 x 10^{-10} mbar) and is consistent with the change of about 0.1 x 10^{-9} – 0.2 x 10^{-9} mbar in the ion-gauge measurement of the pressure within the vacuum chamber when the status of deposition switches between on and off. Moreover, the pressure could still be somewhat lower than the calculated value as the temperature in the gas phase could drop from the evaporation temperature upon adiabatic expansion of the molecular beam in the UHV chamber. For comparison, the vapour pressure of solid-phase perylene at room temperature is estimated as 10^{-8} – 10^{-7} Pa (10^{-10} – 10^{-9} mbar)[56] based on extrapolation of vapour pressure data[73,74]. In other words, the pressure of gas-phase perylene in the molecular beam is about the estimated vapour pressure of solid-phase perylene at room temperature. Growth of perylene on surfaces requires supersaturation i.e. the pressure of gas-phase perylene over the surface must exceed the equilibrium vapour pressure[46]. The reason for the constant RAIR absorption intensities at 770 cm^{-1} and 813 cm^{-1} in the multilayer regime therefore can be termination of growth under the state of equilibrium.

The rise in RAIR absorption intensities at 770 cm^{-1} and 813 cm^{-1} in the multilayer is observed within a short period of time. The multilayer can be estimated to consist of no more than equivalent to three monolayers based on the time period needed for monolayer saturation, but the RAIR absorption intensities for these bands in the multilayer are much greater than three times those for the counterpart bands of the same vibrational modes at monolayer saturation. However, a decrease in growth rate is expected upon monolayer saturation as a saturated monolayer of perylene on metal surfaces can be considered as an inert surface to deposition of perylene[48,49,51]. Indeed, the inert character of the saturated monolayer as a surface to the multilayer is evident from the absence of red shift for the RAIR bands of the multilayer. The main reason for the rise in RAIR absorption intensities must be an increased absorption coefficient of the molecules in the multilayer.

IR Spectrum after Anneal Treatment

Figure 3-3 shows in green-coloured line the baseline-corrected spectrum after anneal treatment of multilayer perylene at 450 K. The spectrum shows RAIR bands at 736 cm^{-1}, 752 cm^{-1}, 783 cm^{-1}, 809 cm^{-1}, 1238 cm^{-1}, and 1320 cm^{-1}. The loss of the RAIR bands at 770 cm^{-1} and 813 cm^{-1} is consistent with desorption of the multilayer[31,54,61]. CW group has demonstrated differences in thermal stabilities between the monolayer and the multilayer[31,54]. The RAIR bands at 736 cm^{-1}, 783 cm^{-1}, 1238 cm^{-1}, and 1320 cm^{-1} possess frequencies close to the respective vibrational modes at 740 cm^{-1} ($\Delta\overline{\upsilon}_{770cm^{-1}} = 30$ cm^{-1}), 785 cm^{-1} ($\Delta\overline{\upsilon}_{813cm^{-1}} = 28$ cm^{-1}), 1240 cm^{-1}, and 1325 cm^{-1} of perylene molecules deposited at room temperature in direct contact with the metal surface. These RAIR bands must come from the same set of vibrations and therefore intact perylene molecules in the first monolayer must remain on the surface after the anneal treatment. The RAIR bands at 752 cm^{-1} and 809 cm^{-1} cannot find identification other than from the same vibrational modes as those for the IR bands at 736 cm^{-1} and 783 cm^{-1}. The inherent high resolution of RAIRS is known to be sensitive to different levels of molecule-substrate interaction[70].

The two sets of red shifts for the same vibrational modes suggests molecular adsorption into two different chemical environments – the RAIR bands at 736 cm^{-1} ($\Delta\overline{\upsilon}_{770cm^{-1}} = 34$ cm^{-1}) and 783 cm^{-1} ($\Delta\overline{\upsilon}_{813cm^{-1}} = 30$ cm^{-1}) from increased substrate-molecule interaction at one adsorption position whilst those at 752 cm^{-1} ($\Delta\overline{\upsilon}_{770cm^{-1}} = 18$ cm^{-1}) and 809 cm^{-1} ($\Delta\overline{\upsilon}_{813cm^{-1}} = 4$ cm^{-1}) from decreased substrate-molecule interaction at another. These facts are consistent with the report from CW group on the transformation of saturated monolayers into a commensurate (5x5) superstructure – the adsorption occurs in two different sites on the adsorbate-induced reconstruction of the Cu(110) surface[31,55]. Note $\Delta\overline{\upsilon}_{770\ cm^{-1}}$ relates to the shifts in frequencies of the same vibrational modes from 770 cm^{-1} whilst $\Delta\overline{\upsilon}_{813cm^{-1}}$ relates to those from 813 cm^{-1}.

The relative absorption intensities between the RAIR bands differ from those between the respective bands of the same vibrational modes in the saturated monolayer deposited at room temperature. The relative absorption

intensities between the RAIR bands at 736 cm^{-1} and 783 cm^{-1} follow those of an isolated free molecule of perylene for the same vibrational modes. The RAIR absorption intensities at 1238 cm^{-1} seems to be stronger but the IR adsorption at 1320 cm^{-1} is now much weaker. The changes in relative absorption intensities could be related to possible reduction in intermolecular interaction from decrease in coverage upon transformation into the (5x5) superstructure[31,55].

3.4 STM Characterization of Perylene on the Cu(110) Surface

STM measurements in the sub-monolayer show no image of perylene – a manifestation of the mobile behaviour on metal surfaces[26–35]. Changes in features of step edges from rough to smooth suggest suppression of Cu-atom diffusion at these sites.

Figure 3-5 shows STM topographic images of a monolayer after a total deposition time period of eight minutes. The STM images are centered at the same location. The suppression of molecular diffusion permits resolution of individual molecules. The 525 Å x 633 Å STM image in Figure 3-5a shows domains of various well-ordered superstructures from a large perspective. Four different superstructures are apparent and the respective unit cells are designated as A in purple, B in blue, C in green, and D in yellow on the 206 Å x 250 Å STM image in Figure 3-5b.

Superstructures A and B consist of molecular chains in the <110> direction. Both NR group and CW group have reported formation of molecular chains in the same direction[31,35,52,55]. The domains of these superstructures are connected to step edges and extend to the lower terrace of the step[35,55] for a length of up to 1400 Å. Figure 3-6 shows STM topographic images at the same scale after a total deposition time period of 15 minutes. However, Figure 3-6a shows more molecular-chain formations than Figure 3-6b. The amount of the molecular-chain formations seems correlated with the amount of steps. Perhaps the nucleation of molecular chain occurs at step edge. Another possible factor to affect the formation of molecular chains is the direction of step edge. The STM images in Figure 3-7 show no molecular chain extends from step edges parallel to the <110> direction alone. The observation seems to suggest nucleation of the molecular chains cannot occur for step edges in the <001> direction.

Domains of superstructures C and D measure up to a size of 800 Å in one dimension. In some cases however domains tend to extent in the direction of one of the unit vectors as the domain boundaries follow the same direction as

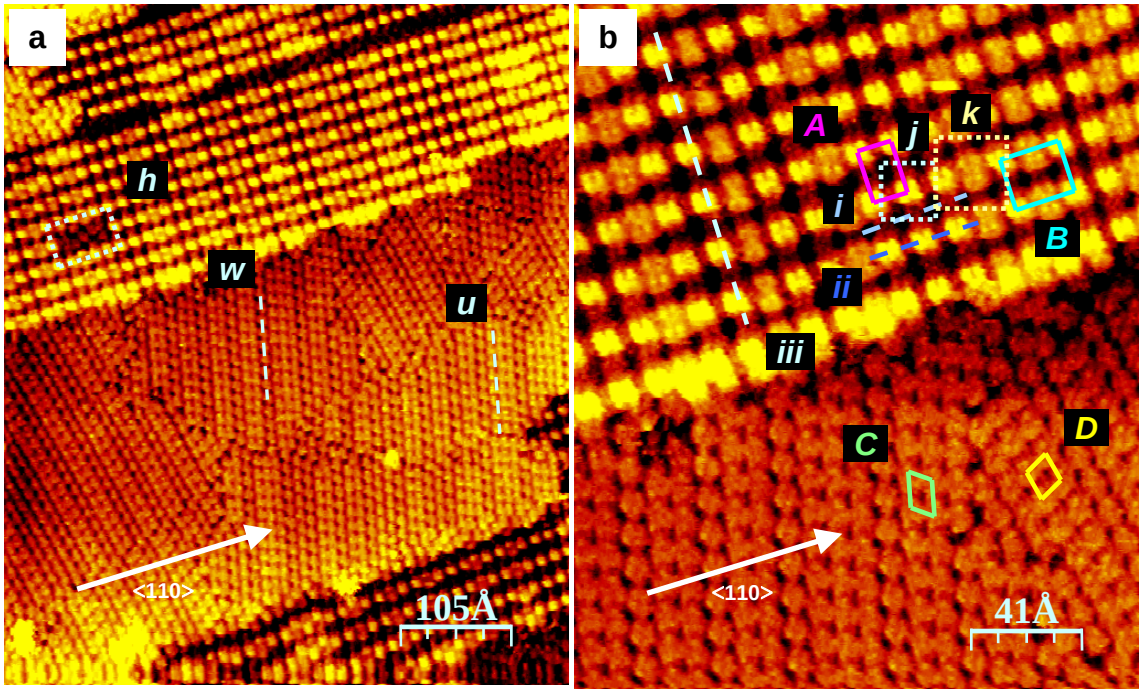

Figure 3-5. STM topographic images of perylene on a Cu(110) surface at monolayer coverage after a total deposition time period of 8 minutes: (a) 525 Å x 633 Å image measured at U = -1030 mV and I = 0.18 nA, corrected with calibration factors X = 1.050 and Y = 1.266 for 500 Å x 500 Å image scans; (b) 206 Å x 250 Å image measured at U = -1030 mV and I = 0.19 nA, corrected with calibration factors X = 1.031 and Y = 1.251 for 200 Å x 200 Å image scans.

shown in Figure 3-7a; the prevalence of the case is apparent from the large perspective of 1500 Å x 1500 Å STM image in Figure 3-7b.

The monolayer of perylene was annealed to some temperature around 400 K, above the start of multilayer desorption. The absence of direct temperature measurement of the sample in the experimental setup prohibited measurement of temperature. The estimate of the temperature was based on experience of the setup. The 1000 Å x 1000 Å STM image in Figure 3-8a shows the anneal treatment caused transformation into a phase with almost perfect and uniform order throughout the surface. The superstructure consists of molecular chains in the <110> direction. The present work names the phase as the temperature-induced uniform superstructure for ease of reference. The high-resolution 206 Å x 206 Å close-up view in Figure 3-8b shows resemblance of the superstructure with superstructure A of the monolayer prior to the anneal treatment.

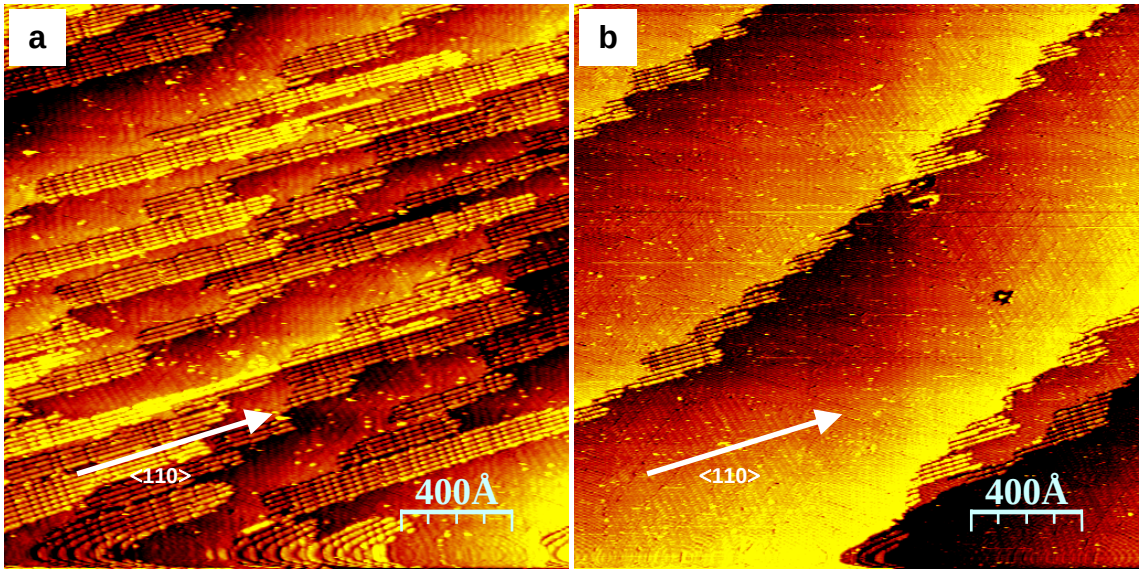

Figure 3-6. 2000 Å x 2000 Å STM topographic images of perylene on a Cu(110) surface at monolayer coverage after a total deposition time period of 15 minutes from two separate experiments. The images are not post-calibrated to correct dimensions. STM measurements were performed at: (a) U = -1633 mV and I = 0.22 nA; (b) U = -1250 mV and I = 0.18 nA.

Further anneal treatment of the temperature-induced uniform phase at temperature around 500 K leads to a disordered arrangement of molecules on the Cu(110) surface as shown from the 525 Å x 633 Å STM image in Figure 3-9a. The STM images alone cannot be used to confirm whether the perylene molecules are intact on the Cu(110) surface after the anneal treatment. A close view from the 206 Å x 250 STM image in Figure 3-9b reveals some molecules exhibit regular shapes whilst others exhibit unusual and irregular shapes in comparison to the regular shape of perylene molecules observed so far. Some of the molecules somehow form short molecular chains. These observations could suggest partial decomposition and chemical-bond formations between some perylene molecules. Indeed, the appearance of huge voids and gaps between entities on the surface could be a consequence of extra spaces created therefrom and partial desorption of perylene molecules. Recent report has shown perylene molecules on Cu(110) surface can couple to one another into oligomers from 595 K[75].

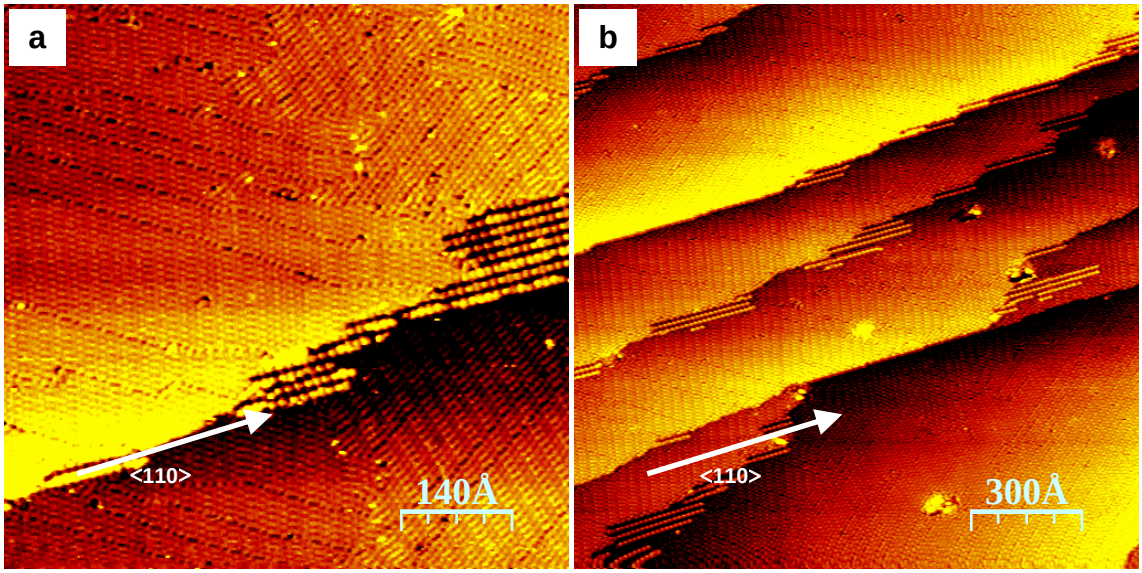

Figure 3-7. STM topographic images of perylene on a Cu(110) surface at monolayer coverage: (a) 700 Å x 700 Å image measured at U = -1250 mV and I = 0.14 nA; (b) 1500 Å x 1500 Å image measured at U = -1277 mV and I = 0.13 nA. The images are not post-calibrated to correct dimensions.

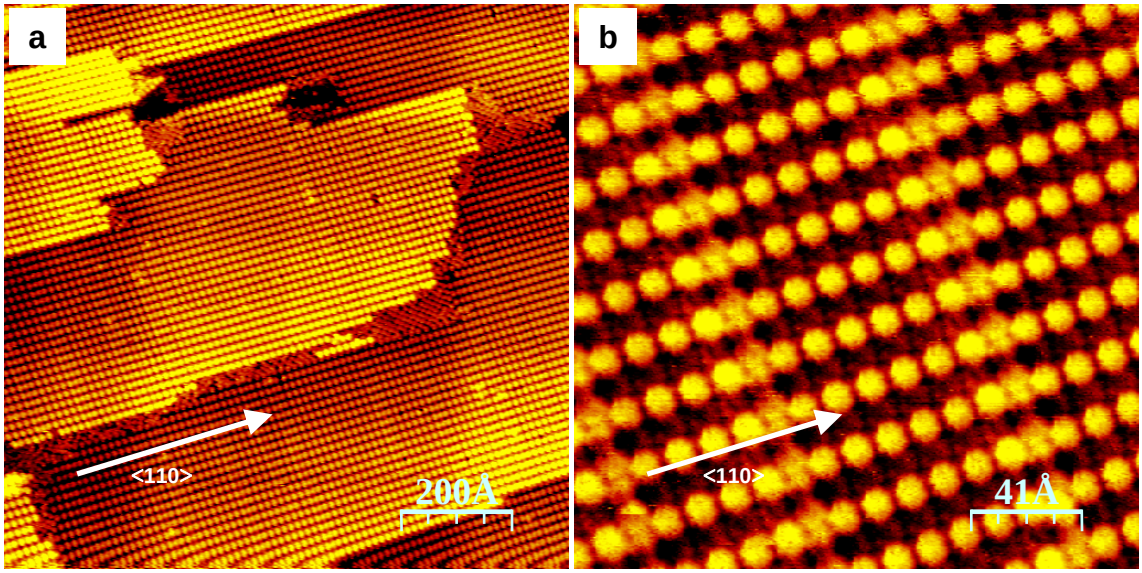

Figure 3-8. STM topographic images of perylene on a Cu(110) surface subsequent to anneal treatment at some temperature around 400 K after monolayer saturation: (a) 1000 Å x 1000 Å image measured at U = -575 mV and I = 0.18 nA, not post-calibrated to correct dimensions; (b) 206 Å x 206 Å image measured at U = -1130 mV and I = 0.10 nA, corrected with calibration factors X = 1.031 and Y = 1.251 for 200 Å x 200 Å image scans.

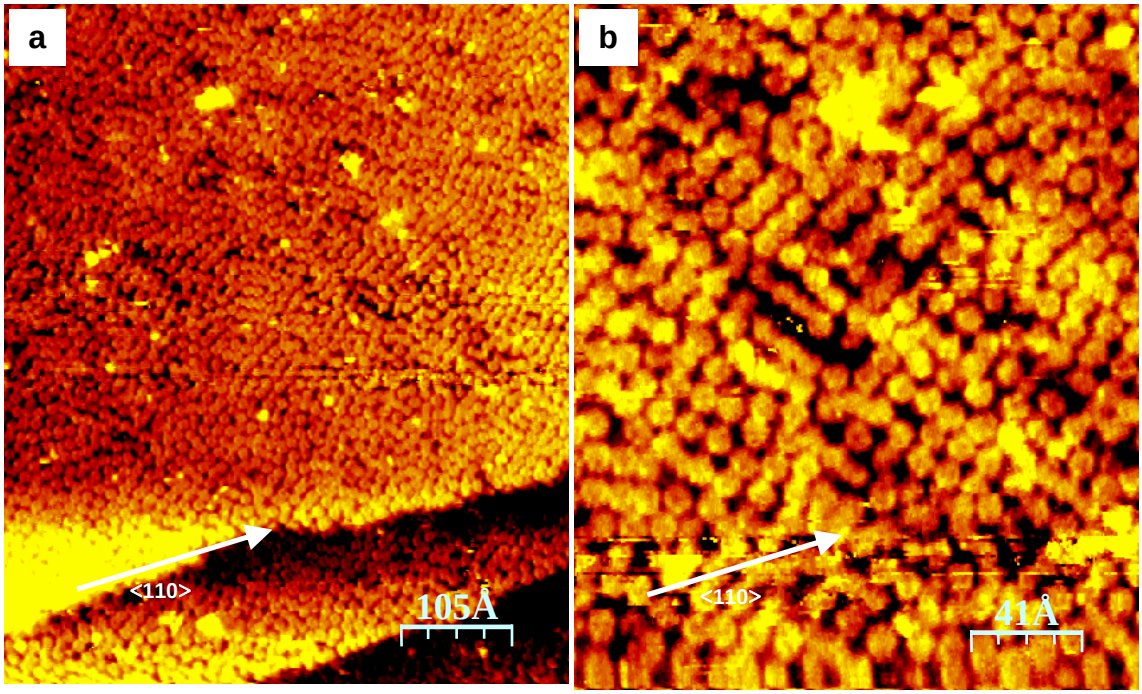

Figure 3-9. STM topographic images of perylene on a Cu(110) surface after anneal treatment of the temperature-induced uniform phase at some temperature around 500 K: (a) 525 Å x 633 Å image measured at U = -831 mV and I = 0.25 nA, corrected with calibration factors X = 1.050 and Y = 1.266 for 500 Å x 500 Å image scans; (b) 206 Å x 250 Å image measured at U = -735 mV and I = 0.22 nA, corrected with calibration factors X = 1.031 and Y = 1.251 for 200 Å x 200 Å image scans.

3.5 Commensurate (5x5) Superstructure of Perylene on the Cu(110) Surface

Temperature-Induced Uniform Phase

The CW group has reported accurate identification of commensurate (5 x 5) superstructure as the main phase of perylene on Cu(110) surface upon anneal treatment of saturated monolayer up to 450 K[31]. Agreement in two-dimensional features and structural measurements identifies the present temperature-induced uniform phase as shown in Figure 3-8 to be a monolayer of the commensurate (5 x 5) superstructure. The observation of multilayer desorption upon anneal treatment at elevated temperatures from the RAIRS measurements supports the assertion that the superstructure occurs as a monolayer phase[31,54,61].

The present STM measurements demonstrate possible resolution of sub-molecular features despite considerable atomic-scale vibrations at room temperature. Figure 3-10 shows sub-molecular resolution for the temperature-induced uniform phase; the inset shows the spatial distribution of the highest occupied molecular orbital (HOMO) and the lowest unoccupied molecular orbitals (LUMO) of perylene. The consistent appearance at different image sizes shows the sub-molecular features are real and not mere artefacts. The negative bias potential applied to the sample in the STM measurements suggests the sub-molecular features come from the occupied molecular orbitals of perylene. Indeed, the sub-molecular features can be compared with the spatial distribution of the HOMO, and also with the calculated partial charge density of perylene on Ag(110) surface[39]. CW group has presented sub-molecular resolution of the spatial distribution of the LUMO of perylene in the (5 x 5) superstructure from low-temperature STM measurements[52,55]. The dark regions in-between the visible bright molecular chains of perylene molecules possess a certain amount of image contrast and resolution to suggest the presence of another set of molecular chains positioned in-phase to the other.

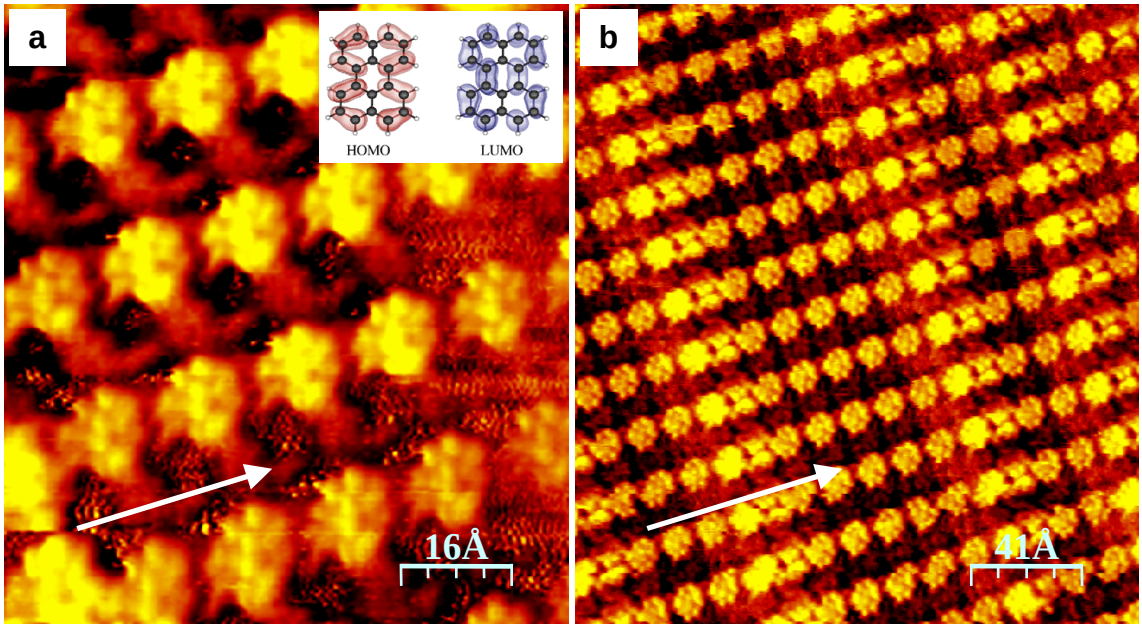

Figure 3-10. STM topographic image of perylene on a Cu(110) surface after anneal treatment of saturated monolayer at some temperature around 400 K: (a) 79 Å x 87 Å image measured at U = -478 mV and I = 0.20 nA, corrected with calibration factors X = 1.129 and Y = 1.241 for 70 Å x 70 Å image scans; (b) 206 Å x 226 Å image measured at U = -524 mV and I = 0.16 nA, corrected with calibration factors X = 1.031 and Y = 1.251 for 200 Å x 200 Å image scans. Inset in (a) shows the spatial distribution of the HOMO and the LUMO of perylene (adapted from reference[52]).

2D Geometrical Model

A method of analysis to complement the limitation in spatial resolution of STM towards elucidation of molecular superstructure at well-defined surface is the use of models to reproduce spatial observations and access further information. The first approximation to the spatial observation is the creation of a simple but precise geometrical representation without sophisticated theoretical calculation. The basic starting point is knowledge of the superstructure unit cell, the molecular structure, the van der Waals dimensions of the molecule, and the structure of the substrate.

Perylene is a simple case because the molecular structure is rigid and planar. The molecule has rectangular shape with van der Waals dimensions of 11.3 Å x 8.7 Å parallel to the axes of symmetry in the plane of the molecule[31,52]. The molecular structure is known from reports of XRD analysis[76]. Adsorption at metal surfaces in flat-down orientation almost preserves the molecular structure so the creation of geometrical models can proceed in two dimensions. The structure of Cu(110) surface can be established from the known crystal structure of Cu.

CW group has proposed adsorbate-induced reconstruction of the Cu(110) surface for the commensurate (5 x 5) superstructure[55]. Here the presence of dark and bright channels parallel to the <100> direction in the STM images for the commensurate (5 x 5) superstructure cannot find explanation in the context of a monolayer phase other than an effect of adsorbate-induced reconstruction of the Cu(110) surface. For the model to match the features and the unit cell of the commensurate (5 x 5) superstructure from the STM images, one therefore leads to the same proposal of the CW group as shown in Figure 3-11. The inset shows a side view of the perylene-induced reconstruction. The need for an anneal treatment at elevated temperature to transform the monolayer into a uniform commensurate (5x5) superstructure supports the existence of adsorbate-induced surface reconstruction as some activation barrier must be overcome to displace Cu atoms on the surface. The black-coloured skeleton represents the molecular structure of perylene. The contour of the molecule corresponds to the van der Waals radius of the peripheral

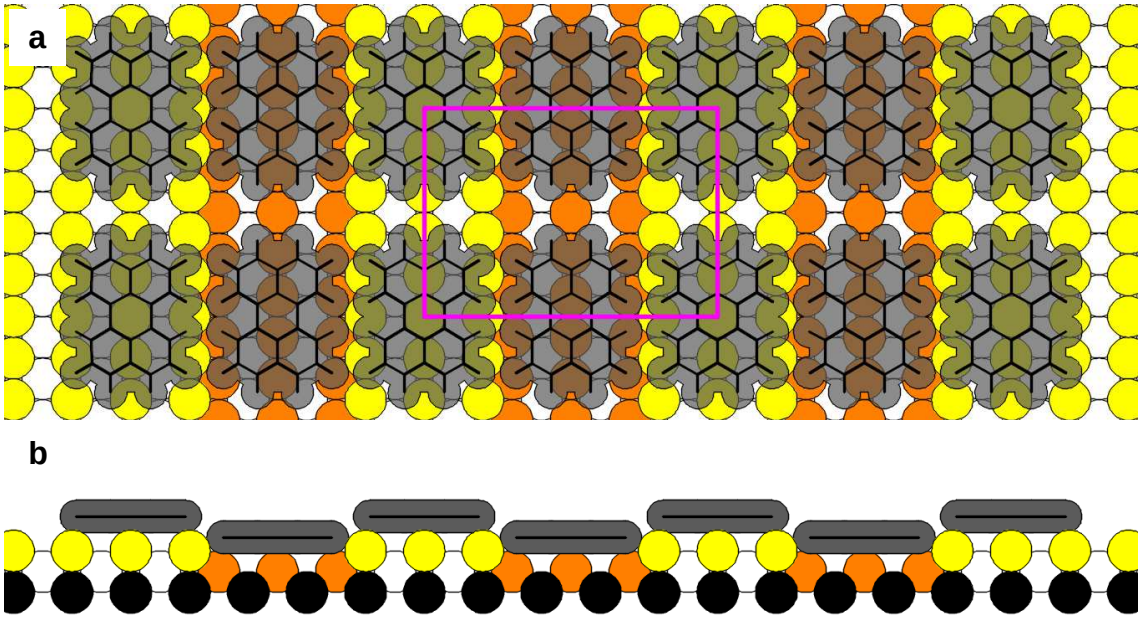

Figure 3-11. (a) 2D geometrical model of the commensurate (5x5) superstructure of perylene on a Cu(110) surface in agreement with STM measurements[55]. The structure of the Cu(110) surface shows perylene-induced surface reconstruction into a periodic pattern of upper and lower terraces. Yellow-coloured solid circles represent Cu atoms on the close-packed rows at upper terraces whereas orange-coloured solid circles represent those at lower terraces. The black skeleton shows the molecular structure of perylene. The contour of the grey-coloured shade around the skeleton outlines the shape of the molecule based on the border line between van der Waals repulsion and attraction. The purple-coloured rectangular frame indicates the unit cell. (b) Side view of the perylene-induced surface reconstruction.

hydrogen atoms. The rectangular frame in purple colour outlines the unit cell. The molecules at the corners of the unit cell correspond to the bright protrusions in the STM images. Note the periodic surface reconstruction and the close-packed organization of molecules cannot exist together for the superstructure unless there exists a strict 5-fold commensurate relation in the <100> direction. Moreover, the strict 5-fold commensurate relation in the <110> direction stems from the close-packed periodic location of molecules at equivalent adsorption sites on the molecular chains.

The model of the surface reconstruction in Figure 3-11 shows periodic formation of upper and lower terraces whose narrow widths allow no more than an entire footprint of a perylene molecule to be in full contact with the metal surface. The height separation between adjacent terraces is equivalent to a monatomic step on the Cu(110) surface. The adsorbate-induced surface reconstruction can be appreciated as favourable when the synergetic factors of

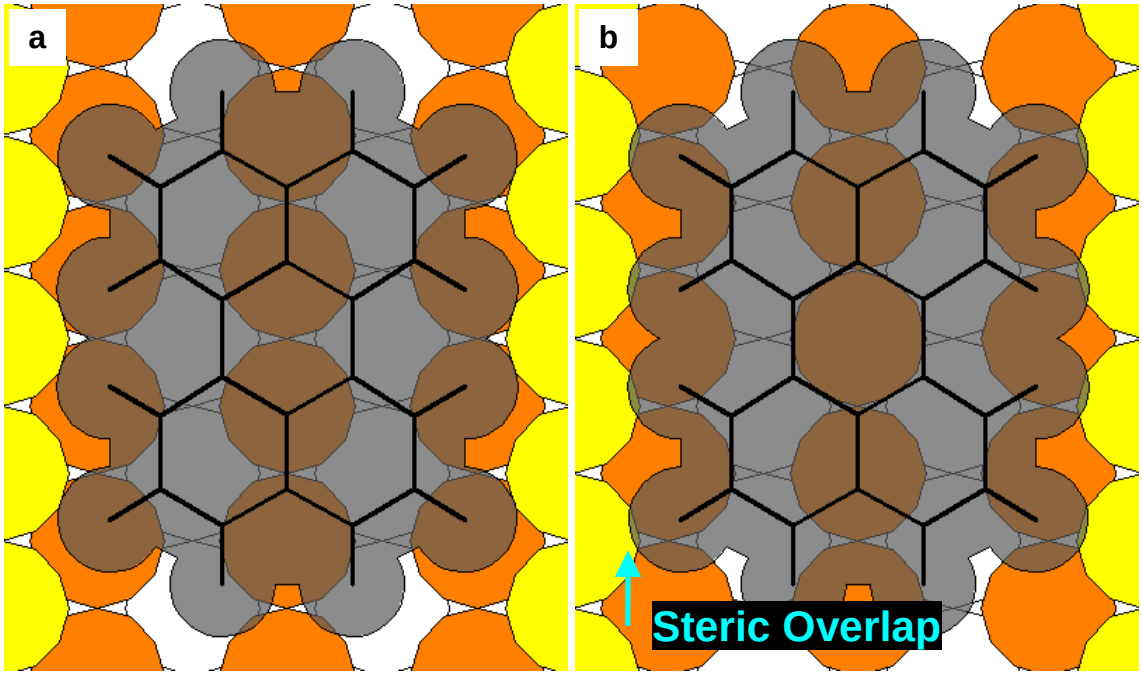

Figure 3-12. Models of perylene-molecule adsorption whose molecular centers are positioned on: (a) the short-bridge site and (b) the atop site on the lower terrace of the Cu(110) surface reconstruction.

match in both dimensions and symmetries between the structures of the perylene molecule and the Cu(110) surface combine together to produce the effect. Each terrace consists of three rows of closed-packed Cu atoms on the top-most layer so the adsorption of a perylene molecule somewhere at the center of these rows would preserve mirror plane on the long molecular axis. Moreover, the surface reconstruction provides a close-packed organization of molecules whilst the molecule-substrate interaction is maximized. Suppose the surface reconstruction does not occur, then the same molecular arrangement requires adsorption of half the population centered on the lower close-packed row of Cu atoms. However, a non-reconstructed Cu(110) surface can not explain the observations for the commensurate (5x5) superstructure. Hence, the model of the surface reconstruction suggests a far more favourable state of adsorption can be achieved when centered on the upper close-packed atomic row than on the lower close-packed atomic row despite the cost of surface reconstruction.

The possible range of adsorption sites for the center of perylene molecule can be reduced to positions between the atop site and the bridge site

at the top-most layer of Cu atoms on the surface. Adsorption at the atop site and the bridge site preserve the two-fold symmetry of both the perylene molecule and the Cu(110) surface, and therefore are expected to lead to the highest adsorption energies[55].

Models of adsorption at the atop site and at the bridge site on the lower terrace of the reconstruction are shown in Figure 3-12. Close inspection of these models reveals adsorption on the lower terrace of the reconstruction leads to some overlap of the van der Waals radius of the peripheral hydrogen atoms with the atomic spheres of the Cu atoms in the upper terraces of the surface reconstruction, except for adsorption at the bridge site as in Figure 3-12a. The largest overlap occurs for adsorption at the atop site as can be seen in Figure 3-12b; one location of the overlap is indicated with an arrow. At the bridge site, the interspersed arrangement between the C–H bonds at the long edge of the molecule and the peripheral Cu atoms avoids overlap. The overlap suggests some repulsion from steric hindrance exists. The model for the commensurate (5 x 5) superstructure in Figure 3-11 therefore positions the perylene molecules on the lower terrace of the reconstruction at the bridge site.

Molecules on the upper terraces are positioned at the atop site to become in-phase with the molecules at the bridge site on the lower terraces. Adsorption must be much more favourable at the atop site than at the bridge site, otherwise the molecular chains on the upper terraces of the surface reconstruction would not demonstrate in-phase position relative to those on the lower terraces. The reactive site of perylene molecule which forms a chemical bond with Ag(111) surface has been reported to be located on the central carbon ring of the molecule[27]; suppose the same is true for perylene on Cu(110) surface, then adsorption at the atop site therefore must enable the shortest bond length and the strongest bond between the molecule and the surface atom. Indeed, theoretical calculation of perylene on a Cu(100) surface has reported the atop site more favourable than the bridge site[30].

The considerations made so far suggest the model in Figure 3-11 corresponds to the most favourable adsorption configuration. Hence the commensurate (5 x 5) superstructure must be a thermodynamic phase.

The existence of the two different adsorption configurations is consistent with the RAIRS measurements for perylene on the Cu(110) surface after anneal treatment. The extent of red shift in the vibrational frequencies for the same vibrational mode must depend on the amount of molecule-substrate interaction. The set of prominent RAIR bands at 736 cm^{-1} and 783 cm^{-1} could correspond to the more-favourable adsorption at the atop site on the upper terraces of the surface reconstruction whilst the other set of prominent RAIR bands at 752 cm^{-1} and 809 cm^{-1} could correspond to the less-favourable adsorption at the bridge site on the lower terraces of the surface reconstruction. However, these associations remain to be confirmed from theoretical calculations.

Preference for adsorption at the atop site alone cannot be supposed to impose in-phase formation of molecular chains in a commensurate (5 x 5) superstructure. Moreover, the van der Waals interaction between flat-down perylene molecules in the same plane must be too weak to predispose order in two dimensions as suggested from the mobile behaviour in sub-monolayer coverage and the reported intermolecular interaction whose magnitude is comparable to the thermal activation at room temperature based on theoretical calculations[35,43]. The existence of repulsion from steric hindrance is plausible as a means of interaction to force adsorption at the bridge site on the lower terraces despite the more-favourable atop adsorption site. However, even the mechanism of repulsion to lock adsorption at the bridge site on the lower terraces and the preference for adsorption at the atop site on the upper terraces together cannot suppose to impose the dominance and the almost perfect order of commensurate (5 x 5) superstructure in the temperature-induced uniform phase. Possible adsorption at the atop sites and at the bridge sites other than those depicted in Figure 3-11 would lead to deviation from in-phase formation of molecular chains. These considerations point to the presence of another interaction at work. Perhaps the peripheral C–H bonds of perylene lock together between molecules in adjacent molecular chains[34].

Superstructure A

The STM measurements for Superstructure A in Figure 3-5 describe the (5 x 5) superstructure. However, the image resolution does not provide direct evidence for the number, arrangement, and orientation of perylene molecules within one unit cell. The unit cell for superstructure A permits accommodation of up to two perylene molecules based on the van der Waals dimensions. Moreover, the hole in region *h* enclosed with dashed line in Figure 3-5a shows clear presence of molecules at lower height level comparable to the height level of the dark regions in-between the visible bright molecular chains in the <110> direction. A question emerges whether perylene molecules are present in these dark regions. Measurement scans of height profiles at certain positions of superstructure A are of interest. Dashed lines indicated as *i*, *ii*, and *iii* in Figure 3-5b are the representative scan lines; the height profiles are shown in Figure 3-13. The pattern of protrusion and depression with a height difference of up to 0.9 ± 0.1 Å for scan line *i* reflects the presence of molecules. A pattern of protrusion and depression but less pronounced is also apparent for scan line *ii* with a height difference of up to 0.5 ± 0.1 Å. The periodicities of the patterns and the widths of the protrusions coincide between scan lines *i* and *ii*. These facts suggest the dark regions include molecules in the same phase and in the same orientation as those in the visible bright top-most molecular chains[55]. The height profile for scan line *iii* across the dark and the bright regions shows a height difference of up to 1.3 ± 0.2 Å, in agreement with the calculated height of 1.276-Å for mono-atomic steps on the Cu(110) surface[55]. The STM image in Figure 3-14a provides a better view of the dark regions to suggest indeed the presence of molecules therein. Further evidence is the remarkable appearance and resolution of some molecular chains next to bright molecular chains in the dark region indicated as *g* on the STM image in Figure 3-14b.

A blown-up image of a single protrusion in superstructure A is shown in Figure 3-15. The image is a 20 Å x 20 Å cropped reproduction of region *j* enclosed with a dashed line in Figure 3-5b. The general shape and size of the protrusion possesses some agreement with the rectangular feature and planar dimensions of perylene molecules so each protrusion can be associated with a

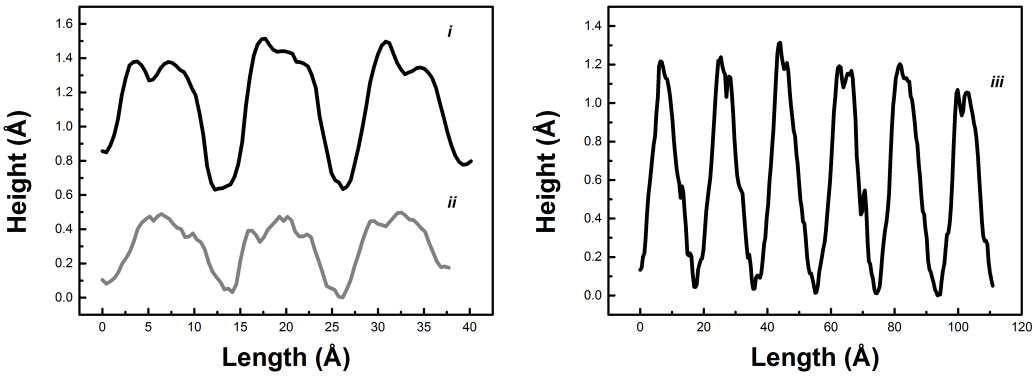

Figure 3-14. Height profiles to the scan lines *i*, *ii*, *iii* in Figure 3-5b. The height profiles are acquired from the STM image subsequent to application of image-smoothening process using the SPM-image analysis software WSxM to reduce sharp changes from noise[78].

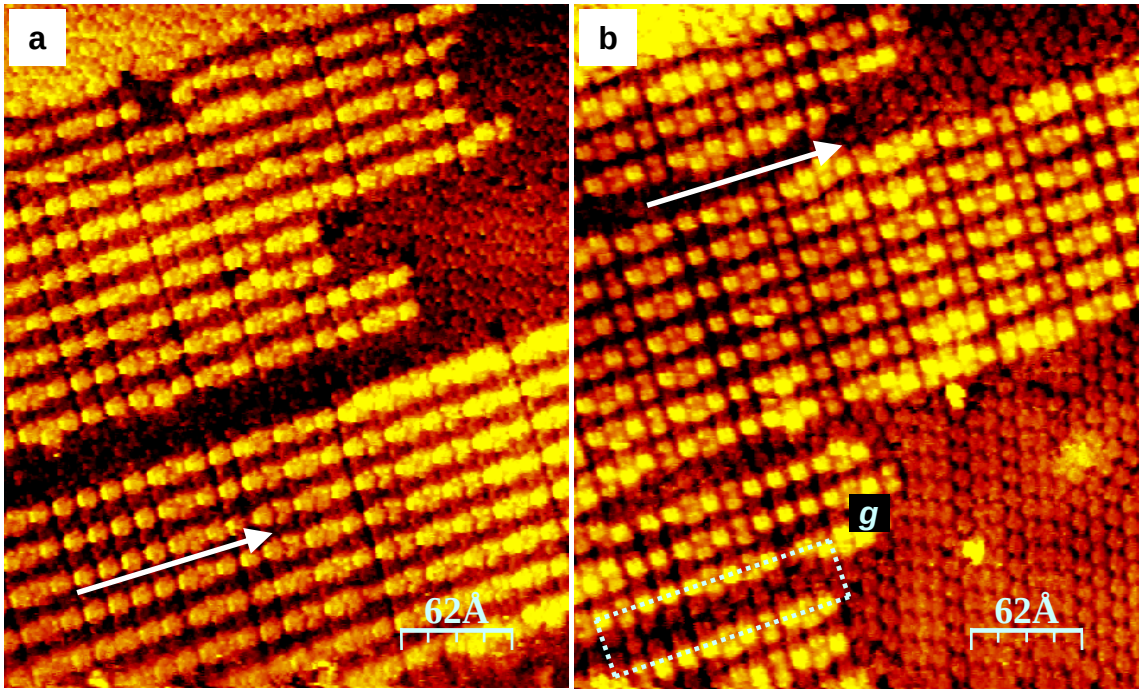

Figure 3-13. 311 Å x 377 Å STM topographic images of perylene on a Cu(110) surface at monolayer coverage after a total deposition time period of 8 minutes. Image dimensions are corrected using calibration factors X = 1.037 and Y = 1.256 for 300 Å x 300 Å image scans. STM measurements were performed at (a) U = -758 mV and I = 0.12 nA, (b) U = -1062 mV and I = 0.12 nA.

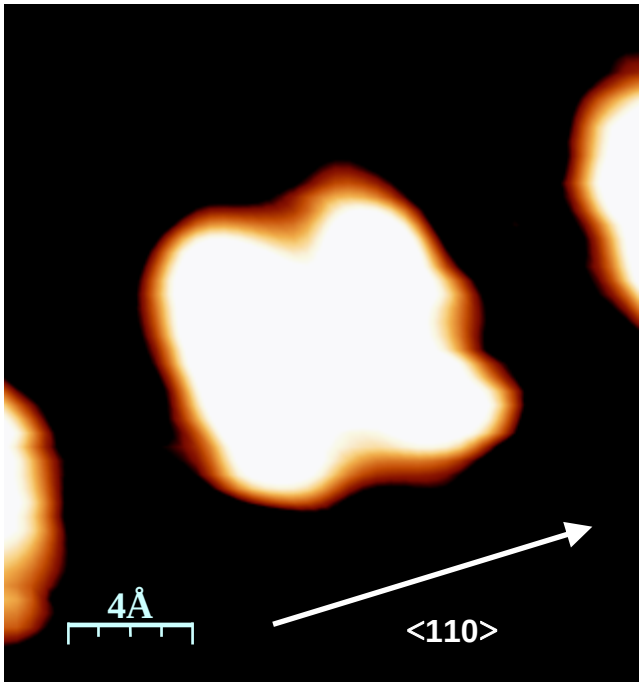

Figure 3-15. 20 Å x 20 Å cropped reproduction of the region enclosed with dashed line and indicated as *j* on the STM image in Figure 3-5b to focus on a single rectangular protrusion in superstructure A. The image is presented at high image contrast subsequent to application of image-smoothening process to provide better general impression of the shape of the protrusion.

molecule of perylene in the flat-down orientation. The orientation of the rectangular protrusion shows the high-symmetry axes of the perylene molecule match the high-symmetry axes of the Cu(110) surface. However, the absolute orientation – whether the long molecular axis is in the <110> or <100> direction – can not be ascertained from the image resolution and from the aspect ratio of the rectangular protrusion.

NR group has proposed formation of molecular chains as in Figure 3-5 – Figure 3-6 to be an initial development of a multilayer structure[35]. However, the outcome of the analysis for superstructure A points to the commensurate (5 x 5) superstructure[31]. The occurrence of molecular chains connected to step edges could suggest the mobile nature of Cu atoms at steps enables the adsorbate-induced surface reconstruction despite at room temperature but of limited extent.

3.6 Commensurate (8x5) Superstructure of Perylene on the Cu(110) Surface

The STM images in Figure 3-5 show a seamless coexistence between superstructure B and superstructure A without domain boundaries at the interface to separate them. The protrusions located at the corners of the rectangular blue-colored unit cell for superstructure B in Figure 3-5b are shared between the two superstructures at the interface. Then superstructure B in common with superstructure A based on the proposed model for the commensurate (5x5) superstructure must be a commensurate superstructure in the monolayer, must include the adsorbate-induced reconstruction of the Cu(110) surface, and must position molecules at the atop sites and at the bridge sites.

The rectangular protrusions located at the center of the long edges of the unit cell are longer in the <001> direction and distinct from those on the corners. A blown-up image of the protrusion is shown in Figure 3-16. The image is a 25 Å x 25 Å cropped reproduction of region *k* enclosed with a dashed line in Figure 3-5b. The protrusion can be associated with one perylene molecule in flat-down orientation with the long molecular axis in the <001> direction on the basis of the rectangular shape, dimensions, and orientation. The molecular orientation is reasonable from the preservation of the two-fold symmetry of both the perylene molecule and the Cu(110) surface but must be a meta-stable state based on the limited occurrence. The two different protrusions in superstructure B provides comparison between perylene molecules at perpendicular orientation to each other and therefore supports the molecular orientation proposed for superstructure A.

The proposed 2D geometrical model for superstructure B is the commensurate (8x5) superstructure shown in Figure 3-17, which allows the unit cell to accommodate compact adsorption of three non-equivalent molecules at the atop sites without overlap between molecules, but leaves bare Cu(110) surface in the local area at the center of the unit cell. However, the lack of an adsorbed molecule at the center of the unit cell should lead to an absence of

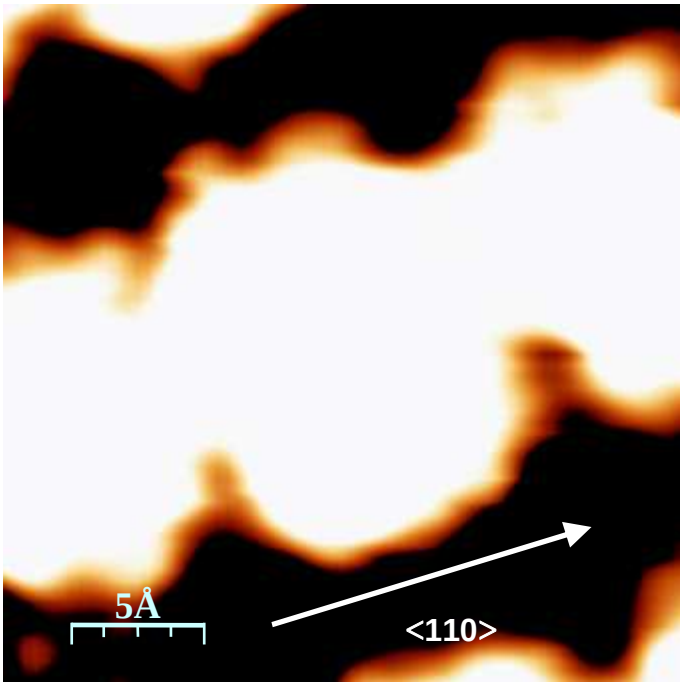

Figure 3-16. 25 Å x 25 Å cropped reproduction of the region enclosed with dashed line and indicated as *k* on the STM image in Figure 3-5b to focus on a single rectangular protrusion in superstructure B. The image is presented at high image contrast subsequent to application of an image-smoothening process to provide better general impression of the shape of the protrusion.

adsorbate-induced surface reconstruction in the local area but must be favorable towards increased metal-surface contact for the molecule whose long molecular axis is oriented in the <001> direction. On the other hand, the molecular orientation in the <001> direction could be the means to preserve the two-fold symmetry of both the perylene molecule and the Cu(110) surface in the absence of the adsorbate-induced surface reconstruction in the commensurate (5x5) superstructure.

Superstructure B resembles the centered orthorhombic crystal of perylene on Cu(110) surface in the report from NR group based on comparison of STM images. Both structures are 8-fold commensurate in the <110> direction. However, the measurements of the unit cells in the <001> direction are about 1 Å off from each other and the details of interpretation are in essence distinct from each other – in particular, the present superstructure is proposed in a monolayer as opposed to a multilayer[52].

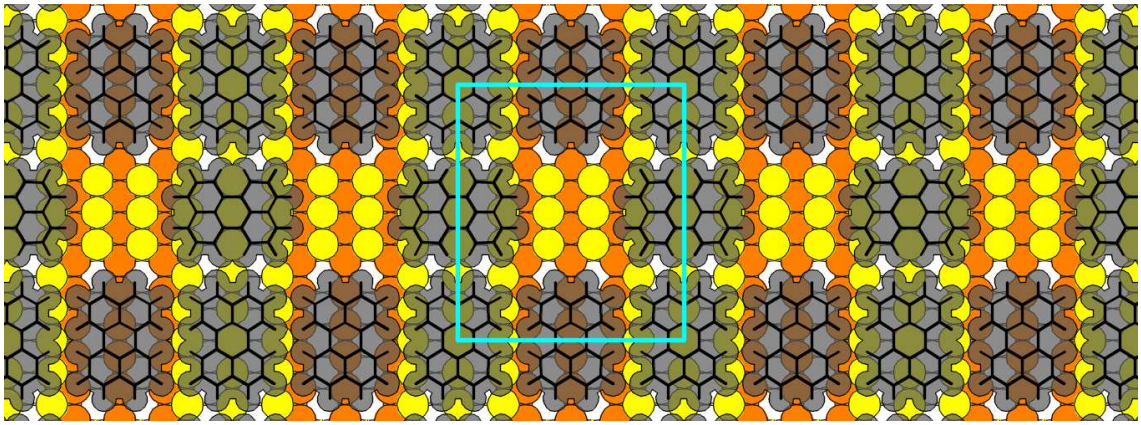

Figure 3-17. Model of commensurate (8x5) superstructure consisting of three non-equivalent perylene molecules in the unit cell. Explanations of the schematic representations are similar to those in Figure 3-11.

3.7 Commensurate Chiral Superstructures of Perylene on the Cu(110) Surface

Superstructures C and D can be described in two-dimensional lattices with structural parameters

$$\begin{pmatrix} 3 & \mp 2 \\ 1 & \pm 3 \end{pmatrix}$$

in the matrix notation. The two sets of lattice on the surface are non-identical mirror images of each other, hence enantiomorphs. Formation of equivalent enantiomorphs of molecular superstructures on (110)-oriented metal surfaces is a well-known chiral phenomenon as an expression of the two-fold symmetry of the surface underneath the superstructure[77]. NR group has reported formation of a set of chiral superstructures at 450 K with the same combinations of structural parameters but in distinct order[35].

The commensurate character of the lattices means a preference of perylene molecule for adsorption at a particular site on the surface. The adsorption site for the center of the perylene molecule is postulated to be at the atop site. The model-based analysis for the commensurate (5x5) superstructure in section 3.5 deduces a preference for adsorption at the atop site. Moreover, the RAIR bands at 740 cm^{-1} ($\Delta\overline{\upsilon}_{770cm^{-1}} = 30$ cm^{-1}) and 785 cm^{-1} ($\Delta\overline{\upsilon}_{813cm^{-1}} = 28$ cm^{-1}) from the deposition on the substrate at room temperature could perhaps also pertain to adsorption at the atop site. Recall section 3.5 notes the RAIR bands of the same set of vibrational modes at 736 cm^{-1} ($\Delta\overline{\upsilon}_{770cm^{-1}} = 34$ cm^{-1}) and 783 cm^{-1} ($\Delta\overline{\upsilon}_{813cm^{-1}} = 30$ cm^{-1}) could correspond to adsorption at the atop site. The amounts of red shift are almost equal between the two sets of RAIR bands to indicate comparable molecule-substrate interactions; the differences could perhaps come from mere difference in molecular orientation.

The molecular orientations are not apparent from the shape of the molecules in the STM measurements. The possible molecular orientations can be deduced from creation of 2D geometrical models. The molecular models avoid mutual overlap in the two-dimensional lattices for superstructures C and D

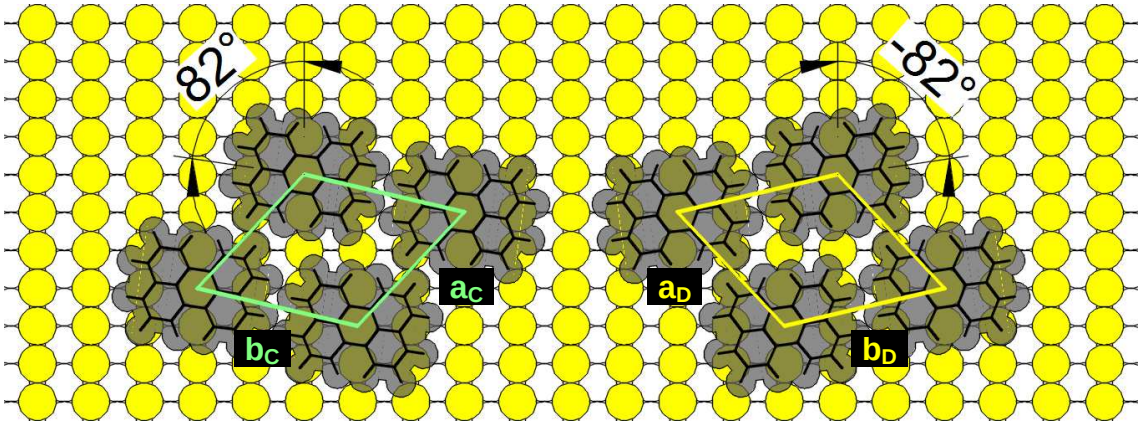

Figure 3-18. Models of superstructures based on the commensurate two-dimensional lattices for superstructure C and D.

just when the long molecular axis is about ±82° from the <110> direction. The superstructure models based on these molecular orientations and the two-dimensional lattices are shown in Figure 3-18. The model on the left side under the green-coloured unit cell corresponds to the matrix notation

$$\begin{pmatrix} 3 & -2 \\ 1 & 3 \end{pmatrix}$$

whilst the model on the right side under the yellow-coloured unit cell corresponds to the matrix notation

$$\begin{pmatrix} 3 & 2 \\ 1 & -3 \end{pmatrix}$$

No other molecular orientation shows the distinct space gap at the center of four perylene molecules to be consistent with the STM topographic depression at the center of four protrusions on the corners of the unit cells indicated for superstructures C and D in Figure 3-5b. The long molecular axes are noted to be close to the <001> direction – just rotated ±8°. The molecules could be predisposed towards orientation in the <001> direction to preserve the two-fold symmetry of both the perylene molecule and the Cu(110) surface in the absence of the adsorbate-induced surface reconstruction in the commensurate (5x5) superstructure.

The 311 Å x 377 Å STM image in Figure 3-19 shows close view of the actual superstructures. Close inspection of superstructures C and D from the STM measurements shows the actual superstructures deviate from the

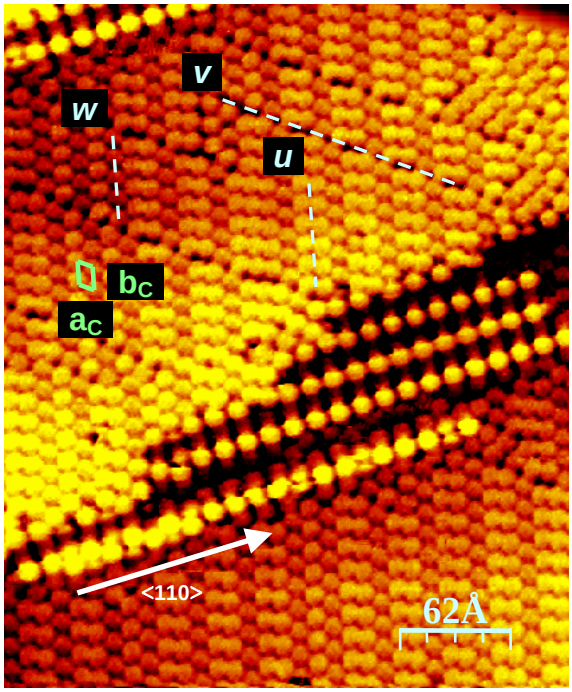

Figure 3-19. 311 Å x 377 Å STM topographic image of perylene on a Cu(110) surface at monolayer coverage. Image dimensions are corrected using calibration factors X = 1.037 and Y = 1.256 for 300 Å x 300 Å image scans. STM measurements were performed at U = -1201 mV and I = 0.13 nA.

superstructure models in Figure 3-18. The possible reason for the deviation could be intermolecular repulsion as can be seen from the close contact with subtle overlap between the molecules in the superstructure models – hence the superstructure models are somewhat too compact. The actual superstructures can be seen as some random pattern of monomeric, dimeric, trimeric, and tetrameric molecular rows interspersed with monomeric molecular rows of another form. However, the monomeric and the dimeric molecular rows appear often in succession whilst the trimeric and the tetrameric molecular rows seldom appear, so in effect the monolayer develops periodic order in two dimensions over some distance.

The actual superstructures can be described as combinations between the basic frameworks from the superstructure models in Figure 3-18 and perturbations from two forms of deviations. One form of deviation can be seen as displacement of an entire portion of the superstructure from the continuous periodic framework of the two-dimensional lattice, and is indicated with dashed line *u* between two molecular rows in Figure 3-5 and Figure 3-19. The form of

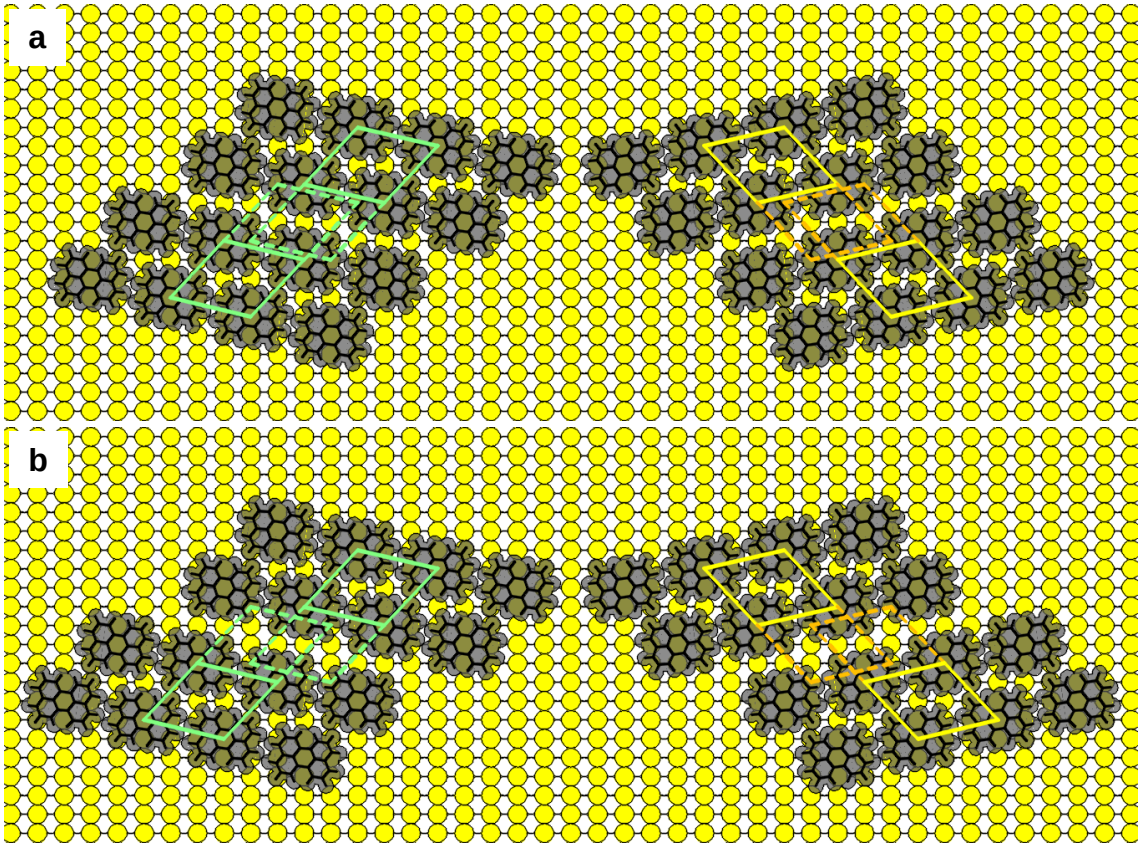

Figure 3-20. Models of the form of deviation described as shift in position of one portion of the superstructure from another portion in the <001> direction.

deviation manifests in formation of dimeric, trimeric, and tetrameric molecular rows in the direction of unit vector $\mathbf{b_C}$ for superstructure C and in the direction of unit vector $\mathbf{b_D}$ for superstructure D. In other words, the formation of dimeric, trimeric, and tetrameric molecular rows can be viewed as deviations in the basic framework of the superstructure. The form of deviation can be described as an outcome of a shift in position of one portion of the superstructure from another portion in one or two units of interatomic Cu distance in the <001> direction from the models in Figure 3-20. The models correspond to the least possible amount of space between molecules at the defect location to be consistent with the close contact between molecules in the actual superstructures and the close-packed nature of the monolayer whilst adsorption remains at the atop site. The creation of space between molecules at the defect location could be a mechanism to relieve possible intermolecular repulsion from internal compression in the monolayer.

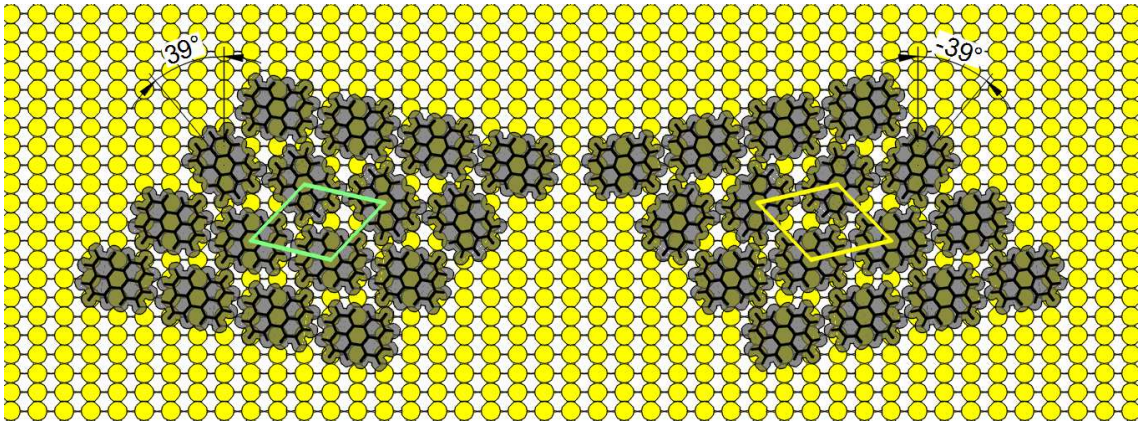

Figure 3-21. Models of the form of deviation described as uniform molecular meta-stable orientation at ±39° in an entire molecular row in the direction of b_C in superstructure C and b_D in superstructure D.

The other form of deviation can be seen as a uniform meta-stable orientation of molecules in an entire molecular row in the direction of unit vector $\mathbf{b_C}$ for superstructure C and in the direction of unit vector $\mathbf{b_D}$ for superstructure D, and is indicated with dashed line *w* on molecular row in Figure 3-5 and Figure 3-19. The distinction of molecular orientations can be made upon comparison of shape or orientation of the protrusions between adjacent molecular rows. Moreover, the molecular rows of meta-stable orientation are somewhat dark in the shade of image contrast compared to the molecular rows of the proper molecular orientation at ±82°. The meta-stable orientation can be described as the long molecular axis about ±39° from the <110> direction to have the least amount of steric overlap between molecular models whilst the continuous periodic framework of the two-dimensional lattice is preserved as shown in Figure 3-21. Close inspection shows the STM measurements somewhat resemble the models in relation to some features of the molecular orientations. The existence of the meta-stable orientation could show a predisposition towards a centered superposition of aromatic nuclei atop Cu atoms at ±30° as shown in Figure 3-22. The meta-stable orientation appears in the monomeric molecular rows interposed between monomeric, dimeric, trimeric, and tetrameric rows of molecules at ±82° orientation. Exploration of the models shows an appearance of the meta-stable orientation in consecutive molecular rows next to each other could be unfavourable as adsorption at the

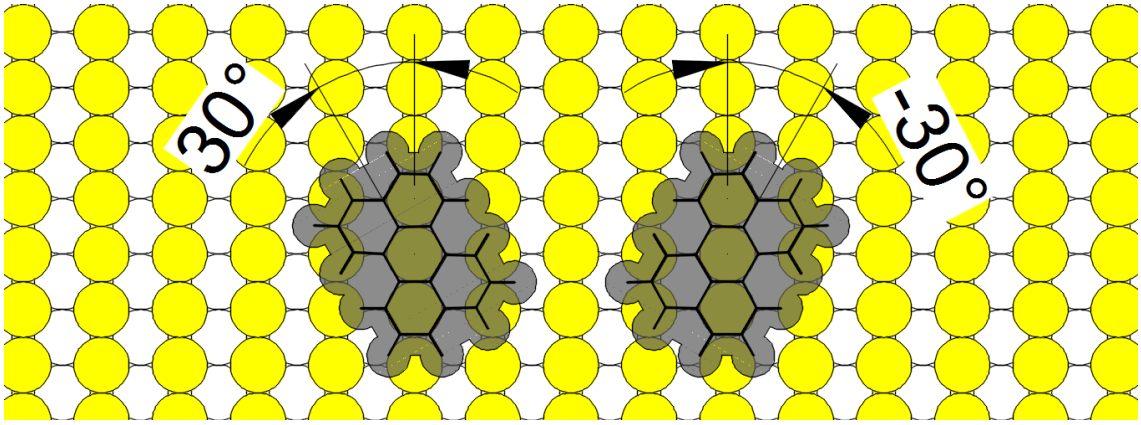

Figure 3-22. Models to show the molecular orientation at ±30° could be favourable as the aromatic nuclei of perylene are centered atop Cu atoms.

long-bridge site happens from the second molecular row for a close-packed monolayer; indeed, the case is never observed.

The models for one of the most common cases in the actual superstructures for superstructures C and D are shown in Figure 3-23 to illustrate the concept of the superstructures as combination between the basic framework from the superstructure models in Figure 3-18 and the perturbations from the two forms of deviations. The models are composed of the monomeric molecular rows of the molecular meta-stable orientation at ±39° interposed between the dimeric molecular rows of the proper molecular orientation at ±82°. The two-dimensional lattices are continuous until the appearance of the dimeric molecular rows. The formation of superstructures C and D can seem to be understood as a complex combination of various factors: the close-packed nature of the monolayer, the preference for one specific adsorption site, the competition between the two different molecular orientations, and the disposition in the two-dimensional lattices due to relaxation of intermolecular repulsion.

Domain boundaries are present between adjacent domains of the same enantiomorph as indicated with dashed line *v* in Figure 3-19. The domain boundaries can be described as an outcome of a shift in position of one portion of the superstructure from another portion in one or two units of the interatomic Cu distance in the <110> direction from the illustrations in Figure 3-24. The defect leads to noticeable space between molecules at the domain boundaries,

in contrast to the almost no adjustment in space between molecules for the first form of deviation i.e. shift in relative positions between portions of the superstructure in the <001> direction.

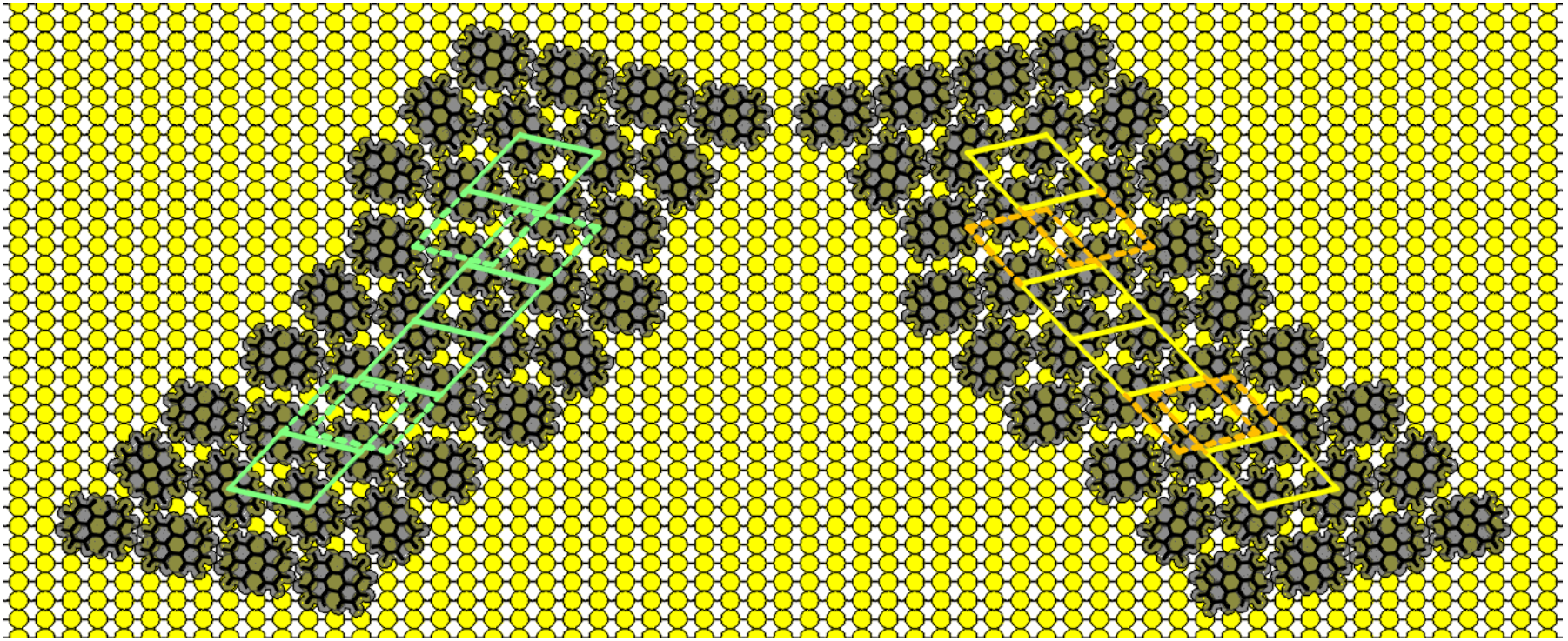

Figure 3-23. Models to represent superstructures C and D as combination between the basic framework from perfect commensurate superstructure model and the perturbation from two forms of defect. The basic framework refers to molecules at ±82° orientation in the two-dimensional lattices indicated with green and yellow frames. The two forms of defect refer to the disruption in the two-dimensional lattices at the formation of dimeric molecular rows and to the molecular misorientation at ±39° in an entire molecular row. The misorientation defect never appears in consecutive molecular rows next to each other so at least one molecular row of the proper molecular orientation at ±82° must separate monomeric molecular rows of the misorientation defect.

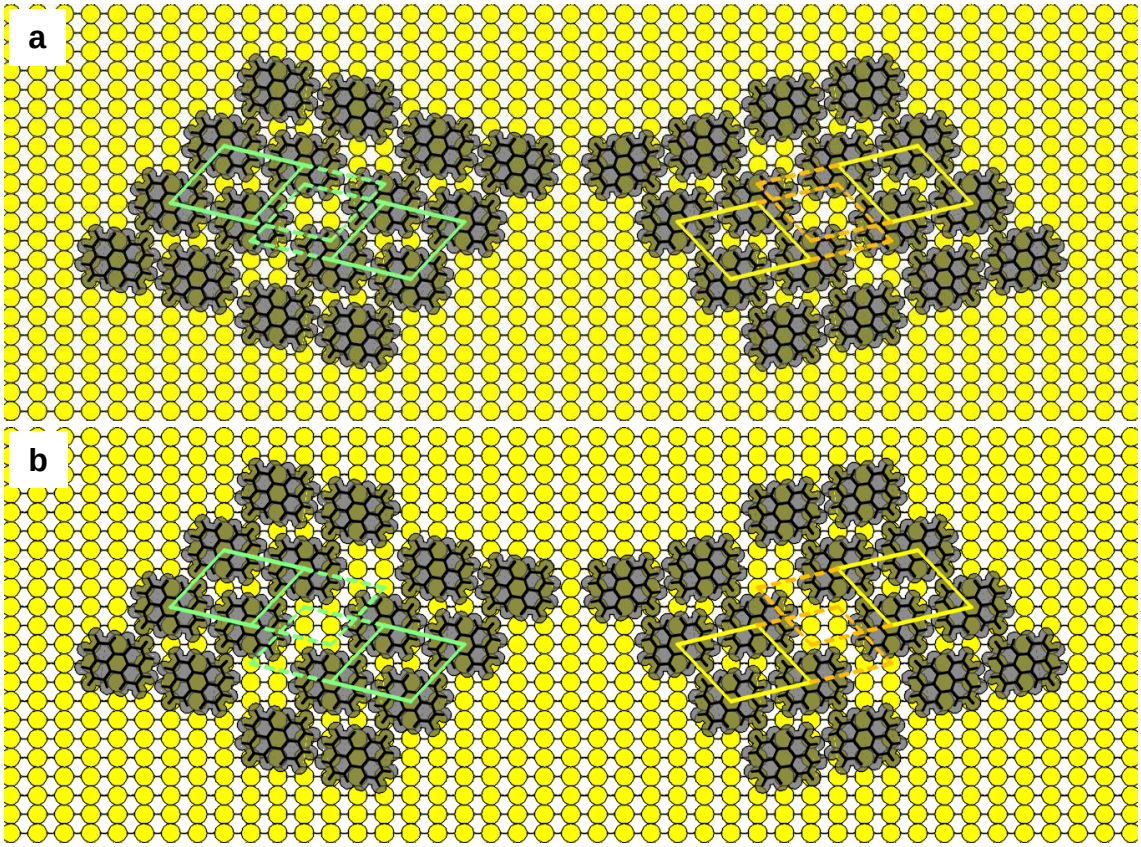

Figure 3-24. Models to describe domain boundaries between adjacent domains of the same enantiomorph as outcome of shift in position of one portion of the superstructure from another portion in the <110> direction.

3.8 Conclusion to Perylene on the Cu(110) Surface

RAIRS measurements demonstrate the molecule-substrate interaction as red shifts in vibrational frequencies for perylene molecules in direct contact with the Cu(110) surface. Termination of growth under deposition condition close to equilibrium explains the almost constant RAIR absorption intensities of the multilayer after coverage of about 3 ML. Anneal treatment at about 450 K leads to multilayer desorption and two sets of red shift in vibrational frequencies for the monolayer. STM measurements demonstrate four superstructures in the monolayer for deposition on the substrate at room temperature. The monolayer transforms into an almost uniform phase of commensurate (5x5) superstructure on the entire surface upon anneal treatment at about 400 K. 2D geometrical models complement some information from the STM measurements. Two of the superstructures occur as molecular chains of commensurate (5x5) and (8x5) superstructures in continuous coexistence over some limited distance from step edges towards the <110> direction. The (8x5) superstructure resembles the two-dimensional structure of the novel epitaxial multilayer in the report of NR group[52]. The other two superstructures are enantiomorphs and dominate the monolayer. The enantiomorphs are described as superstructures based on combinations between basic frameworks of commensurate superstructure models and perturbations from two forms of deviation – in particular, molecular meta-stable orientation in an entire molecular row and displacement of one portion of the commensurate two-dimensional lattice in the <001> direction. In effect, the superstructures are composed of monomeric molecular rows of molecular orientation at ±39° interposed between monomeric, dimeric, trimeric, and tetrameric molecular rows of molecular orientation at ±82°. The model for the commensurate (5x5) superstructure points to adsorption on two different sites, one at the atop site whilst the other at the short-bridge site, and is consistent with the two sets of red shifts in vibrational frequencies from RAIRS measurements. In contrast, the RAIRS measurements up to the monolayer from deposition on the substrate at room temperature show just one set of red shift

and is consistent with commensurate adsorption at the atop site for the chiral superstructure models.

Prospects for further work on perylene on Cu(110) surface can include verification of the red-shifts in vibrational frequencies from RAIRS measurements of deuterated perylene on Cu(110) surface and theoretical studies of the proposed models for the (5x5), (8x5), and commensurate chiral superstructures to explore the intricate details, and the intermolecular and molecule-substrate interactions. Moreover, the theoretical studies could perhaps support the RAIRS measurements.

,

References

1. Camerman, A. & Trotter, J. The crystal and molecular structure of perylene. *Proc. R. Soc. A Math. Phys. Eng. Sci.* **279,** 129–146 (1964).

2. Skancke, P. N. *et al.* Semi-empirical molecular orbital studies of aromatic hydrocarbons. II. *Acta Chem. Scand.* **19,** 401–413 (1965).

3. Goodwin, T. H. 943. Calculated bond lengths in some cyclic compounds. Part VII. The series naphthalene, perylene, terrylene, quaterrylene, and the lengths of low-order bonds. *J. Chem. Soc.* 4851 (1960).

4. Coulson, C. A. & Skancke, P. N. 534. Some abnormally long carbon-carbon bonds. *J. Chem. Soc.* 2775 (1962).

5. Dewar, M. J. S. & Gleicher, G. J. Ground states of conjugated molecules. II. Allowance for molecular geometry 1a,b. *J. Am. Chem. Soc.* **87,** 685–692 (1965).

6. Gleicher, G. J. Bond deformations in conjugated molecules. *J. Org. Chem.* **33,** 3964–3966 (1968).

7. Lo, D. H. & Whitehead, M. A. Accurate heats of atomization and accurate bond lengths: I. Benzenoid hydrocarbons. *Can. J. Chem.* **46,** 2027–2040 (1968).

8. Pauling, L. Bond numbers and bond lengths in tetrabenzo[de,no,st,c1d1]heptacene and other condensed aromatic hydrocarbons: a valence-bond treatment. *Acta Crystallogr. Sect. B Struct. Crystallogr. Cryst. Chem.* **36,** 1898–1901 (1980).

9. Allinger, N. L. & Sprague, J. T. Conformational analysis. XC. Calculation of the structures of hydrocarbons containing delocalized electronic systems by the molecular mechanics method. *J. Am. Chem. Soc.* **95,** 3893–3907 (1973).

10. Traetteberg, M. An electron diffraction investigation of the peri-bonds in perylene. *Proc. R. Soc. A Math. Phys. Eng. Sci.* **283,** 557–575 (1965).

11. Cyvin, S. J., Cyvin, B. N. & Klaeboe, P. Condensed aromatics. Part XIX perylene. *Spectrosc. Lett.* **16,** 239–248 (1983).

12. Dallinga, G., Toneman, L. H. & Traetteberg, M. Electron diffraction by gases: the length of the peri-bonds in perylene. *Recl. des Trav. Chim. des Pays-Bas* **86,** 795–800 (2010).

13. Donaldson, D. M., Robertson, J. M. & White, J. G. The crystal and molecular structure of perylene. *Proc. R. Soc. A Math. Phys. Eng. Sci.* **220,** 311–321 (1953).

14. Gutman, I., Đurđević, J., Radenković, S. & Matović, Z. Anomalous cyclic conjugation in the perylene/bisanthrene homologous series. *Monatshefte für Chemie - Chem. Mon.* **143,** 1649–1653 (2012).

15. Gready, J. E. The value of the π-bond order-bond length relationship in geometry prediction and chemical bonding interpretation. *J. Comput. Chem.* **5,** 411–426 (1984).

16. Clar, E. Absorption spectra of aromatic hydrocarbons at low temperatures. LV-Aromatic hydrocarbons. *Spectrochim. Acta* **4,** 116–121 (1950).

17. Shilstone, G. N., Zannoni, C. & Veracini, C. A. Solute alignment in liquid crystal solvents. The Saupe ordering matrix for perylene and pyrene. *Liq. Cryst.* **6,** 303–317 (1989).

18. Langhals, H. & Kinzel, S. Thermochromism of perylenes: dynamics in aromatics. *Spectrochim. Acta. A. Mol. Biomol. Spectrosc.* **78,** 1212–4 (2011).

19. Fillaux, F. Butterfly motion of isolated perylene in its ground and first excited singlet states. *Chem. Phys. Lett.* **114,** 384–387 (1985).

20. Jones, B. a *et al.* High-mobility air-stable n-type semiconductors with processing versatility: dicyanoperylene-3,4:9,10-bis(dicarboximides). *Angew. Chem. Int. Ed. Engl.* **43,** 6363–6 (2004).

21. Chen, Z., Debije, M. G., Debaerdemaeker, T., Osswald, P. & Würthner, F. Tetrachloro-substituted perylene bisimide dyes as promising n-type organic semiconductors: studies on structural, electrochemical and charge transport properties. *Chemphyschem* **5,** 137–40 (2004).

22. Tanaka, J. The electronic spectra of aromatic molecular crystals. II. The crystal structure and spectra of perylene. *Bull. Chem. Soc. Jpn.* **36,** 1237–1249 (1963).

23. Inokuchi, H., Kuroda, H. & Akamatu, H. On the electrical conductivity of the organic thin films: perylene, coronene and violanthrene. *Bull. Chem. Soc. Jpn.* **34,** 749–753 (1961).

24. Zimmermann, U. *et al.* NEXAFS and ARUP spectroscopy of an organic single crystal: α-perylene. *Mol. Cryst. Liq. Cryst. Sci. Technol. Sect. A. Mol. Cryst. Liq. Cryst.* **339,** 231–259 (2000).

25. Datta, A., Mohakud, S. & Pati, S. K. Comparing the electron and hole mobilities in the α and β phases of perylene: role of π-stacking. *J. Mater. Chem.* **17,** 1933 (2007).

26. Gao, L. *et al.* Understanding and controlling the weakly interacting interface in perylene⁄Ag(110). *Phys. Rev. B* **73,** 075424 (2006).

27. Eremtchenko, M., Bauer, D., Schaefer, J. A. & Tautz, F. S. Structure, bonding, and growth at a metal–organic interface in the weak chemisorption regime: perylene–Ag(111). *J. Mater. Res.* **19,** 2028–2039 (2004).

28. Gao, L. *et al.* Structural evolution at the initial growth stage of perylene on Au(111). *Surf. Sci.* **601,** 3179–3185 (2007).

29. Manandhar, K., Sambur, J. B. & Parkinson, B. A. Morphologies, structures, and interfacial electronic structure of perylene on Au(111). *J. Appl. Phys.* **107,** 063716 (2010).

30. Hu, F., Zhang, H., Mao, H., Liao, Q. & He, P. The initial growth behavior of perylene on Cu(100). *J. Chem. Phys.* **134,** 194702 (2011).

31. Söhnchen, S., Hänel, K., Birkner, A., Witte, G. & Wöll, C. Molecular beam deposition of perylene on copper: formation of ordered phases. *Chem. Mater.* **17,** 5297–5304 (2005).

32. Lu, B. *et al.* Perylene monolayer on the Ru(0001) surface. *Appl. Phys. Lett.* **86,** 061915 (2005).

33. Seidel, C., Ellerbrake, R., Gross, L. & Fuchs, H. Structural transitions of perylene and coronene on silver and gold surfaces: a molecular-beam epitaxy LEED study. *Phys. Rev. B* **64,** 195418 (2001).

34. Gross, L., Seidel, C. & Fuchs, H. Organic monolayers with uniform domain orientation and reduced antiphase boundaries – MBE of perylene on Au(110). *Org. Electron.* **3,** 1–7 (2002).

35. Chen, Q., McDowall, A. J. & Richardson, N. V. Growth and evolution of perylene thin films on Cu(110). *Chem. Mater.* **15,** 4113–4117 (2003).

36. Honying, M. *et al.* The growth of perylene on Ru(0001). *J. Chem. Phys.* **121,** 6972–7 (2004).

37. Han, H. *et al.* The electronic states of ordered thin films of perylene on Ag (110). *Phys. B Condens. Matter* **352,** 36–41 (2004).

38. Han, H. *et al.* The ordered thin-film growth of organic semiconductor on Ag(110). *J. Chem. Phys.* **124,** 054716 (2006).

39. Deng, Z. *et al.* Selective analysis of molecular states by functionalized scanning tunneling microscopy Tips. *Phys. Rev. Lett.* **96,** 156102 (2006).

40. Yoshimoto, S., Tsutsumi, E., Fujii, O., Narita, R. & Itaya, K. Effect of underlying coronene and perylene adlayers for [60]fullerene molecular assembly. *Chem. Commun.* 1188–90 (2005).

41. Wang, D., Wan, L.-J., Xu, Q.-M., Wang, C. & Bai, C.-L. Adlayer structures of pyrene and perylene on Cu(111): an in situ STM study. *Surf. Sci.* **478,** L320–L326 (2001).

42. Kang, S. J. *et al.* Electronic structure of perylene on Au studied by ultraviolet photoelectron spectroscopy and density functional theory. *Synth. Met.* **151,** 120–123 (2005).

43. Dou, W. *et al.* Aggregation of organic molecules on silver surface with the balance between molecule–substrate interaction and intermolecular interaction. *Chem. Phys. Lett.* **470,** 126–130 (2009).

44. Yau, S.-L., Kim, Y.-G. & Itaya, K. In situ scanning tunneling microscopy of benzene adsorbed on Rh(111) and Pt(111) in HF solution. *J. Am. Chem. Soc.* **118,** 7795–7803 (1996).

45. Yannoulis, P., Dudde, R., Frank, K. H. & Koch, E. E. Orientation of aromatic hydrocarbons on metal surfaces as determined by nexafs. *Surf. Sci.* **189-190,** 519–528 (1987).

46. Verlaak, S., Steudel, S., Heremans, P., Janssen, D. & Deleuze, M. Nucleation of organic semiconductors on inert substrates. *Phys. Rev. B* **68,** 195409 (2003).

47. Ercolessi, F., Bartolini, A., Garofalo, M., Parrinello, M. & Tosatti, E. Au surface reconstructions in the glue model. *Surf. Sci.* **189-190,** 636–640 (1987).

48. Liu, X., Mohamed, S. H., Ngaruiya, J. M., Wuttig, M. & Michely, T. Modifying the growth of organic thin films by a self-assembled monolayer. *J. Appl. Phys.* **93,** 4852 (2003).

49. Beigmohamadi, M. *et al.* Structure and morphology of perylene films grown on different substrates. *J. Appl. Phys.* **104,** 013505 (2008).

50. Witte, G., Hänel, K., Söhnchen, S. & Wöll, C. Growth and morphology of thin films of aromatic molecules on metals: the case of perylene. *Appl. Phys. A* **82,** 447–455 (2006).

51. Zorba, S., Yan, L., Watkins, N. J. & Gao, Y. Kinetic roughening study of perylene on glass and Au substrates. *Appl. Phys. Lett.* **81,** 5195 (2002).

52. Chen, Q., Rada, T., McDowall, A. & Richardson, N. V. Epitaxial growth of a crystalline organic semiconductor: perylene/Cu{110}. *Chem. Mater.* **14,** 743–749 (2002).

53. Witte, G. & Wöll, C. Growth of aromatic molecules on solid substrates for applications in organic electronics. *J. Mater. Res.* **19,** 1889–1916 (2004).

54. Hänel, K. *et al.* Organic molecular-beam deposition of perylene on Cu(110): results from near-edge x-ray absorption spectroscopy, x-ray photoelectron spectroscopy, and atomic force microscopy. *J. Mater. Res.* **19,** 2049–2056 (2004).

55. Witte, G., Hänel, K., Busse, C., Birkner, A. & Wöll, C. Molecules coining patterns into a metal: the hard core of soft matter. *Chem. Mater.* **19,** 4228–4233 (2007).

56. Casu, M. B. *et al.* Nucleation in organic thin film growth: perylene on Al_2O_3 /Ni_3Al(111). *J. Phys. Chem. C* **113,** 10990–10996 (2009).

57. Simonsen, J. B., Handke, B., Li, Z. & Møller, P. J. A study of the interaction between perylene and the TiO_2(110)-(1×1) surface-based on XPS, UPS and NEXAFS measurements. *Surf. Sci.* **603,** 1270–1275 (2009).

58. Beigmohamadi, M. *et al.* Evolution of dislocations in perylene films with thickness and deposition rate. *Phys. status solidi – Rapid Res. Lett.* **2,** 1–3 (2008).

59. Casu, M. B., Yu, X., Schmitt, S., Heske, C. & Umbach, E. Morphology of perylene thin films on SiO_x/Si(100) and SiO_2/Si(100): A spectroscopic and microscopic study of the influence of the preparation parameters. *Chem. Phys. Lett.* **479,** 76–80 (2009).

60. Effertz, C., Beigmohamadi, M., Niyamakom, P., Schulz, P. & Wuttig, M. Influence of dielectric surface modification on growth, structure and transport properties of perylene films. *Phys. status solidi* **245,** 782–787 (2008).

61. Unwin, P. J. & Jones, T. S. Vibrational properties of ordered perylene thin films on GaAs(100) and InAs(111)A. *Surf. Sci.* **532-535,** 1011–1016 (2003).

62. Casu, M. B., Yu, X., Schmitt, S., Heske, C. & Umbach, E. Influence of the preparation conditions on the morphology of perylene thin films on Si(111) and Si(100). *J. Chem. Phys.* **129,** 244708 (2008).

63. Taborski, J., Väterlein, P., Dietz, H., Zimmermann, U. & Umbach, E. NEXAFS investigations on ordered adsorbate layers of large aromatic molecules. *J. Electron Spectros. Relat. Phenomena* **75,** 129–147 (1995).

64. Ambrosino, F. & Califano, S. The vibrational spectrum of perylene. *Spectrochim. Acta* **21,** 1401–1409 (1965).

65. Szczepanski, J., Chapo, C. & Vala, M. Visible and infrared spectra of matrix-isolated perylene cations. *Chem. Phys. Lett.* **205,** 434–439 (1993).

66. Hudgins, D. M. & Sandford, S. A. Infrared spectroscopy of matrix isolated polycyclic aromatic hydrocarbons. 2. PAHs Containing five or more rings. *J. Phys. Chem. A* **102,** 344–352 (1998).

67. Ding, L., Schulz, P., Farahzadi, A., Shportko, K. V & Wuttig, M. Investigation of intermolecular interactions in perylene films on Au(111) by infrared spectroscopy. *J. Chem. Phys.* **136,** 054503 (2012).

68. Langhoff, S. R. Theoretical infrared spectra for polycyclic aromatic hydrocarbon neutrals, cations, and anions. *J. Phys. Chem.* **100,** 2819–2841 (1996).

69. Ong, K. K., Jensen, J. O. & Hameka, H. F. Theoretical studies of the infrared and Raman spectra of perylene. *J. Mol. Struct. THEOCHEM* **459,** 131–144 (1999).

70. Attard, G. & Barnes, C. *Surfaces*. (Oxford University Press, 1998).

71. Bertsch, A. *et al.* Vibrations on the (110) surface of FCC metals. *Vacuum* **46,** 625–628 (1995).

72. Oura, K., Lifshits, V. G., Saranin, A., Zotov, A. V. & Katayama, M. in *Surf. Sci. An Introd.* 19–46 (Springer Berlin Heidelberg, 2003).

73. Oja, V. & Suuberg, E. M. Vapor pressures and enthalpies of sublimation of polycyclic aromatic hydrocarbons and their derivatives. *J. Chem. Eng. Data* **43,** 486–492 (1998).

74. Inokuchi, H., Shiba, S., Handa, T. & Akamatu, H. Heats of sublimation of condensed polynuclear aromatic hydrocarbons. *Bull. Chem. Soc. Jpn.* **25,** 299–302 (1952).

75. Haq, S. *et al.* Versatile bottom-up construction of diverse macromolecules on a surface observed by scanning tunneling microscopy. *ACS Nano* **8,** 8856–70 (2014).

76. Näther, C., Bock, H., Havlas, Z. & Hauck, T. Solvent-shared and solvent-separated ion multiples of perylene radical anions and dianions: an

exemplary case of alkali metal cation solvation. *Organometallics* **17,** 4707–4715 (1998).

77. Barlow, S. M. & Raval, R. Complex organic molecules at metal surfaces: bonding, organisation and chirality. *Surf. Sci. Rep.* **50,** 201–341 (2003).

78. Horcas, I. *et al.* WSXM: a software for scanning probe microscopy and a tool for nanotechnology. *Rev. Sci. Instrum.* **78,** 013705 (2007).

Chapter 4
Structural Characterization of Graphene on Cu(110) Surface Based on Thermal Decomposition of Perylene

This chapter presents the outcome of experiments in graphene formation based on thermal decomposition of perylene. The first section explains the electron diffraction pattern of graphene formation at high growth temperatures. The second section shows real-space pictures of graphene formation at high growth temperatures and describes the Moiré superstructures of graphene on Cu(110) surface based on simple two-dimensional models. A statistical distribution of epitaxial orientation in the graphene overlayer is presented from a number of graphene domains whose Moiré patterns are visible in STM data. The last section describes graphene formation at low growth temperatures. Graphene formation at low and high growth temperatures are compared and the possible mechanisms of formation are discussed.

4.1 LEED Characterization of Epitaxial Graphene on the Cu(110) Surface

Direct Inspection of the LEED Pattern

Simple inspection of a LEED pattern has been shown to be a means to recognize the presence of graphene on a substrate[1–21]. LEED measurements were performed to test for graphene formation on the Cu(110) surface after thermal decomposition of perylene on the surface at 1250 K in experimental setup 1. Figure 4-1a shows the outcome of first-order diffraction for electron beam energy of 68 eV. The diffraction takes the form of a quasi-circular pattern of arcs, a hexagonal pattern of 12 sharp spots in pair-wise arrangement, and a rectangular pattern of 8 sharp spots. Four of the sharp spots in rectangular arrangement are somewhat coincident with four of the 12 sharp spots in

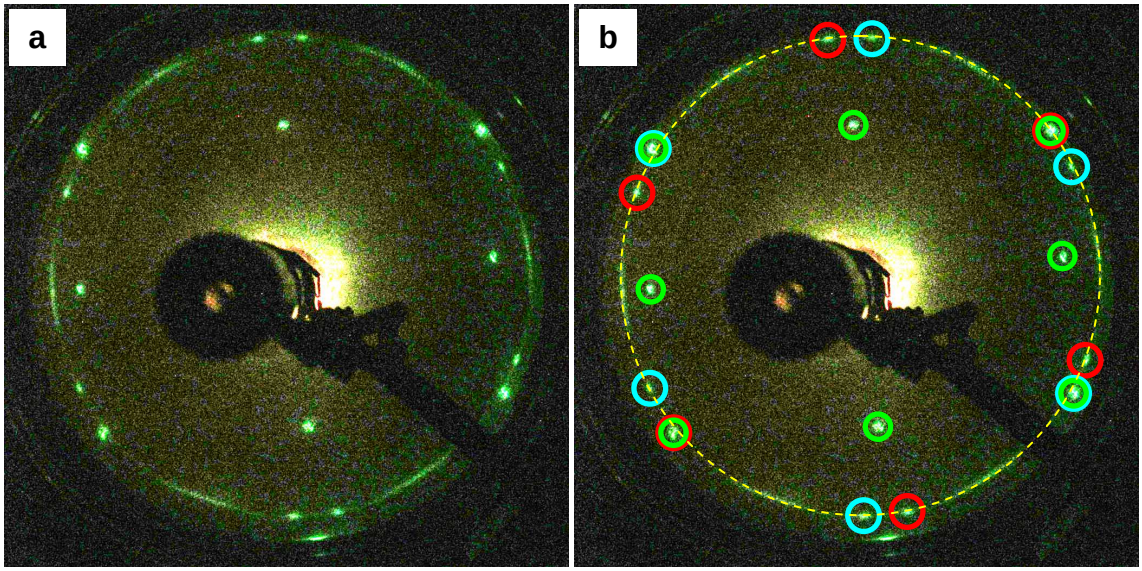

Figure 4-1. LEED pattern measured with electron beam at energy of 68 eV after an attempt to prepare an overlayer of graphene on Cu(110) surface through thermal decomposition of perylene on the surface at 1250 K.

hexagonal arrangement so these particular four spots appear broader and more intense. The set of 8 sharp spots in the rectangular arrangement are highlighted with green circles in Figure 4-1b and are known beforehand to have come from the structure of the Cu(110) surface. The rectangular arrangement is consistent with the two-dimensional lattice of the Cu(110) surface. The set of 12 sharp spots in the hexagonal arrangement are indicated in Figure 4-1b with circles in red and blue colour in order to distinguish the components in each pair of spots. The quasi-circular pattern is superimposed with a dashed circle in yellow colour. Adjustment of electron beam to higher energies was made to observe the pattern from high-order diffraction; the phenomenon revealed more spots for the rectangular pattern but lost the circular and hexagonal pattern without formation of other features. The investigation of structure formation on the Cu(110) surface is therefore limited to first-order diffraction phenomenon. Similar LEED patterns were obtained from repeated experiments.

The evidence for the presence of a superstructure on the Cu(110) surface is the formation of the hexagonal pattern of sharp spots and the quasi-circular pattern of arcs. Both of these patterns are positioned the same distance from the centre of the diffraction pattern, possess hexagonal symmetry, and maintain the mirror symmetry of the rectangular diffraction pattern from the

Cu(110) surface. Hexagonal symmetry in diffraction patterns reflects hexagonal order in long-range periodic structures. In general, a hexagonal structure at one epitaxial orientation causes a diffraction pattern composed of six sharp spots. The 12 sharp diffraction spots in the hexagonal pattern suggest the presence of a hexagonal structure at two different but symmetrical epitaxial orientations. The quasi-circular pattern is often observed from a distribution of rotational disorder in the hexagonal structures at other epitaxial orientations[1]. Rotational disorder of graphite sheets in HOPG is well-known to produce circular diffraction pattern in LEED measurements. Moreover, graphene on metal surfaces is known to form circular and hexagonal diffraction patterns[1–21].

Accurate analysis of the LEED pattern through direct measurement on the image is hampered due to the presence of distortion. Direct measurements of distances and angular orientations on the pattern produce inconsistent values for equivalent diffraction spots. The distortion in the LEED pattern comes from improper location of the sample from the LEED optics and from improper position and orientation of the camera towards the LEED optics. Nonetheless, measurement of distances on a LEED pattern can be used to estimate the real-space periodic dimensions of a structure based on known diffraction spots as the reference. LEED patterns can be considered as a reproduction of the 2D reciprocal lattices for ordered surface structures. The ratio between the distance to the Cu(110)-surface diffraction spots from the center of the LEED pattern and the distance to the points equivalent to these diffraction spots in reciprocal space can be used as a conversion factor between the LEED measurements and the reciprocal space. An average value of 2.93 $Å^{-1}$ for the magnitudes of the fundamental translation vectors in reciprocal space is found equivalent to the measurement of the distance to the hexagonal diffraction patterns from the centre. Then the lattice constant of the hexagonal structure upon calculation from the basic relation between the fundamental translation vectors $\mathbf{a}_{Gr}^*$, $\mathbf{b}_{Gr}^*$ in reciprocal space and the fundamental translation vectors $\mathbf{a}_{Gr}$, $\mathbf{b}_{Gr}$ in real space[22] is 2.48 Å, which agrees well with the honeycomb structure of graphene.

Model to the LEED Pattern

Another approach to the analysis of the LEED pattern is the creation of reciprocal lattice models and subsequent comparison with those from the observations. Such an approach however can not be done without an initial assumption for the presence of particular structures involved in the diffraction phenomenon. The model for the diffraction pattern can start with the assumption of the presence of graphene on the Cu(110) surface. Graphene is modeled based on the structure of the basal plane of graphite. The Cu(110) surface is modeled based on the (110)-oriented lattice plane in the face-centered cubic structure of Cu. The models of the reciprocal lattices are introduced in Chapter 2 Section 2.1.

The epitaxial orientation θ of graphene on Cu(110) surface can be specified as the angle to the armchair arrangement of carbon atoms in the $\langle\bar{1},1,0,0\rangle$ direction on the basal plane of graphite from the non close-packed atomic rows in the $\langle 0,0,1\rangle$ direction on the (110)-oriented single-crystal Cu substrate. The same epitaxial orientation θ can be viewed as the angle to the zigzag arrangement of carbon atoms in the $\langle 1,1,\bar{2},0\rangle$ direction on the basal plane of graphite to the close-packed atomic rows in the $\langle 1,1,0\rangle$ direction on the Cu substrate. The possible epitaxial orientations can be reduced to the angles -30° to +30° as a consequence of the hexagonal symmetry in the structure of graphene. Figure 4-2 shows the superimposition of reciprocal lattices between graphene and Cu(110) surface at the epitaxial orientation of 0°, as well as the crystallographic directions on graphene and (001)-oriented Cu substrate at the orientations of the reciprocal lattices. The green dashed circles represent circular paths through equivalent reciprocal lattice points of Cu(110) surface about the origin. The indices of one of the equivalent lattice points on the circles are indicated in the figure. A noticeable feature of the superimposition is the near coincidence of the green dashed circles with certain sets of equivalent reciprocal lattice points of graphene, hence the near coincidence between certain reciprocal lattice points of graphene and those of Cu(110) surface at certain epitaxial orientations.

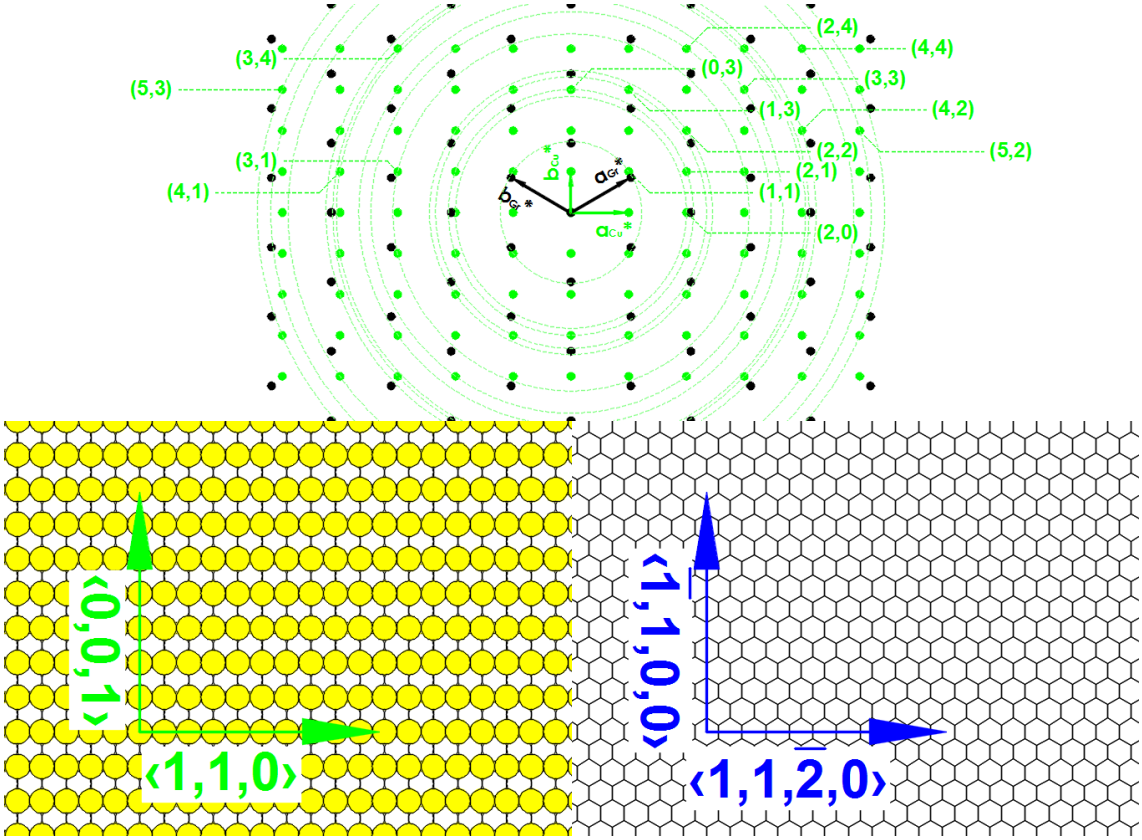

Figure 4-2. A superimposition of the reciprocal lattices for graphene and Cu(110) surface. The green-coloured dashed circles pass through certain points of the reciprocal lattice for Cu(110) surface. The coordinates for the representative of each set of lattice points which are related through symmetry hence fall on the same circle are indicated.

Figure 4-3a shows the superimposition of reciprocal lattice points at epitaxial orientations of ±5°, i.e. when the reciprocal lattice points of graphene nearest to the 1st green dashed circle of the smallest radius make the closest approach to the reciprocal lattice points of Cu(110) on the same circle. The reciprocal lattice points (1,1) of Cu(110) surface and (1,0) of graphene are near-coincident together at the epitaxial orientation of +5° when graphene in Figure 4-2 is rotated 5° anti-clockwise with respect to the Cu(110) surface; so too are the equivalent points in the opposite direction – i.e. $(\bar{1},\bar{1})$ of Cu(110) surface and $(\bar{1},0)$ of graphene. The same is true for the point $(\bar{1},1)$ of Cu(110) surface and (0,1) of graphene as well as the equivalent points in the opposite direction at the epitaxial orientation of -5° when rotated the same amount but clockwise. The low-index reciprocal lattice points within the interior of the black dashed circle in Figure 4-3a reveals a close match with the LEED pattern in

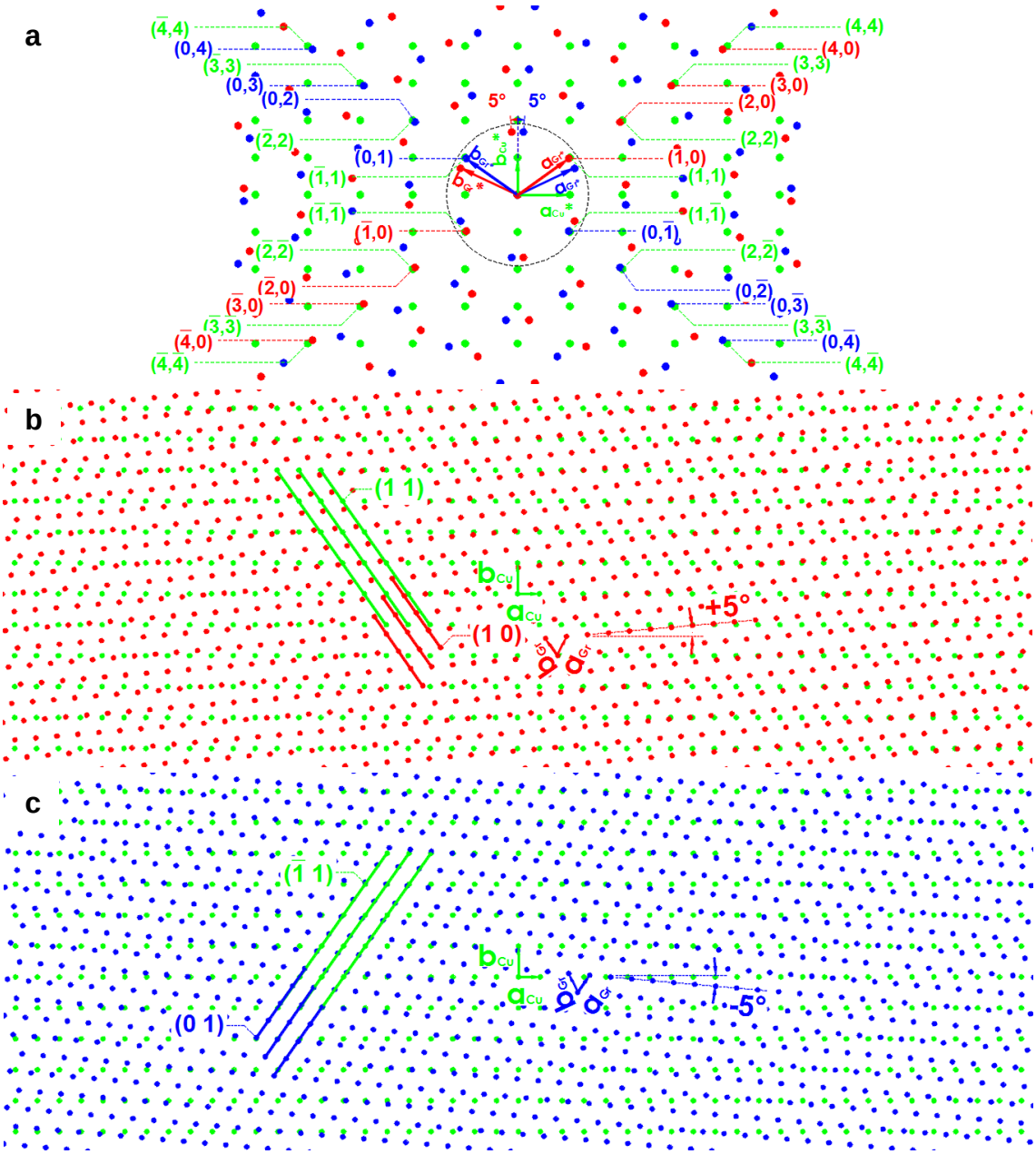

Figure 4-3. (a) A superimposition of reciprocal lattices for two graphene orientations at an angle of 5° on Cu(110) surface; reference of rotation based on the orientation in Figure 4-2. The reciprocal lattices for graphene in blue colour and in red colour are mirror images to each other. The rotation leads to the closest approach between the reciprocal lattice points equivalent to (1,0) of graphene and (1,1) of Cu(110) surface. These orientations also lead to the closest approach for the equivalent points with higher sets of indices. The black-colored dashed circle emphasizes the low-index reciprocal lattice points. (b) & (c) The superimposition of lattices in real space for the graphene orientations in (a).

Figure 4-1 for the case of the sharp diffraction spots. The match between the model and the LEED measurement therefore confirms the presence of graphene. The set of 12 sharp diffraction spots in hexagonal arrangement from

graphene in the LEED pattern therefore is composed of two sets of diffraction pattern – each set composed of 6 diffraction spots in hexagonal arrangement, one set from the epitaxial orientation at +5° whilst the other set from the epitaxial orientation at -5°. Figure 4-3b shows the superimposition of real-space lattices for the epitaxial orientation at +5° whilst Figure 4-3c for the epitaxial orientation at -5°. These superimpositions of lattices are mirror images to each other in juxtaposition but do not merge together onto each other into a single identical object and are therefore considered as chiral lattices with respect to the substrate.

The analysis and discussion made hitherto accounts for the origin of the sharp diffraction spots observed from the LEED measurement in Figure 4-1 and leads to the conclusion for the presence of epitaxial graphene domains with orientations at ±5°. These results are consistent with a recent publication on a LEED measurement of epitaxial graphene on Cu(110) surface[19]. However, the present LEED measurement shows a distinct feature not found in the report – the quasi-circular diffraction pattern. Measurement of the range of angular positions of the quasi-circular diffraction pattern shows correspondence to epitaxial orientations of about $\left|\pm 19^{\circ}\right| - \left|\pm 30^{\circ}\right|$. A closer inspection of the LEED measurement also reveals the presence of some amount of brightness however weak for other points on the circular path through the diffraction pattern of graphene. Thus rotational disorder exists for the entire spectrum of epitaxial orientations to some extent.

Assessment of Energetics of the Epitaxial Orientations

The most stable epitaxial orientations are at ±5° as evident from the bright appearance of the hexagonal pattern of sharp diffraction spots from graphene. The less-intense brightness for the quasi-circular diffraction pattern suggests less stable epitaxial orientations. A simple explanation to the energetics of epitaxial orientation can be attempted based on a reasonable argument. The arrangement of a particular adsorption site on a surface or an overlayer should follow the real-space lattice. Then the real-space lattice points of graphene and Cu(110) surface can be considered as the most reactive adsorption sites for interaction between the surface and the overlayer. As a consequence, the most stable epitaxial orientation should occur when the real-space lattice points of graphene and Cu(110) surface position at the closest coincidence in the highest number.

The consequence of the near coincidence in reciprocal lattice points between graphene and Cu(110) surface at certain epitaxial orientations is apparent from the relation between the magnitude G_{hk} of the translation vector to a reciprocal lattice point (h,k) and the interplanar distance d_{hk} for real-space lattice planes at orientation (hk) normal to the plane of the two-dimensional lattice of the surface in Equation (2-4). For example, the near-coincident reciprocal lattice points (1,0) of graphene and (1,1) of Cu(110) surface at the epitaxial orientation of +5° correspond to the real-space lattice plane orientations (10) to graphene and (11) to Cu(110) surface as shown in Figure 4-3b. In the same manner, the near-coincident reciprocal lattice points (0,1) of graphene and $(\bar{1},1)$ of Cu(110) surface at the epitaxial orientation of -5° correspond to the real-space lattice plane orientations (01) to graphene and $(\bar{1}1)$ to Cu(110) surface as shown in Figure 4-3c. In general, the near coincidence between reciprocal lattice points at the epitaxial orientations of ±5° refers to the $\{10\bar{1}\}_{MB}$ planes of graphene and the {11} planes of Cu(110) surface. Note, the subscript MB is used here to make an explicit indication of the use of Miller-Bravais notation and is meant to avoid confusion with the Miller notation. The orientations of the planes related to the near-coincident reciprocal

lattice points match together and the interplanar distances are almost equal. Planes can be considered to consist of lattice points. Then a considerable portion of the real-space lattice points from graphene and Cu(110) surface can be almost coplanar together at the plane orientations related to the near-coincident reciprocal lattice points. In other words, graphene and Cu(110) surface possess some chances of local commensurate character to each other i.e. some local match in real-space lattice points together between graphene and Cu(110) surface. The plane orientations can therefore be a basis to determine stable epitaxial orientations. The mismatch M_d between the plane orientations from graphene and Cu(110) surface in terms of the interplanar distance d_{hk} can be defined as

$$M_d = \frac{d_{Gr,hk} - d_{Cu,hk}}{d_{Cu,hk}} = \frac{G_{Cu,hk}}{G_{Gr,hk}} - 1 \qquad \textbf{(4-1)}$$

and provides some measure of destabilization at these epitaxial orientations. The expression is analogous to the definition of lattice mismatch in general texts elsewhere[23]. Moreover, the chances of a match in real-space lattice points can be supposed to become better as d_{hk} increases because the lattice points are concentrated in a smaller number of planes. Overall, the most stable epitaxial orientations correspond to the near coincidence of reciprocal lattice points where the related plane orientations possess the lowest indices and the least M_d.

The epitaxial orientations with near coincidence in certain reciprocal lattice points between graphene and Cu(110) surface are considered for reciprocal lattice points with an index number of up to 5. Values of d_{hk} or G_{hk} can be obtained from direct measurements on the lattice models or from computations. Table 4-1 sums up the important structural features for each of these epitaxial orientations. The structural features include the epitaxial orientation θ for both rotational directions; a representative (hk) of the matched plane orientations; the designation for the plane orientations equivalent to the representative planes, $\{hk\}$ in the case of Cu(110) surface and $\{h'k'i'\}_{MB}$ in the case of graphene; the magnitudes G_{hk} of the reciprocal lattice vectors; the

interplanar distance d_{hk}; the interplanar mismatch M_d. Also included in the table is the rank to designate the position in the order of d_{hk}; the epitaxial orientation of largest d_{hk}, in other words the plane orientation with the lowest indices, is specified as 1.

Assessment of the epitaxial orientations in Table 4-1 shows agreement with the distribution of epitaxial orientation in the LEED pattern for graphene in Figure 4-1. The reciprocal lattice vector from the origin to (1,0) of graphene has a magnitude of 2.94 $Å^{-1}$ whilst to the (1,1) of Cu(110) surface has a magnitude of 3.01 $Å^{-1}$. The M_d of the plane orientations equivalent to these reciprocal lattice points at the epitaxial orientations of ±5° is found to be 2.38 %. These plane orientations possess the lowest indices in Table 4-1 to position as the 1st in the d_{hk} rank. Other epitaxial orientations in particular at ±19°, ±30°, and ±25° possess M_d comparable to the value for the epitaxial orientations at ±5° but follows the rank of the epitaxial orientations at ±5° in terms of position in d_{hk} to become 3rd, 4th, and 5th. Close coincidence in real-space lattice points between graphene and Cu(110) surface can be related to the amount of interaction. The most frequent close-coincidence in lattice points happens for the lowest M_d and the lowest-index plane orientations, and explains a reason for the epitaxial orientations at ±5° to be the most stable as evident from the bright appearance of the hexagonal pattern of sharp diffraction spots from graphene. The interaction potential as a function of epitaxial orientation must be deep at the epitaxial orientations of ±5° to prevent rotational disorder around these epitaxial orientations at the growth temperature. The epitaxial orientations at ±19°, ±30°, and ±25° constitute partial components for the quasi-circular diffraction pattern. The less-frequent occurrence of close coincidence in real-space lattice points between graphene and Cu(110) surface for these epitaxial orientations is consistent with the less-stable nature of the epitaxial orientations for the quasi-circular diffraction pattern. Perhaps the extent of the weakness of interaction between graphene and Cu(110) surface at the epitaxial orientations of ±19°, ±30°, and ±25° could allow some rotation at the growth temperatures of

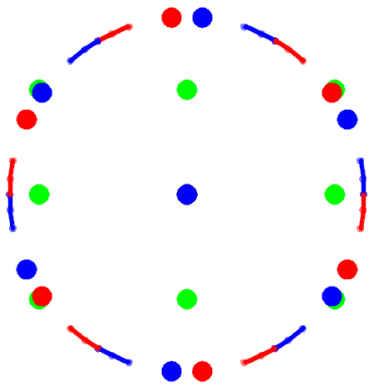

Figure 4-4. A model of superimpositions of reciprocal lattice for graphene orientations at 5°, 19°, 25°, and 30° on Cu(110) surface to provide explanation to the observed LEED pattern shown in Figure 4-1; reference of rotation based on the orientation in Figure 4-2. The reciprocal lattice points are shown within the low-index region. The solid arc superimposed on the orientations at 19°, 25°, and 30° indicates a certain amount of orientation disorder within such range due to a low degree of stabilization for the epitaxial orientations at 19°, 25°, and 30°

graphene and cause the rotational disorder; then the interaction potential as a function of epitaxial orientation must be shallow and broad at these epitaxial orientations. Note the upper and lower limits of the rotational disorder from the LEED measurement coincide with the epitaxial orientations at ±19° and ±30° considered as favourable from the assessment of coincidence in lattice points alone. Epitaxial orientations below $|\pm 5°|$ and in-between $|\pm 5°| - |\pm 19°|$ can be considered to be not so favourable from the apparent absence of LEED patterns for these regions. The reason could be explained as a lack of close match in lattice points because the rest of the epitaxial orientations considered in Table 4-1 possess high M_d's close to 3% and above, or positions lower than 5th in the d_{hk} rank. The long gap of unfavourable epitaxial orientations between the stable orientations at $|\pm 5°|$ and $|\pm 19°|$ must constitute a high interaction potential barrier to hinder further extension of the rotational disorder. Comprehensive explanation to the energetics of epitaxial orientation can be found from detailed theoretical calculation of models and interaction energies.

Figure 4-4 shows a model of superimposition of reciprocal lattices within the low-index region between graphene and Cu(110) surface at the favourable epitaxial orientations of ±5°, ±19°, ±30°, and ±25°. The sizes of the points are not made to correspond to the width of the actual diffraction spots but to

emphasize the strength of a particular epitaxial orientation. The solid arcs between the epitaxial orientations at ±19°, ±25°, and ±30° are drawn to indicate the rotational disorder. The model shows a good reproduction of the measured LEED pattern so the assessment of coincidence in lattice points indeed provides a simple but good explanation for the distribution of epitaxial orientation.

Table 4-1. Structural features of certain epitaxial orientations with close coincidence in reciprocal lattice points based on a model of graphene on Cu(110) surface.

θ (°)	Cu(110) Surface				Graphene				M_d (%)	Rank
	(hk)	$\{hk\}$	$G_{Cu,hk}$ (Å^{-1})	$d_{Cu,hk}$ (Å)	(hk)	$\{h'k'i'\}_{MB}$	$G_{Gr,hk}$ (Å^{-1})	$d_{Gr,hk}$ (Å^{-1})		
0	(20)	{20}	4.92	1.28	$(1\bar{1})$	$\{11\bar{2}\}$	5.11	1.23	-3.60	2
2	(31)	{31}	7.59	0.83	$(2\bar{1})$	$\{12\bar{3}\}$	7.80	0.81	-2.75	6
3	(42)	{42}	10.44	0.60	$(3\bar{1})$	$\{13\bar{4}\}$	10.63	0.59	-1.76	10
4	(53)	{53}	13.37	0.47	$(4\bar{1})$	$\{14\bar{5}\}$	13.51	0.47	-1.05	12
5	(11)	{11}	3.01	2.08	(10)	$\{01\bar{1}\}$	2.95	2.13	2.25	1
9	(52)	{52}	12.79	0.49	$(3\bar{2})$	$\{23\bar{5}\}$	12.85	0.49	-0.48	11
10	(41)	{41}	10.00	0.63	$(2\bar{2})$	$\{22\bar{4}\}$	10.21	0.62	-2.11	8
17	$(\bar{3}4)$	$\{\bar{3}4\}$	10.15	0.62	(24)	$\{\bar{4}22\}$	10.21	0.62	-0.63	9
18	$(\bar{5}3)$	$\{\bar{5}3\}$	13.37	0.47	(15)	$\{\bar{5}14\}$	13.51	0.47	-1.05	12
19	(21)	{21}	5.22	1.20	$(1\bar{1})$	$\{11\bar{2}\}$	5.11	1.23	2.25	3
22	(52)	{52}	12.79	0.49	$(2\bar{3})$	$\{32\bar{5}\}$	12.85	0.49	-0.48	11
24	(31)	{31}	7.59	0.83	$(1\bar{2})$	$\{21\bar{3}\}$	7.80	0.81	-2.75	6
24	$(\bar{4}2)$	$\{\bar{4}2\}$	10.44	0.60	(14)	$\{\bar{4}13\}$	10.63	0.59	-1.76	10
25	$(\bar{1}3)$	$\{\bar{1}3\}$	5.77	1.09	(22)	$\{\bar{2}20\}$	5.90	1.07	-2.10	5
25	(24)	{24}	8.53	0.74	(30)	$\{03\bar{3}\}$	8.84	0.71	-3.59	7
30	(03)	{03}	5.22	1.20	(21)	$\{\bar{1}2\bar{1}\}$	5.11	1.23	2.26	4

4.2 STM Characterization of Epitaxial Graphene on the Cu(110) Surface

STM measurements were performed to image graphene formation on the Cu(110) surface after thermal decomposition of perylene on the surface in experimental setup 3. Figure 4-5 and Figure 4-6 show some of the STM topographic images after completion of the entire process at growth temperatures estimated to be around 1000 K – 1250 K. The large-scale STM image in Figure 4-5a shows the presence of round-shaped islands on the surface comprised of narrow terraces and numerous step-edges. These islands cover about 25% of the surface area and can reach a size of up to 150 nm in diameter of an equivalent circle with the same area. Repetition of the graphene preparation process four times leads to saturation of the surface.

The theoretical limit to the maximum possible surface-area coverage $\Theta_{max,lim}$ of graphene on the Cu(110) surface from a single process of the preparation can be achieved when the entire amount of carbon in a saturated monolayer of commensurate (5x5) perylene superstructure is 100% converted into graphene. The surface area within a single unit cell of the (5x5) perylene superstructure includes two molecules of perylene. Each perylene molecule contains 20 carbon atoms. Thus the maximum amount of carbon within the (5x5) unit cell is 40 atoms. The surface area $A_{\mathbf{Gr}}$ within a single primitive unit cell of graphene can be computed from the cross products of the primitive translation vectors i.e.

$$A_{\mathbf{Gr}} = \left| \mathbf{a}_{\mathbf{Gr}} \times \mathbf{b}_{\mathbf{Gr}} \right| = \frac{\sqrt{3}}{2} a_{Gr} \cdot b_{Gr} \qquad \textbf{(4-2)}$$

Each primitive unit cell of graphene is associated with two carbon atoms. The 40 carbon atoms from two molecules of perylene within a unit cell of the (5x5) perylene superstructure would take up a maximum area of 20 times $A_{\mathbf{Gr}}$ when converted into graphene. Thus $\Theta_{max,lim}$ can be computed as

$$\Theta_{max,lim} = \frac{20 \cdot \frac{\sqrt{3}}{2} a_{Gr} \cdot b_{Gr}}{5a_{Cu} \cdot 5b_{Cu}} \qquad \textbf{(4-3)}$$

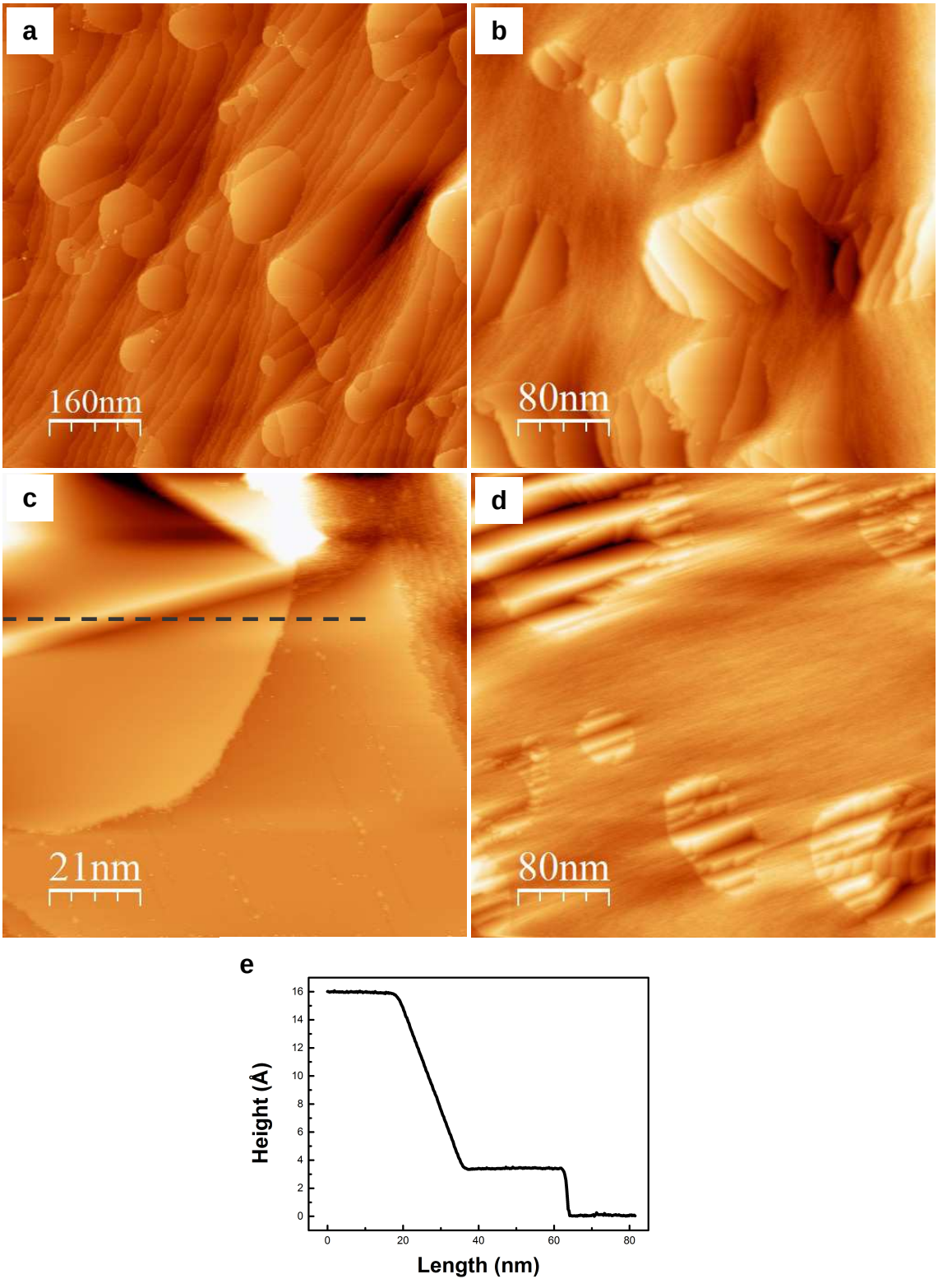

Figure 4-5. Various STM topographic images of graphene islands from four different regions on Cu(110) surface upon preparation at the highest temperatures of the present experiment: (a) 8000 Å x 8000 Å measured at U = -1000 mV and I = 0.20 nA; (b) 4000 Å x 4000 Å measured at U = -1000 mV and I = 0.20 nA; (c) 1043 Å x 1043 Å measured at U = -1100 mV and I = 0.20 nA, the grey-colour dashed line across the image is a scan line; (d) 4000 Å x 4000 Å measured at U = -987 mV and I = 0.36 nA. The images are not post-calibrated to correct dimensions. (e) Height profile corresponding to the grey-colour dashed scan line in (c).

which finds a value of 45% upon substitution of the magnitudes of the translation vectors. Assume the islands are graphene. Then comparison of the surface-area coverage from STM measurements with the theoretical limit shows the effectiveness of the preparation process is about 56% – i.e. the percentage of the entire amount of carbon from perylene converted into graphene. Reports have demonstrated no desorption of intact perylene molecules from the monolayer regime even when decomposition temperatures had been reached[24,25] so the rest of the amount of carbon can be presumed to desorb as volatile hydrocarbon fragments. A note worth some mention is the presence of an adsorbate-induced surface reconstruction on the Cu(110) surface into a narrow stripe pattern of upper and lower terraces underneath the commensurate (5x5) superstructure of perylene. The surface reconstruction therefore leads to half of the amount of perylene molecules to be found on the upper terraces whilst the other half on the lower terraces. Such proportion of distribution almost coincides with the 56% effectiveness of the present preparation process. Thus an open question remains whether the surface reconstruction is correlated with the effectiveness of the decomposition process or whether the close match between these numbers is just a matter of coincidence.

Several features of the islands resemble those reported for graphene on metal surfaces. One feature, common to reports of graphene on metal surfaces, is the continuous extension of graphene over step edges on the substrate surface underneath. The feature is apparent from the presence of step edges on the islands in the figures shown. Rounded-shape islands of graphene have been observed as well on Cu(111) surface[26]. The rounded shapes represent an insignificant influence from the symmetry of the Cu-atom arrangement on the surface in comparison to the effect of high temperature during growth. These shapes however contrast with the anisotropic growth of graphene on Cu(100) surface where lobe-shaped islands grow in the directions of the high-symmetry axes of the surface[27,28]. The presence of numerous step edges on the Cu(110) surface should somehow exert some influence towards distortion from perfect round shapes for the graphene islands. However the interaction of the edges of

graphene islands with the step edges is not adequate to pin graphene edges onto the step edges, in contrast to the case of graphene on Ru(0001)[29]. Perhaps up-step growth of graphene islands over step edges can be seen from the presence of some graphene edges close to the upper edge of a step on the Cu surface as in the portion of the island indicated with a grey dashed rectangle *h* in Figure 4-6d.

The interaction between graphene and the Cu(110) surface seems to widen the terraces underneath graphene islands. The phenomenon is apparent in Figure 4-5b where an enormous number of step edges and narrow terraces surround graphene islands on large flat terraces. Figure 4-5c shows a portion near an edge of an island and a stepped region on the island. Measurement scan of height profile is performed along the grey dashed line on the image. The corresponding height profile on the scan line is shown in Figure 4-5e; the step edge underneath the particular graphene overlayer measures a height of 12.5 Å which is equivalent to about 9 monatomic steps of the Cu(110) surface. The edge of the island is found to have a height of about 3.4 Å. However the height of graphene from the surface is noted to be no more than about 2 Å from measurements to be shown in Section 4.3 so the height of the island edge in Figure 4-5c is about a Cu-monatomic step higher. The height measurement shows the island edge terminates with a step edge of the Cu surface underneath. However the situation would be rather unusual if the step edge on the substrate surface assumed the natural shape of the overlayer on its own. The observation therefore suggests expansion of terraces through movement of surface step edges with the front of graphene-island growth as reported from a real-time growth experiment for graphene on Ru(0001)[30]. Figure 4-5d shows a region where graphene islands induce complex facet formations on the substrate surface underneath the islands. Large-area faceting of substrate surface has been reported with formation of graphene on high-index Ni surfaces[14]. The appearance of the facet formations is quite unusual in the present experiments and could be attributed to the abnormal amount of step edges in the region of the substrate. The observations of increase in terrace sizes, increase in step heights, and facet formations could point towards an

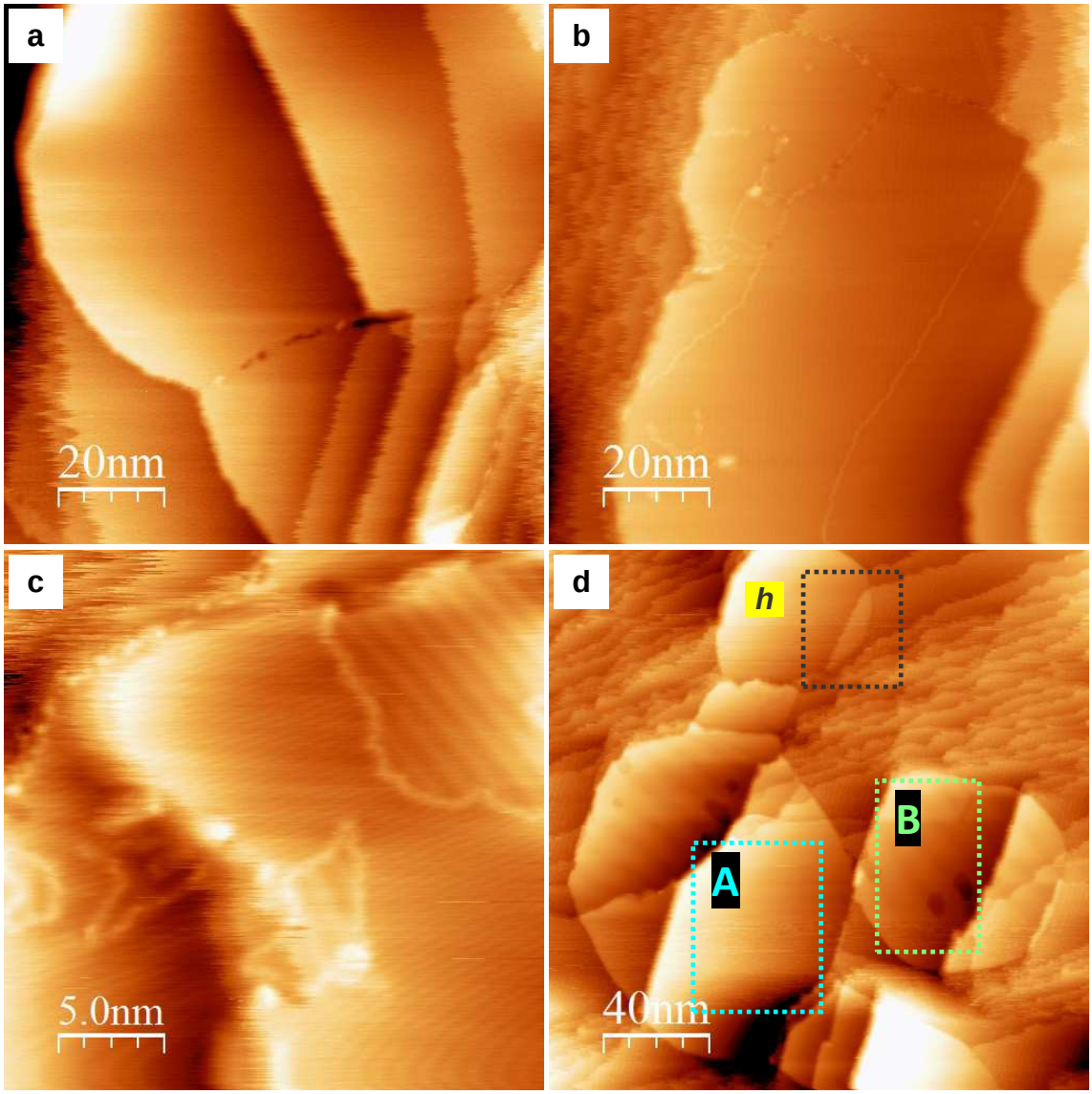

Figure 4-6. Various STM topographic images of graphene islands from four different regions on Cu(110) surface upon preparation at the highest temperatures of the present experiment: (a) 1000 Å x 1000 measured at U = -1000 mV and I = 0.20 nA; (b) 1000 Å x 1000 Å measured at U = -1000 mV and I = 0.20 nA; (c) 250 Å x 250 Å measured at U = -1000 mV and I = 0.20 nA; (d) 2000 Å x 2000 Å measured at U = +874 mV and I = 0.20 nA. The images are not post-calibrated to correct dimensions

induced process of Cu-atom transport during growth of graphene islands due to some favorable interaction between the graphene overlayer and the Cu(110) surface. Close inspection of STM images as in Figure 4-6a reveals some unhindered diffusion of copper atoms at steps underneath graphene islands from the images of rough step edges to suggest weak interaction between the graphene overlayer and the Cu(110) surface.

Figure 4-6b shows graphene islands can be composed of multiple domains. A closer look as in Figure 4-6c shows domains possess different large-scale stripe patterns. The origin of the stripe patterns can be revealed from atomic-resolution STM images. Figure 4-6d shows a large view over the area around the island domains at which atomic resolution was best obtained. These domains are indicated with a blue dashed rectangle as A and a green dashed rectangle as B. The complex patterns from the atomic-resolution data are shown in Figure 4-7 – Figure 4-9.

Moiré Superstructure for Domain A

Complex patterns from an incommensurate epitaxial overlayer of graphene on well-defined metal surfaces has been observed from STM measurements[31,32]. These patterns are often termed as Moiré and arise from a combination of electronic corrugation[33] and geometric corrugation[34] of the overlayer due to interaction with the substrate. Moiré superstructures are known to manifest large-scale periodic patterns – large-scale hexagonal patterns on metal surfaces with hexagonal structure[12,13,26,35] whereas large-scale stripe patterns on metal surfaces with cubic structure[28]. Manifestation of Moiré superstructures as large-scale stripe patterns for the present case is reasonable from the rectangular structure of Cu(110) surface. The complex patterns in domains A and B from the atomic-resolution data in Figure 4-7 – Figure 4-9 must be Moiré patterns for graphene on Cu(110) surface.

Figure 4-7 and Figure 4-8 show atomic-resolution STM images of domain A in Figure 4-6d. The patterns observed in the STM images were verified from successive scans at different magnifications and scan directions. Calibration factors are stated in the caption for each figure where standard calibration images, based on atomic-resolution STM images of well-ordered p(2x1) adsorption of oxygen on the surface of the same Cu substrate, are available for the same image size and the same scan direction.

Figure 4-7a shows a large-scale view of the atomic-scale origin of the large-scale stripe pattern for domain A and reveals what seems to be simple stripe-patterned modulation of dark and bright regions, in fact turns out to have complicated atomic structure behind the pattern. The period of separation between stripes measures about 64 ± 6 Å. The direction of the stripes is oriented on the surface at about –78° from the <110> direction on the surface of the Cu substrate. Figure 4-7b is scanned at 45° at the same scan dimension. The height profile for the measurement scan on the grey dashed line *i* is shown in the inset to show the corrugation of the stripe-patterned modulation. The height profile is applied with a minor smoothening process using the SPM-image analysis software WSxM just to reduce some obtrusive features from

noise. The difference in height between the maxima and the minima of the stripe pattern is found to be about 0.4 Å.

Figure 4-7c is scanned at a dimension of 100 Å x 100 Å. The hexagonal arrangement of dark depressions and the scale of the distances in between points to the honeycomb structure of graphene. A streak pattern of bright protrusions and dark depressions as indicated with dashed lines in green and blue colour are prominent on the bright region of the large-scale stripe pattern. The image of the honeycomb structure as a hexagonal pattern of dark depressions is more apparent on the dark region of the large-scale stripe pattern. Figure 4-7d shows the same image after application of an FFT filter; the essential features of the atomic-scale structure appear clear and smooth without the obtrusive features of noise.

Figure 4-8 reveals changes in the level of emphasis on certain features of the structure of graphene on the Cu(110) surface in the images. These variations can be attributed to changes in the condition of the STM tip due to changes in the applied bias voltage between the sample and the tip, the current, or some incidental chemical functionalization of the tip. Figure 4-8a shows balanced emphasis on the streak pattern of bright protrusions and dark depressions and on the pattern of the honeycomb structure of graphene. Figure 4-8b focuses more emphasis on the streak pattern of bright protrusions and dark depressions whilst Figure 4-8c and Figure 4-8d focus more emphasis on the pattern of the honeycomb structure. On the one hand, the image of the honeycomb structure in Figure 4-8c appears as bright spots. On the other hand, the image of the honeycomb structure in Figure 4-8d appears as dark spots. The images of the honeycomb structure of graphene show an apparent distortion from a uniform hexagonal arrangement. The distortion could neither be due to an unstable piezoelectric scanner of the STM instrument nor to an unstable STM tip because the appearance of such a distortion pattern is uniform within these images and consistent at different scan directions. Perhaps the distortion could be an effect of strain in the graphene overlayer due to an interaction with the Cu substrate and an effect of the atomic-scale corrugation of Cu(110) surface.

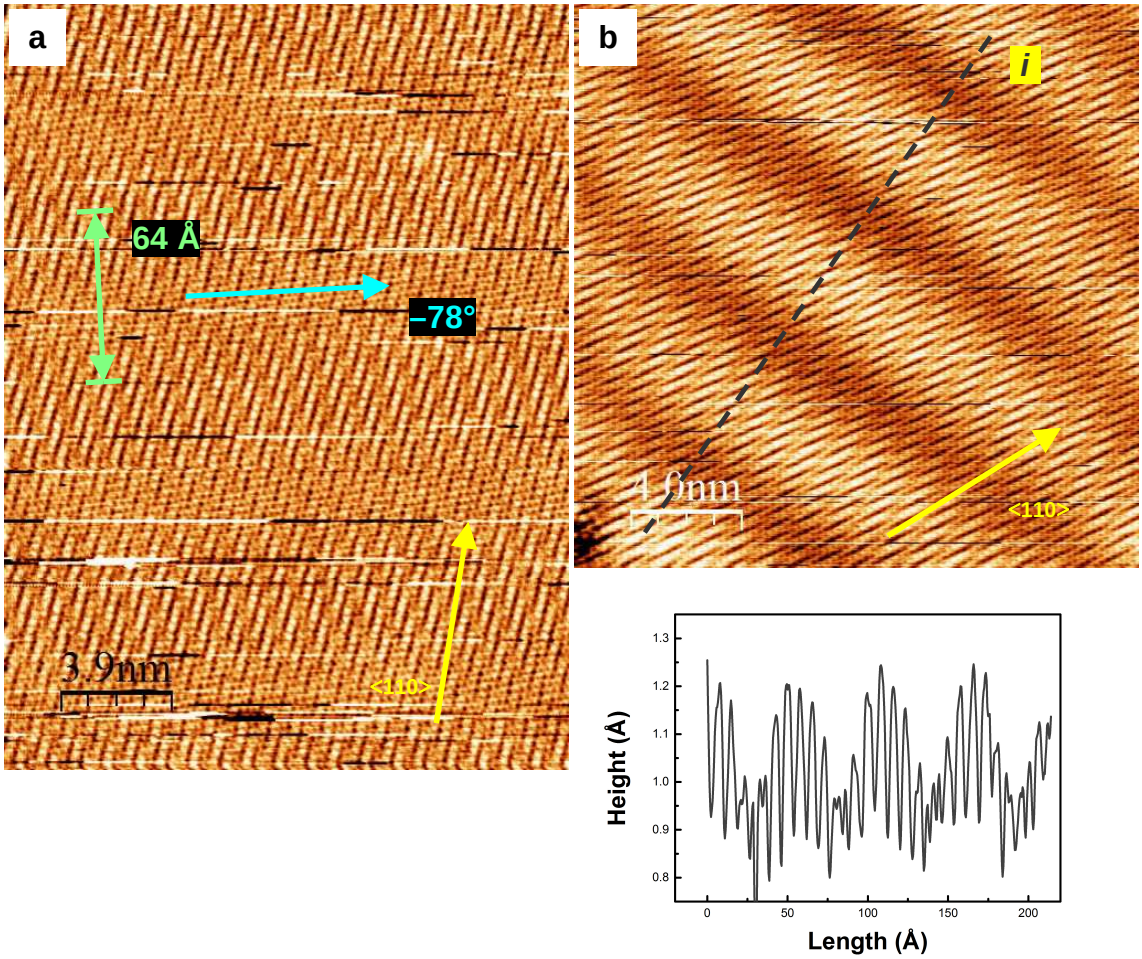

Figure 4-7. Atomic-resolution STM topographic images of an area within domain A in Figure 4-6d. (a) 193 Å x 261 Å image measured at U = +155 mV and I = 0.40 nA, corrected with calibration factors X = 0.963 and Y = 1.305 for 200 Å x 200 Å image scans. (b) 200 Å x 200 Å image measured at U = +155 mV and I = 0.40 nA, scanned at an angle of 45° relative to (a), not post-calibrated to correct dimensions. (c) 93 Å x 149 Å image measured at U = +155 mV and I = 0.40 nA, corrected with calibration factors X = 0.934 and Y = 1.495 for 100 Å x 100 Å image scans. (d) FFT-filtered STM image in (c). Inset in (b): height profile corresponding to scan line *i* in (b). The height profile is applied with a smoothening process using the SPM image-analysis software WSxM to reduce some obtrusive effects of noise.

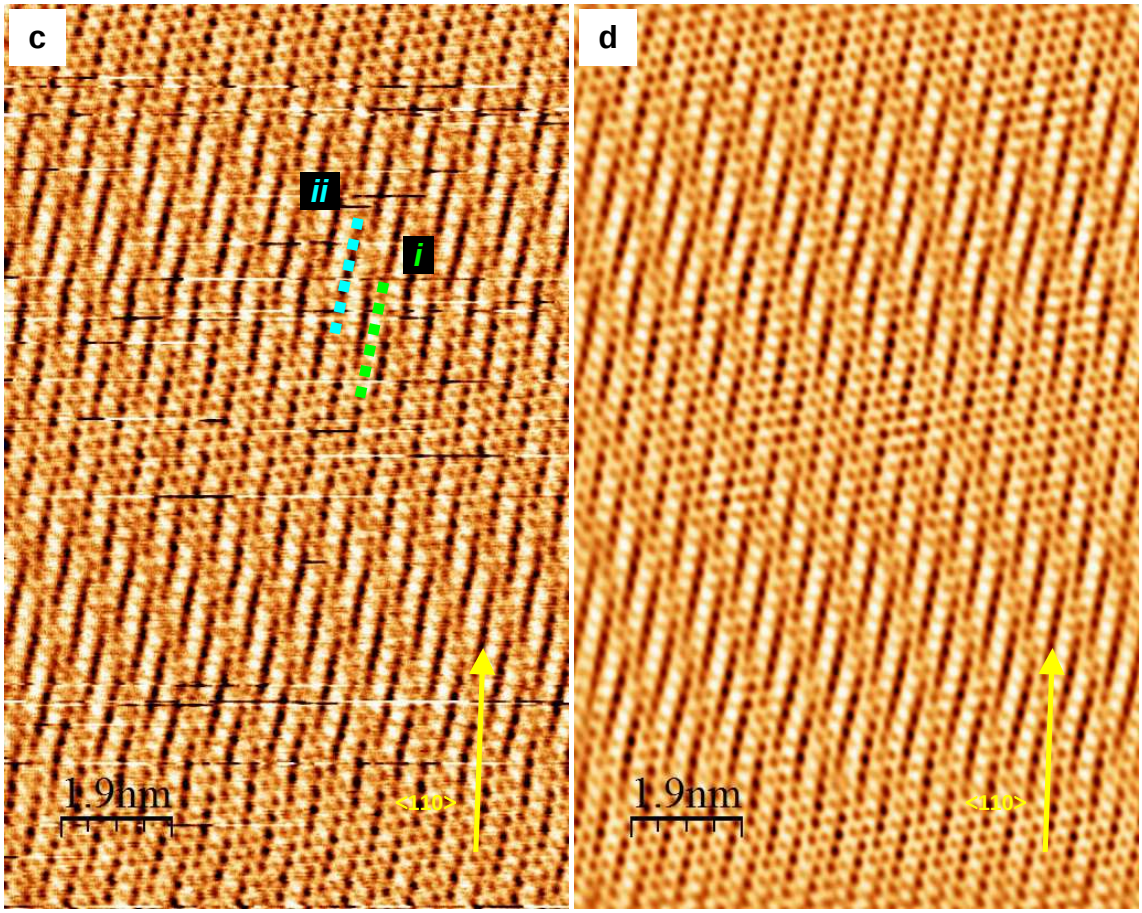

Figure 4-7 (Continuation). Atomic-resolution STM topographic images of an area within domain A in Figure 4-6d. (a) 193 Å x 261 Å image measured at U = +155 mV and I = 0.40 nA, corrected with calibration factors X = 0.963 and Y = 1.305 for 200 Å x 200 Å image scans. (b) 200 Å x 200 Å image measured at U = +155 mV and I = 0.40 nA, scanned at an angle of 45° relative to (a), not post-calibrated to correct dimensions. (c) 93 Å x 149 Å image measured at U = +155 mV and I = 0.40 nA, corrected with calibration factors X = 0.934 and Y = 1.495 for 100 Å x 100 Å image scans. (d) FFT-filtered STM image in (c). Inset in (b): height profile corresponding to scan line *i* in (b). The height profile is applied with a smoothening process using the SPM image-analysis software WSxM to reduce some obtrusive effects of noise.

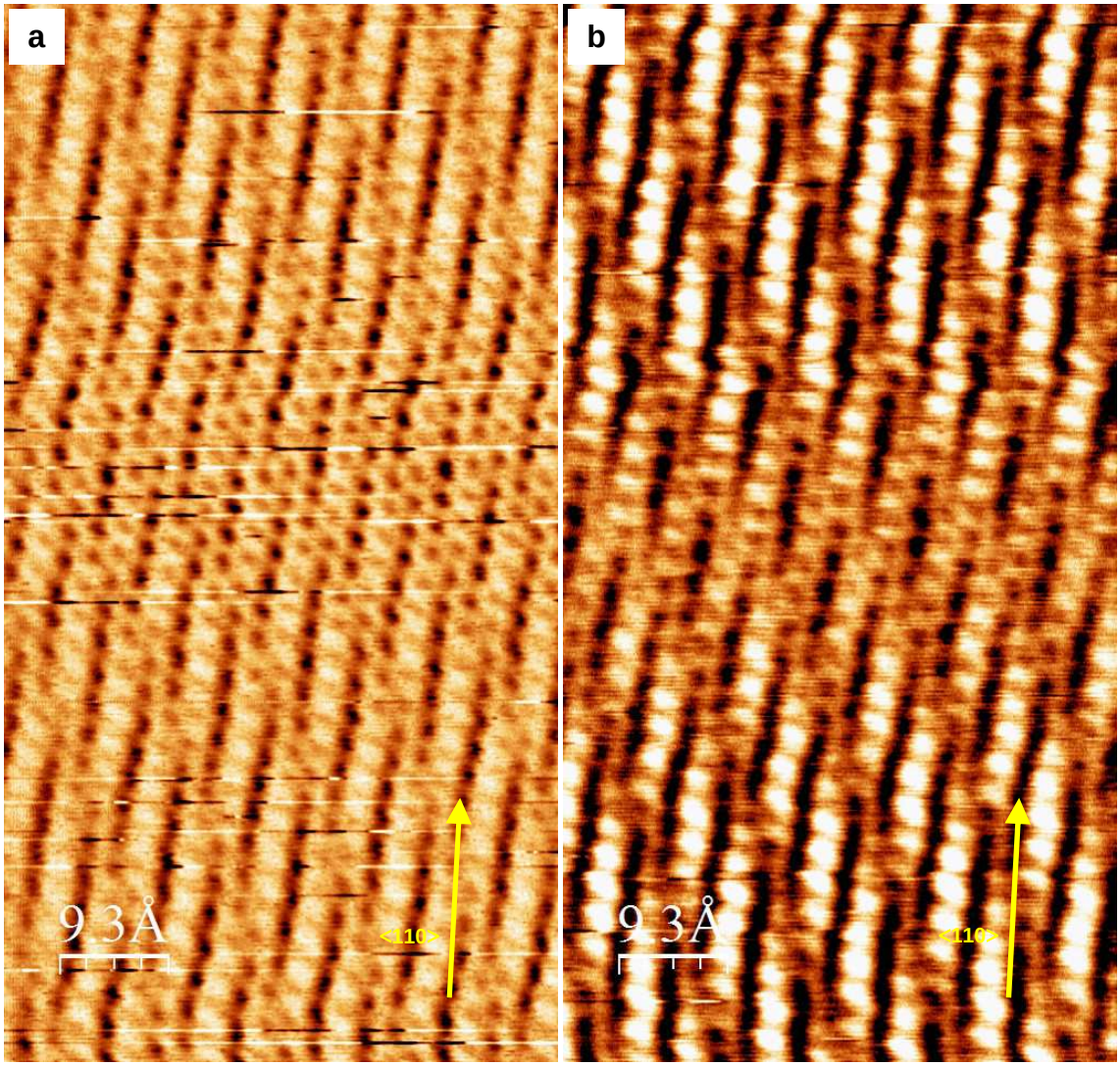

Figure 4-8. 46 Å x 89 Å atomic-resolution STM topographic image of an area within domain A in Figure 4-6d. Image dimensions are corrected using calibration factors X = 0.927 and Y = 1.771 for 50 Å x 50 Å image scans. STM measurements were performed at (a) U = +155 mV and I = 0.40 nA, (b) U = +258 mV and I = 0.80 nA, (c) U = +80 mV and I = 0.40 nA, (d) U = +85 mV and I = 0.40 nA.

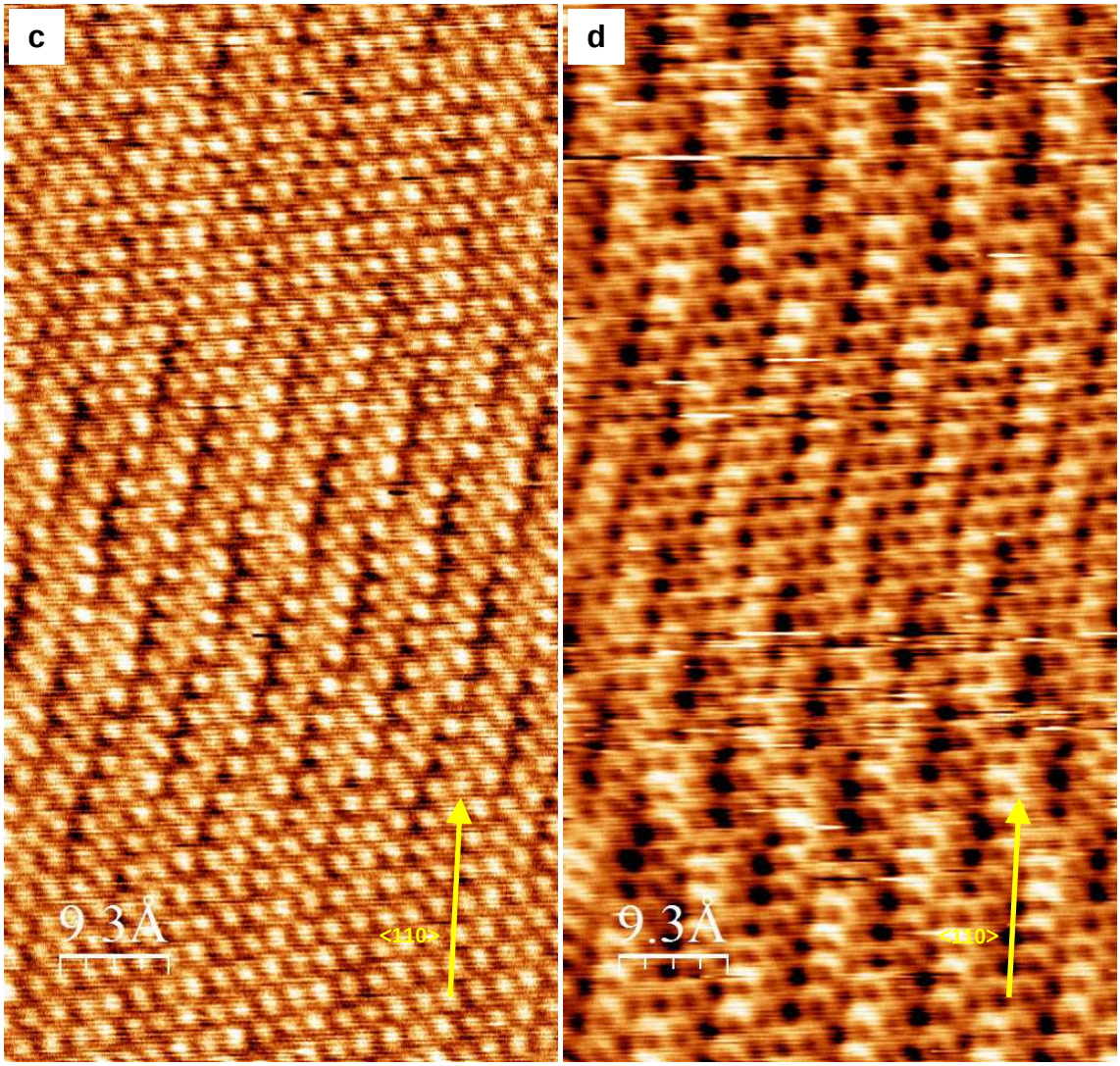

Figure 4-8 (Continuation). 46 Å x 89 Å atomic-resolution STM topographic image of an area within domain A in Figure 4-6d. Image dimensions are corrected using calibration factors X = 0.927 and Y = 1.771 for 50 Å x 50 Å image scans. STM measurements were performed at (a) U = +155 mV and I = 0.40 nA, (b) U = +258 mV and I = 0.80 nA, (c) U = +80 mV and I = 0.40 nA, (d) U = +85 mV and I = 0.40 nA.

Moiré Superstructure for Domain B

Figure 4-9a, b show high-resolution STM images of domain B in Figure 4-6d though the levels of contrast, sharpness, and noise are not on a par with the quality of the images for domain A. Figure 4-9a shows a large-scale view of the atomic-scale origin of the large-scale stripe pattern for domain B. The period of separation between stripes measures about 99 ± 10 Å after use of calibration factors. The direction of the stripes is oriented on the surface at about +44° from the <110> direction on the surface of the Cu substrate. The height profile for the measurement scan along the grey dashed line *ii* in Figure 4-9a is shown in Figure 4-9c. The height profile is applied with a smoothening process using the SPM-image analysis software WSxM to reduce some obtrusive features from noise. The difference in height between the maxima and the minima of the stripe pattern is found to be about 0.4 Å. Figure 4-9b shows a closer view at a dimension of 50 Å x 50 Å.

The structure pattern in the domain bears resemblance to the structure pattern in domain A. The present conditions of the STM tip seem to provide more emphasis on the streak pattern of bright protrusions and dark depressions of the structure rather than the honeycomb structure of graphene. The image of the honeycomb structure seems to appear as bright protrusions and apparent in particular on the dark regions of the large-scale stripe pattern.

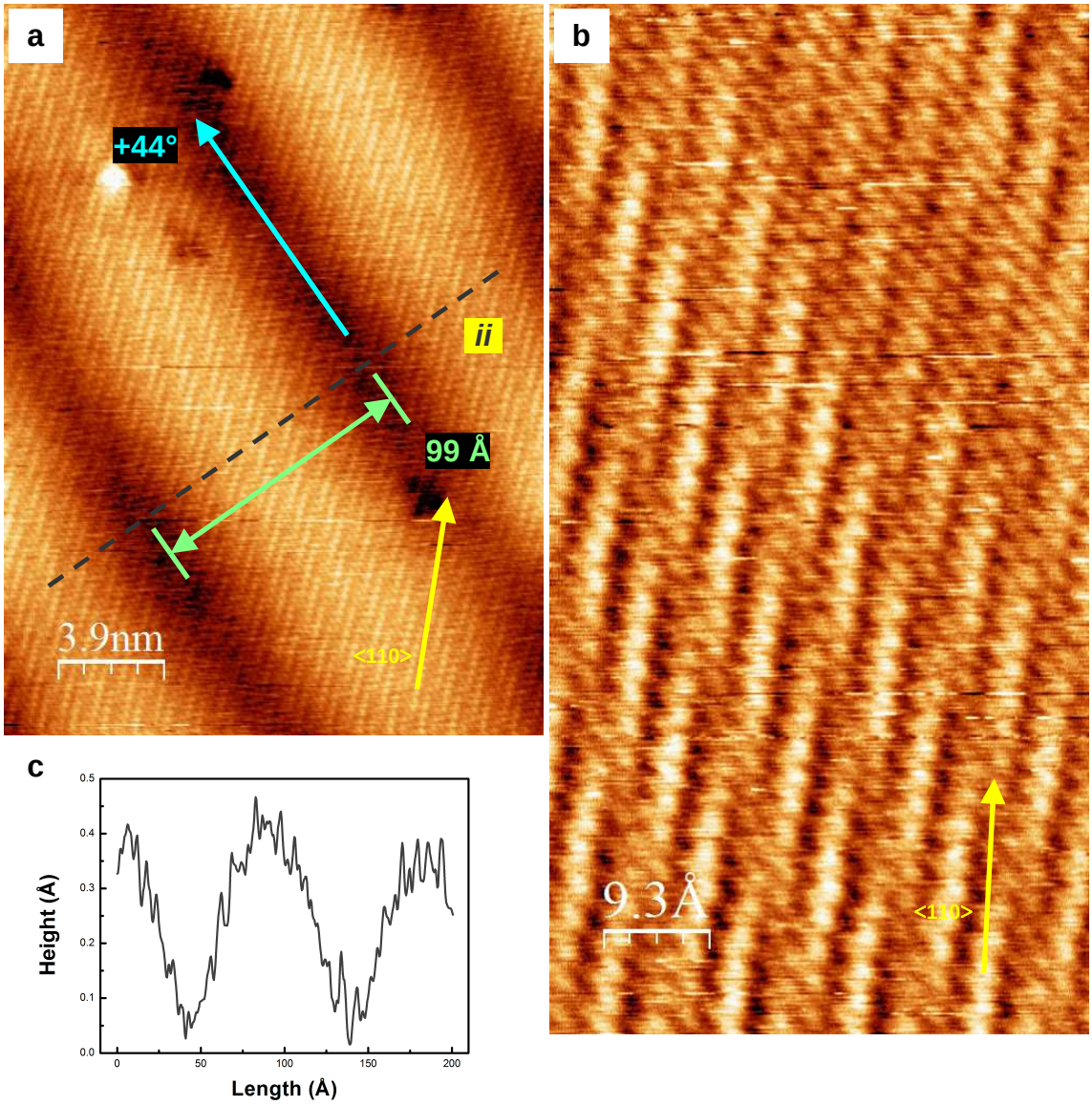

Figure 4-9. Atomic-resolution STM topographic image of an area within domain B in Figure 4-6d: (a) 193 Å x 261 Å image measured at U = +475 mV and I = 0.80 nA, corrected with calibration factors X = 0.963 and Y = 1.305 for 200 Å x 200 Å image scans; (b) 46 Å x 89 Å image measured at U = +475 mV and I = 0.80 nA, corrected with calibration factors X = 0.927 and Y = 1.771 for 50 Å x 50 Å image scans. (c) Height profile corresponding to scan line *ii* in (a). The height profile is applied with a smoothening process using the SPM image-analysis software WSxM to reduce some obtrusive effects of noise.

Comparison of Moiré Superstructure with 2D Geometrical Models of Superimposed Structures and Estimation of Epitaxial Orientation

An approach to find an explanation for the observations from the STM images is the creation of hard-sphere and carbon-skeleton models for direct visual comparison. The first approximation to the model for graphene on the Cu(110) surface is the direct superimposition of 2D geometrical structures between graphene and Cu(110) surface[35]. The 2D geometrical structure of graphene is created as a skeleton to represent the network of sp^2-bonded carbon atoms with C–C bond length of 1.42 Å. The 2D geometrical structure of Cu(110) surface is created as solid circles to represent Cu atoms on the surface. The superimposition of graphene is adjusted in terms of the epitaxial orientation θ as in Section 4.1. Models were created at an interval of 1°.

The 2D geometrical models of graphene on Cu(110) surface can be perceived to form large-scale stripe patterns of bright and dark regions at finite angular orientations. The period of separation for the large-scale stripes and the direction of the stripes relative to the ⟨1,1,0⟩ direction of the Cu(110) surface are noted from each model. The graph in Figure 4-10 summarizes the variation in the period of separation and the orientation of the large-scale stripe patterns with change in epitaxial orientation of graphene on Cu(110) surface in the models. The period of separation increases up to a maximum of 94 Å at an epitaxial orientation of $\left|\pm 5°\right|$ upon rotation from 0° and from thence gradual decrease occurs up to 8 Å upon further rotation to epitaxial orientations of $\left|\pm 23°\right|$. Simultaneous with the change in the period of separation is the change in the orientation of the stripes. The direction of change in the orientation of the stripes is opposite to the sense of graphene rotation relative to the Cu(110) surface. The orientation of the stripe pattern changes clockwise from +18° to -132° for the case of anti-clockwise change in epitaxial orientation of graphene on the Cu(110) surface from +1° to +23°; the same manner of change but in the opposite sense happens for the opposite case. The stripe pattern becomes hard to recognize between $\left|\pm 24°\right|$ and $\left|\pm 26°\right|$ – i.e. the stripes are somewhat discontinuous, an effect of gradual transition from chiral to an achiral pattern at the epitaxial orientations of ±30°. The stripe patterns at epitaxial orientations

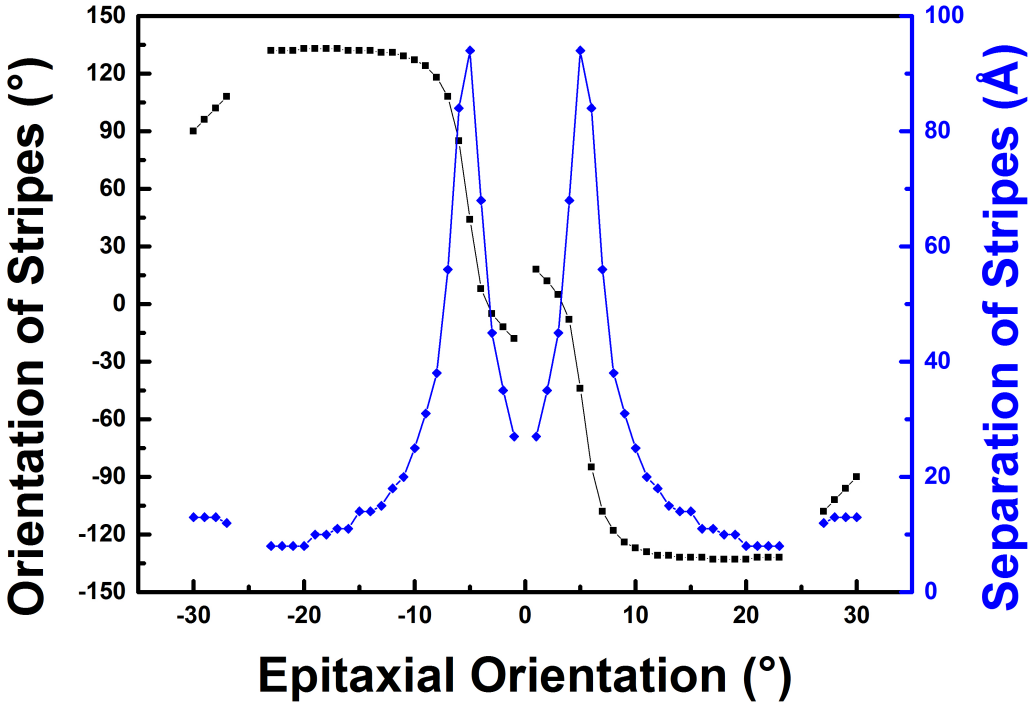

Figure 4-10. Graph which summarizes the trend in the distance of separation and the orientation of the stripe patterns as the epitaxial orientation changes in the 2D geometrical models for graphene on Cu(110) surface.

close to ±30° approach a horizontal orientation. A non-superimposable mirror-image pattern at an epitaxial orientation of –θ exists for each pattern at an epitaxial orientation of +θ except for the epitaxial orientations at 0° and ±30°. The phenomenon relates to the existence of chiral structures. The patterns at the epitaxial orientations of 0° and ±30° no longer possess non-superimposable images and are therefore achiral structures.

An important point in the 2D geometrical models is the association of a unique stripe pattern to each epitaxial orientation of graphene on the Cu(110) surface. Thus the epitaxial orientation of graphene on the Cu(110) surface can be estimated based on comparison of the period of separation and the orientation of the stripes between STM measurements and the models. The STM measurements of 64 ± 6 Å and –78° for the respective parameters show domain A corresponds closest to the epitaxial orientation of -7°. The model for the epitaxial orientation has stripes of 56 Å period and -72° orientation as shown in Figure 4-11. For reference, the model for the epitaxial orientation of -6° has

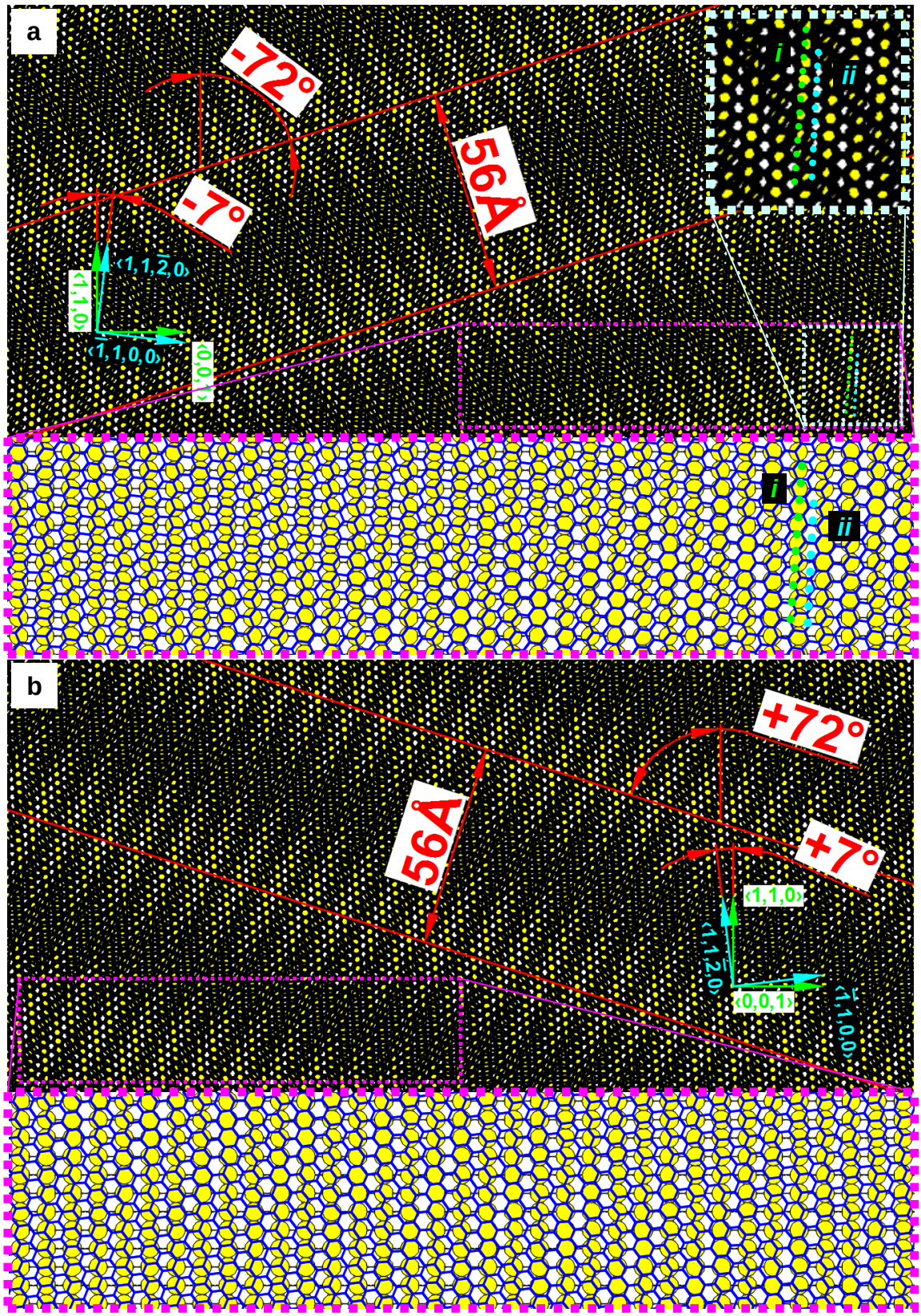

Figure 4-11. 2D geometrical model of Moiré superstructure for graphene on Cu(110) surface based on direct superimposition of individual structures from the basal plane of graphite and the free surface of Cu(110) at an epitaxial orientation of (a) +7°, (b) -7° between the zigzag ⟨1,1,$\bar{2}$,0⟩ direction of graphene and the close-packed ⟨1,1,0⟩ direction of Cu. The lower panels show the honeycomb structure relative to the Cu(110) surface. The green and blue lines in (a) indicate two features in the Moiré superstructure (cf. Figure 4-7c).

stripes of 84 Å period and +85° orientation and the model for the epitaxial orientation of -8° has stripes of 38 Å period and -62° orientation. The observation of some discrepancies in the parameters between the measurement and the model could come from two possible reasons. First, the actual epitaxial orientation could deviate from -7° towards -6°. Second, the actual structures of epitaxial graphene on the Cu(110) surface could deviate from the mere 2D approximations as the actual positions of carbon atoms could possess some distortion, perhaps due to the interaction with the surface and the corrugation of the surface. Sophisticated theoretical models based on calculations could provide further clarification. The mirror image to the model is also shown in Figure 4-11 to emphasize the chiral behaviour of the Moiré superstructures for graphene on Cu(110) surface. The relevant directions are shown in green color for Cu(110) surface and in blue color for graphene in each model.

Comparison of the STM measurements of 99 ± 10 Å for the distance between stripes and +44° for the orientation of the stripes with the model in Figure 4-12 show domain B corresponds to the epitaxial orientation of -5°. The model for the epitaxial orientation possesses stripes of 94 Å period and +44° orientation as shown in Figure 4-12.

Visual comparison of the atomic-scale structure reveals close resemblance between the STM images and the models both for domains A and B. The bright regions of the large-scale stripe pattern can be seen as areas where a major portion of the carbon aromatic rings are centered close to the atop sites on the upper and lower close-packed atomic rows of Cu(110) surface. On the other hand, the dark regions of the large-scale stripe pattern can be seen as areas where the edges of the carbon aromatic rings are close to the atop sites on the close-packed atomic rows of the Cu surface. Further comparison from here refers to domain A but applies to domain B as well. The streaks of bright protrusions on the bright regions of large-scale stripe patterns as indicated with a green dashed line in Figure 4-7c can be explained as regions where the carbon aromatic rings of graphene are centered close to the atop sites on the upper close-packed atomic rows of the Cu(110) surface.

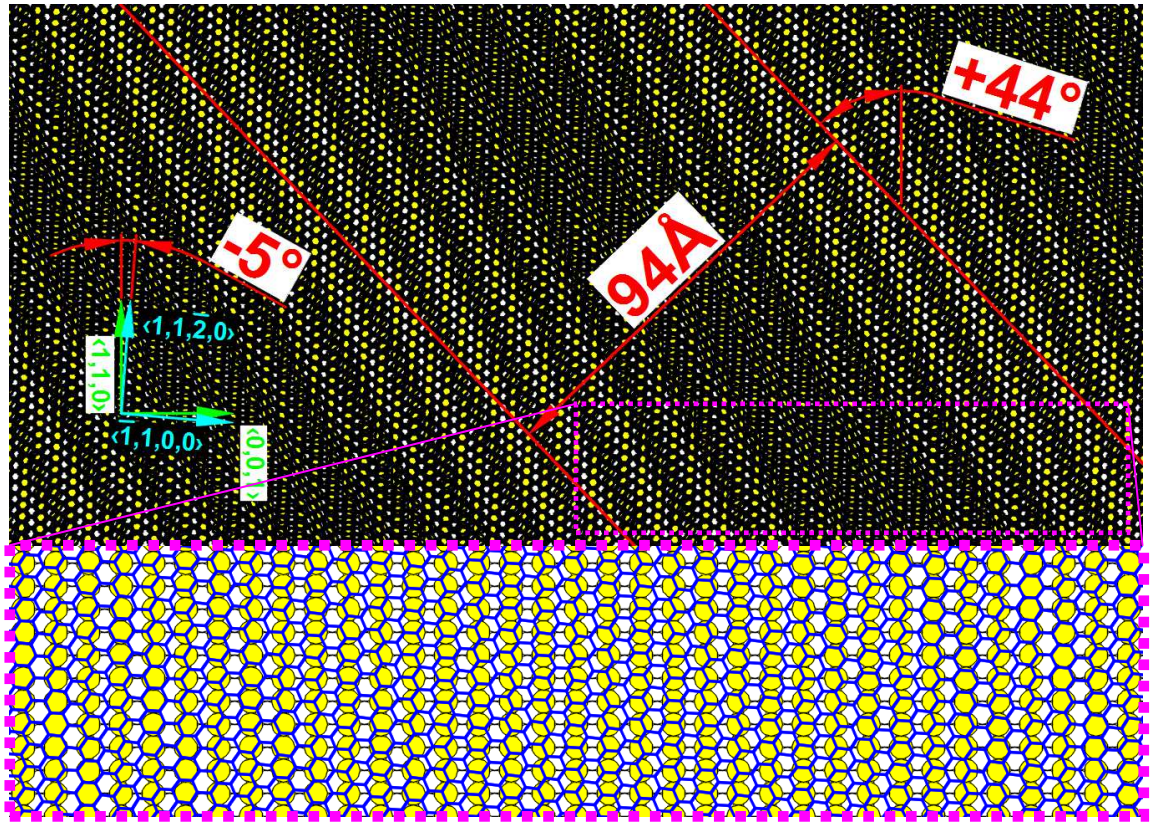

Figure 4-12. 2D geometrical model of Moiré superstructure for graphene on Cu(110) surface based on direct superimposition of individual structures from the basal plane of graphite and the free surface of Cu(110) at an epitaxial orientation of -5° between the zigzag ⟨1,1,$\bar{2}$,0⟩ direction of graphene and the close-packed ⟨1,1,0⟩ direction of Cu. The lower panel shows the honeycomb structure relative to the Cu(110) surface.

These bright protrusions are represented as the yellow streaks within the bright regions of the large-scale stripes in the models as indicated with a green dashed line on the inset in Figure 4-11b. In-between these yellow streaks in the model are regions which appear as white streaks where the carbon aromatic rings of graphene are centered close to the atop sites on the lower close-packed atomic rows of the Cu(110) surface as indicated with a blue dashed line on the inset in Figure 4-11b. Strong image contrast can be observed between the streaks of bright protrusions and of dark depressions in the STM images. The major contribution to the deep image-brightness contrast between these bright and dark streaks could come from the electronic corrugation due to the effect of height from the substrate Cu atom to graphene. The yellow streaks in the model could appear with so much brightness in the STM images because of an electronic effect due to a close contact between carbon aromatic rings and

the atop sites on the upper close-packed rows of Cu atoms. On the other hand, the white streaks in the model could appear with much pronounced depression because of an electronic effect due to a gap between carbon aromatic rings and the atop sites on the lower close-packed rows of Cu atoms. The actual geometrical corrugation across the upper and the lower close-packed atomic rows on the Cu(110) surface must be just a minor contribution, otherwise the nature of the periodic deformation on graphene would appear to cause an unfavourable amount of elastic strain.

Statistical Distribution of Epitaxial Orientation

The epitaxial orientation can be estimated even in the absence of accurate calibration. First, measurements of the distance and the orientation of the stripes act as two independent means to determine the epitaxial orientation so mutual confirmation is possible. Second, the sudden variations in these parameters with change in epitaxial orientation as depicted in Figure 4-10 surpass the reasonable amount of measurement error for the STM instrument. Indeed, measurements of the parameters both prior to and subsequent to application of post-calibration factors for the cases of domain A and B come to close agreement in the estimate of the epitaxial orientations.

A fair number of domains with sufficient topographic contrast to notice a stripe pattern are observed from a collection of large-scale STM images. The post-calibration factors for scans over 400 Å in Experiment Set-Up No. 3 are estimated as 0.98 in X axis and 1.10 in Y axis. Therefore, a statistical distribution of epitaxial orientation can be derived despite the absence of accurate calibration factors for the size of these images. Distance measurements on these domains are allocated a tolerance of 10% based on the precision of post-calibration. Indeed, the allocated tolerance in distance measurements for purposes of estimation of the epitaxial orientation is found to be reasonable upon verification of the epitaxial orientation from the orientation of the stripe pattern. Orientation measurements on the domains are allocated a tolerance of ±10° based on the image distortion of the post-calibration standard. The association of epitaxial orientation to each observation of stripe pattern in an STM image is made when the period and orientation of stripes in the model for a particular epitaxial orientation corresponds to those in the observation within the limits of the allocated tolerances. In most cases, multiple associations of epitaxial orientation for each observation are inevitable. Then, the observation is divided so the number of counts distributed to these epitaxial orientations is just a fraction of one observation. Consider for example the observation of the stripe pattern in the island domain shown in Figure 4-13. The period and the orientation of the stripe pattern are measured to have some value in the range 12 Å – 15 Å and -76° – -96°. The models which agree with

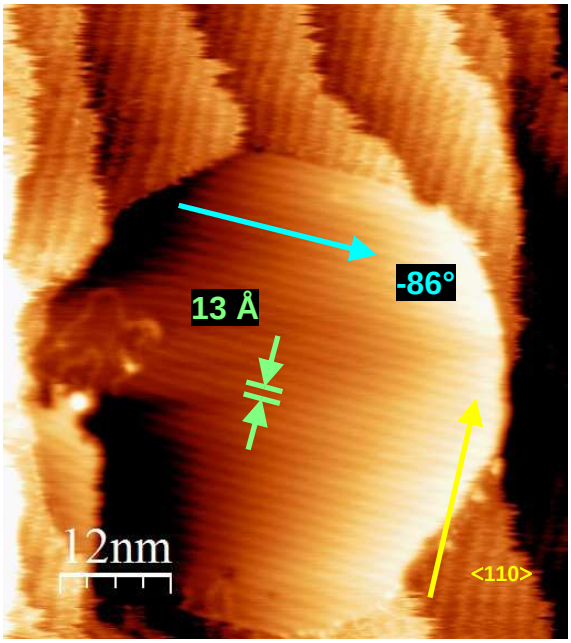

Figure 4-13. 588 Å x 660 Å STM topographic image of an island domain whose stripe-patterned superstructure is resolved. The image dimensions are corrected with calibration factors X = 0.98 and Y = 1.10 for 600 Å x 600 Å image scans. STM measurements were performed at U = -1000 mV and I = 0.20 nA.

these measurements are the epitaxial orientations of -28°, -29°, and ±30° as shown in Figure 4-14. Thus the number of counts distributed to each of the epitaxial orientations $|\pm 28°|$, $|\pm 29°|$, and $|\pm 30°|$ is just ⅓.

Figure 4-15 shows the statistical distribution of epitaxial orientation. The red solid line is drawn on the graph as just a guide to the actual plot of discrete measurement points for the benefit of the viewer but is not a statistical model to the data. A total number of 42 island domains are found to have resolved stripe patterns. Note however a major portion of the total number of island domains observed in the entire set of STM images from the present investigation are found without resolution of stripes or any other pattern so these observations are excluded from the statistics. The total number of counts for each epitaxial orientation in the statistical distribution is expressed in terms of percentage count relative to the total number of 42 observations. No number of counts is assigned to the range $|\pm 24°| - |\pm 26°|$ due to a lack of clear distinction of the patterns in the models. The correspondence of the stripe patterns between the STM measurements and the models shows the 2D geometrical models do provide a good approximation to the observations.

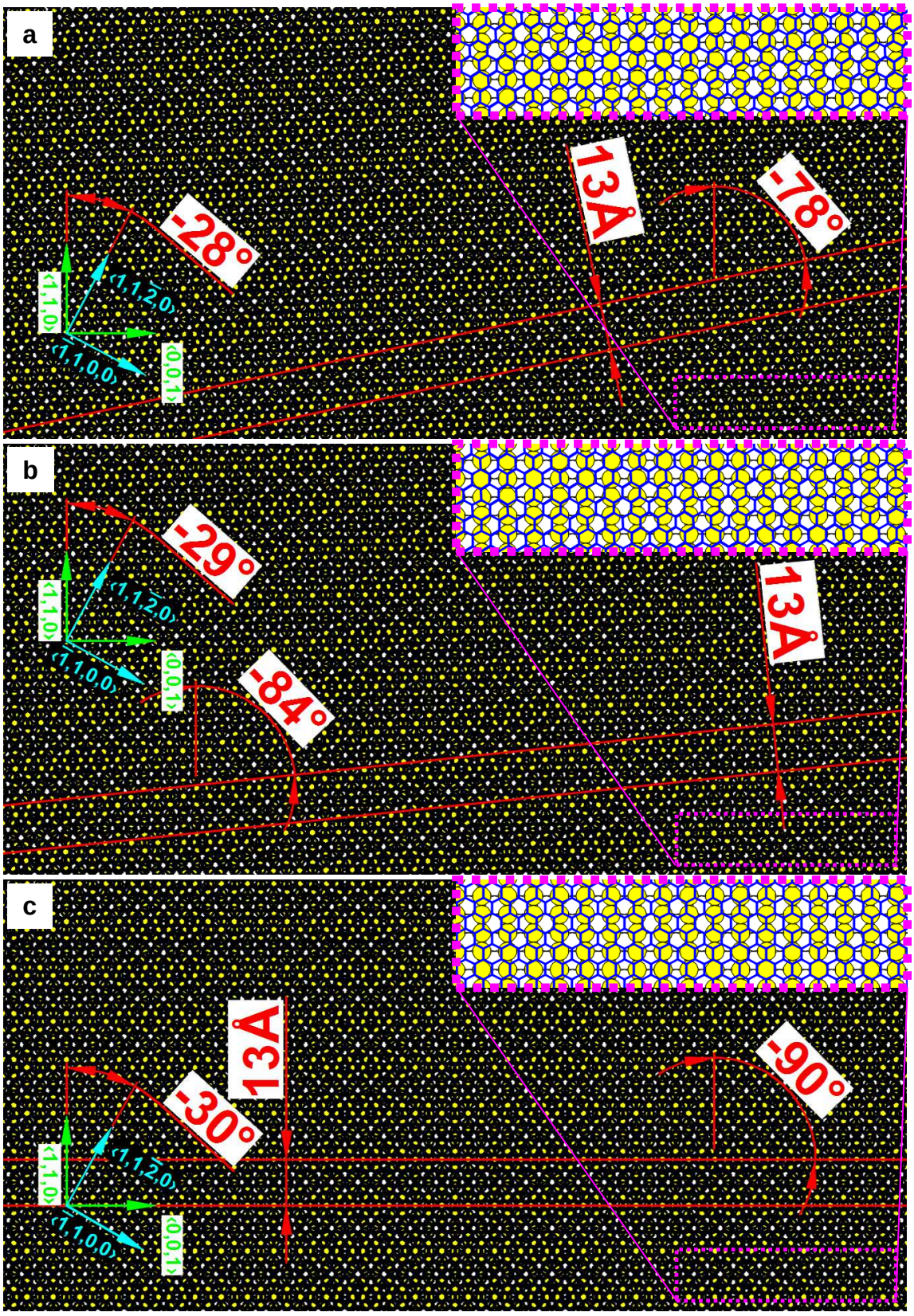

Figure 4-14. 2D geometrical model of Moiré superstructure for graphene on Cu(110) surface based on direct superimposition of individual structures from the basal plane of graphite and the free surface of Cu(110) at an epitaxial orientation of (a) -28°, (b) -29°, and (c) ±30° between the zigzag ⟨1,1,$\bar{2}$,0⟩ direction of graphene and the close-packed ⟨1,1,0⟩ direction of Cu. The insets on the upper right corners of the models show the honeycomb structure relative to the Cu(110) surface structure.

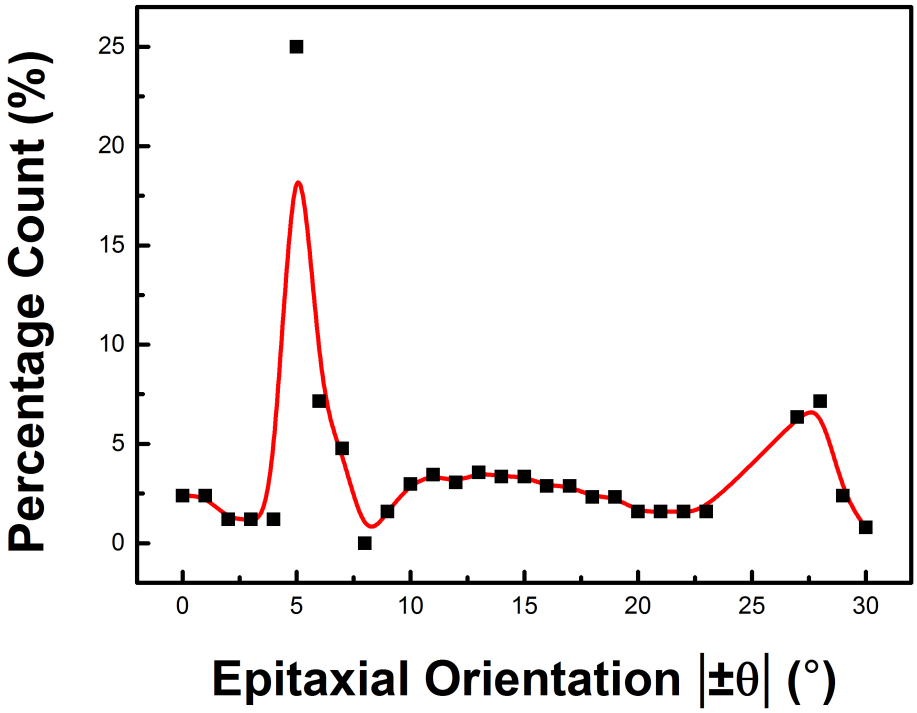

Figure 4-15. Statistical distribution of epitaxial orientation in terms of percentage count from a total number of 42 observations of domains whose stripe patterns are resolved in large-scale STM images. The actual plot is shown as the square symbols on discrete points; the red-colour solid line is drawn as a guide to the plot for the viewer.

The statistical distribution of epitaxial orientation tends to be broad and low in the range $|\pm 9°| - |\pm 30°|$. The reason comes from the small changes in the period and the orientation of the stripe pattern in the models within such a range so a unit observation of stripe pattern would be divided among several epitaxial orientations within the limits of allocated measurement error. On the other hand, the estimation of epitaxial orientation in the range $|\pm 0°| - |\pm 9°|$ falls within a narrow range because of the drastic changes in the period and the orientation of the stripe pattern so the statistical distribution tends to be narrow and intense for the peak at $|\pm 5°|$. Thus the strength and broadness of the peaks in the statistical distribution is not just related to the number of counts and tolerance of measurements but also to the variation of the plot in Figure 4-10.

The statistical distribution of epitaxial orientation based on observations from STM measurements shows close agreement with the distribution of

brightness in the LEED pattern shown in the former section. The highest chances of appearance together with the highest level of confidence in the estimated epitaxial orientation occur around the most stable epitaxial orientations at │±5°│. Somewhere between │±25°│ and │±30°│ there could be stable epitaxial orientations based on the presence of another peak. However, the assessment of epitaxial orientation in the former section points to stable epitaxial orientations at │±25°│ and │±30°│. Then perhaps the peak between │±25°│ and │±30°│ could also be a manifestation of frequent rotations between these two orientations at the growth temperature. Some counts appear between the orientations at │±5°│ and │±30°│ though uncertain to a considerable extent. Low chances of appearance seem to be the case for the achiral orientations at 0° and │±30°│. The statistical distribution shows an extent of rotational disorder for the entire spectrum of epitaxial orientations, in agreement with the presence of some brightness in the LEED pattern however weak for the epitaxial orientations considered unfavorable in the former section.

The exact reason for the statistical distribution remains quite unclear without a sophisticated theoretical model. Nevertheless certain remarks on the structure can be mentioned in relation to the statistical distribution. The most stable epitaxial orientations at │±5°│ coincide with the Moiré superstructure of the largest period of separation in the stripe pattern. The large-scale periodic pattern in the Moiré superstructure of graphene has been reported to come from a major contribution of geometrical deformation[34]. Perhaps the largest period of separation in the stripe pattern allows graphene on the Cu(110) surface to handle geometrical deformation with the least amount of destabilization. The small changes in the period of separation and orientation of the large-scale stripes in the region │±9°│ – │±30°│ could perhaps mean small differences in interaction to be consistent with the rotational disorder.

4.3 Development of Graphene on the Cu(110) Surface

LEED Characterization of Graphene Formation at 800 K – 1000 K Growth Temperature

Figure 4-16 shows the LEED pattern for a graphene overlayer on the Cu(110) surface prepared based on thermal decomposition of perylene to some temperature 800 K – 1000 K. The prominent spots in rectangular arrangement come from the first-order diffraction on the Cu(110) surface. The diffraction pattern is moved off the centre of the LEED optics to make a portion of the diffraction pattern from graphene visible onto the range of detection on the screen. The presence of graphene is evident from the appearance of a pattern comparable to what has been described for the LEED pattern of graphene heated up to 1250 K as shown in Figure 4-1. However, certain features in the LEED pattern for the low growth temperature show distinction. The circular diffraction pattern from graphene is diffuse and manifests almost even brightness throughout the entire circle. Note Figure 4-16 cannot show the entire circular diffraction pattern but just the upper portion. The almost even brightness in the circular diffraction pattern shows randomness in epitaxial orientation. Some preference nonetheless exists for the epitaxial orientations at ±5° as evident from some enhancement in brightness at the two symmetrical points on the circular diffraction pattern. The diffuse character of the circular LEED pattern for graphene suggests the preparation conditions tend to produce minute domains at random epitaxial orientations. Recent report of LEED measurements for graphene on Cu(110) surface based on thermal decomposition of ethane has described an appearance of randomness in orientation to a certain extent for growth temperatures lower than 1000 K[19]. Thus predisposition towards disorder in epitaxial orientations seems to be a distinct feature for a graphene overlayer on Cu(110) surfaces at low growth temperatures. Possible reasons for the present randomness in epitaxial orientation include the influence of the size of islands or domains[16] and the thermal activation towards rotation at the growth temperature.

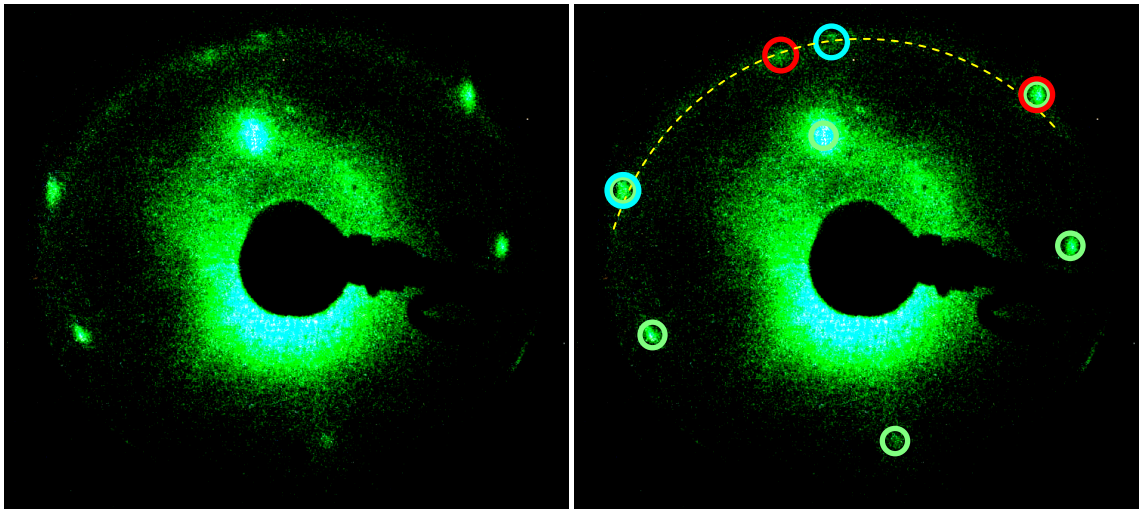

Figure 4-16. LEED pattern of a graphene overlayer on Cu(110) surface prepared through thermal decomposition of perylene up to some temperature much lower than 1250 K.

Compare to the LEED pattern for the graphene overlayer heated to 1250 K as shown in Figure 4-1. The sharpness of the LEED pattern and the appearance of diffraction spots suggest evolution of the graphene overlayer into large domains with preference towards particular epitaxial orientations as the growth temperature increases. Disorder in epitaxial orientation nonetheless remains to a certain extent as evident from the semi-circular diffraction pattern as described in Section 4.1. However, the recent report of LEED measurements for graphene on Cu(110) surface based on thermal decomposition of ethane has demonstrated no appearance of the semi-circular diffraction pattern despite the growth temperature ramped to no more than 1000 K[19], in contrast to 1250 K here. Note the use of ethane has been reported to require multiple sequences of hydrocarbon exposure to Cu surface at room temperature and thermal decomposition to the specified temperature in order to achieve a sufficient amount of graphene on the surface[19,26], whereas the use of perylene needs just one. Thus the persistence of the semi-circular diffraction pattern in the present case could be related to a high rate of graphene formation consequent upon a substantial amount of accessible carbon prior to the process. A high rate of graphene formation could lead to certain kinetic hindrances and trap numerous domains at less favourable epitaxial orientations.

STM Characterization of Graphene Formation at 800 K – 1000 K Growth Temperature

Figure 4-17 – Figure 4-20 show STM images of initial formation of graphene overlayer at an estimated growth temperature of 800 K – 1000 K. The large-scale STM image in Figure 4-17a provides a large overview of the overlayer with a dark contrast. The overlayer formation appears as a network of islands interconnected through narrow bridges. The sizes of the islands are non-uniform but no more than about 50 nm. The shapes of the islands are irregular but tend to be rounded. The common observation of attachment to step edges on the Cu surface seems to suggest the events of nucleation could have occurred at these sites. The close-up view in Figure 4-17b shows the presence of multiple domains, as evident from the clear appearance of dark boundaries on the overlayer. The shapes of the domains are quite non-uniform and irregular. The sizes of the domains are also non-uniform and some even come as small as a spot on the image. The small dimensions of the domains in the overlayer are in agreement with the diffuse character of the LEED pattern for graphene in Figure 4-16. The domains must possess almost random epitaxial orientations as the LEED pattern suggests.

Figure 4-18 and Figure 4-19 show STM images of scans on the same portion of the overlayer. The STM image in Figure 4-18a shows a large-scale view. Clusters gathered at the edges of the graphene overlayer as seen apparent from the close-up view in Figure 4-18b is a common observation for the present overlayer. These clusters are no more than 1 nm in size; the height profile in Figure 4-18c demonstrates a size of about 7 Å for one of the clusters. Moiré patterns are observed to appear even at the present stage of growth where domains are small. The large-scale stripes of Moiré patterns are observed with pronounced contrast in Figure 4-18a and are observed even for one domain the size of about 5 nm across the stripe pattern. Figure 4-19a and Figure 4-19b show image enlargements of regions from the STM image in Figure 4-18a within the gray-coloured dashed rectangles which are designated as *u* and *v*. These image enlargements provide better distinction for the large-scale stripe patterns than the close-up view in Figure 4-18b. Comparison of the

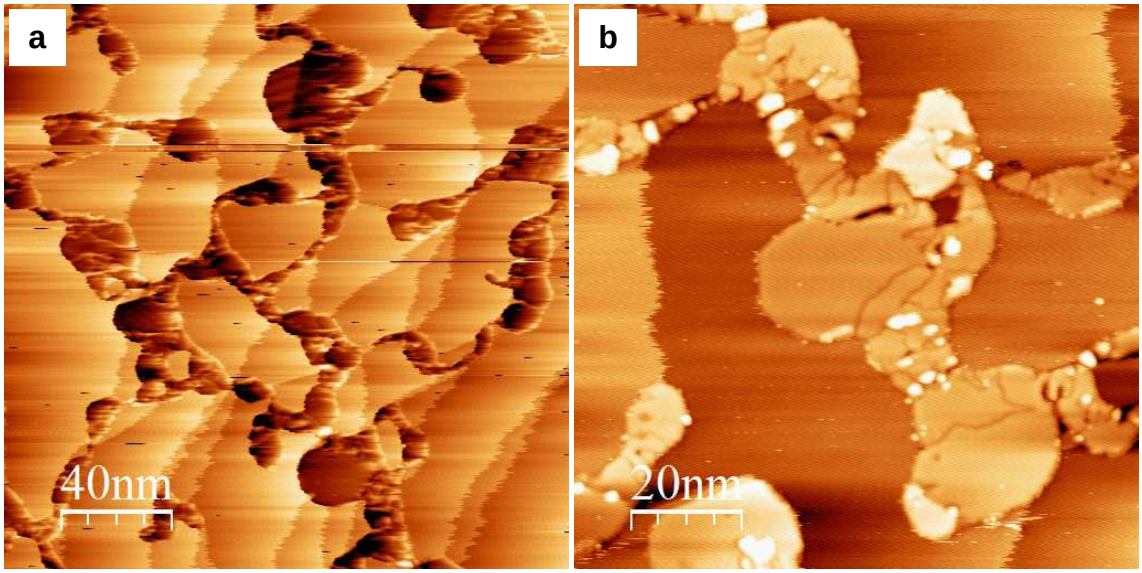

Figure 4-17. STM topographic images of initial growth formation of graphene overlayer on Cu(110) surface based on thermal decomposition of perylene at an estimated growth temperature of 800 K – 1000 K: (a) 2000 Å x 2000 Å measured at U = -1000 mV and I = 0.20 nA; (b) 1000 Å x 1000 Å measured at U = -1816 mV and I = 0.70 nA. The images are not calibrated to correct dimensions.

measured period and angular orientation of the large-scale stripe patterns with those of the models reveals the measured domain in Figure 4-19a corresponds to an epitaxial orientation in the range -30° to -28° and the measured domain on the upper portion of the image in Figure 4-19b corresponds to an epitaxial orientation in the range +27° to +28°. Figure 4-19c and Figure 4-19d show closer views into the Moiré patterns of the domains in Figure 4-19a and Figure 4-19b. The STM image of the domain in Figure 4-19c reveals a resolution of hexagonal arrangement which is visible as dark spots on some areas and bright spots on other areas of the same domain. The distance between spots appears in the length scale of the honeycomb structure of graphene. These observations provide strong support to the presumption of graphene formation. Figure 4-19d shows two different domains of different epitaxial orientations in the same image scan. The domain in the upper portion of the image reveals atomic resolution of the honeycomb structure whilst the other domain in the lower portion does not. Such observation perhaps suggests different STM tip conditions are required to achieve atomic resolution of the honeycomb structure for different epitaxial orientations; the reason could be differences in electronic states due to possible differences in substrate-overlayer interaction. On the

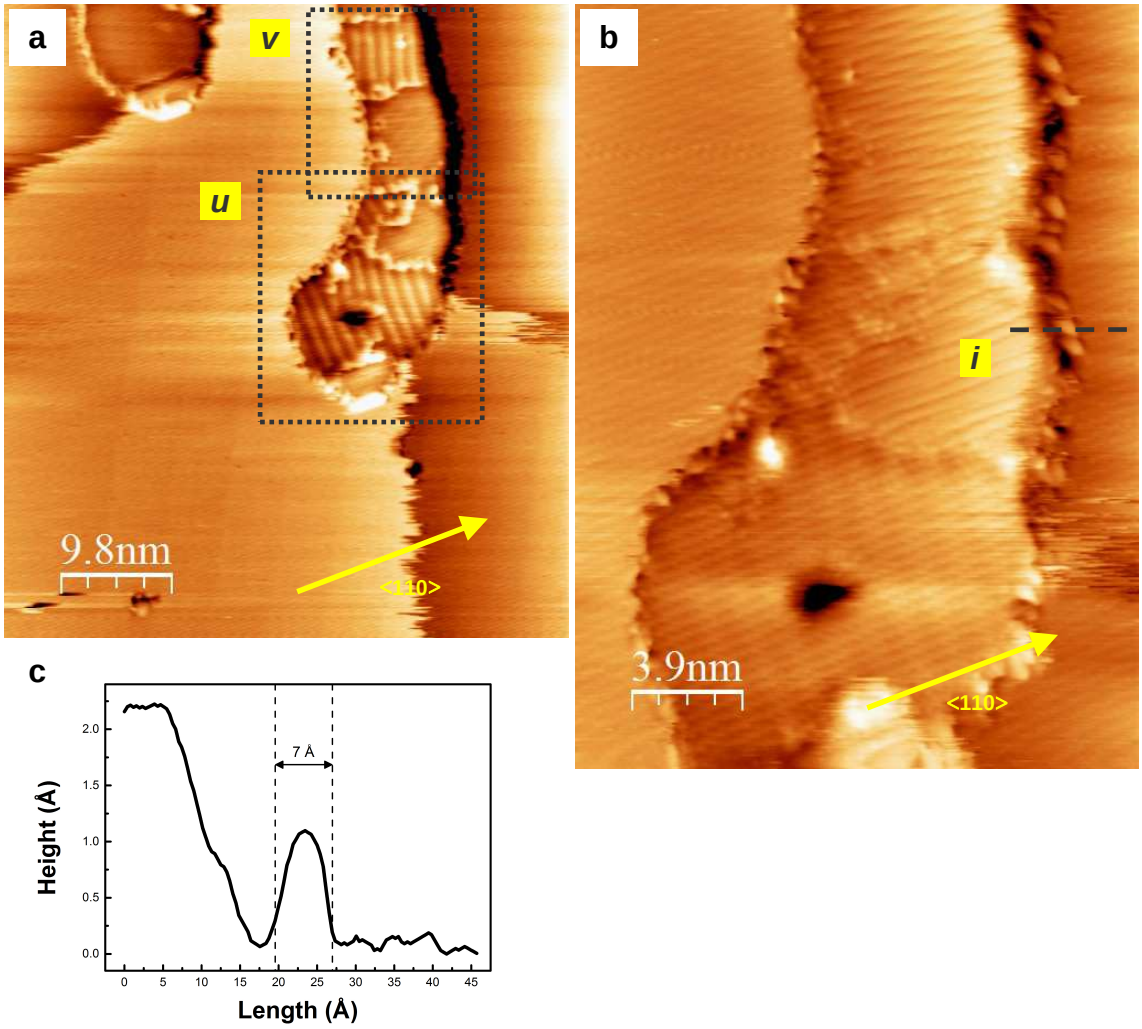

Figure 4-18. STM topographic images of initial growth formation of graphene overlayer on Cu(110) surface based on thermal decomposition of perylene at an estimated growth temperature of 800 K – 1000 K: (a) 490 Å x 550 Å measured at U = -1071 mV and I = 0.19 nA, corrected with calibration factors X = 0.98 and Y = 1.10 for 500 Å x 500 Å image scans; (b) 193 Å x 261 Å measured at U = -1071 mV and I = 0.19 nA, corrected with calibration factors X = 0.963 and Y = 1.305 for 200 Å x 200 Å image scans, the grey-colour dashed line corresponds to a measurement scan of height profile in (c) across one of the clusters gathered at the edges of the island.

other hand, the consistent observation of atomic resolution for the domains with estimated epitaxial orientations in the range $|\pm 27°|$ – $|\pm 30°|$ could also find explanation for the differences in resolution from possible enhancement to the corrugation of the honeycomb structure due to geometric effects of the natural atomic-scale corrugation of the substrate surface and electronic effects of interactions between graphene and the Cu(110) surface as graphene approaches the achiral epitaxial orientation at $|\pm 30°|$. Recall in Section 4.2 that the aromatic rings of graphene possess enhanced brightness atop Cu atoms on

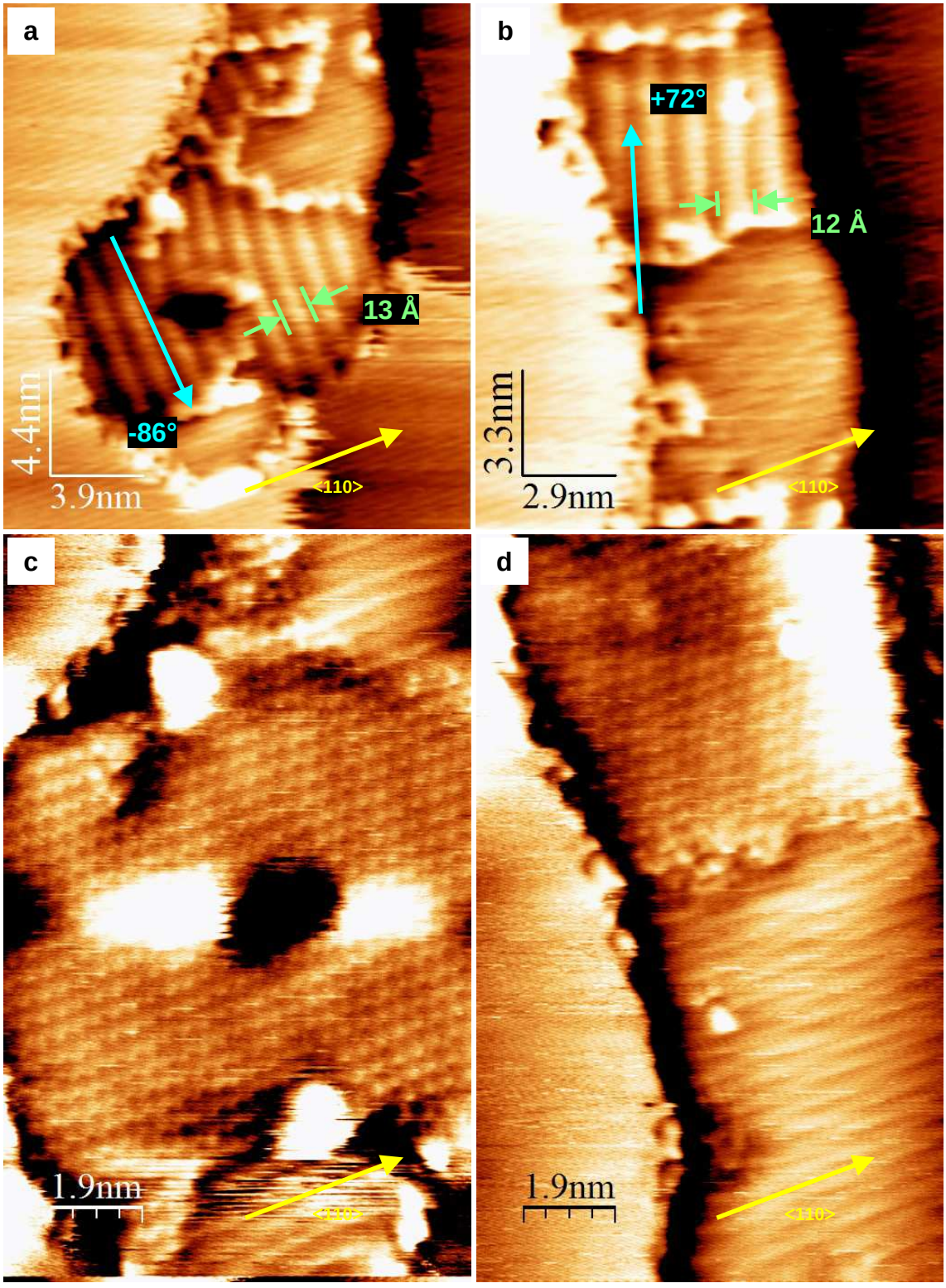

Figure 4-19. (a) 194 Å x 218 Å image enlargement of the region within the gray-colour dashed rectangle designated as *u* from the STM image in Figure 4-18a; (b) 146 Å x 164 Å image enlargement of the region within the gray-colour dashed rectangle designated as *v* from the STM image in Figure 4-18a; (c) – (d) 93 Å x 149 Å STM topographic images of the domains of interest in (a) – (b), measured at U = -1071 mV and I = 0.19 nA, corrected with calibration factors X = 0.934 and Y = 1.495 for 100 Å x 100 Å image scans.

the upper close-packed rows whereas enhanced darkness on the lower close-packed rows.

STM Height Measurements of Graphene Overlayer on the Cu(110) Surface

The large proportion of flat terraces from the Cu surface which surround the present overlayer allows proper thickness measurement of graphene on the Cu(110) surface from the STM images. The height profiles for the measurement scans along the gray-colour dashed lines *i*, *ii*, *iii*, and *iv* in Figure 4-20a and Figure 4-20b are shown together in Figure 4-20c. The STM images have been applied with a flattening process using the SPM-image analysis software WSxM before measurement of the height profiles to make sure areas of the same level are horizontal. The height profile for scan line *i* provides a measurement of 1.3 Å for the height of a monatomic step-edge on the Cu surface; moreover measurements of height for a monatomic step-edge on the Cu surface from various STM images range 1.3 Å – 1.5 Å. The distance of separation between (110) planes within the crystal structure of Cu is 1.276 Å and an experimental measurement of the height for a monatomic step-edge on Cu(110) surface has been reported as 1.3 Å in the literature[25]. Comparison with these values confirms a reasonable error and calibration in height measurement for the present STM instrument. The measured heights of graphene islands are found to be inconsistent to one another. Some graphene islands are found to be lower than 1 Å, some are a few tenths of an angstrom higher than 2 Å, and others are almost as high as a monatomic step edge on the Cu surface. The average height for a single layer of graphene on Ru(0001) has been reported about 1.8 Å based on STM measurements[11]. The actual height of a single layer of graphene on Cu(110) surface can be estimated as the sum of ½ the separation of 3.35 Å between basal planes in graphite and ½ the separation of 1.3 Å between terraces on Cu(110) surface, hence the value of 2.3 Å. Graphite has a low density of states at the Fermi level compared to metals and a large effective barrier to electron tunneling due to the limitation of tunneling to electron states whose momentum vectors are high and parallel to the surface plane[36]. Then STM measurement of height can be expected to be lower than the estimated value. These reasons and the comparison with the reported measurement on Ru(0001) find the present measurements within reasonable range and the heights correspond to no more than a single layer of graphene. One possible

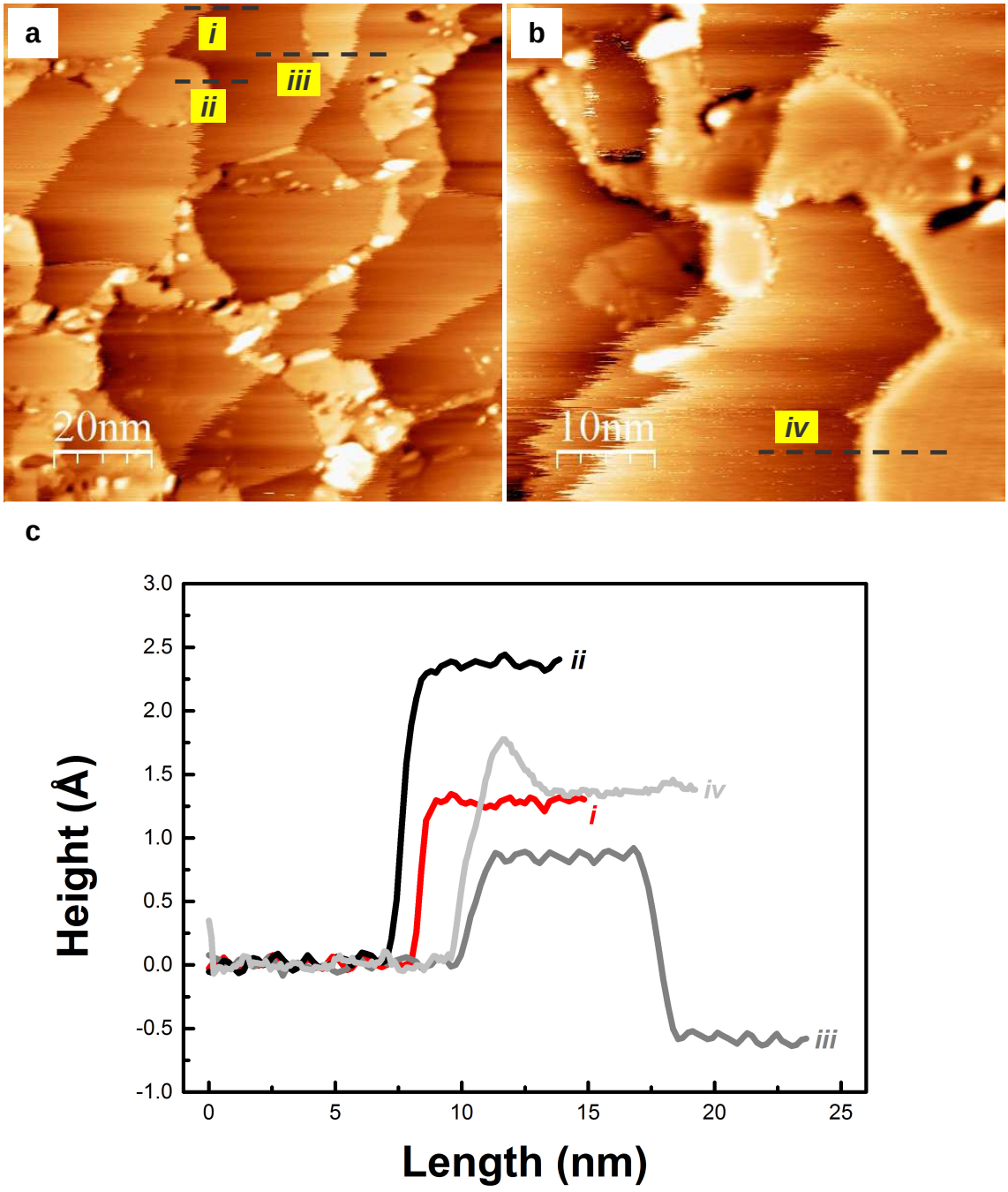

Figure 4-20. STM topographic images of initial growth formation of graphene overlayer on Cu(110) surface based on thermal decomposition of perylene at an estimated growth temperature of 800 K – 1000 K: (a) 1000 Å x 1000 Å measured at U = -1000 mV and I = 0.20 nA, not post-calibrated to correct dimensions; (b) 500 Å x 500 Å measured at U = -1816 mV and I = 0.40 nA, not post-calibrated to correct dimensions. The grey-colour dashed lines designated as *i*, *ii*, *iii*, *iv* correspond to measurement scans of height profiles in (c) in order to measure the height of graphene overlayer on Cu(110) surface. The height profiles are acquired from the STM images subsequent to application of an image-flattening technique to level the surface in the horizontal direction using the SPM image-analysis software WSxM.

reason for the variation of height measurements for a single layer of graphene is the location of the overlayer edge relative to a step edge on the surface. First, the overlayer edge could be attached to the lower side of the step edge as could be the case for scan line *iii*. Second, the overlayer edge could be coincident on the upper side of the step edge as could be the case for scan line *ii*. Third, the overlayer edge could be detached at a distance from the step edge as could be the case for scan line *iv*. Other possible reasons could be differences in STM-tip condition between instances of measurements and differences in chemical state for different domains in the graphene overlayer. The differences in chemical state could perhaps be possible when the strength of interaction through charge transfer between graphene and Cu(110) surface varies among different epitaxial orientations on Cu(110) surface, where the relative arrangement of atomic positions between graphene and Cu(110) surface are also different. Variation of the strength of interaction among epitaxial orientations could be evident from the statistical distribution of epitaxial orientation and the distribution of brightness in LEED pattern described in Sections 4.1 and 4.2. However, a presentation of evidence for the variation of height as a function of epitaxial orientation based on STM measurements could prove to be almost impossible because the effect of the STM-tip condition could not be separated for a common STM tip unless deliberate functionalization of the tip was made and the conditions were defined. Moreover the chance of finding appropriate domains in appropriate locations with enough resolution of superstructure pattern for determination of both epitaxial orientation and height from STM measurements is not high. Thus the present investigation could not provide a clear comment on the variation of height with epitaxial orientation so such phenomenon remains a conjecture.

The portion of the overlayer at the location of scan line *iii* on the STM image in Figure 4-20a traverses a step edge of the Cu surface. The presence of the step edge underneath the overlayer is apparent from the characteristic rough appearance due to the mobile behaviour of Cu atoms. Indeed, the height profile of scan line *iii* in Figure 4-20c shows a change in height equivalent to about a monatomic step on the Cu(110) surface. These observations show

graphene can be continuous over step edges on the Cu surface underneath even at the present stage of growth and despite the low growth temperature.

Discussion of Possible Mechanism of Graphene Formation at 800 K – 1000 K Growth Temperature

Separate carbon entities are presumed to form upon thermal decomposition of perylene. The nucleation of a graphene overlayer is assumed to proceed through a combination of separate carbon entities into graphene clusters and subsequent capture of other carbon entities into the existing graphene clusters. As shown in Section 4.2, the effective amount of carbon present for conversion into graphene is 56% of the entire carbon source, whilst the rest of the amount of carbon can be presumed to desorb as volatile hydrocarbon fragments because intact perylene molecules do not desorb from the monolayer[24,25]. In other words, about half of the number of carbon atoms in each molecule of perylene on average leads to graphene formation. Thus the carbon entities could be as large as the carbon skeleton of a naphthalene molecule. Note the carbon skeleton of perylene molecules can be considered to be a simple fragment of graphene. One report has described the growth of graphene on Ru(0001) surface as an addition not of carbon ad-atoms but of some cluster of a few carbon atoms[37]. Moreover, the absence of carbide formation is known for copper so carbon ad-atoms as the carbon entities could be unstable[38]. Measurements of Wöll *et. al.* has indicated thermal decomposition of perylene on Cu(110) surface at temperatures as low as 500 K [25]. Recent work has shown oligomeric formation of perylene on Cu(110) surface annealed up to 620 K [39]. Additional STM measurements of the thermal decomposition at 600 – 800 K are therefore desirable to provide more evidence of the form of the carbon entities.

The use of perylene compares to the common use of simple hydrocarbon precursors such as methane and ethane in the thermal-decomposition method of graphene preparation on Cu surfaces. The simple hydrocarbons precursors cannot be expected to decompose into carbon entities more complex than carbon dimers on surfaces[40,41]. The use of simple hydrocarbon precursors requires considerable periods of time and exposure has to be done at substantial pressures in order to obtain sufficient coverage of graphene overlayer on Cu surfaces[19,26,42]. On the other hand, perylene demonstrates high

effectiveness of conversion into graphene. One reason for the difference between simple hydrocarbons and perylene in the amount of effort required to form graphene could be related to desorption of these precursor molecules before thermal decomposition occurs. Another reason could be related to desorption of carbon entities deposited on Cu surface from these precursor molecules. Large-size carbon entities are expected to reduce chances of desorption at growth temperatures. Then perhaps the possible decomposition of perylene into large-sized carbon entities could be supported from the high effectiveness of conversion into graphene.

The presence of domains in the present graphene overlayer is a natural consequence of possible variation in epitaxial orientation upon nucleation. Therefore domains are manifestations of separate nucleations. The presence of a large number of domains in small sizes suggests a high rate of nucleation for the preparation conditions of the present graphene overlayer. Moreover, the clusters gathered at the edges of the graphene overlayer are perhaps an outcome of stable nucleation of graphene. Indeed, the measurement of height in Figure 4-18c for one of the clusters corresponds to the height measurements for the graphene overlayer. The possible factors considered to exert important influence on the rate of nucleation include small critical island size, high concentration of the reactant carbon entities on the surface, presence of step edges on the substrate surface, and low thermal activation at the growth temperature.

A small critical island size reduces the required minimum for the number of collisions with carbon entities hence short periods of time in order to reach a stable nucleation. The critical island size must be small, a few aromatic nuclei, as the electron delocalization provides additional stabilization to a hexagonal network of strong sp^2 carbon-carbon bonds. Indeed, the clusters gathered at the edges of the graphene overlayer can be as small as 0.5 nm. Then the critical island size for graphene on Cu(110) surface should be not more than a cluster equivalent to the carbon skeleton of pyrene composed of 4 aromatic rings or 16 carbon atoms. However, the critical island size is expected to be not less than six carbon atoms otherwise an aromatic unit of the honeycomb structure in

graphene cannot stand. Suppose the possible formation of carbon entities as large as the carbon skeleton of naphthalene is a stable nucleation of graphene on its own, then subsequent combination and capture of these could be considered more appropriate as a process of dynamic coalescence rather than nucleation.

A high concentration of carbon entities on the surface reduces the mean free path between collisions. Hence the distances between nucleation sites are short. The initial concentration of carbon entities in the present method of graphene preparation must be high as the effective amount of carbon equivalent to about a quarter of a monolayer of graphene is pre-adsorbed on the surface before graphene formation. Suppose the carbon entities could be as large as the carbon skeleton of naphthalene, then the concentration can be derived to be at least 0.9 nm^{-2}; however, the concentration cannot be more than 9.5 C-atoms per nm^{-2} based on calculation of the carbon-atom concentration in graphene from the basal-plane structure of graphite.

Step edges on the surface in general act as sites for heterogeneous nucleation. The presence of some considerable amount thereof on the present substrate surface should effect an increase in the events of stable nucleation. Note the frequent association of the overlayer to step edges on the Cu surface as pointed out earlier.

Low thermal activation towards diffusion of carbon entities reduces displacement on the surface before an event of collision occurs so nucleation would tend to dominate over incorporation of the carbon entities into the existent cluster formations. Moreover, low thermal activation towards detachment of carbon entities from the existing cluster formations reduces the effort of development into stable nucleation. Perhaps the amount of thermal activation at the present growth temperature is low compared to both the diffusion barrier for the carbon entities on the surface and the strength of sp^2 carbon-carbon bonds in the cluster formation. A high diffusion barrier could be possible when the carbon entities could be as large as the carbon skeleton of naphthalene. A strong sp^2 carbon-carbon bond can be expected as graphene is

one of the most stable allotropes of pure carbon and is a material known for stable character and remarkable strength.

The interconnected network formation of the graphene overlayer from numerous domains and appearance of clusters gathered at the edges suggests the evolution of graphene formation had reached the stage of coalescence and percolation. At first, the domains must be somehow separate from one another as islands at an earlier stage prior to the formation of the present overlayer because the initial distribution of perylene on the surface is even and uniform. Later on, the domains must reach a point of contact and then connect all together into a continuous overlayer. The continuous connection of domains in the overlayer can be viewed as an effort to reduce the cost of energy associated with island edges; perhaps some bonds could form despite atomic mismatch between epitaxial orientations at the interface of adjacent domains. The nature of coalescence and percolation must be ‘dynamic’ i.e. the supposed separate islands at an earlier stage must diffuse over the surface, as the spatial distribution of the domains on the surface is uneven and the sizes of the domains are too small to reach one another without movement for an even distribution. Note the present concept of percolation is not in accordance with the usual sense because the common definition refers to the eventual interconnection of static islands at high coverages as the growth process approaches complete monolayer coverage, whereas the coverage of the present overlayer is much lower; moreover, the description of ‘dynamic’ for the term then becomes inconsistent in the strict sense of static islands.

The network formation of the present overlayer somehow resembles the shape of a dendrite and therefore must be unfavourable due to the presence of an enormous amount of edges. The common mechanism to reduce the edges of a dendrite and transform into compact islands is diffusion of atoms at the edges. The persistence of the shape however suggests the thermal activation at the present growth temperature is too weak to break the carbon-carbon bonds even at the edges for such diffusion to occur.

Discussion of Possible Mechanism of Graphene Formation at 1000 K – 1250 K Growth Temperature

The graphene overlayers considered in Section 4.2 correspond to growth temperatures estimated to be higher than 1000 K. The close agreement between the statistical distribution of epitaxial orientation in Figure 4-15 and the LEED pattern in Figure 4-1 for the graphene overlayer prepared at 1250 K supports the temperature estimation as reasonable. The STM images in Figure 4-5 and Figure 4-6 shows the formation of graphene as compact islands separated from one another upon increase in growth temperature, in contrast to the percolated network formation at low growth temperature. Moreover, a considerable increase in size of domains together with an equivalent decrease in number is apparent. The differences in graphene formation between low and high growth temperatures point to morphological evolution of the overlayer with increased thermal activation, in agreement with the changes in the sharpness of the LEED pattern as described for Figure 4-16. The morphological evolution is favourable from the perspective of a reduction in the amount of defects from edges and domain boundaries.

Possible mechanisms for the morphological evolution are considered. Dissolution of carbon into the substrate and subsequent segregation of a graphene overlayer onto the surface is ruled out as a mechanism of reformation for the meantime, because carbon is known to be insoluble in copper[38]. Then the percolated network formation of a graphene overlayer at low growth temperature must break up into separate portions on the surface and reform into compact islands with increase in domain size as the temperature ramps upwards. The common mechanism to a transition in shape from dendritic to compact is the diffusion of atoms down the edges to find a more favourable site. However, the mechanism in known to occur in cases where the atomic scale dimension of the branches of a dendrite make the edges unstable whereas the network formation of the graphene overlayer at low growth temperature possesses smooth round edges. The mechanism of edge-diffusion alone nonetheless cannot be expected to cause considerable change in size and number of the domains so another process of dominant influence must be at

work. The increase in size of domains must be at the expense of a reduction in the number of domains. The mechanism of coalescence does not seem reasonable as domain boundaries form upon contact between separate domains at random epitaxial orientations, unless some other processes in addition merge the domains together into one; the number of domains could be expected to remain almost the same for such a mechanism. Then the plausible mechanism could be perhaps some process comparable to Ostwald ripening – i.e. the growth of domains on the portions of the overlayer with large dimensions due to a net diffusion flux of carbon entities detached from portions of the overlayer with small dimensions. The chemical potential has an inverse relation to the dimensions of an overlayer formation in accordance with the Gibbs-Thompson relation; high chemical potential relates to a high outward pressure of atoms towards detachment. Notice the percolated network formation of the overlayer at low growth temperature possesses small dimensions in particular at the interconnections. Then perhaps there exists a high outward pressure of atoms at these locations compared to the other portions of the network formation. Increased thermal activation at high temperatures could raise the outward pressure to considerable levels and cause the morphological evolution of the overlayer to proceed.

4.4 Conclusion to Structural Characterization of Graphene on Cu(110) Surface Based on Thermal Decomposition of Perylene

Synthesis of graphene on the Cu(110) surface can be achieved through thermal decomposition of a saturated monolayer of perylene at high temperatures up to 1250 K under UHV conditions. The formation of graphene is confirmed from LEED measurement. The distribution of epitaxial orientation in the LEED pattern exhibits particular preference for the most stable epitaxial orientations at ±5° and rotational disorder for the less stable epitaxial orientations around ±30°; the epitaxial orientation can be specified in terms of the $\langle 1,1,\bar{2},0 \rangle$ direction of graphene with respect to the $\langle 1,1,0 \rangle$ direction on the surface of (110)-oriented single-crystal Cu substrate. Correlation with the extent of match in position of real-space lattice points between graphene and Cu(110) surface provides simple explanation to the distribution of epitaxial orientation.

STM topographic measurements provide images of the formation of graphene. The effectiveness of conversion of the carbon content from the stage of pre-adsorption of a saturated monolayer of (5x5)-superstructure perylene exceeds 50% based on calculation from the surface-area coverage of graphene islands. The features of the islands demonstrate resemblance to those in reports of graphene on other well-defined metal surfaces. The actual superstructures are described in the first approximation as Moiré patterns from direct superimposition of the component structures in two dimensions at particular epitaxial orientations. Comparison between the actual superstructures and the approximations in terms of the nano-scale periodic modulations of bright and dark stripes in the Moiré patterns allows estimation of epitaxial orientation. The statistical distribution of epitaxial orientation agrees with the LEED pattern. The region of the rotational disorder manifests a stable epitaxial orientation somewhere between $\left|\pm 25^\circ\right|$ and $\left|\pm 30^\circ\right|$, second to the most stable one at $\left|\pm 5^\circ\right|$.

Graphene overlayer on the Cu(110) surface prepared based on thermal decomposition of perylene demonstrates different morphologies as the growth

temperature ramps to high temperatures from LEED and STM measurements. Increase in domain size and development of preference in epitaxial orientation has been observed. The epitaxial orientation is predisposed to almost complete randomness towards low growth temperatures.

The graphene overlayer heated up to a growth temperature lower than 1000 K forms an enormous number of minute domains connected together in a network formation with clusters gathered at the edges. The formation has been considered as an outcome of dynamic coalescence and percolation, subsequent to a large amount of nucleation under the possible factors of small critical island size, high concentration of reactant carbon species, complex structure for the reactant carbon species, low thermal activation, and the presence of step edges on the surface. The presence of a large amount of edges in view of the network formation has been considered as a manifestation of kinetic suppression due to the well-known strength of carbon-carbon bonds in graphene and low thermal activation at low growth temperature. Moiré superstructures have been observed even for the stage of growth at low temperature and determination of the epitaxial orientation has been possible from the large-scale stripe patterns. Variation in the extent of image resolution has been observed for different epitaxial orientations; pronounced resolution of the honeycomb structure has been observed for epitaxial orientations close to ±30°. The measured height of the overlayer has been found to be inconsistent but nonetheless remains no more than equivalent to a single layer. The overlayer has been found to be continuous over step edges on the Cu surface underneath even for the stage of growth at low temperature.

The graphene overlayer heated to a growth temperature above 1000 K has been observed as a few number of compact islands with sizeable domains. Persistence of randomness in epitaxial orientation despite high growth temperature has been associated with a substantial amount of carbon accessible for graphene formation. The morphological differences between the growth temperatures has been considered as an outcome of evolution based on a mechanism in the principle of Gibbs-Thompson relation – a net flow of carbon between separate islands or portions of the overlayer with different dimensions.

The outcome of the measurements is a proof of possible opportunities. Prospects for further work on graphene on Cu(110) surface can include Raman spectroscopic measurements for chemical identification of graphene existence, theoretical studies of the energetics of epitaxial orientation, and further investigations on the morphological evolution in more detail. Other prospects for possible topics of future investigation on the formation of graphene on Cu(110) based on thermal decomposition include the quantitative determination of fundamental factors in the process of nucleation and growth, and the effects of variations in the process variables – in particular, the structure of the carbon skeleton in the hydrocarbon precursor, the pre-adsorption in comparison to the real-time deposition of hydrocarbon precursors, the effective amount of pre-adsorbed carbon before growth temperature ramp, the growth temperature, and the graphene coverage. Perhaps on one extreme end in the spectrum of control for graphene growth, one can envision a graphene overlayer whose domains are so small to be considered almost amorphous. A matter of possible interest in the aspect of chemical modification is the introduction of some hetero-aromatic groups into the hydrocarbon precursor to attempt insertion of some dopants into the graphene overlayer.

References

1. May, J. W. Platinum surface LEED rings. *Surf. Sci.* **17,** 267–270 (1969).

2. Shelton, J. C., Patil, H. R. & Blakely, J. M. Equilibrium segregation of carbon to a nickel (111) surface: a surface phase transition. *Surf. Sci.* **43,** 493–520 (1974).

3. Lang, B. A LEED study of the deposition of carbon on platinum crystal surfaces. *Surf. Sci.* **53,** 317–329 (1975).

4. Nieuwenhuys, B., Hagen, D., Rovida, G. & Somorjai, G. LEED, AES and thermal desorption studies of chemisorbed hydrogen and hydrocarbons (C_2H_2, C_2H_4, C_6H_6, C_6H_{12}) on the (111) and stepped [6(111) × (100)] iridium crystal surfaces; comparison with platinum. *Surf. Sci.* **59,** 155–176 (1976).

5. Castner, D., Sexton, B. & Somorjai, G. LEED and thermal desorption studies of small molecules (H_2, O_2, CO, CO_2, NO, C_2H_4, C_2H_2 and C) chemisorbed on the rhodium (111) and (100) surfaces. *Surf. Sci.* **71,** 519–540 (1978).

6. Hamilton, J. C. Carbon layer formation on the Pt (111) surface as a function of temperature. *J. Vac. Sci. Technol.* **15,** 559 (1978).

7. Eizenberg, M. & Blakely, J. M. Carbon monolayer phase condensation on Ni(111). *Surf. Sci.* **82,** 228–236 (1979).

8. Zi-Pu, H., Ogletree, D. F., Van Hove, M. A. & Somorjai, G. A. LEED theory for incommensurate overlayers: application to graphite on Pt(111). *Surf. Sci.* **180,** 433–459 (1987).

9. Wu, M.-C., Xu, Q. & Goodman, D. W. Investigations of graphitic overlayers formed from methane decomposition on Ru(0001) and Ru(11-20) catalysts with scanning tunneling microscopy and high-resolution electron energy loss spectroscopy. *J. Phys. Chem.* **98,** 5104–5110 (1994).

10. Ueta, H. *et al.* Highly oriented monolayer graphite formation on Pt(111) by a supersonic methane beam. *Surf. Sci.* **560,** 183–190 (2004).

11. Marchini, S., Günther, S. & Wintterlin, J. Scanning tunneling microscopy of graphene on Ru(0001). *Phys. Rev. B* **76,** 075429 (2007).

12. Martoccia, D. *et al.* Graphene on Ru(0001): a 25×25 supercell. *Phys. Rev. Lett.* **101,** 126102 (2008).

13. N'Diaye, A. T., Coraux, J., Plasa, T. N., Busse, C. & Michely, T. Structure of epitaxial graphene on Ir(111). *New J. Phys.* **10,** 043033 (2008).

14. Usachov, D. *et al.* Experimental and theoretical study of the morphology of commensurate and incommensurate graphene layers on Ni single-crystal surfaces. *Phys. Rev. B* **78,** 085403 (2008).

15. Usachov, D. Y. *et al.* Graphene morphology on Ni single-crystal surfaces: experimental and theoretical investigation. *Bull. Russ. Acad. Sci. Phys.* **73,** 679–682 (2009).

16. Fedorov, A. V. *et al.* Structure of graphene on the Ni(110) surface. *Phys. Solid State* **53,** 1952–1956 (2011).

17. Meng, L. *et al.* Multi-oriented Moiré superstructures of graphene on Ir(111): experimental observations and theoretical models. *J. Phys. Condens. Matter* **24,** 314214 (2012).

18. Vinogradov, N. A. *et al.* Formation and structure of graphene waves on Fe(110). *Phys. Rev. Lett.* **109,** 026101 (2012).

19. Wilson, N. R. *et al.* Weak mismatch epitaxy and structural feedback in graphene growth on copper foil. *Nano Res.* **6,** 99–112 (2013).

20. Lyon, H. B. Low-energy electron-diffraction study of the clean (100), (111), and (110) faces of platinum. *J. Chem. Phys.* **46,** 2539 (1967).

21. Morgan, A. E. & Somorjai, G. A. Low energy electron diffraction studies of gas adsorption on the platinum (100) single crystal surface. *Surf. Sci.* **12,** 405–425 (1968).

22. Oura, K., Katayama, M., Zotov, A. V., Lifshits, V. G. & Saranin, A. A. *Surf. Sci. An Introd.* 3–18 (Springer Berlin Heidelberg, 2003).

23. Oura, K., Katayama, M., Zotov, A. V., Lifshits, V. G. & Saranin, A. A. *Surf. Sci. An Introd.* 357–387 (Springer Berlin Heidelberg, 2003).

24. Hänel, K. *et al.* Organic molecular-beam deposition of perylene on Cu(110): results from near-edge x-ray absorption spectroscopy, x-ray photoelectron spectroscopy, and atomic force microscopy. *J. Mater. Res.* **19,** 2049–2056 (2004).

25. Söhnchen, S., Hänel, K., Birkner, A., Witte, G. & Wöll, C. Molecular beam deposition of perylene on copper: formation of ordered phases. *Chem. Mater.* **17,** 5297–5304 (2005).

26. Gao, L., Guest, J. R. & Guisinger, N. P. Epitaxial graphene on Cu(111). *Nano Lett.* **10,** 3512–6 (2010).

27. Wofford, J. M., Nie, S., McCarty, K. F., Bartelt, N. C. & Dubon, O. D. Graphene islands on Cu foils: the interplay between shape, orientation, and defects. *Nano Lett.* **10,** 4890–6 (2010).

28. Rasool, H. I. *et al.* Atomic-scale characterization of graphene grown on copper (100) single crystals. *J. Am. Chem. Soc.* **133,** 12536–43 (2011).

29. Sutter, P. W., Flege, J.-I. & Sutter, E. A. Epitaxial graphene on ruthenium. *Nat. Mater.* **7,** 406–11 (2008).

30. Günther, S. *et al.* Single terrace growth of graphene on a metal surface. *Nano Lett.* **11,** 1895–900 (2011).

31. Batzill, M. The surface science of graphene: metal interfaces, CVD synthesis, nanoribbons, chemical modifications, and defects. *Surf. Sci. Rep.* **67,** 83–115 (2012).

32. Wintterlin, J. & Bocquet, M.-L. Graphene on metal surfaces. *Surf. Sci.* **603,** 1841–1852 (2009).

33. Vázquez de Parga, A. *et al.* Periodically rippled graphene: growth and spatially resolved electronic structure. *Phys. Rev. Lett.* **100,** 056807 (2008).

34. Wang, B., Bocquet, M.-L., Marchini, S., Günther, S. & Wintterlin, J. Chemical origin of a graphene Moiré overlayer on Ru(0001). *Phys. Chem. Chem. Phys.* **10,** 3530 (2008).

35. Land, T. A., Michely, T., Behm, R. J., Hemminger, J. C. & Comsa, G. STM investigation of single layer graphite structures produced on Pt(111) by hydrocarbon decomposition. *Surf. Sci.* **264,** 261–270 (1992).

36. Tersoff, J. Anomalous corrugations in scanning tunneling microscopy: imaging of individual states. *Phys. Rev. Lett.* **57,** 440–443 (1986).

37. Loginova, E., Bartelt, N. C., Feibelman, P. J. & McCarty, K. F. Evidence for graphene growth by C cluster attachment. *New J. Phys.* **10,** 093026 (2008).

38. Predel, B. *Phase Equilibria, Crystallogr. Thermodyn. Data Bin. Alloy. B-Ba – C-Zr* (Madelung, O.) **5b,** (Springer-Verlag, 1992).

39. Haq, S. *et al.* Versatile bottom-up construction of diverse macromolecules on a surface observed by scanning tunneling microscopy. *ACS Nano* **8,** 8856–70 (2014).

40. Riikonen, S., Krasheninnikov, A. V., Halonen, L. & Nieminen, R. M. The role of stable and mobile carbon adspecies in copper-promoted graphene growth. *J. Phys. Chem. C* **116,** 5802–5809 (2012).

41. Seah, C.-M., Chai, S.-P. & Mohamed, A. R. Mechanisms of graphene growth by chemical vapour deposition on transition metals. *Carbon N. Y.* **70,** 1–21 (2014).

42. Li, X. *et al.* Large-area synthesis of high-quality and uniform graphene films on copper foils. *Science* **324,** 1312–4 (2009).

Chapter 5
Self-Assembled Co-TPP Superstructure on Sub-monolayer Graphene on Cu(110) Surface

This chapter introduces facts about the chemical structure and molecular structure of Co-TPP. The next section presents the outcome of STM measurements of a Co-TPP overlayer on sub-monolayer graphene on Cu(110) surface. The sub-monolayer graphene is prepared based on the method of thermal decomposition of perylene as described in Chapter 4. The present studies describe the growth of the Co-TPP overlayer, the self-assembled Co-TPP structure on top of graphene islands, and the self-healing character of the self-assembled Co-TPP superstructure.

5.1 Related Facts about Co-TPP

The chemical structure of cobalt-tetraphenylporphyrin (Co-TPP) is shown in Figure 5-1. Porphyrins are defined in general as hetero-aromatic organic compounds composed of four pyrrole subunits interconnected together into a large flat macrocycle and are modified through attachment of some chemical functions to certain carbon atoms at the edges and coordination of a metal atom at the core. The hetero-aromatic porphine skeleton is flexible but stable and inert to most chemical reactions. The delocalized nature of valence electrons in the conjugated π-orbitals makes porphyrins an organic semiconductor material[1]. The two locations for possible modification of the compound are the key features to allow wide variation in functional properties. The coordinated metal at the centre assumes the role of an active site and can interact with the surface of a substrate support and bind some additional axial ligands. Substituents at the edges of the porphine base possess rotational degrees of freedom. Proper choice of these substituents together with the flexible porphine base allows for conformational adaptation of the molecule to the local environment. For Co-TPP, the substituents are four phenyl moieties attached to carbon atoms at

symmetrical points on the edges of the porphine macrocycle and the guest atom at the centre of the porphine macrocycle is cobalt.

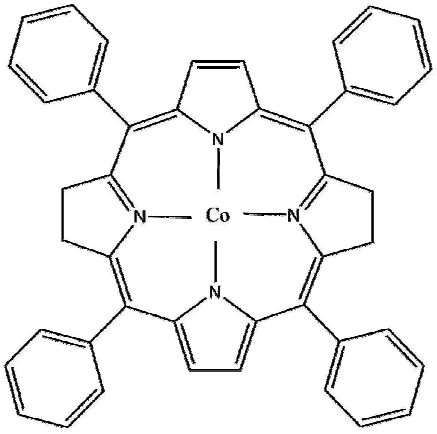

Figure 5-1. Chemical structure of 5,10,15,20-tetraphehyl-21H,23H-porphine cobalt(II) – also known as cobalt-tetraphenylporphyrin (Co-TPP).

5.2 STM Characterization of Co-TPP on Sub-monolayer Graphene on the Cu(110) Surface

Growth of Co-TPP Overlayer

STM measurements were performed at intervals between periods of Co-TPP deposition on sub-monolayer graphene on the Cu(110) surface. Figure 5-2 shows Co-TPP molecules accumulate on the bare Cu surface around graphene islands in the initial period of deposition. The distribution of molecules is almost uniform on the bare Cu surface as can be seen from the overview in Figure 5-2a. In contrast, no adsorption is imaged on top of graphene islands as can be seen from the close-up view in Figure 5-2b. Molecules on top of graphene islands could be too mobile or unstable under the STM tip. Indeed, observation of somewhat enhanced accumulations around edges of graphene-islands could be due to molecules adsorbed on top of graphene islands which moved from there later on. The STM images in Figure 5-2c and Figure 5-2d are obtained in succession at the same location on the Cu surface near an edge of the graphene island; mobile behaviour of Co-TPP molecules on the Cu surface is evident from changes in the distribution of the adsorbed molecules. Graphene is inert to some extent – a reason to expect pronounced mobile or unstable behaviour from molecules on top of graphene islands.

Subsequent STM measurements show molecules continue to accumulate on the Cu surface around graphene islands with increased exposure. The overview in Figure 5-3a and the close-up view in Figure 5-3b show molecules almost saturate the entire Cu surface whilst the top of graphene islands remains free of molecules. Further deposition leads to formation of self-assembled superstructure of Co-TPP molecules on top of some graphene islands but almost no obvious addition to the accumulation on the Cu surface as shown from the overview in Figure 5-3c and the close-up view in Figure 5-3d. Past report of experiment in adsorption of Co-TPP on Cu(110) surface mentioned several distinct superstructures can form[2]. Here the Co-TPP molecules on the Cu(110) surface can be seen to form aggregates of

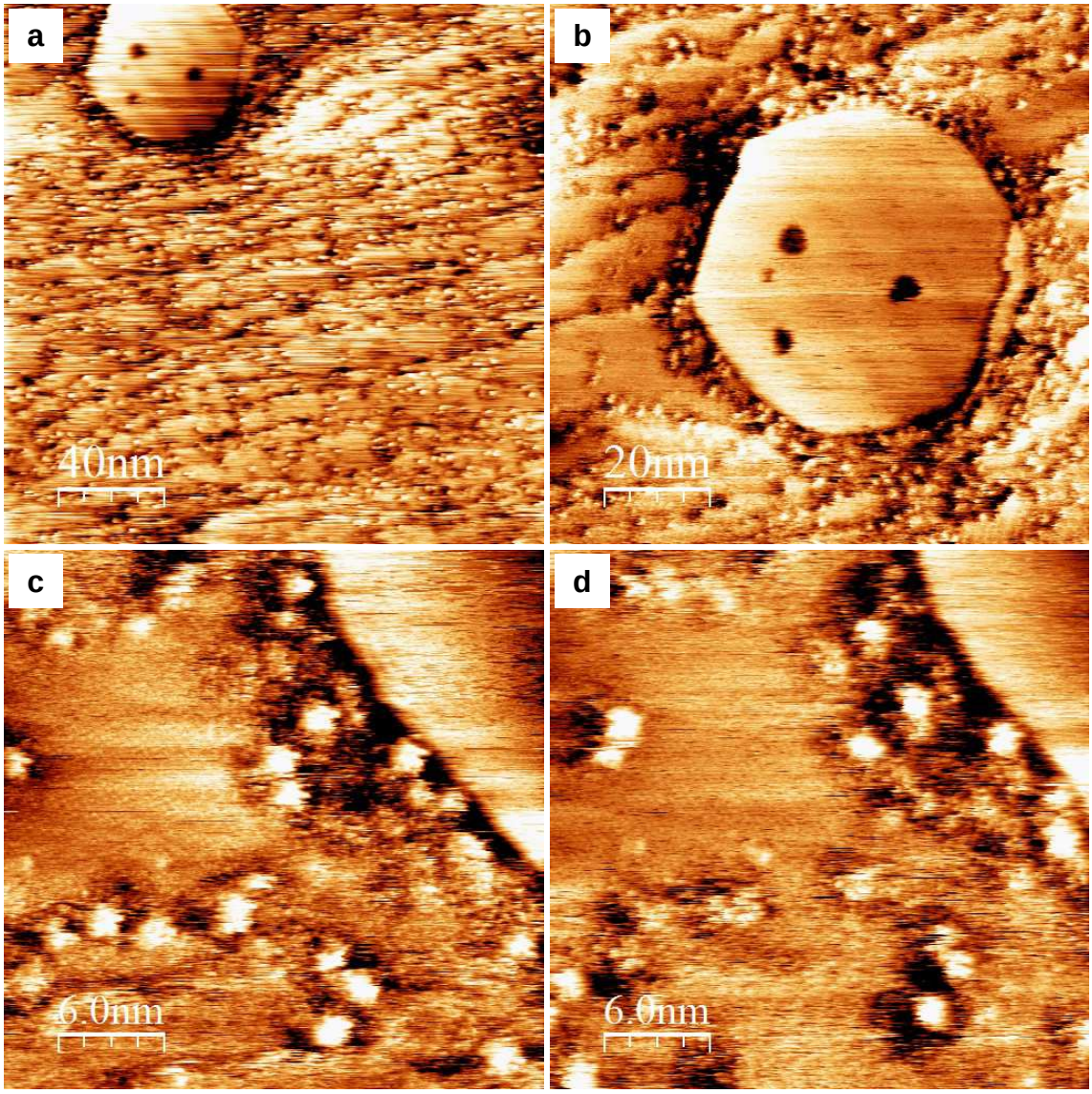

Figure 5-2. STM topographic images of Co-TPP molecules on sub-monolayer graphene on Cu(110) surface at initial period of deposition: (a) 2000 Å x 2000 Å image to show overview of accumulation of Co-TPP molecules on Cu(110) surface around graphene islands; (b) 1000 Å x 1000 Å image to show close-up view of emptiness on top of graphene islands; (c), (d) 300 Å x 300 Å images in succession at same location, around an edge of the graphene island at the upper right corner of the image, to show mobile behaviour of Co-TPP molecules on Cu(110) surface from the variation in distribution of molecules. STM measurements were performed at U = +1000 mV and I = 0.20 nA.

some superstructures. However, details of these superstructures on the bare areas of the Cu(110) surface are not the focus of the present studies.

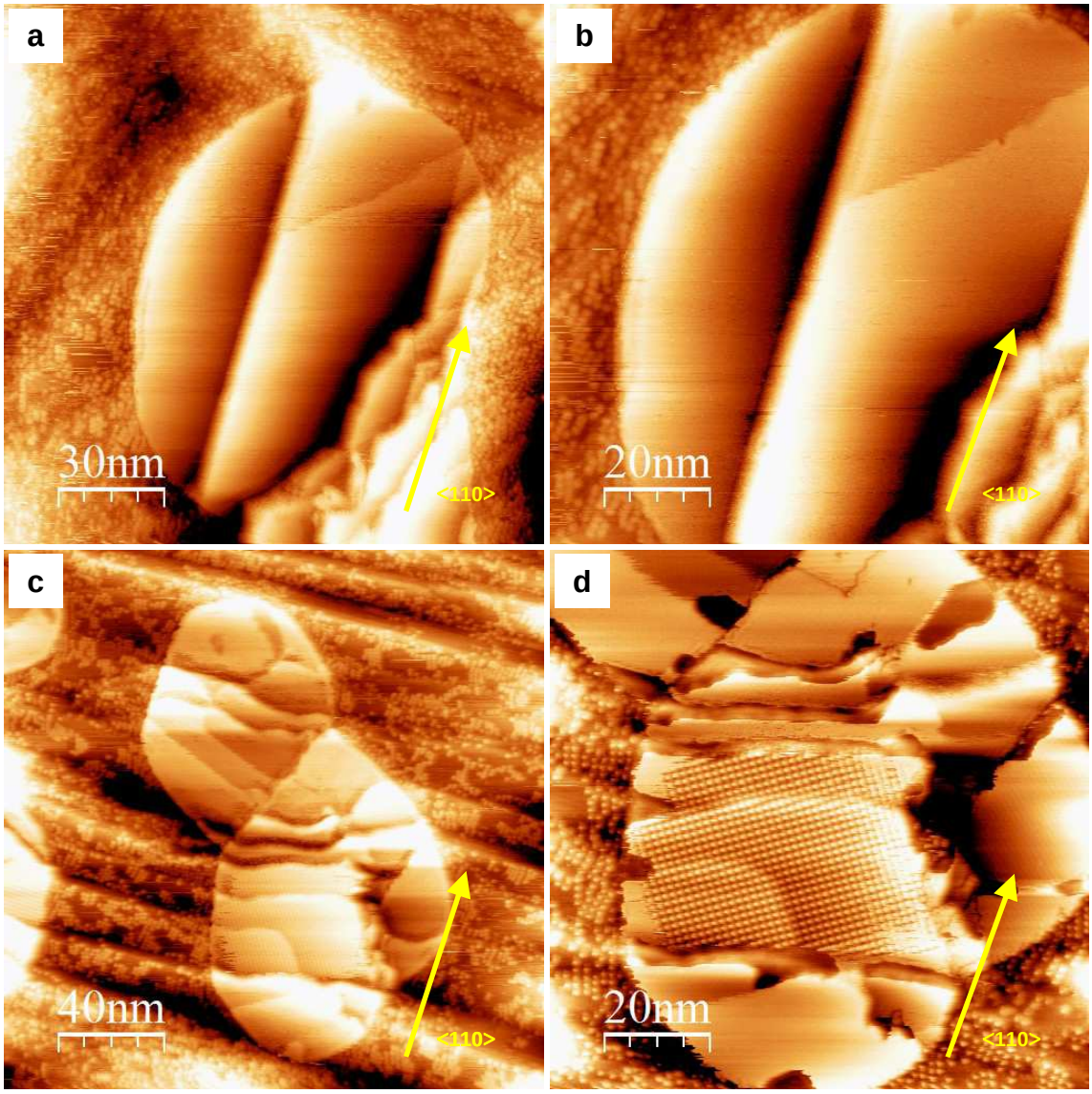

Figure 5-3. STM topographic images of Co-TPP molecules on sub-monolayer graphene on Cu(110) surface after continued periods of deposition: (a) overview in 1500 Å x 1500 Å image, (b) close-up view in 1000 Å x 1000 Å image to show almost saturation of Co-TPP molecules on Cu(110) surface around graphene islands whilst emptiness remains on top of graphene islands; (c) overview in 2000 Å x 2000 Å image, (d) close-up view in 1000 Å x 1000 Å image to show formation of self-assembled superstructure of Co-TPP molecules on top of some graphene islands but almost no obvious addition to the accumulation on the Cu surface after further deposition. STM measurements were performed at U = +1816 mV and I = 0.20 nA except for the image in (d) at U = +874 mV and I = 0.40 nA.

Self-Assembled Co-TPP Superstructure on Graphene Islands

STM measurements of self-assembled superstructure of Co-TPP molecules on graphene were focused on two separate islands. The first set of measurements were made on the island in Figure 5-4a. Close-up view of the Co-TPP superstructure is shown in Figure 5-4b. The superstructure is described in a rectangular unit cell, where $\mathbf{a_1}$ measures a distance of 15.5 ± 1.5 Å at +30° from the <110> direction of the Cu(110) surface and $\mathbf{b_1}$ measures a distance 13.5 ± 1.3 Å at -60° from the <110> direction. The unit cell occupies a mean area of 209 $Å^2$ (171 $Å^2$ – 252 $Å^2$). For comparison, the Co-TPP superstructure on Ag(111) surface has been described as incommensurate in a square unit cell of 14.0 Å in dimensions and 196 $Å^2$ in area[3]. On a more-reactive Cu(110) surface, a prominent Co-TPP superstructure has been described as commensurate in an oblique unit cell of parameters 15.3 Å, 16.9 Å in dimensions, 45° in included angle, and 184 $Å^2$ in area[2]. Note each of the unit cells accommodates one Co-TPP molecule so the dimensions of the unit cells correspond to the intermolecular distances. Comparison reveals the intermolecular distances on graphene and Ag(110) are somewhat short compared to those on Cu(110) surface but the Co-TPP superstructure is most dense-packed on Cu(110) surface and least dense-packed on graphene. Perhaps the reason for these observations could be related to the molecule-substrate interaction as Cu(110) surface is the most reactive whilst graphene is the most stable and almost inert.

The STM measurements alone are not adequate to make the facts on the molecular orientation and the 3D molecular conformation clear despite the resolution of sub-molecular features. On Ag(111) surface, the porphine macrocycle has been reported to possess a saddle-shape conformation[3]. On Cu(110) surface, the porphine macrocycle has been reported almost planar whilst the phenyl substituents stand upright on the surface to allow π-interaction between adjacent Co-TPP molecules[2]. The conformation on graphene can be different from those on metal surfaces as the set of interactions in the complex system of Co-TPP on graphene on Cu(110) surface can be distinct from those on metal surfaces. Unlike metal surfaces, graphene can interact with porphyrins

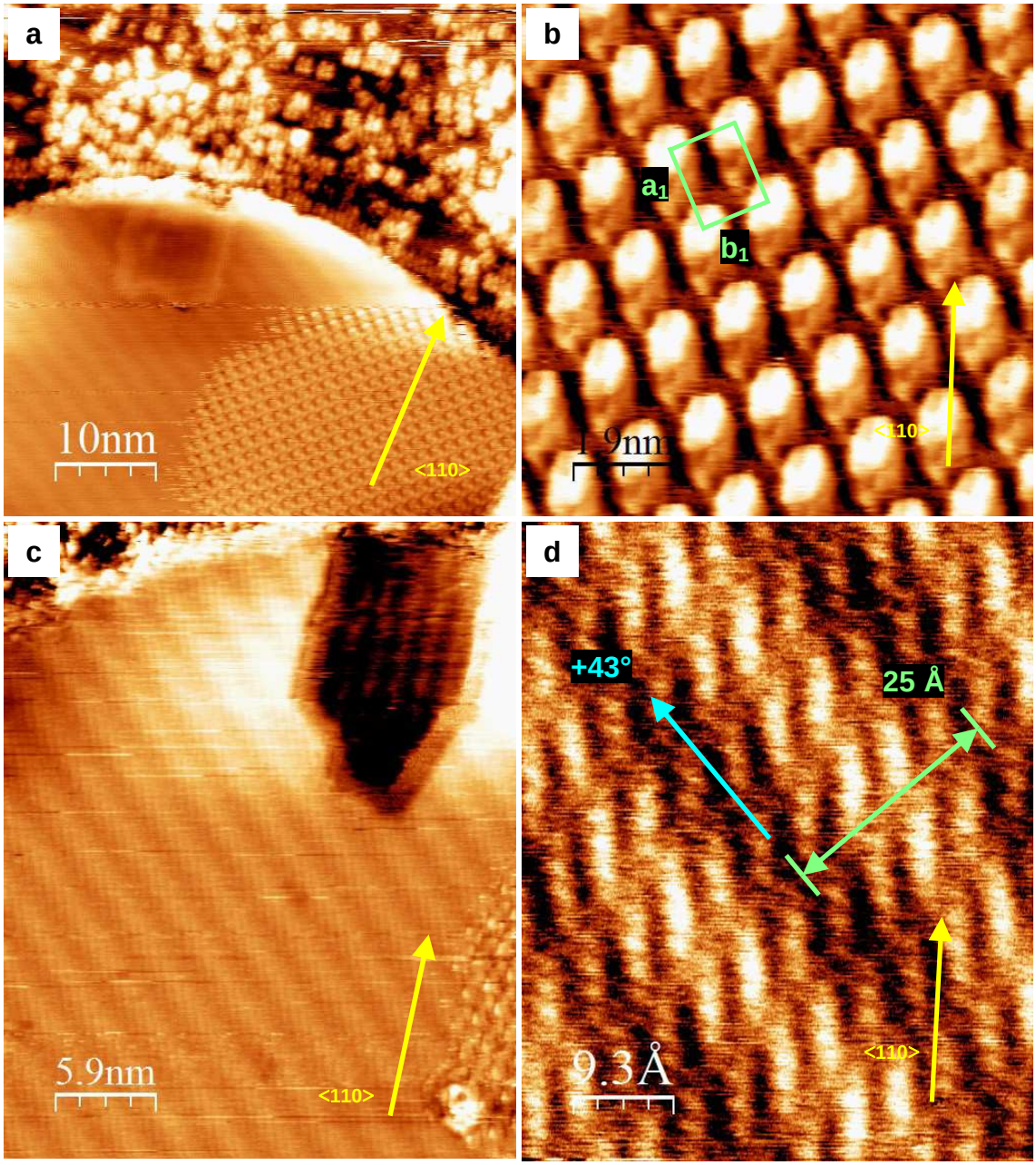

Figure 5-4. STM topographic images around self-assembled superstructure of Co-TPP molecules on top of graphene island on Cu(110) surface: (a) overview in 500 Å x 500 Å image, measured at U = +1816 mV and I = 0.20 nA; (b) the self-assembled superstructure of Co-TPP molecules in 93 Å x 93 Å image, measured at U = +76 mV and I = 0.20 nA, corrected with calibration factors X = 0.934 and Y = 1.495 for 100 Å x 100 Å image scans; (c) the stripe-patterned modulation of the Moiré superstructure for the graphene island around the self-assembled Co-TPP superstructure in 295 Å x 367 Å image, measured at U = +76 mV and I = 0.20 nA, corrected with calibration factors X = 0.984 and Y = 1.224 for 300 Å x 300 Å image scans; (d) atomic-resolution 46 Å x 58 Å image of the Moiré superstructure, measured at U = +141 mV and I = 0.20 nA, corrected with calibration factors X = 0.927 and Y = 1.771 for 50 Å x 50 Å image scans.

in terms of ππ interactions. Formation of chemical bonds to graphene is possible for porphyrins[4,5]. The substrate support to the graphene overlayer and

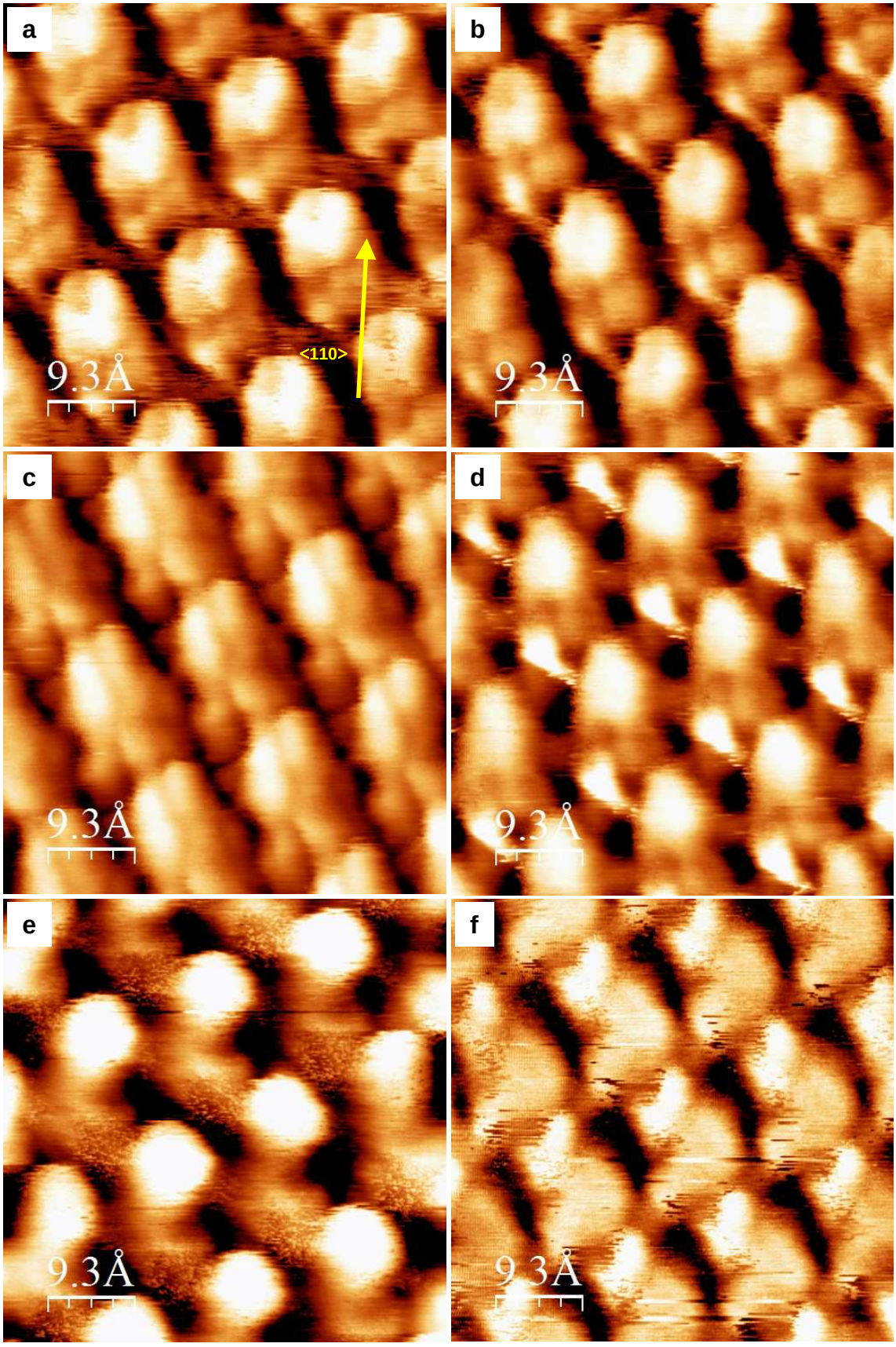

Figure 5-5. High-resolution 46 Å x 46 Å STM topographic images of the Co-TPP superstructure on graphene at various tunneling voltages at I = 0.20 nA, corrected with calibration factors X = 0.927 and Y = 1.771 for 50 Å x 50 Å image scans: (a) U = +76 mV; (b), (c) U = +141 mV; (d) U = +258 mV; (e) U = +874 mV; (f) U = +1816 mV.

the coordinated metal atom can influence the interaction between porphyrins and graphene[6,7]. Further elucidation can be found from theoretical calculations. Recent developments in DFT calculations account for the influence of substrate support to adsorption of porphine on the Moiré superstructure of graphene[5]. Figure 5-5 shows high-resolution images of the Co-TPP superstructure at different tunneling voltages for future reference.

Figure 5-4a also shows the Co-TPP superstructure does not cover a portion of the graphene island but faint stripes akin to a Moiré pattern can be observed. Indeed, Figure 5-4c shows a clear view of the stripes whilst a portion of the Co-TPP superstructure can be seen at the lower-right corner of the image. The atomic-resolution image in Figure 5-4d shows the stripe-patterned modulation comes from the Moiré superstructure of an exposed area of the graphene island around the Co-TPP superstructure. The observation of the Moiré superstructure is not trivial but establishes a proof of one important fact i.e. the absence of Co-TPP superstructure is real and not just an effect of the STM-tip condition. Therefore, whenever the Co-TPP superstructure does not cover an area of a graphene island, the area can be considered free of Co-TPP superstructure and the chances of an STM-tip effect can be considered improbable. The period of separation between stripes measures about 25 ± 3 Å after use of post-calibration factors. The direction of the stripes is oriented on the surface at about +43° from the <110> direction on the surface of the Cu substrate. The epitaxial orientation of the graphene island can therefore be estimated to be about +10°.

The second set of measurements were made on the island in Figure 5-3c and Figure 5-3d. Close-up view of the Co-TPP superstructure is shown in Figure 5-6a. The superstructure is described in a rectangular unit cell, where $\mathbf{a_2}$ measures a distance of 17.0 ± 1.7 Å at +25° from the <110> direction and $\mathbf{b_2}$ measures a distance 13.3 ± 1.3 Å at -65° from the <110> direction. The dimensions of the unit cell agree with those of the first superstructure in the limits of precision, but certain differences between the two superstructures can be pointed out. First, the superstructure orientations possess a minor difference of 5°. Second, the dimension of $\mathbf{a_2}$ is longer than the dimension of $\mathbf{a_1}$ to some

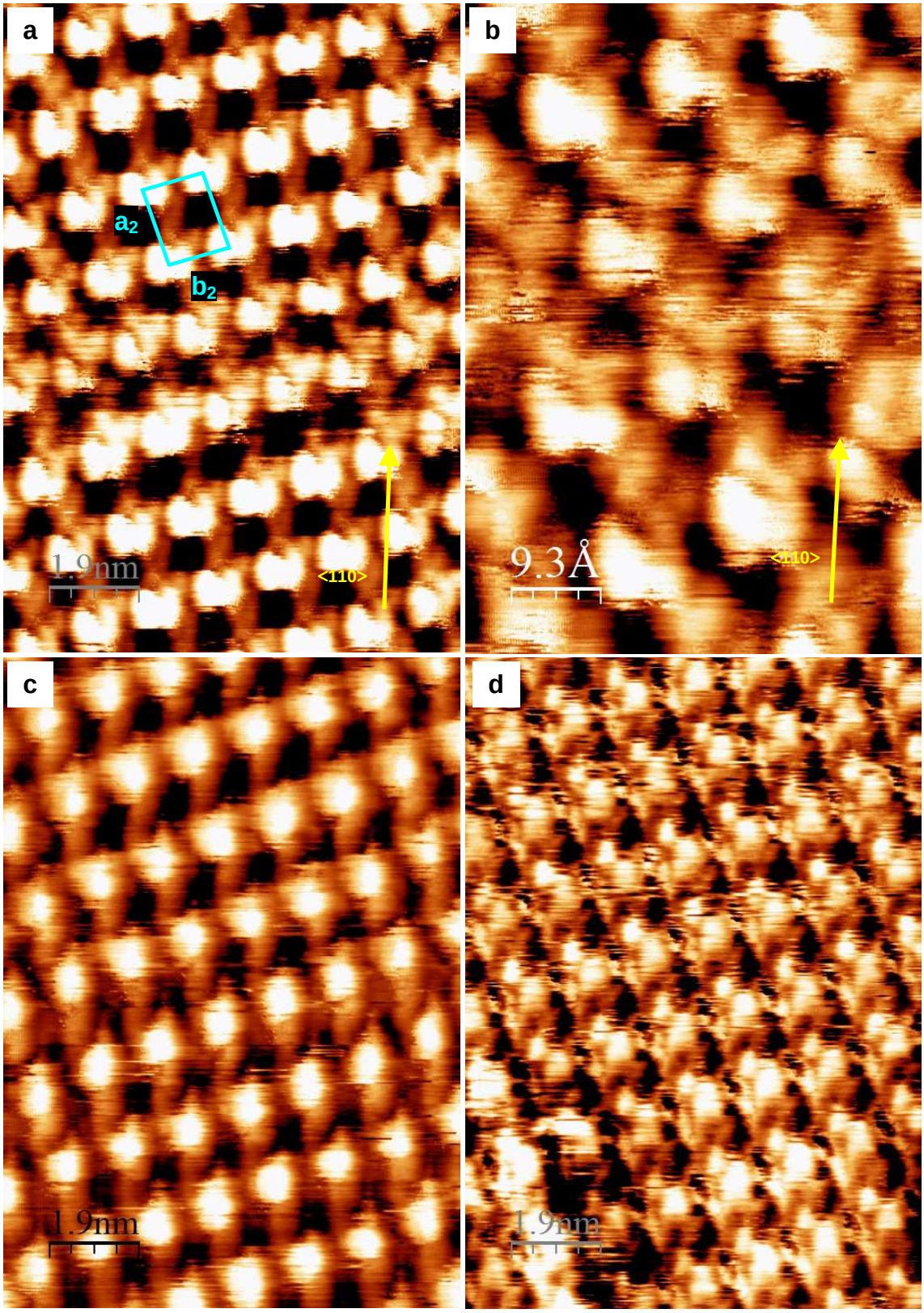

Figure 5-6. High-resolution STM topographic images of Co-TPP superstructure on graphene in another island: 93 Å x 133 Å images, measured at (a) U = +874 mV and I = 0.40 nA, (b) close-up view of (a) in 46 Å x 66 Å image, measured at U = +874 mV and I = 0.40 nA, (c) U = +292 mV and I = 0.20 nA, (d) U = +258 mV and I = 0.20 nA. The images are corrected with calibration factors X = 0.934 and Y = 1.495 for 100 Å x 100 Å image scans, and with calibration factors X = 0.927 and Y = 1.771 for 50 Å x 50 Å image scans.

extent. Third, the sub-molecular view in Figure 5-6b shows features different from those in Figure 5-5. Other measurements for the superstructure are shown in Figure 5-6c and Figure 5-6d but the features also cannot compare to the features of the first superstructure. These facts suggest the two superstructures described here are not identical to each other and Co-TPP molecules perhaps form diverse superstructures on graphene from subtle differences to one another. No measurement was made for the stripe-patterned modulation on the graphene below the second superstructure so as a consequence no comment on the role of Moiré superstructure on the formation of Co-TPP superstructure can be made so far. Past reports show the Moiré superstructure of graphene can influence the location of adsorption and can act as a template to formation of molecular superstructures[8–13]. Nonetheless, the organization of the achiral Co-TPP molecules is chiral with respect to the stripe-patterned modulation of the Moiré superstructure on the Cu(110) surface. The complex system of Co-TPP molecules on graphene on the (110)-oriented Cu substrate therefore represents a double chiral structure.

Figure 5-7a and Figure 5-7c show the order in the Co-TPP superstructures are continuous even across surface steps. Figure 5-7a corresponds to the second superstructure whilst Figure 5-7c corresponds to the first superstructure. The Figure 5-7b shows the height profile to the scan line in Figure 5-7a. The change in height corresponds to a mono-atomic step. On the other hand, the height profile in Figure 5-7d for the scan line in Figure 5-7c shows no less than bi-atomic step. The latter suggests the continuous character of Co-TPP superstructure on graphene is independent of the topographic nature of the Cu(110) surface.

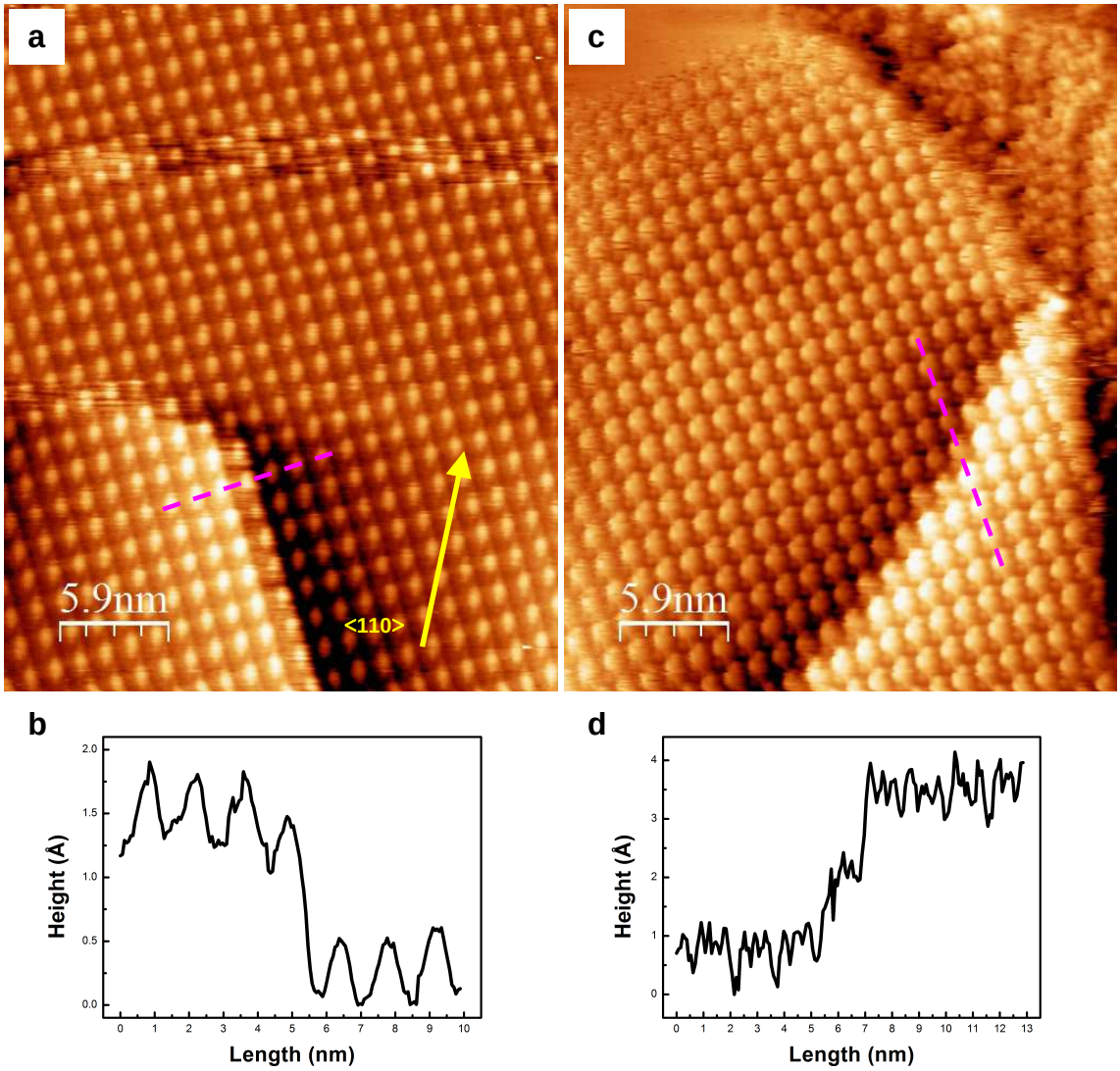

Figure 5-7. STM topographic measurements to show the continuous character of Co-TPP superstructure on graphene over Cu(110) surface steps. (a) 295 Å x 367 Å image over a mono-atomic step, measured at U = +1816 mV and I = 0.20 nA; (b) height profile for the scan line over the surface step in (a); (c) 295 Å x 367 Å image over a multi-atomic step, measured at U = +141 mV and I = 0.20 nA; (d) height profile for the scan line over the surface step in (c). The images are corrected with calibration factors X = 0.984 and Y = 1.224 for 300 Å x 300 Å image scans.

Intrinsic Self-Healing Character of Self-Assembled Co-TPP Superstructure

Repeated STM measurements were performed on one island of the Co-TPP superstructure on top of a graphene island. The sequence of events in Figure 5-8 shows some part of the Co-TPP superstructure ceases to exist for some reason at one point in time but tends to reform afterwards. In other words, the evidence demonstrates Co-TPP molecules on graphene can re-assemble into the superstructure from demolition, hence the potential for application as a self-healing material in two dimensions. Another sequence of events in Figure 5-9 shows the Co-TPP superstructure reproduces an extension to another location and ceases to exist at one location.

The STM tip proves to be the source of demolition from a number of evidences. Figure 5-10 shows an overview and close-up views from scans in various directions to demonstrate the island edge of the superstructure tends to be parallel to the horizontal direction of scan as the dashed lines indicate. Perhaps, the observation also demonstrates the concept of creating nano-patterned self-assembled superstructure under the manipulation of STM is possible. Figure 5-11 shows an example of dual scans in both forward and backward directions. A clear increase in size of the superstructure island can be seen towards the horizontal direction for the backward scan in comparison to the forward scan from the overviews in Figure 5-11a and Figure 5-11b. The image is jagged and blurred around the edge where the STM tip crosses onto or out of the superstructure island as can be seen from the close-up views in Figure 5-11c and Figure 5-11d. These observations show STM tip tends to move Co-TPP molecules and demolish the superstructure as the scan approaches the island edge in both directions. The demolition becomes improbable when the scan has moved onto or is restricted on the island from the edges. The increase in size of the superstructure island in the backward scan in comparison to the forward scan presents two facts. One is the step-up approach of the STM tip across the island edge in the forward scan causes more demolition than the step-down departure from the top of the island in the backward scan. The other is the Co-TPP molecules tend to re-assemble into the superstructure from the demolition after the STM tip crosses onto the

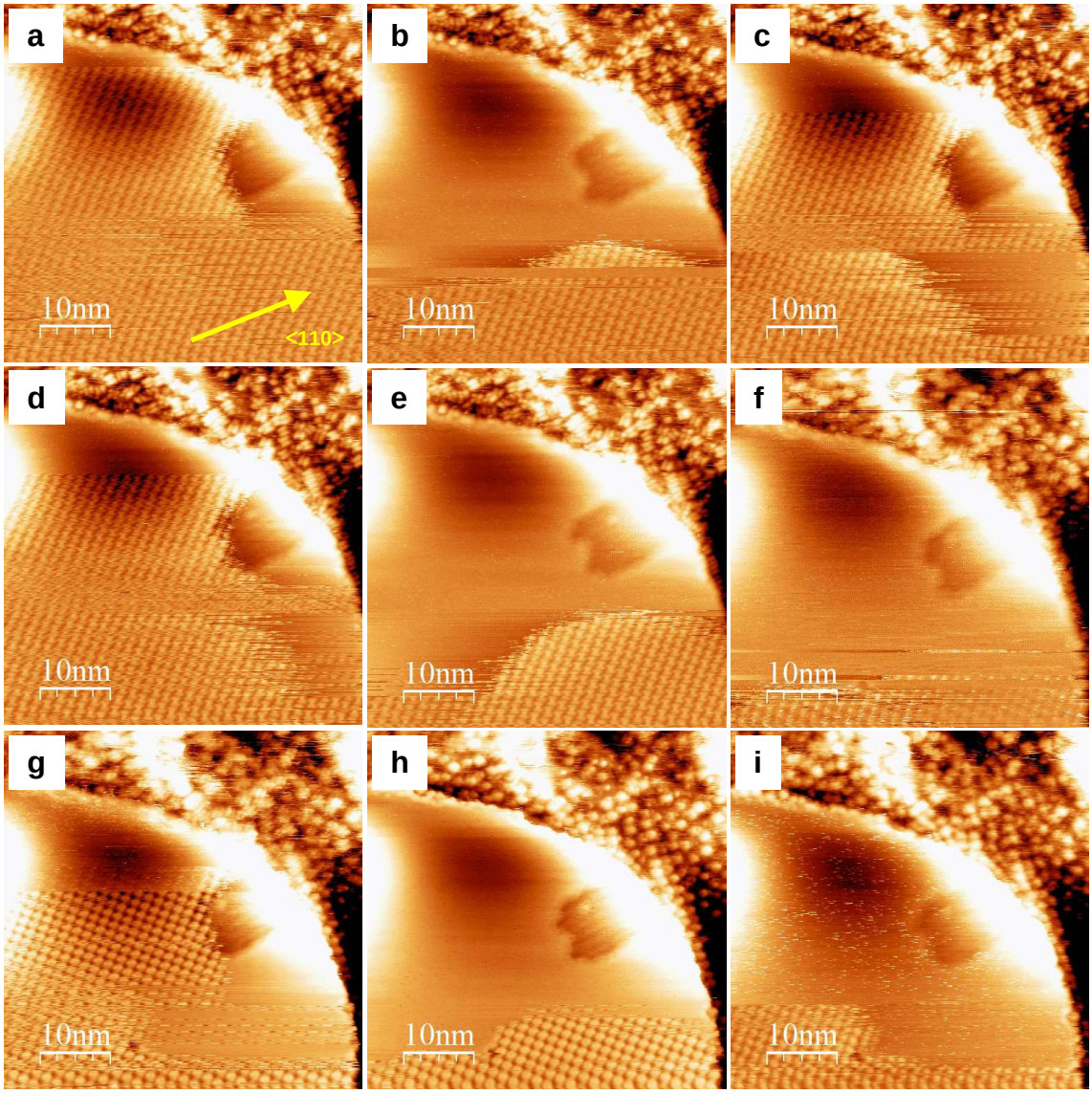

Figure 5-8. Sequence of 500 Å x 500 Å STM topographic images of self-assembled superstructure of Co-TPP molecules on top of graphene island on Cu(110) surface at same location to show the superstructure tends to recover from demolition. STM measurements were performed at 45°-scan direction, U = +1816 mV, and I = 0.20 nA.

superstructure island in the forward scan in the meantime whilst the STM tip is over the island before the backward scan steps down from the island. Figure 5-12 shows measurements at reduced voltages of 141 mV for (a) and 76 mV for (b). The same island in Figure 5-11 was measured at 1816 mV. These measurements show reduction in voltage decreases the island size and increases the extent of blur in the Co-TPP superstructure from the island edges towards the interior of the island. One can expect further reduction in voltage would lead to complete demolition of the island. The sequence of events in

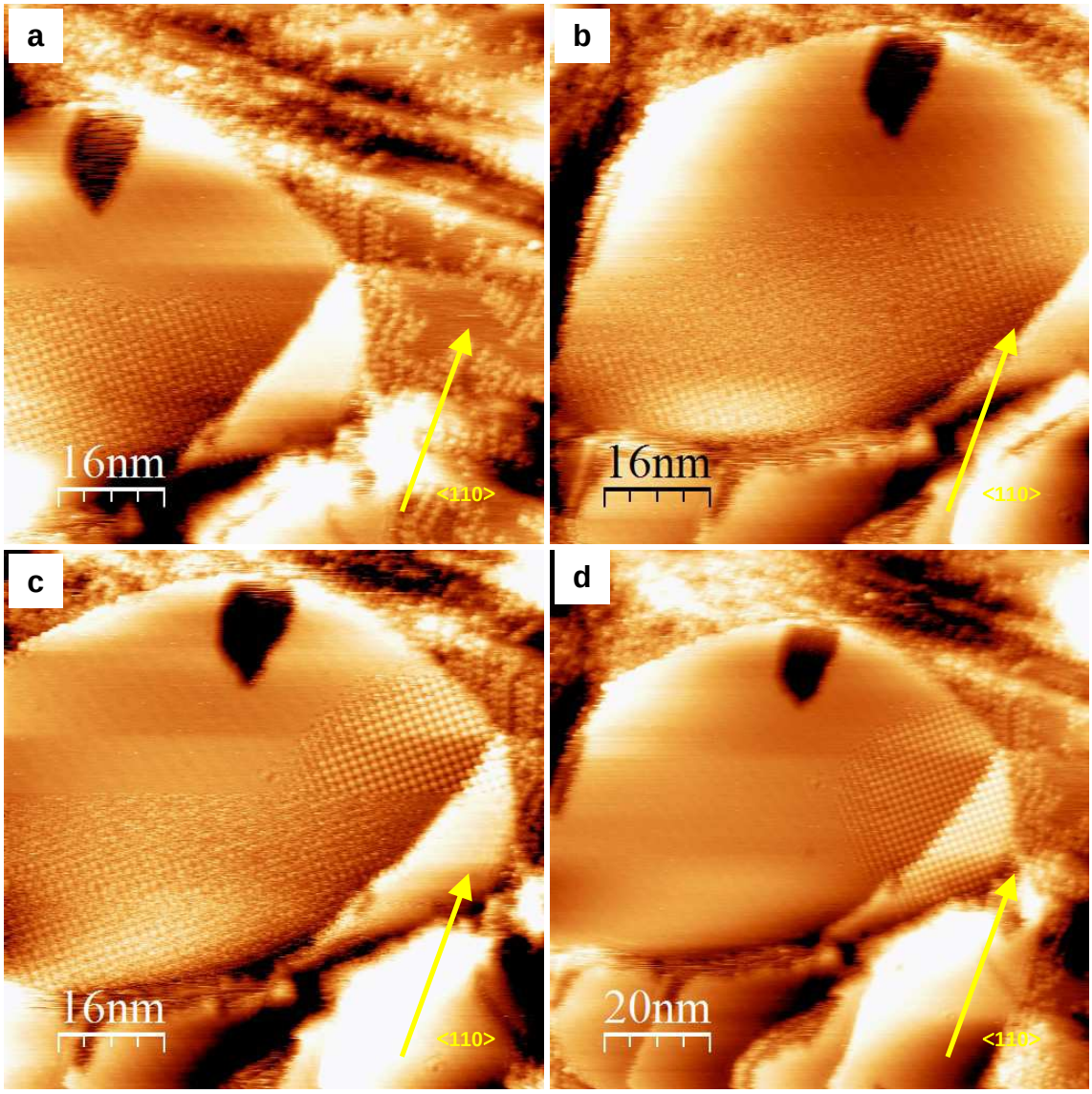

Figure 5-9. Sequence of STM topographic images of self-assembled superstructure of Co-TPP molecules on top of graphene island on Cu(110) surface around same location to show the superstructure reproduces an extension to another location but ceases to exist at one location: (a) – (c) 800 Å x 800 Å image; (d) 1000 Å x 1000 Å image. STM measurements were performed at U = +141 mV and I = 0.20 nA.

Figure 5-13 shows measurements for voltage decrease from 910 mV to 269 mV and subsequent increase to 874 mV and demonstrates the superstructure can recover from partial demolition upon reversion of voltage. For the island in Figure 5-13, the demolition starts below 495 mV and complete demolition can be expected below 269 mV.

The exact reason for the demolition is unknown. One could expect the demolition of the superstructure must come from increased mechanical contact as the STM tip narrows down the distance to the surface. Whilst voltage affects

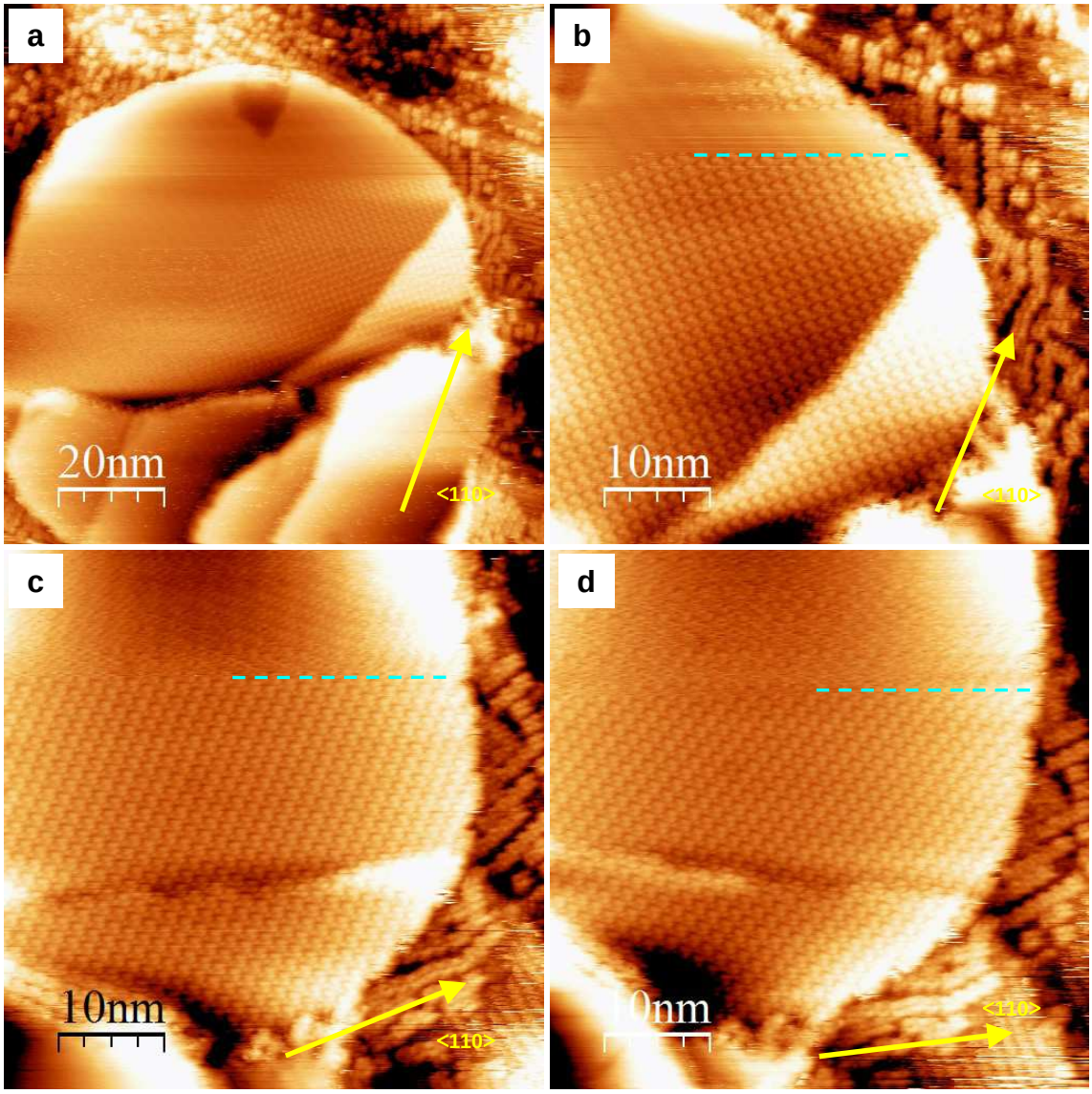

Figure 5-10. STM topographic images of self-assembled superstructure of Co-TPP molecules on top of graphene island on Cu(110) surface at various scan directions at same location to demonstrate evidence of influence from the STM tip as the island edge of the superstructure tends to be parallel to the horizontal direction of scan: (a) overview in 1000 Å x 1000 Å image at 0°-scan direction; close-up view in 500 Å x 500 Å image at (b) 0°, (c) 45°, (d) 60°-scan direction. The dashed lines indicate the island edge of the Co-TPP superstructure. STM measurements were performed at U = +1816 mV and I = 0.20 nA.

the distance between STM tip and surface to some extent, one can remember the current holds the main control. However, mechanical contact does not seem to be the main reason for the demolition as Figure 5-13d shows the island recovers back to the original size in Figure 5-13b despite the tunneling current at 0.4 nA not returned to 0.2 nA. The observation suggests decrease in voltage effects demolition of the superstructure for some other reason.

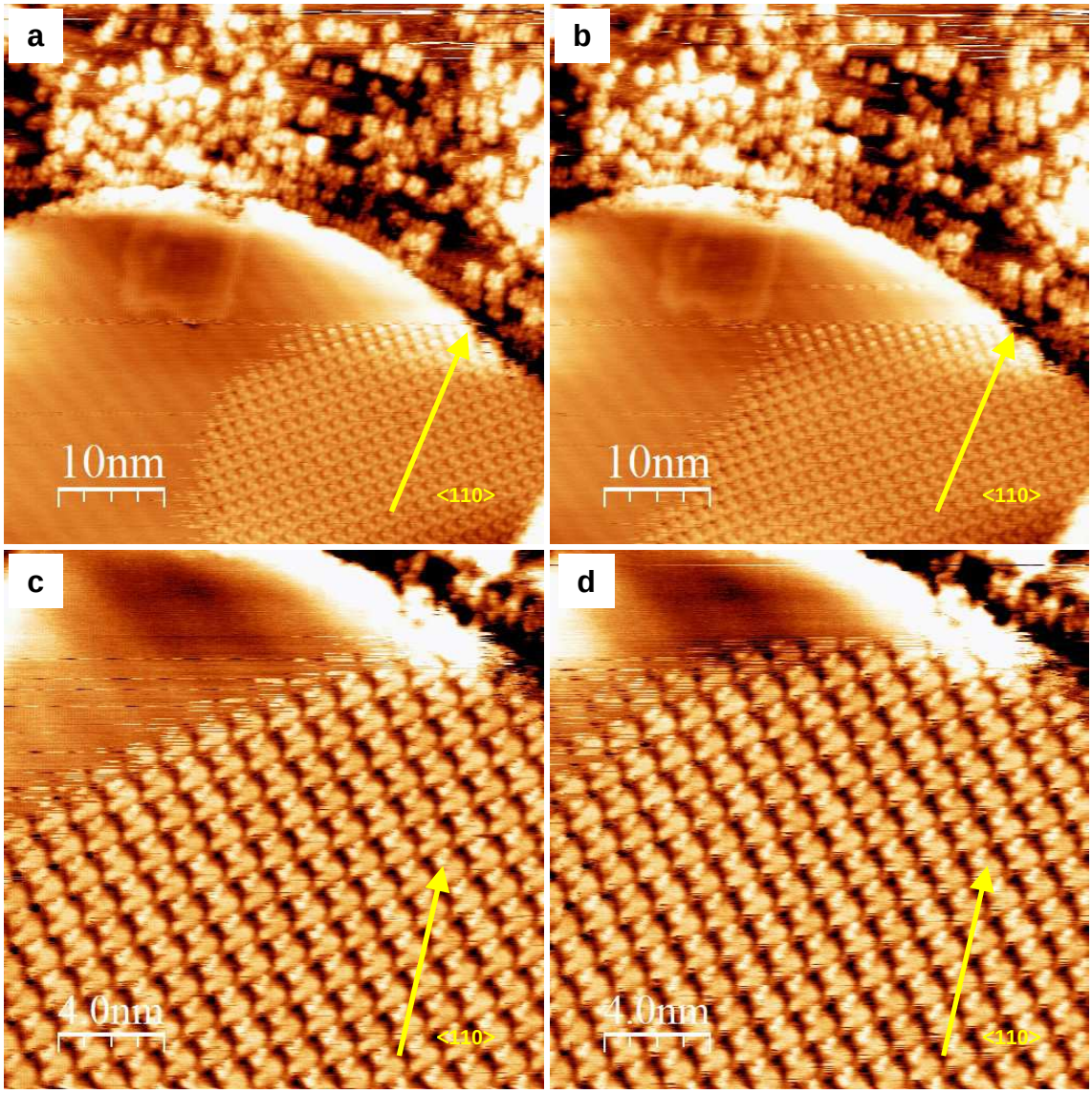

Figure 5-11. STM topographic images of self-assembled superstructure of Co-TPP molecules on top of graphene island on Cu(110) surface at same location to show the STM tip tends to move Co-TPP molecules and demolish the superstructure as the STM tip crosses onto or out of the superstructure island, but demolition becomes improbable when the scan has moved onto or is restricted on the island from the edges. Moreover, the step-up approach of the STM tip across the island edge causes more demolition than the step-down departure from the top of the island, but the Co-TPP molecules tend to re-assemble into the superstructure from the demolition after the STM tip crosses onto the superstructure island in the meantime whilst the STM tip is over the island. Overview in 500 Å x 500 Å image for (a) forward scan and (b) backward scan; close-up view in 200 Å x 200 Å image for (c) forward scan and (d) backward scan. STM measurements were performed at U = +1816 mV and I = 0.20 nA.

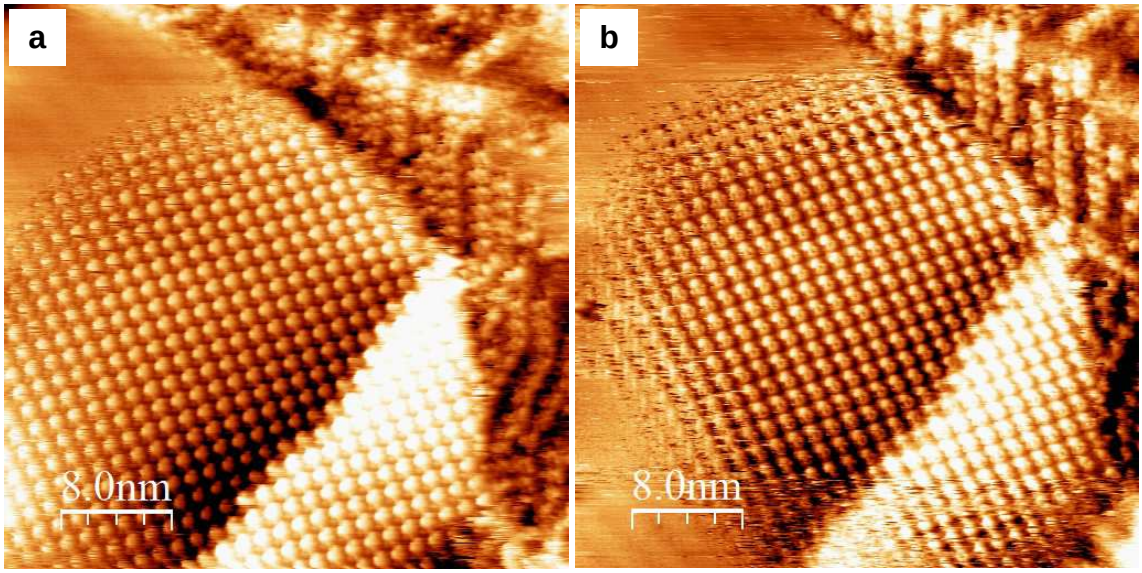

Figure 5-12. 400 Å x 400 Å STM topographic images of self-assembled superstructure of Co-TPP molecules on top of graphene island on Cu(110) surface around same location to demonstrate evidence of influence from the STM tip as reduction in tunneling voltage decreases the island size and increases the extent of blur in the Co-TPP superstructure from the island edges towards the interior of the island. Measurements at: (a) U = +141 mV and I = 0.20 nA; (b) U = +76 mV and I = 0.20 nA.

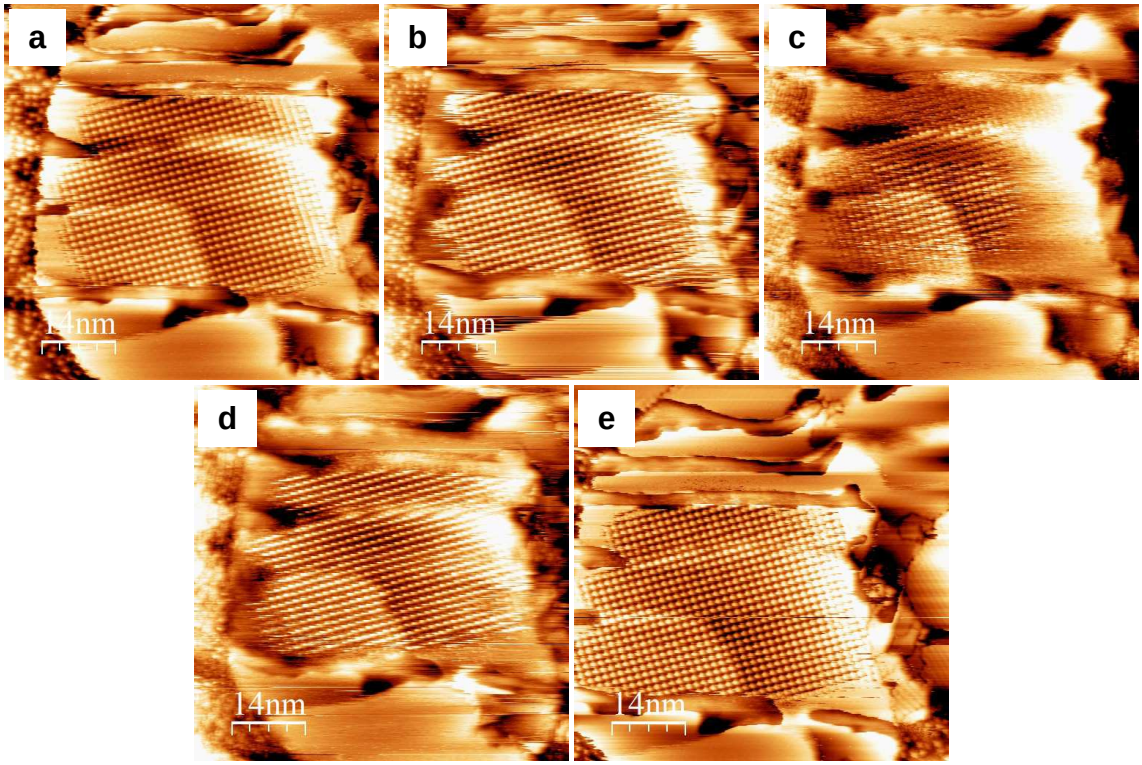

Figure 5-13. Sequence of 700 Å x 700 Å STM topographic images of self-assembled superstructure of Co-TPP molecules on top of graphene island on Cu(110) surface around same location to show demolition of the superstructure at decreased tunneling voltage but can recover upon reversion of voltage. Demolition for the particular island starts below 495 mV and complete demolition can be expected below 269 mV: (a) U = +910 mV and I = 0.20 nA; (b) U = +495 mV and I = 0.20 nA; (c) U = +269 mV and I = 0.40 nA; (d) U = +495 mV and I = 0.40 nA; (e) U = +874 mV and I = 0.40 nA. The increase in tunneling current does not seem to exert much influence.

5.3 Conclusion to Self-Assembled Co-TPP Superstructure on Sub-monolayer Graphene on Cu(110) Surface

The growth of a Co-TPP superstructure on top of graphene islands is observed upon adequate accumulation of the molecules on the Cu(110) surface. The superstructures possess subtle deviation from each other, but in essence consist of one molecule in a rectangular unit cell and are continuous over surface steps. Demolition of the superstructure happens as the STM tip crosses the edge of the superstructure islands and becomes more effective at reduced tunneling voltages. However, the Co-TPP molecules on graphene tend to re-assemble into the superstructure from demolition – in other words, the behaviour demonstrates possible application as a self-healing material in two dimensions.

Prospects for further work on Co-TPP on sub-monolayer graphene on Cu(110) surface can include exploration of the Co-TPP superstructure in relation to the Moiré superstructure and theoretical studies to elucidate the details of the Co-TPP superstructure, and the intermolecular and molecule-substrate interactions.

References

1. Eley, D. D. & Spivey, D. I. Semiconductivity of organic substances.–Part 8.-Porphyrins and dipyrromethenes. *Trans. Faraday Soc.* **58,** 405 (1962).

2. Donovan, P., Robin, A., Dyer, M. S., Persson, M. & Raval, R. Unexpected deformations induced by surface interaction and chiral self-assembly of Co(II)-tetraphenylporphyrin (Co-TPP) adsorbed on Cu(110): a combined STM and periodic DFT study. *Chemistry* **16,** 11641–52 (2010).

3. Auwärter, W. *et al.* Site-specific electronic and geometric interface structure of Co-tetraphenyl-porphyrin layers on Ag(111). *Phys. Rev. B* **81,** 245403 (2010).

4. Altenburg, S. J., Lattelais, M., Wang, B., Bocquet, M.-L. & Berndt, R. Reaction of phthalocyanines with graphene on Ir(111). *J. Am. Chem. Soc.* (2015).

5. Lattelais, M. & Bocquet, M.-L. Cycloaddition of metal porphines on metal-supported graphene: a computational study. *J. Phys. Chem. C* **119,** 9234–9241 (2015).

6. Geng, F. *et al.* Tunneling electron induced luminescence from porphyrin molecules on monolayer graphene. *J. Lumin.* **157,** 39–45 (2015).

7. Dou, W., Huang, S., Zhang, R. Q. & Lee, C. S. Molecule-substrate interaction channels of metal-phthalocyanines on graphene on Ni(111) surface. *J. Chem. Phys.* **134,** 094705 (2011).

8. Barja, S. *et al.* Self-organization of electron acceptor molecules on graphene. *Chem. Commun.* **46,** 8198–200 (2010).

9. Pollard, A. J. *et al.* Supramolecular assemblies formed on an epitaxial graphene superstructure. *Angew. Chemie (International ed.)* **49,** 1794–9 (2010).

10. Roos, M. *et al.* Intermolecular vs molecule-substrate interactions: a combined STM and theoretical study of supramolecular phases on graphene/Ru(0001). *Beilstein J. Nanotechnol.* **2,** 365–73 (2011).

11. Mao, J. *et al.* Tunability of supramolecular Kagome lattices of magnetic phthalocyanines using graphene-based moire patterns as templates. *J. Am. Chem. Soc.* **131,** 14136–7 (2009).

12. Zhang, H. G. *et al.* Assembly of iron phthalocyanine and pentacene molecules on a graphene monolayer grown on Ru(0001). *Phys. Rev. B* **84,** 245436 (2011).

13. Zhou, H. *et al.* Template-directed assembly of pentacene molecules on epitaxial graphene on Ru(0001). *Nano Res.* **6,** 131–137 (2013).